

Cleavage Fracture Micromechanisms of High Strength Steel and its Heat-Affected Zones

Morete Barbosa Bertolo, V.

DOI

[10.4233/uuid:ac984b23-c4e1-4bf4-9668-5e3d54aec3ff](https://doi.org/10.4233/uuid:ac984b23-c4e1-4bf4-9668-5e3d54aec3ff)

Publication date

2023

Document Version

Final published version

Citation (APA)

Morete Barbosa Bertolo, V. (2023). *Cleavage Fracture Micromechanisms of High Strength Steel and its Heat-Affected Zones*. [Dissertation (TU Delft), Delft University of Technology].
<https://doi.org/10.4233/uuid:ac984b23-c4e1-4bf4-9668-5e3d54aec3ff>

Important note

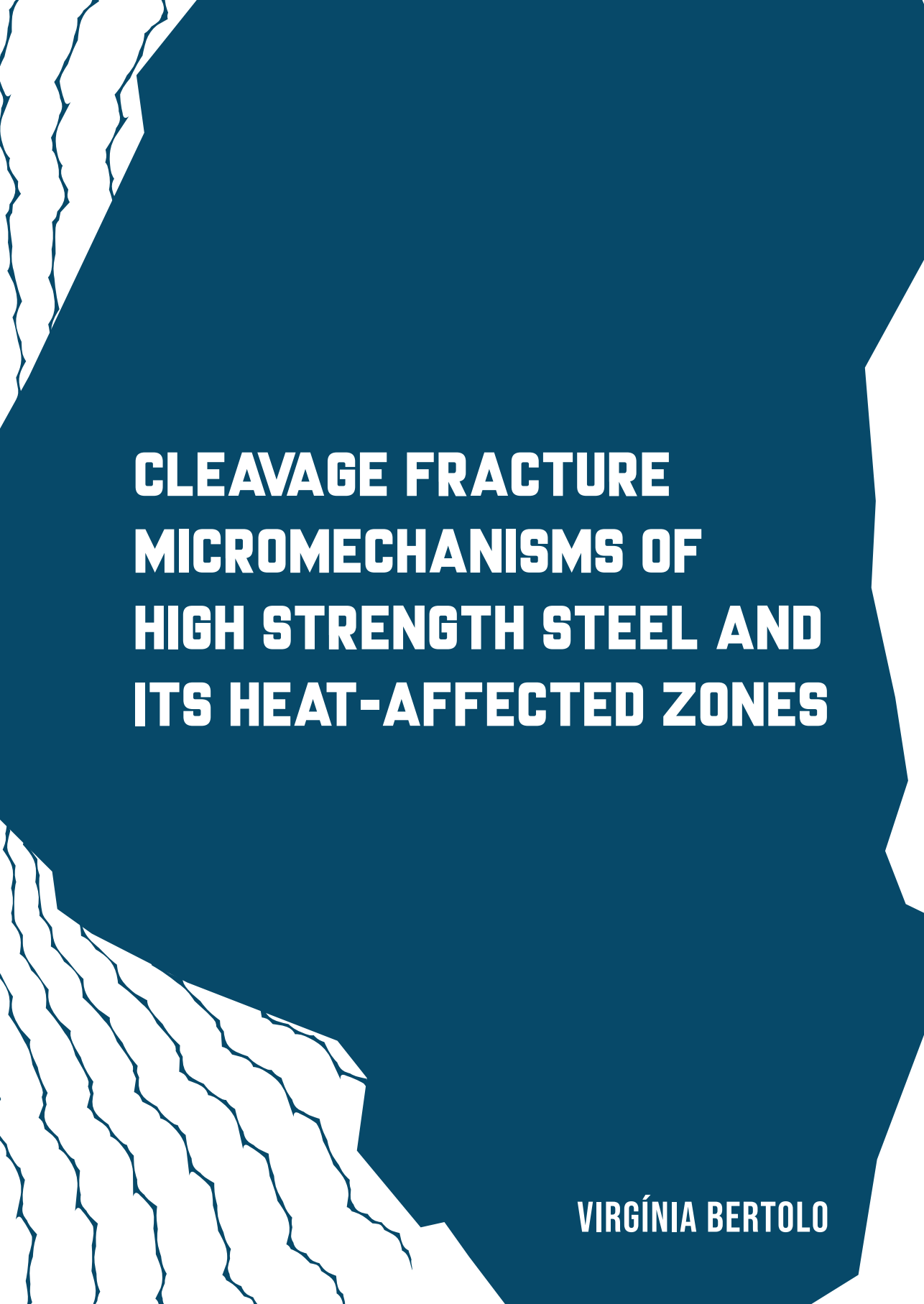
To cite this publication, please use the final published version (if applicable).
Please check the document version above.

Copyright

Other than for strictly personal use, it is not permitted to download, forward or distribute the text or part of it, without the consent of the author(s) and/or copyright holder(s), unless the work is under an open content license such as Creative Commons.

Takedown policy

Please contact us and provide details if you believe this document breaches copyrights.
We will remove access to the work immediately and investigate your claim.



CLEAVAGE FRACTURE MICROMECHANISMS OF HIGH STRENGTH STEEL AND ITS HEAT-AFFECTED ZONES

VIRGÍNIA BERTOLO

CLEAVAGE FRACTURE MICROMECHANISMS OF HIGH STRENGTH STEEL AND ITS HEAT-AFFECTED ZONES

CLEAVAGE FRACTURE MICROMECHANISMS OF HIGH STRENGTH STEEL AND ITS HEAT-AFFECTED ZONES

Dissertation

for the purpose of obtaining the degree of doctor
at Delft University of Technology,
by the authority of the Rector Magnificus, Prof. Dr. Ir. T.H.J.J. van der Hagen,
chair of the Board of Doctorates,
to be defended publicly on Friday 24 March 2023 at 10:00 a.m.

by

Virgínia MORETE BARBOSA BERTOLO

Master of Science in Metallurgical and Materials Engineering,
Universidade Federal do Rio de Janeiro, Brazil,
Born in Rio de Janeiro, Brazil.

This dissertation has been approved by the promotor.

Composition of the doctoral committee:

Rector Magnificus,	chairperson
Prof. dr. ir. J. Sietsma,	Delft University of Technology, promotor
Dr. V. Popovich,	Delft University of Technology, copromotor
Dr. C. L. Walters,	Delft University of Technology, copromotor

Independent members:

Dr. I. Sabirov,	Madrid Institute for Advanced Studies
Prof. dr. ir. P. Verleysen,	Ghent University
Prof. dr. L. Delannay,	Louvain Catholic University
Prof. dr. M. J. Santofimia Navarro,	Delft University of Technology

Reserve Member:

Prof. dr. ir. L. A. I. Kestens,	Delft University of Technology
---------------------------------	--------------------------------



Lloyd's
Register



Ministerie van Defensie

This research was carried out with the financial support of the Netherlands Organization for Scientific Research (NWO) under project number 16350.

Keywords: High strength steels, multiphase, microstructural characterisation, cleavage, fracture toughness, heat-affected zones, grain refinement

Printed by: ProefschriftMaken

Cover: The cover art represents a cleavage facet and river lines converging to a likely initiation size — features that are typically observed in cleavage fracture surfaces.

Cover by: Gabi Motta

Copyright © 2023 by V. Morete Barbosa Bertolo

E-mail: v.moretebarbosabertolo@tudelft.nl/vmbbertolo@gmail.com

ISBN 978-94-6469-265-5

An electronic version of this dissertation is available at

<http://repository.tudelft.nl/>.

CONTENTS

Summary	vii
1 Introduction	1
1.1 Material-related challenges	2
1.1.1 Strength <i>vs</i> Toughness	2
1.1.2 Ductile-to-brittle transition	3
1.1.3 Inhomogeneous microstructures	4
1.2 Research Objectives and Thesis Outline.	4
References	5
2 Theoretical Background	9
2.1 High Strength Steels.	10
2.1.1 Hot rolling	10
2.1.2 Quenched and tempered steels	10
2.1.3 Thick-section high strength steels	12
2.2 Welds and their complex microstructures.	14
2.3 Cleavage Fracture.	16
2.4 Microstructural Features Affecting Cleavage Fracture	17
2.4.1 Grains	18
2.4.2 Carbides	18
2.4.3 Inclusions	19
2.4.4 M-A Constituents	20
2.4.5 Centreline Segregation Bands	20
2.4.6 Residual stresses	21
2.5 Conclusions.	23
References	23
3 A Comprehensive Quantitative Characterisation of the Multiphase Microstructure of a Thick-Section High Strength Steel	31
3.1 Introduction	32
3.2 Materials and methods	34
3.3 Results	37
3.3.1 Through-thickness microstructural characterisation.	37
3.3.2 Hardness Measurements.	50
3.3.3 Through-Thickness Fracture Behaviour	53
3.4 Discussion	53
3.4.1 Through Thickness Microstructural Inhomogeneity	53
3.4.2 Microstructure – Hardness Relationship	56
3.4.3 Potential Microstructural Aspects Affecting Fracture Toughness	57
3.5 Conclusions.	58
References	60

4	Cleavage Fracture Micromechanisms in Thick-Section Quenched and Tempered S690 High Strength Steels	67
4.1	Introduction	68
4.2	Materials and Methods	70
4.2.1	Material	70
4.2.2	Methods	72
4.2.2.1	Characterisation of Fracture Properties	72
4.2.2.2	Characterisation of Fracture Surface and Profile	74
4.3	Results and Discussion	75
4.3.1	Effect of Notch Orientation and Constraint	76
4.3.2	Microstructural Factors Controlling Cleavage Crack Initiation	80
4.3.3	Microstructural Factors Affecting Cleavage Crack Propagation.	83
4.3.4	Conclusions	90
	References	92
5	Cleavage Fracture Micromechanisms in Simulated Heat Affected Zones of S690 High Strength Steels	97
5.1	Introduction	98
5.1.1	Materials and Methods.	99
5.2	Results	103
5.2.1	Microstructural Characterisation of HAZs	103
5.2.2	Mechanical Behaviour of Simulated HAZs	110
5.2.3	Microstructural features affecting cleavage fracture in HAZs.	112
5.2.3.1	Cleavage Initiation	112
5.2.3.2	Cleavage Propagation.	113
5.3	Discussion	114
5.4	Conclusions.	122
	References	123
6	Grain Refinement by Rapid Cyclic Heating and its Effect on Cleavage Fracture Behaviour of an S690 High Strength Steel	129
6.1	Introduction	130
6.2	Materials and Methods	131
6.3	Results	135
6.4	Discussion	141
6.4.1	Microstructural Transformations due to Grain Refinement	141
6.4.2	Grain Refinement Effect on Mechanical and Fracture Behaviour.	145
6.5	Conclusions.	147
	References	148
7	General Discussion and Conclusions	153
8	Recommendations	157
	Acknowledgements	161
	Curriculum Vitæ	165
	List of Publications	167

SUMMARY

The use of materials in increasingly severe service conditions raises concerns about structural safety with respect to cleavage fracture. There are three main material-related challenges that structures face under harsh environments: 1) the trade-off between strength and toughness; 2) the ductile-to-brittle transition behaviour of BCC high strength steels; 3) the inhomogeneous microstructures found in multiphase steels, thick-section steels, and welded structures. Therefore, the objective of this research is to systematically investigate the cleavage fracture micromechanisms in high strength steels considering diverse microstructures (e.g., as-received commercial steel, thermally simulated heat-affected zones, and grain refined microstructure) and experimental conditions (e.g., plastic constraint and temperature). Thereby, this study provides a thorough understanding of the effect of the microstructural details on cleavage fracture behaviour of high strength steel structures allowing for failure control and improvement of cleavage-resistant steel's design.

For this purpose, a through-thickness in-depth microstructural characterisation of a commercially available 80-mm thick-section quenched and tempered S690 high strength steel was performed. The top quarter and middle sections of the plate were examined by optical microscopy, scanning electron microscopy with energy-dispersive X-ray spectroscopy (SEM/EDS), electron probe microanalyser (EPMA), electron backscatter diffraction (EBSD), and hardness measurements (micro-Vickers and nanoindentation). The cleavage fracture behaviour was analysed via three-point bending tests at $-100\text{ }^{\circ}\text{C}$, a temperature where the material is on the lower shelf of the ductile-to-brittle transition curve (cleavage is dominant). The effect of notch orientation and plastic constraint on fracture behaviour was analysed by placing the notch parallel and perpendicular to the rolling direction and varying the crack depth-to-width ratio (a/W): 0.5, 0.25, and 0.1. Afterwards, the fracture surface was analysed by SEM to identify the crack initiation site and the transverse section of the fracture surface was analysed by SEM and EBSD to determine the microstructural role in crack propagation. The middle section of the steel plate has been identified as the most critical for fracture toughness due to its high density and large sizes of cubic Nb-rich inclusions, larger prior austenite grain (PAG) sizes, and the presence of hard segregation bands. The criticality of the middle section was confirmed by fracture toughness tests. The fracture toughness of the middle section is the lowest and results from the crack initiation from Nb-rich inclusions. The embrittling effect of these particles is also seen when varying the crack plastic constraint. It is widely known that a lower plastic constraint leads to an increase in plastic contribution during fracture. However, it has been observed that the plastic constraint effect on fracture toughness is significant only when the crack initiates from oxides, while its influence is none or is minor when the crack initiates from more brittle inclusions, e.g., Nb-rich. Thus, brittle hard particles are considered the most critical initiation sites for cleavage fracture in the sampled high strength steel. Regarding the crack propagation, it is predominantly transgranular along $\{001\}$ and $\{110\}$ planes where the crack deflects in PAGs and packets and block boundaries of tempered lath

martensite and lath bainite when the neighbouring sub-structure has a different Bain axis. In a few specimens, local intergranular fracture was seen and mainly attributed to the presence of Nb-rich inclusions at the PAG boundaries.

Structural components are commonly joined by welding, and the welding thermal input is responsible for the generation of poor-toughness microstructures in the heat-affected zone (HAZ). Thus, thermal simulations of the most critical areas, coarse-grained and intercritically reheated HAZ (CGHAZ and ICCGHAZ, respectively), were carried out via Gleeble, and their microstructures and cleavage fracture toughness and micromechanisms were investigated. The same techniques used for the as-received steel were applied here, but the three-point bending tests were performed at $-40\text{ }^{\circ}\text{C}$, which corresponds to the lower shelf of the ductile-to-brittle transition curve of HAZ. In general, martensite-austenite (M-A) constituents are recognised as the most critical features in the HAZs. In this work, although Nb-rich inclusions remain present in the HAZ, the M-A constituents are the ones observed triggering fracture in both CGHAZ and ICCGHAZ. However, the fact that they are small makes them ineffective in reaching the critical crack length for fracture. In this case, the crack propagation step is of high relevance for the crack to extend to the critical length and the matrix phases are the critical and determinant microstructural features. In this case, the CGHAZ, mostly auto-tempered martensite, presented the lowest CTOD values compared to the ICCGHAZs, mostly granular bainite. The M-A constituents were also observed to play a role in the propagation process. M-A constituents with internal high-angle sub-structures boundaries and internal plastic strains are able to deflect or arrest secondary cracks. Moreover, the crack interaction with grain boundaries in the propagation step was similar to what was observed for the commercially available steel.

Finally, as grain refinement is a well-founded procedure to simultaneously increase material strength and toughness this work investigated whether grain refinement would result in fracture toughness improvement in the presence of such detrimental Nb-rich inclusions. For this, a rapid cyclic heat treatment was performed for grain refinement followed by quenching and tempering steps to produce a final microstructure equivalent to that of the as-received material for comparison. The microstructure and the fracture behaviour at $-100\text{ }^{\circ}\text{C}$, tested temperature for the as-received steel, were characterised using most of the techniques previously mentioned. It has been observed that the PAG was effectively reduced by 55% compared to the as-received material, leading to fracture toughness improvement. However, the improvement level depends on the initiation site. Nb-rich inclusions are observed to trigger fracture on specimens that result in the lowest CTOD values. On the other hand, oxide inclusions and carbides result in the highest CTOD values. The grain refinement treatment led to an increase by factors up to 2.5 and 8.6 in the lower- and upper-bound of fracture toughness values, respectively.

An interesting observation in tested low-constraint specimens and grain-refined specimens, where plastic deformation has a larger contribution, is that alternative initiation sites are activated. For instance, in high-constraint specimens of the as-received steel, Nb-rich inclusions are the only identified initiation sites for the middle section. In low-constraint specimens, oxides, and in grain refined specimens, oxides and probably cementite particles, are observed triggering fracture. This is attributed to the fact that, if an Nb-rich inclusion is not located in front of the crack tip, the crack will propagate in a

stable manner, expanding the plastic zone ahead of the crack tip and sampling a larger amount of microstructural features that could not be present in the previous fracture steps. Then, the chance of other features getting involved in the fracture process is increased.

These findings provide insights into the governing micromechanisms of cleavage fracture in the base material and critical HAZ — CGHAZ and ICCGHAZ — of high strength steel structures. Therefore, this study works as manual of fundamental knowledge for structural failure analysis and design of new high strength steels.

1

INTRODUCTION

Cleavage fracture is a major concern in structural integrity assessments. Its characteristic of low or no plastic deformation makes it not detectable in advance, leading the structure to fail suddenly. Despite the advances in structural steel design, many factors can influence the material performance and result in serious practical implications. Over the years, increasingly severe environments have been explored, submitting structures (e.g., offshore equipment for installing green energy farms and decommissioning old structures) to very high stresses, high strain rates, and low temperatures. These are known parameters to affect the performance of body-centered cubic (BCC) steels, such as high strength steels (HSS), that transition from ductile to brittle behaviour with temperature reduction and strain rate increase [1]. Moreover, structural components' properties are usually compromised by welding thermal input. Welding is the most used method to join parts, and the thermal profile is known to generate heat-affected zones with potentially poor toughness [2–4].

As a highly localised phenomenon, cleavage fracture exhibits strong sensitivity to material microstructure. Features such as phases and brittle second-phase particles, and their parameters such as size, morphology, and area fraction influence the cleavage fracture micromechanisms and the final fracture toughness [5]. Hence, establishing an accurate relationship between microstructure and fracture toughness is essential for failure assessment and optimal steel design. However, in multiphase materials such as HSS and welded structures, providing this relation is challenging. The interaction between different microstructural features results in locally different combinations of strength and toughness, affecting the material's performance. For this reason, relying on only a single microstructural feature to predict the overall fracture behavior of the material is not a reliable measure. Hence, a probabilistic approach, based on experimental investigation supported by modelling analyses [6–9], is required in order to guarantee the steel's structural integrity during service.

1.1. MATERIAL-RELATED CHALLENGES

Many material-related challenges are faced when applying BCC, multiphase HSS at low temperatures in order to meet structural requirements. First, the trade-off between strength and toughness since an increase in one of these properties frequently leads to a decrease in the other [10]. Second, the ductile-to-brittle transition behaviour of BCC steels with the reduction of temperature [11]. Lastly, the inhomogeneous and complex microstructure of structural steels that results in a high variation of properties making it difficult to predict cleavage fracture [12, 13]. These topics will be further discussed in the next sections.

1.1.1. STRENGTH *vs* TOUGHNESS

In order to withstand high applied loads in structural applications and resist fracture, structural steels must have an attractive combination of high strength and toughness. However, in general, these properties are mutually exclusive [10]. Tough materials must have the ability to distribute high local stresses by enduring deformation, showing a balance between strength and ductility. On the other hand, high-strength materials expe-

rience limited deformation which causes a tendency to be brittle [14]. Figure 1.1 shows the generalised relationship between fracture toughness and yield strength for ductile materials.

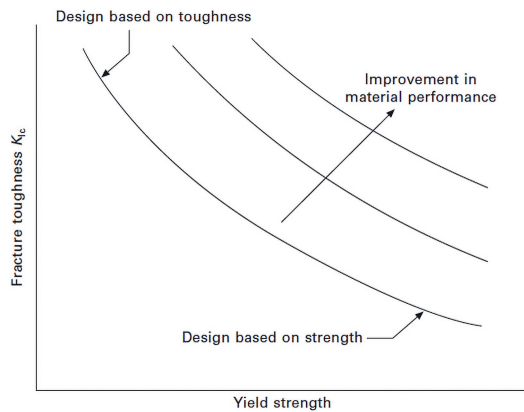


Figure 1.1: Generic schematic illustration showing the relationship between fracture toughness and yield strength in ductile metals [15].

However, an improved balance between strength and toughness can be achieved in structural steels by the development of optimum microstructures through chemical composition control to obtain cleaner alloys and advanced steel processing conditions [16]. The only reported way to simultaneously increase strength and toughness is grain refinement [17–22]. The effect of microstructure on mechanical properties and fracture toughness is the overall topic of this dissertation.

1.1.2. DUCTILE-TO-BRITTLE TRANSITION

The ductile-to-brittle transition (DBT), well-known in BCC metals, is characterised by a sudden and pronounced drop in toughness with decreasing temperature (Fig. 1.2). This phenomenon is not an inherent property of a given material and is influenced by internal and external aspects such as stress triaxiality, temperature, and strain rate. A larger stress triaxiality lowers the plastic strain and thus smaller plastic zones are involved in the fracture process. The effect of temperature is related to the lack of low-activation energy slip systems of the BCC crystal lattice and the increase of Peierls-Nabarro stress to move free dislocations in the matrix with the reduction of temperature [23]. At high loading rates, as in impact tests, there may be insufficient time for dislocations to move past obstacles and cause plastic deformation [24]. Hence, there is generally an increase in the strength with increasing load rate which usually results in a reduction of fracture toughness. As a result of these factors, the plastic deformation process is hampered making the material more prone to brittle fracture. The external aspect that this research focuses on is temperature.

As BCC steels are usually used as engineering materials, under severe environmental conditions, their fracture process is dominated by cleavage, which may cause catas-

trophic failure. Thus, structural applications face critical challenges at low-temperature service conditions.

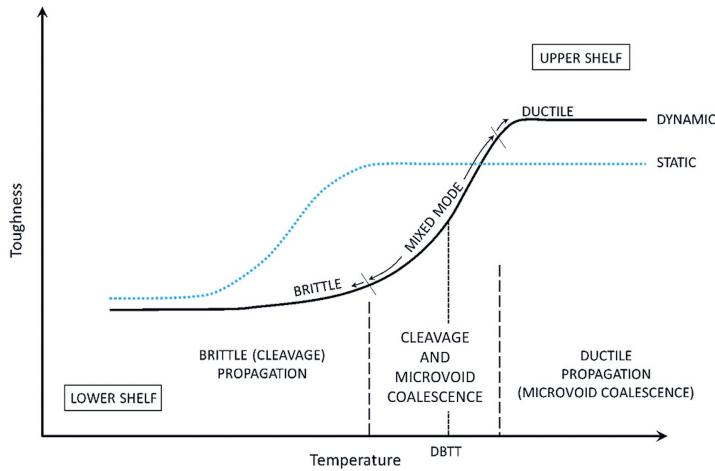


Figure 1.2: Generic schematic illustration of the ductile-to-brittle transition curve of ferritic steels under static and dynamic loading.

1.1.3. INHOMOGENEOUS MICROSTRUCTURES

The material microstructure plays an important role in the cleavage fracture process. Many authors observed a large scatter of properties in steels caused by microstructural and metallurgical inhomogeneities [12, 13, 25, 26]. The non-homogeneous microstructures are a consequence of the material and its manufacturing process. In terms of material, high strength steels have a favourable combination of properties through their multiphase microstructure including various bcc-microconstituents like martensite and bainite. Additionally, as the tendency is toward design to support higher loads, the use of thick sections is frequent. Consequently, non-uniform cooling rates and strain levels are experienced in the thickness direction during the thermomechanical processing route, resulting in a through-thickness microstructural variation. In terms of the manufacturing process, welding is a traditional joining method for structural components. The welded joints have a complex multiple-zone composition, including welds, fusion zone, and heat-affected zones (HAZ). Each of these areas has specific microstructural features and characteristic properties [27, 28].

1.2. RESEARCH OBJECTIVES AND THESIS OUTLINE

The challenge of establishing a cleavage fracture criterion for failure prediction in multiphase steels is acknowledged. Thus, many studies in the literature investigate the varia-

tion of properties resulting from inhomogeneous microstructures [12, 13, 25, 26]. However, these studies are insufficient in terms of adequate systematic microstructural and fracture data for experimental and modelling assessment of cleavage fracture.

Therefore, this work is aimed at developing a microstructure-based failure criterion for prospective high strength steel structures with the potential for cleavage fracture. Thereby, a quantitative relationship between microstructure and cleavage fracture of a commercially available 80-mm thick S690 quenched and tempered HSS has been established. In view of structural components that are generally joined by welding, thermal simulations of the most critical HAZ, CGHAZ and ICCGHAZ were performed, and the microstructure-cleavage fracture relation was also determined. Finally, a thermal profile aimed at grain refinement has been proposed to evaluate the potential of smaller grain sizes for fracture toughness improvement in multiphase high strength steels. For this purpose, the microstructure of the as-received HSS, simulated HAZs and grain refined material were comprehensively characterised, and their cleavage fracture toughness was measured. Afterwards, the investigation of the fracture surfaces allowed the identification of weak microstructural links and governing cleavage fracture initiation and propagation micromechanisms.

The theoretical background on high strength steels, cleavage fracture, and microstructural aspects affecting cleavage fracture is presented in **chapter 2** for a clear understanding of this work. In **chapter 3**, the through-thickness microstructure of the 80 mm thick commercially available S690QL high strength steel has been comprehensively characterised and quantified. Then, the potential critical microstructural features for cleavage fracture were identified. The criticality of these features was analysed in **chapter 4**, where the through-thickness cleavage fracture initiation and propagation micromechanisms have been determined. Furthermore, the effect of crack orientation and plastic constraint on cleavage fracture toughness is investigated. Considering that the welding thermal profile locally modifies the microstructure of the base steel, generating brittle zones, in **chapter 5** the microstructure of the CGHAZ and ICCGHAZ was characterised and their cleavage fracture behaviour was studied. Hence, it was analysed if the fracture toughness and micromechanisms of the base material were altered. In **chapter 6**, a heat treatment, based on rapid cyclic heating, is proposed with the aim of promoting grain refinement and studying the effect of grain size reduction on the cleavage fracture toughness of HSS. Although the Hall-Petch relationship [29, 30] can be extended to predict the relation between cleavage stress and, thus, toughness [19] and grain size this relation is oversimplified and generalised to draw conclusions on complex and multiphase materials. Lastly, **chapter 7** summarises the main findings and contributions of this research to the materials science and mechanical behaviour community and proposes further relevant developments on the comprehension of cleavage fracture micromechanisms.

REFERENCES

- [1] Landes, J. D. (1990). Fracture mechanics and the nuclear industry. *Metallurgical Transactions A*, 21(4), 1097–1104. <https://doi.org/10.1007/BF02656530>
- [2] Mohseni, P., Solberg, J. K., Karlsen, M., Akselsen, O. M., & Østby, E. (2012). Investigation of mechanism of cleavage fracture initiation in intercritically coarse grained heat affected zone of HSLA steel. *Materials Science and Technology*, 28(11), 1261–1268.
- [3] Lee, S., Kim, B. C., & Lee, D. Y. (1989). Fracture mechanism in coarse grained HAZ of HSLA steel welds. *Scripta Metallurgica*, 23(6), 995–1000. [https://doi.org/10.1016/0036-9748\(89\)90284-6](https://doi.org/10.1016/0036-9748(89)90284-6)
- [4] Davis, C. L., & King, J. E. (1994). Cleavage Initiation in the Intercritically Reheated Coarse-Grained Heat-Affected Zone : Part I . Fractographic Evidence. *Metallurgical and Materials Transactions A*, 25A, 563–573.
- [5] Chen, J. H., & Cao, R. (2015). *Micromechanism of Cleavage Fracture of Metals*. Butterworth-Heinemann. <https://doi.org/10.1016/B978-0-12-800765-5.00003-4>
- [6] Jiang, Q., Bertolo, V. M., Popovich, V. A., Sietsma, J., & Walters, C. L. (2021). Relating matrix stress to local stress on a hard microstructural inclusion for understanding cleavage fracture in high strength steel. *International Journal of Fracture*, 232, 1–21. <https://doi.org/https://doi.org/10.1007/s10704-021-00587-y>
- [7] Jiang, Q., Bertolo, V. M., Pallaspuro, S., Popovich, V., Sietsma, J., & Walters, C. L. (2023). Microstructure-based cleavage parameters in bainitic, martensitic, and ferritic steels. *Engineering Fracture Mechanics*, 281, 109146. <https://doi.org/10.1016/J.ENGFRACMECH.2023.109146>
- [8] Jiang, Q., Bertolo, V. M., Popovich, V. A., Sietsma, J., & Walters, C. L. (2022). Microstructure-informed statistical modelling of cleavage fracture in high strength steels considering through-thickness inhomogeneities. *Engineering Fracture Mechanics*, 267(108432). <https://doi.org/https://doi.org/10.1016/j.engfracmech.2022.108432>
- [9] Jiang, Q., Bertolo, V., Popovich, V., Sietsma, J., & Walters, C. L. (2022). Microstructure-based cleavage modelling to study grain size refinement and simulated heat affected zones of S690 high strength steel. *Under Review in Materials Science and Engineering A*.
- [10] Ritchie, R. O. (2011). The conflicts between strength and toughness. *Nature Materials*, 10, 817–822. <https://doi.org/10.1038/nmat3115>
- [11] Morris Jr., J. W. (1993). *Steels: For low temperature applications* (H. D. McPherson, Ed.). Pergamon Press.
- [12] Liu, H., Zhang, H., & Li, J. (2018). Thickness Dependence of Toughness in Ultra-Heavy Low-Alloyed Steel Plate after Quenching and Tempering. *Metals*, 8(628), 1–11. <https://doi.org/10.3390/met8080628>
- [13] Popovich, V., & Richardson, I. M. (2015). Fracture Toughness of Welded Thick Section High Strength Steels. *TMS 2015 144th Annual Meeting & Exhibition: Supplemental Proceedings*, 1031–1038. <https://doi.org/10.1002/9781119093466.ch125>
- [14] Zhu, H., Zhu, S., Jia, Z., Parvinian, S., Li, Y., Vaaland, O., & Hu, L. (2015). Anomalous scaling law of strength and toughness of cellulose nanopaper. *PNAS Early Edition*, 112(29), 8971–8976. <https://doi.org/10.1073/pnas.1502870112>

- [15] Mouritz, A. P. (2012). Fracture toughness properties of aerospace materials. In *Introduction to aerospace materials* (pp. 454–468). Woodhead Publishing.
- [16] Lücken, H., Kern, A., & Schriever, U. (2008). High-Performance Steel Grades for Special Applications in Ships and Offshore Constructions. *Eighteenth (2008) International Offshore and Polar Engineering Conference*, 211–216.
- [17] Kim, H. J., Kim, Y. H., & Morris, J. W. (1998). Thermal mechanisms of grain and packet refinement in a lath martensitic steel. *ISIJ International*, 38(11), 1277–1285. <https://doi.org/10.2355/isijinternational.38.1277>
- [18] Song, R., Ponge, D., & Raabe, D. (2005). Mechanical properties of an ultra-fine grained C-Mn steel processed by warm deformation and annealing. *Acta Materialia*, 53(18), 4881–4892. <https://doi.org/10.1016/j.actamat.2005.07.009>
- [19] Morris Jr, J. W. (2001). The influence of grain size on the mechanical properties of steel. [https://doi.org/10.1016/S0965-9773\(97\)00137-2](https://doi.org/10.1016/S0965-9773(97)00137-2)
- [20] Park, M. H., Shibata, A., & Tsuji, N. (2020). Challenging Ultra Grain Refinement of Ferrite in Low-C Steel Only by Heat Treatment. *Frontiers in Materials*, 7(November), 1–10. <https://doi.org/10.3389/fmats.2020.604792>
- [21] Li, X., Zhao, J., Dong, L., Devesh Kumar Misra, R., Wang, X., Wang, X., & Shang, C. (2020). The significance of coherent transformation on grain refinement and consequent enhancement in toughness. *Materials*, 13(22), 1–15. <https://doi.org/10.3390/ma13225095>
- [22] Smoljan, B. (2004). An analysis of combined cyclic heat treatment performance. *Journal of Materials Processing Technology*, 155-156(1-3), 1704–1707. <https://doi.org/10.1016/j.jmatprotec.2004.04.121>
- [23] Heslop, J., & Petch, N. J. (1956). LXXXVIII. The stress to move a free dislocation in alpha iron. *Philosophical Magazine*, 1(9), 866–873. <https://doi.org/10.1080/14786435608238163>
- [24] Maleque, M. A., & Salit, M. S. (2013). Chapter 2: Mechanical Failure of Materials. In *Materials selection and design* (1ed, pp. 17–38). Springer Singapore.
- [25] Wang, Q., Ye, Q., Wang, Z., Kan, L., & Wang, H. (2020). Thickness Effect on Microstructure, Strength, and Toughness of a Quenched and Tempered 178 mm Thickness Steel Plate. *Metals*, 10(5), 1–16. <https://doi.org/10.3390/met10050572>
- [26] Pallaspuro, S. (2018). *On the factors affecting the ductile-brittle transition in as-quenched fully and partially martensitic low-carbon steels* (Doctoral dissertation). University of Oulu. <https://doi.org/10.13140/RG.2.2.32092.90245>
- [27] Billingham, J., Sharp, J. V., Spurrier, J., & Kilgallon, P. J. (2003). *Review of the performance of high strength steels used offshore* (tech. rep.). Bedfordshire.
- [28] Katsuyuki, I., Takaki, F., & Shinichi, S. (2014). *Offshore Structural Steel Plates for Extreme Low Temperature Service with Excellent HAZ Toughness* (tech. rep. No. 23). JFE GIHO.
- [29] Hall, E. O. (1951). The deformation and ageing of mild steel: III Discussion of results. *Proceedings of the Physical Society. Section B*, 64(9), 747–753. <https://doi.org/10.1088/0370-1301/64/9/303>
- [30] Petch, N. (1953). The cleavage strength of polycrystals. *J. Iron Steel Inst.*, 174(25).

2

THEORETICAL BACKGROUND

2.1. HIGH STRENGTH STEELS

High strength steels (HSS) are a class of modern high-performance steels, with yield strength higher than 550 MPa, developed aiming the replacement of conventional structural steels due to their favourable combination of properties [1, 2]. The excellent combination of properties of HSS provides its broad and diverse range of applications, from automotive (e.g. mobile cranes, utility vehicles, forestry machinery, and railcars) to offshore and maritime industries (e.g. offshore platforms) [1]. In addition, its high level of strength allows lighter structural designs, enabling improvements in economic and ecological aspects (e.g., lower transport and manufacturing expenditure, and a decrease in energy of consumption of vehicles and ships) [1, 2].

The optimum balance of strength, ductility, and toughness of HSS is achieved through chemical composition control and thermomechanical process routes which are responsible for providing highly controlled microstructure and resulting properties [2]. The HSS generally contain carbon contents in a range of 0.05% – 2.00%, a maximum manganese content of 2.0%, and small additions of alloying elements such as chromium, nickel, molybdenum, copper, nitrogen, niobium, and boron in order to obtain a proper combination of strength, weldability, and deformability as well as to achieve the required DBT temperatures [1, 3, 4]. Linked with the chemical composition, special rolling and heat treatment techniques must be used in order to obtain the desired properties. Quench-and-temper route is the most used for the production of HSS [5].

2.1.1. HOT ROLLING

In general, the first step of the hot rolling process of steels is to heat the plate/sheet to high temperatures, commonly above 1100 °C, where the austenite phase takes place, in order to make the material sufficiently soft and thus deformable. Subsequently, while maintaining the temperature over 1100 °C, the heated plate is rolled in consecutive passes leading to thickness reduction [6]. The temperature used in the final passes can effectively affect the microstructure. For example, temperatures above the full-recrystallisation temperature make possible the nucleation of new austenite grains, refining the microstructure, while temperatures below the recrystallisation-stop temperature maintain the deformed austenite grains in the elongated shape. Therefore, the temperature must be chosen depending on the desired microstructure and properties. After the rolling process, the material can be either cooled in air or actively cooled, i.e. use of an external device to accelerate the heat transfer, to achieve desired microstructures [7], which is followed by quenching and tempering steps.

2.1.2. QUENCHED AND TEMPERED STEELS

The quenching processing route consists first of heating the material to temperatures above the final temperature of austenite formation (A_{c3}) for sufficient time to have the heat homogeneously distributed from the surface to the centre of the material. Once this time has been reached, the plate/sheet is quickly cooled (fastest cooling is obtained

in water), to acquire the microstructural transformation from austenite to martensite or bainite. Martensite is the hardest and strongest phase in steels and, consequently, the most brittle one due to the supersaturation of carbon. Carbon is trapped in solid solution as the transformation from austenite to martensite is sufficiently fast avoiding the carbon to diffuse. Hence, the quenching step is responsible for producing a fine-grained martensitic or bainitic structure that is usually very strong and is also too brittle to be useful for most applications. Therefore, the tempering treatment should be carried out in order to reduce the strength, relieve some of the residual stress, provide the material with certain ductility and, consequently, improve the toughness [5].

In the tempering step, the plate/sheet is reheated to temperatures near the initial temperature of austenite formation (below the A_{c1} temperature, where austenitic transformation starts) and held at this temperature for a fixed period, then, cooled in air. In general, during martensite tempering, carbon in solid solution (supersaturated) segregates into defects, forms clusters, and then precipitates in the form of carbides. However, other reactions can occur depending on the tempering temperature, such as the transformation of carbides to cementite and the transformation of martensite into ferrite [8]. In the case of bainite tempering, which has a small carbon excess rather than a supersaturated solution, the steel auto-temper, and a great amount of the carbon partitions out or precipitates. In both martensite and bainite tempering cases, the dislocation density is reduced being more pronounced in martensite [8]. Temperature and time play important roles in determining the microstructure and, consequently, mechanical properties of the material. Thus, these parameters should be defined based on the desired properties. For instance, low-temperature tempering results in high strength and hardness, while high-temperature tempering results in less hard steels with increased toughness levels, making them more favourable for structural applications [9].

Lath martensite and lath bainite have a hierarchical structure. As martensite and bainite transform from the austenite, a crystallographic relation between the parent austenite and daughter phases/micro-constituents, martensite, and bainite, is created. The most common orientation relationship (OR) between austenite and martensite/bainite is the Kurdjumov-Sachs (K-S) [10]. In the K-S OR, the phases/micro-constituents are aligned in order for them to share close-packed planes, $(011)_{bcc}$ parallel to $(111)_{fcc}$, and close-packed directions, $[111]_{bcc}$ aligned with $[\bar{1}\bar{1}0]_{fcc}$, minimizing energy. In total, there are 24 K-S orientations between the parent and daughter phases [10]. Another crystallographic parameter in the austenite- lath martensite/bainite transformation is the Bain axis, which refers to the austenitic axis that was compressed during transformation. Both K-S and Bain variants can be identified by the pole figures. For instance, Fig. 2.1 shows a theoretical (001) pole figure of K-S OR where variants belonging to the same plane-parallel relation are represented by identical symbols. Regarding the Bain axes, the variants are represented by different colours.

After the austenitic transformation to lath martensite and lath bainite, the grain boundary remains present and it is referred to as prior austenite grain (PAG). The PAGs are divided into four distinguishable packets that are subdivided into blocks composed of laths [10]. Each packet shares the same habit plane. Figure 2.2 (a) is a schematic illustration of the lath martensitic or lath bainitic structure and Fig. 2.2 (b) is an optical micrograph showing a lath martensitic grain composed of PAG, packet, and block

boundaries.

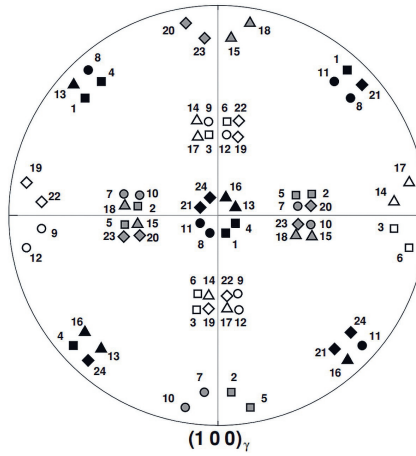


Figure 2.1: (001) pole figure showing the 24 K-S variants of martensite. The K-S variant groups with the same plane-parallel relation are represented by the same symbol and the Bain variants are represented by different colours [11].

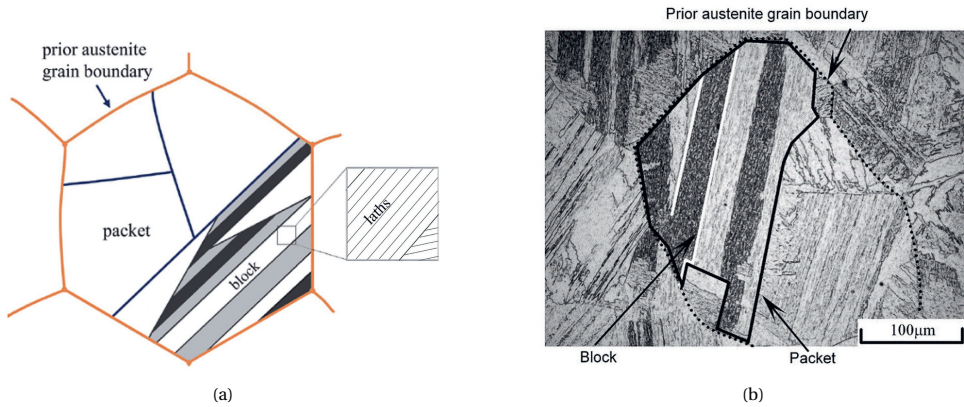


Figure 2.2: (a) Schematic illustration of the martensitic structure (Adapted from [6]) and (b) optical micrograph showing a lath martensitic grain composed of PAG, packet, and block boundaries [12].

2.1.3. THICK-SECTION HIGH STRENGTH STEELS

Thick-section steels (above 60 mm) have been increasingly used due to the design trend of structural materials to withstand higher loads. During the processing route, thick-section steel plates experience non-uniform cooling, where the areas closer to the surface of the material cool faster, exhibiting fine microstructures and low-temperature transformation products (e.g., martensite) while in the middle of the plate cooling is

significantly slower and leads to coarse microstructure and high-temperature transformation products (e.g., bainite). Strain gradients during hot rolling may also occur, where the slab surface experiences larger strains. As a result, more deformation energy is stored close to the surface. Then, the outer part of the plate has more energy for recrystallisation during the subsequent quenching step, generating new grains. Consequently, smaller grain sizes can be found in the areas near the steel plate surface. Hence, grain size may vary along the steel plate thickness.

Additionally, local enrichment of alloying elements and impurity elements in the centre of the steel plates can be produced during the solidification step of thick-section steels. Alloying elements, added to the steel composition in order to obtain desired properties, are evenly distributed in liquid steel during the casting process. Nevertheless, during the solidification stage, these elements segregate and are found to be non-uniformly distributed in the matrix. Afterwards, the rolling process elongates low and high-solute areas, transforms them into layers parallel to the rolling direction, and gives rise to the so-called segregation bands (Fig. 2.3) [13, 14].

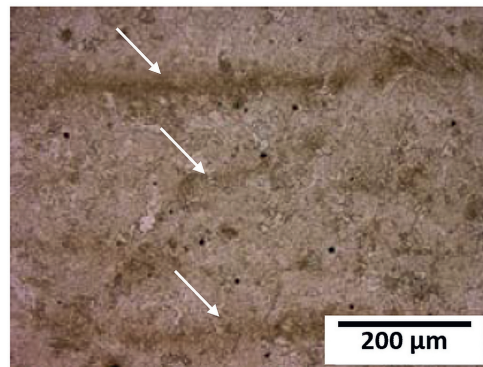


Figure 2.3: Optical micrograph showing segregation bands indicated by white arrows in a high strength steel (Adapted from [15]).

The segregation bands are partly associated with macrosegregation and partly with the shrinkage of the solidifying melt, shrinkage porosity and often with the formation of inclusions [16]. It develops in the middle section of the slab as a result of solidification and transformation processes, fluid flow and also to the constrained liquid supply [16]. During solidification, as most alloying elements are more soluble in the liquid phase than in the solid phase, solutes are rejected from the solidification front into the remaining liquid phase leading to a continual enrichment of the liquid towards the central region [17]. Hence, macrosegregation will form. The volume change due to solidification and the deformation of the slab influence the liquid supply in the liquid-solid (mushy) zone. In case of limited liquid supply, shrinkage porosities will be naturally formed, which is frequently observed in centreline segregation [16]. The banding is inevitable, regardless of the type of steel and, as a result of the sluggish diffusion of substitutional elements, there is not an economically feasible way of eliminating it [14, 18]. The different elemental content between enriched and depleted zones affects microstructural trans-

formations and is reported as having detrimental effects on mechanical performance [14, 19–21].

The microstructure through-thickness varies exhibiting coarse and fine microstructures, as well as a combination of multiple phases. The consequence of such inhomogeneous and multiphase microstructures is a large scatter of properties through the thickness. Some authors [6, 15, 22–24] observed different microstructures and, consequently, different properties through the thickness in different steels. Popovich and Richardson [15] analysed the through-thickness microstructural composition and mechanical properties, such as hardness, strength, and fracture toughness, for three quenched and tempered high strength steels. For all three investigated steels, the top outside section of the plate was composed of refined tempered martensitic structure whilst the middle section showed coarser tempered martensitic and partially bainitic structures, with well-defined centreline segregation bands. As a result of this inhomogeneous microstructure and non-uniform chemical composition, the following was observed: (i) a significant gradient of hardness, where the section closer to the surface presented higher hardness; (ii) tensile strength variation with higher values in the top section; (iii) lower toughness values and higher ductile-to-brittle transition temperature in the middle section. Pallaspuo [6] studied reheated and quenched steel and observed similar differences for the samples taken from the surface and the centreline, namely a substantial scatter of hardness, impact and fracture toughness measurements. The author attributed these results to distinct chemical and microstructural compositions (e.g. enrichment of alloying elements at the centreline, grain, and inclusions size).

2.2. WELDS AND THEIR COMPLEX MICROSTRUCTURES

In general, welding is the conventional method for joining metals. Multi-pass welds, needed for thick-section steel plates, consist of base metal, as-deposited weld metal, and heat-affected zones (HAZ). HAZ are areas of the base material that have been heated and reheated, during successive passes, to temperatures below A_{c1} , between A_{c1} and A_{c3} , and above A_{c3} [25]. Consequently, the HAZ is divided into various sub-regions with different microstructures and properties, where some of which have potentially poor toughness (Fig. 2.4).

As can be seen in Fig. 2.4, each welding pass produces a four-zone microstructural gradient. The first zone from the fusion line is the coarse-grained heated affected zone (CGHAZ), which is composed of enlarged PAG from the successive weld passes that grow quickly as the achieved temperature is close to the melting point. When cooled, the prior austenite can transform to martensite or a mixture of lower bainite and martensite, depending on the carbon equivalent (CE) of the base metal. Then, the second zone from the fusion line is the fine-grained heated affected zone (FGHAZ), which is composed of refined PAG due to the slower austenitic grain growth at lower temperatures. The third zone is the intercritical HAZ (ICHAZ), which is composed of a mixture of ferrite and austenite precipitates along prior austenite grain boundaries that is responsible for the embrittlement of the material in this region upon cooling. Lastly, the fourth zone is the subcritical HAZ (SCCGHAZ), which provides very few changes in properties [27]. Af-

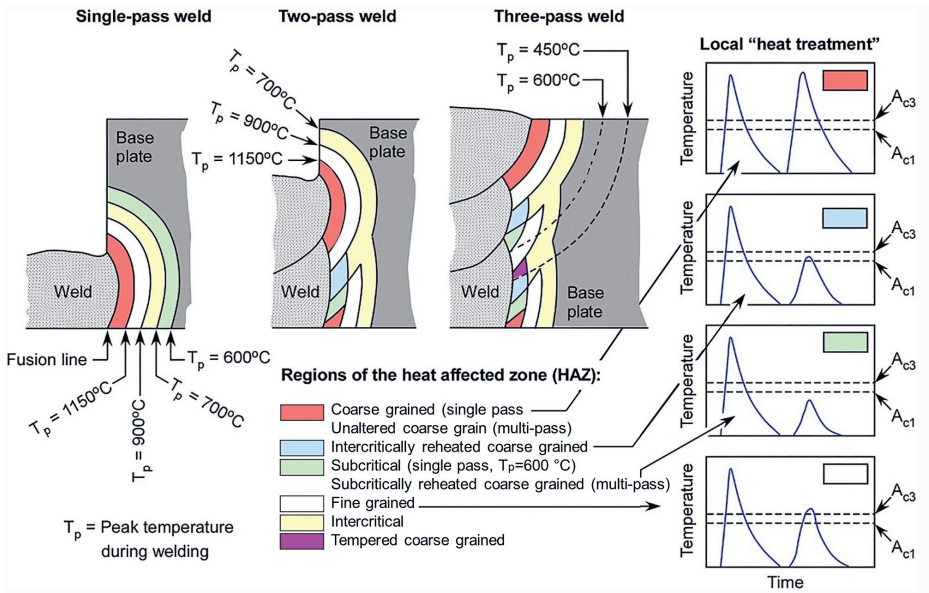


Figure 2.4: Schematic representation of the different HAZ sub-regions in a multi-pass weld (Adapted from [26]).

ter the first pass, the modifications start to occur on top of the prior pass. Then, reheated CGHAZ starts to form.

It is generally accepted that the HAZs are the welded regions that control the low-temperature toughness of the entire structure [25, 28]. The zones with the lowest toughness and, therefore, the most critical for fracture are the CGHAZ and the intercritically reheat CGHAZ (ICCGHAZ) [29, 30]. The severe reduction of low-temperature toughness is mostly attributed to the presence of martensite-austenite (M-A) constituents and large PAG size [28–32]. Consequently, the ductile-to-brittle transition temperature of high strength steels is shifted as a result of welding from around -80°C to approximately -30°C , raising concern in terms of cleavage fracture [15].

In addition to the complex and brittle microstructures formed during the welding process, which degrades the material fracture behaviour, welding-induced defects can also have a detrimental effect. Welding defects such as porosity caused by gases retained in the metal, lack of fusion, and unsatisfactory penetration can occur at weld metal, HAZ, and base metal, and may also result in a significant reduction of performance and also the failure of components under service conditions [33]. However, these defects and their effect on cleavage fracture are out of the scope of this research and will not be further discussed.

As shown in Fig. 2.4, each HAZ and its microstructure are restricted to a very small area. Hence, it is extremely difficult to machine specimens from a welded joint and obtain mechanical and fracture properties of one single area. Moreover, when tests are carried out in a weld joint it is hard to locate the HAZ location where the fracture took place. Therefore, thermo-mechanical simulators (e.g., Gleeble) are very much used to

heat treat a material based on welding thermal profiles and obtain homogeneous microstructures of a certain HAZ over a sufficiently large area to produce test specimens. Note that the welding thermal profile should be specific for each HAZ of interest. It is claimed in the literature that thermal-simulated HAZs may not represent the actual microstructures found in actual welds. For instance, Pirinen [34] observed that the PAG size in simulated HAZ is larger than in real ones. Furthermore, the residual stresses generated during welding are not present in simulated weld zones. Nevertheless, other authors [35–37] report that real and simulated HAZ have similar microstructures and a good agreement was found between the methods. Hence, thermal simulations can be used for weld joint studies.

2.3. CLEAVAGE FRACTURE

Cleavage fracture is a low-energy process that occurs in materials that lack ductility by separation across well-defined crystallographic planes [38]. In BCC steels, these are close to {100}, {112}, and {123} plane of ferrite [38–41]. In general, cleavage is classified as transgranular fracture since cracking occurs across grains, with little or no preference for grain boundaries. However, brittle fracture can also occur in an intergranular manner in case of the grain boundaries contain a brittle film or segregation of detrimental elements, for example [42].

The cleavage microcracking process is recognised as a slip-induced process and comprises the following three sequential steps (Fig. 2.5) [38]:

1. A cleavage crack nucleates and extends in a hard particle as a result of a dislocation pileup driven by the effective shear stress at a fracture plastic strain (Fig. 2.5, step 1). The criterion for this stage is that the plastic strain is equal to or larger than the fracture plastic strain.

2. The hard particle crack propagates through the boundary between the particle and the matrix grain. The propagation is driven by the combined action of the applied tensile stress and the tensile stress induced by the dislocation pileup (Fig. 2.5, step 2). The criterion for this stage is that the normal stress is equal to or larger than the local cleavage stress of a hard particle.

3. The grain-sized crack propagates through the grain boundaries into the contiguous grains driven by the applied tensile stress (Fig. 2.5, step 3). The criterion for this stage is that the normal stress is equal to or larger than the local cleavage stress of a ferrite grain.

Material toughness can be measured either in terms of impact toughness or fracture toughness. The first is obtained by easy and cheap Charpy tests and is used as acceptance tests and pre-qualification of material toughness. This is due to limitations regarding 1) the plastic constraint, as Charpy specimens use a blunt notch instead of a crack-sharp notch similar to actual defects in structures; 2) Dynamic loading instead of quasi-static loading where the extremely high strain rates generally differ from real conditions; 3) Charpy specimen size is small which does not represent the metallurgical variations of the used structural materials; 4) Size-dependent property as the impact toughness vary with the size of the specimen and, therefore, cannot be used as a true material property. The latter is recognised as a true property and has none of the limitations

previously listed.

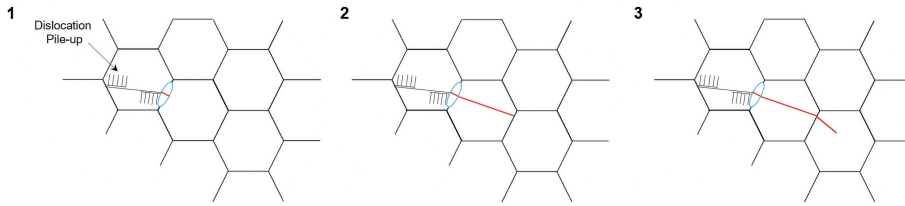


Figure 2.5: A schematic illustration showing the subsequent three stages compromising cleavage cracking on the microscopic scale: 1 slip-induced cracking of a brittle particle, 2 propagating a particle-sized crack across a particle/grain boundary, and 3 propagating a grain-sized crack across a grain/grain boundary.

As a result of the limited or no deformation prior to cleavage fracture, there is virtually no change in the cross-section area of tensile and fracture toughness specimens. The fracture appearance on the microscopic scale of fracture toughness specimens shows a bright and smooth faceted surface due to different orientations of cleavage planes in grains with river lines pattern converging to locations where the fracture was triggered and also indicate the crack growth direction as shown in Fig. 2.6 [38].

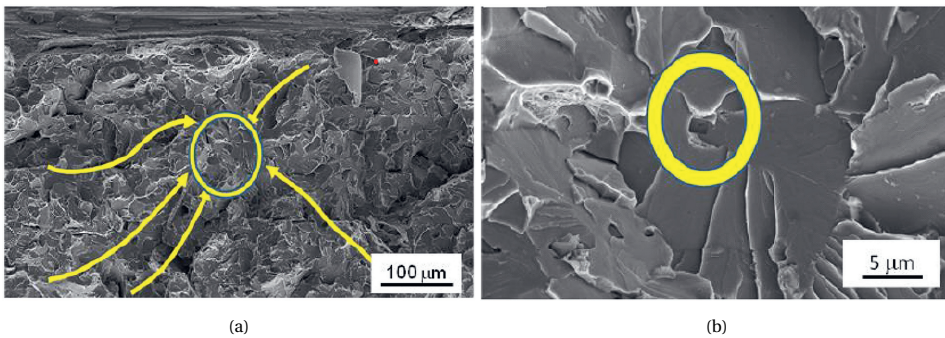


Figure 2.6: SEM micrographs showing (a) river lines pointing to the cleavage initiation site and (b) TiN inclusion that triggered fracture in a low carbon steel sample fractured at -65°C [43].

2.4. MICROSTRUCTURAL FEATURES AFFECTING CLEAVAGE FRACTURE

Microstructure of steels can strongly influence the cleavage fracture micromechanisms [44]. According to recent findings in the literature [6, 15], the main microstructural features governing brittle fracture initiation and propagation in ferritic steels are grains, carbides, inclusions, M-A (martensite-austenite) constituents, and centreline segregation. The impact of those features can be estimated by different parameter studies such as size, phase, orientation, volume fraction, chemical composition, morphology, and

residual stress [25, 45–48]. A review of these microstructural features and parameters and their effects on cleavage fracture is presented below.

2.4.1. GRAINS

2

The relationship between the grains and fracture behaviour of steels is mostly associated with the crack propagation process rather than crack initiation. The effect of grains can be divided into phase types, grain size (for a specific phase), and grain orientations.

Due to factors such as varying chemical composition, peak temperatures, and cooling rates during heat treatments and welding, the resultant steel can be composed of multiple phases. Some examples of phases/micro-constituents that can be found in ferritic steels are ferrite, martensite, bainite (granular bainite, upper bainite and lower bainite) [15, 25, 48–50]. Moreover, the tempered version of martensite and bainite may also be found. Each of these phases has a specific fracture behaviour, and it will affect the global fracture behaviour of the material in different ways. For instance, according to Knott [51], bainite is far more brittle than tempered martensite as the first exhibits a microscopic cleavage fracture stress between 1100–2200 MPa whereas the last, 3100–4000 MPa. The author attributes this behaviour to the size of cementite particles, which is much coarser in bainite (220 nm) than martensite (38 nm), since they act as crack nuclei in the material, determining the size of the initial sharp crack and, consequently, affecting the fracture behaviour. Specifically, in the case of granular bainite, it is detrimental to fracture toughness since the M-A islands are harder than the ferrite matrix aiding debonding and cracking initiation [15, 52].

Regarding grain size, it is widely known that grain refinement leads to simultaneous improvement of strength and toughness of metals [53–58]. The famous Hall-Petch law [59, 60] relates grain size with strength and hardness. Both properties are inversely proportional to the square root of the grain size. These relations are also used to explain the cleavage stress and the ductile-to-brittle transition temperature variation with grain size [55, 61, 62]. It has been reported that the smaller the grain size, the higher the cleavage stress and the lower the ductile-to-brittle transition temperature. Hence, toughness is improved with grain size reduction [55, 61, 62].

In addition, in ferritic steels, a cleavage crack can change its propagation direction as it crosses one grain to the other due to the differences in the orientation of the cleavage planes of two neighbouring grains. For example, when a crack during its propagation path meets a grain with a different orientation and, consequently, a high-angle boundary, it will either require more energy for further crack propagation or a crack path change. Therefore, grain boundaries act as natural barriers in cleavage fracture, and thus might retard or even hinder further crack propagation [23].

2.4.2. CARBIDES

Carbides are reported in the literature as potential cleavage initiation sites. The effect of carbides on steel fracture behaviour depends on the carbide size, shape, volume fraction, and orientation of the elongated carbides with respect to the applied stress.

The carbide size affects the fracture stress. According to Griffith's theory [63], the

larger the particle, the lower its fracture stress and, consequently, the greater the probability of it cracking. Hence, coarse carbides are considered detrimental to the fracture toughness of the steel [45, 64]. Regarding the shape, elongated carbides are more critical than spherical ones due to their tendency to crack preferentially as they build more stress as a result of the fibre-loading mechanism [65]. The volume fraction of carbides also plays an important role in the fracture behaviour of steels [66].

However, identifying the effect of these parameters is not so straightforward since it depends on other factors such as carbide type, size, distribution, and location in the ferritic matrix, i.e., along the grain boundaries or in the grain volume. Pacyna and Witek [66], for example, observed an increase in fracture toughness until a carbide volume fraction of 7.4%, achieving the maximum fracture toughness value and a subsequent continuous reduction of fracture toughness to a volume fraction of 19.2%. The authors attributed this increase in toughness to the grain size reduction caused by the carbides that are placed along the ferrite grain boundaries hindering their movement. Besides that, as there were no or almost no carbides in the grain volume (the crack path) they were not directly involved in the fracture formation. However, with the increase in the volume fraction of carbides, an increase in the number of carbide particles in the grain volume participating in the fracture process was observed. As a consequence, the steel exhibited a reduction of fracture toughness. Moreover, carbide orientation with respect to the applied stress is considered an important parameter affecting cracking [67]. According to Lindley [67], under tension, the more aligned the carbide is to the tensile axis, the greater the number of microcracks formed.

2.4.3. INCLUSIONS

Inclusions and second-phase particles, similarly to carbides, were observed to act as locations for cleavage initiation [15, 23, 45, 68, 69]. For instance, Ghosh et al. and Popovich and Richardson [15, 70] observed coarse complex TiN inclusions with Al_2O_3 core, and CaO inclusions with traces of Al initiating cleavage cracks in steels, respectively.

Regarding the size and distribution, it was observed that larger inclusions, as well as inclusions clusters, act as weakest links allowing for brittle crack initiation and propagation [6, 15, 70]. The volume fraction of inclusions also has an effect on toughness. Garrison and Wojcieszynski [71] confirmed that the reduction of the inclusion volume fraction improves the toughness of steel.

Furthermore, Miao and Knott [68] observed that the chemical composition of inclusions can also impact the mode of cleavage initiation and fracture toughness. In their study, it was observed that inclusions with a “duplex” structure consisting of “cores” of oxides/silicates with sulphide “coatings” initiate cleavage by different modes compared to oxide/silicate inclusions without sulphide coating. Moreover, it is suggested that there is an increase in fracture toughness when the inclusions are covered by the sulphide coating [68].

The morphology of inclusions has also been observed to influence fracture. Elongated (primarily sulphides) and cubic/irregular-shaped inclusions have been previously related to crack initiation, acting as stress concentrators and consequently reducing the toughness compared to inclusions of globular shape [45, 72].

2.4.4. M-A CONSTITUENTS

M-A constituents are recognised as local brittle zones, essentially found within the CG-HAZ and ICCGHAZ of welds [29], showing a detrimental effect on crack initiation and propagation, and a strong influence on the deterioration of fracture toughness due to their higher hardness and brittleness compared with the matrix microstructure [47]. The effect of M-A constituents on cleavage behaviour, as the other microstructural features, depends on some parameters. Size, volume fraction, morphology, distribution, and location in the microstructure are parameters that play an important role.

According to Griffith's theory [63], increasing the size of the M-A constituent cause a reduction in its fracture stress and they are more probable to crack or debond from the matrix during deformation. Hence, large M-A constituents are detrimental to toughness [25, 45, 47, 73]. The volume fraction of the M-A constituent is also expected to influence the fracture behaviour of steels. Laitinen [74] observed that the stress to fracture decreased with increasing the volume fraction of M-A constituents. Furthermore, the morphology of M-A constituents is sensitive to cleavage cracking. M-A constituents can be found mainly in blocky (massive) or slender (elongated) shapes. However, there is no consensus on the effect of morphology M-A constituents on toughness. According to Bayraktar and Kaplan [75], Kumar and Nath [76], and Li and Baker [77], blocky M-A constituents are more critical to cleavage fracture than slender M-A. On the other hand, Kim et al. [28] and Luo et al. [78] observed a more detrimental effect of slender M-A compared to the blocky ones. The effect of distribution and location of this feature was also analysed by [47] who observed a necklace-type M-A decorating the PAG boundaries, typically found in steels. It was proposed that when there is the presence of a necklace-type M-A there is an "overlap of transformation-induced residual tensile stress" and a stress concentration intensification due to a strength mismatch between the constituent and the matrix during deformation. Hence, when the M-A constituent is present in a continuous and interconnected structure it is detrimental to toughness.

2.4.5. CENTRELINE SEGREGATION BANDS

The research of mid-thickness sections of thick steels is important for fracture failure analysis as up to 90% of brittle failures derive from this area [79]. Several studies [15, 49, 80, 81] proposed that centreline segregation can significantly affect the mechanical behaviour of the final product. However, there are also studies that report the beneficial effects of this segregation [6].

Popovich and Richardson [15] observed that the element segregation results in inconsistent transformation products (e.g., martensite and bainite) during hot working which causes non-uniform mechanical properties in S690QT steel. The centreline segregation was pointed out as one of the main causes for the fracture toughness reduction in the mid-section of thick plates of this ferritic steel. The authors also report that centreline segregation may be the prime source of subsurface cracks and porosity. Guo et al. and Su et al. [49, 82] observed the deleterious effect of centreline segregation in Charpy impact toughness. The first reported that the impact toughness deteriorates and the ductile-to-brittle transition temperature increases for specimens with segregation [49].

The later observed that the local regions of elemental segregation lead to an increase in hardness and that specimens extracted from segregated areas present lower Charpy impact toughness [82].

On the other hand, Pallaspuro [6] noticed that, on a local scale of an as-quenched steel, the centreline segregation causes a reduction of the effective coarse grain size, which are viewed to compensate for the detrimental effects related to higher hardness and inclusion content present in the segregation region, resulting in increased fracture toughness. The grain size refinement observed by Pallaspuro [6] can be explained by the concentration of alloying elements that can refine the austenite grain size through solid solution effects on recrystallization and grain growth, and/or the presence of carbides and nitrides that can hold the grain boundaries [83].

2.4.6. RESIDUAL STRESSES

Residual stresses are stress fields that exist in a component in the absence of any external loads and result from thermomechanical processes such as thermal and mechanical treatments and welding. These stresses can be produced either by a structural mismatch between different regions or phases or by an uneven distribution of non-elastic mechanical and thermal strains.

Some microstructural features such as inclusions also play an important role in terms of residual stress. Residual stresses are reported as important factors influencing the structural integrity of engineering structures. Some authors [23, 84, 85] observed that residual stresses affect the crack driving force and the crack tip constraint. Especially in cleavage fracture toughness, this is a relevant aspect affecting failure as cleavage shows a strong sensitivity to the local stresses and deformation fields as a result of its highly localized character of the failure mechanism [86].

The interaction between the steel matrix and inclusions originating during thermal processes can generate large local residual stresses. In general, these residual stresses are developed due to the different thermal expansion coefficients of steel matrix and inclusions during temperature gradient [87]. The chemical composition and shape of inclusions were observed to have an effect on the level of residual stresses between the matrix and inclusions [87]. Gu et al. [87] analysed the residual stress around inclusions of different chemical compositions and shapes: Mg-Al-O, that are usually polygon; Al-Ca-O-S are usually spherical; TiN are usually irregular in shape; and MnS inclusions that are normally observed as spherical, cylindrical or irregular. First, the authors simulated the residual stress around these inclusions separately and assumed a spherical shape for all of them in order to understand the influence of the inclusion type (Fig. 2.7). As can be seen, the maximum stress is on the surface between the inclusion and steel matrix and it varies with inclusion type. The value of Mg-Al-O inclusion is the largest (1950 MPa), followed by TiN and Al-Ca-O-S inclusions (1800 MPa), while the value of MnS inclusion is the smallest (800 MPa). When considering the actual shape of inclusions, the simulation results show that the residual stress on the surface between the inclusion and the matrix changes with the shape of inclusions (Fig. 2.8).

After considering the actual shape of each inclusion, the value of TiN inclusion is now the largest (3500 MPa), followed by Al-Ca-O-S and Mg-Al-O inclusions (3250 and

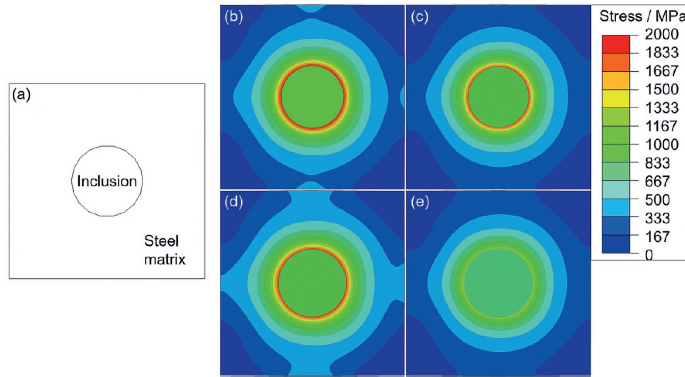


Figure 2.7: (a) Illustration of the model for the residual stress simulation during cooling; residual stress distribution around the spherical inclusion of (b) Mg-Al-O; (c) Al-Ca-O-S; (d) TiN; (e) MnS [87].

2750 MPa, respectively), while the value of MnS inclusion is still the smallest (1500 MPa) [87]. The maximum residual stresses considering inclusions shapes are much larger than the perfect spherical inclusions shapes. Therefore, the shape of inclusions plays an important role in residual stresses between the steel matrix and inclusions. The residual stresses around inclusions were also observed to lead to different effects on mechanical properties of steels. Murakami and Uchida [88] stated that residual stresses around Al_2O_3 inclusions result in debonding from the steel matrix, which act as crack nuclei and consequently affect the mechanical properties of steel.

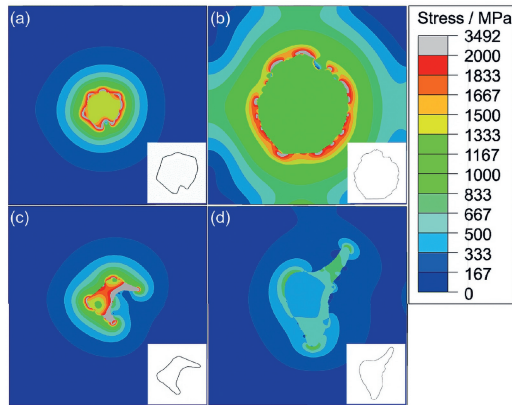


Figure 2.8: (a) Residual stress distributions around the inclusions with their actual shapes: (a) Mg-Al-O; (b) Al-Ca-O-S; (c) TiN; (d) MnS [87].

Residual stresses in welded components arise from thermal strains produced by intense local heating which generates extreme thermal gradients and the uneven cooling that occurs next through the different weldment zones [89, 90]. Especially in multi-pass

welds the configuration of residual stresses in the structure is intensified since multiple thermal cycles cause an irregular distribution of residual stress field across the weld and through-thickness [90]. In welded structures, at the macroscopic level, during rapid cooling, the weld is restrained by the colder base metal. As a result, the weld is in residual tension and the surrounding material is in residual compression. At the microscopic level, residual stresses originate from the restraint of thermal expansion and contraction and volume modification due to phase transformation.

2.5. CONCLUSIONS

Therefore, in general, the effect of individual microstructural features and parameters on cleavage fracture is broadly investigated and reported in literature studies. However, they are generic and lack knowledge of how the interaction between various microstructural features, such as in multiphase steels, affects the cleavage fracture micromechanisms and resulting toughness in multiphase materials. In other words, when a material has various types of inclusions, carbides, and phases with varying sizes, shapes, and internal structures, it is not yet known the role these features play in the fracture initiation and propagation process. Moreover, the available studies are not based on a quantitative and statistical analysis of the microstructure and cleavage fracture micromechanisms, which makes it difficult to establish an accurate relationship.

REFERENCES

- [1] Ilić, A., Ivanović, L., Josifović, D., & Lazić, V. (2012). Advantages of High Strength Steels Applications in Mechanical Constructions. *7th International Symposium Konstruisanje-Oblikovanje-Dizajn (KOD)*, 501–506.
- [2] Lücken, H., Kern, A., & Schriever, U. (2008). High-Performance Steel Grades for Special Applications in Ships and Offshore Constructions. *Eighteenth (2008) International Offshore and Polar Engineering Conference*, 211–216.
- [3] Kern, A., Niessen, T., Schriever, U., & Tschersich, H. (2004). Production and Properties of High-Strength Steel Plates for Offshore Applications. *The Fourteenth (2004) International Offshore and Polar Engineering Conference*, 107–114.
- [4] Mohseni, P. (2012). *Brittle and Ductile Fracture of X80 Arctic Steel* (Doctoral dissertation October). Norwegian University of Science; Technology.
- [5] Billingham, J., Sharp, J. V., Spurrier, J., & Kilgallon, P. J. (2003). *Review of the performance of high strength steels used offshore* (tech. rep.). Bedfordshire.
- [6] Pallaspuro, S. (2018). *On the factors affecting the ductile-brittle transition in as-quenched fully and partially martensitic low-carbon steels* (Doctoral dissertation). University of Oulu. <https://doi.org/10.13140/RG.2.2.32092.90245>
- [7] Komi, J., Karjalainen, L. P., & Porter, D. (2016). Direct-Quenched Structural Steels. In R. Colás & G. E. Totten (Eds.), *Encyclopedia of iron, steels, and their alloys*. CRC Press.
- [8] Keehan, E. (2004). *Effect of Microstructure on Mechanical Properties of High Strength Steel Weld Metals* (Doctoral dissertation). Chalmers University of Technology and Goteborg University. Sweden.
- [9] Jena, P. K., Kumar, K. S., & Singh, A. K. (2014). Effect of Tempering Temperature on Microstructure , Texture and Mechanical Properties of a High Strength Steel. *International Journal of Manufacturing, Materials, and Mechanical Engineering*, 4(3), 33–49. <https://doi.org/10.4018/ijmmme.2014070102>
- [10] Morris Jr, J. W., Kinney, C., Pytlewski, K., & Adachi, Y. (2013a). Microstructure and cleavage in lath martensitic steels. *Science and Technology of Advanced Materials*, 14(014208), 1–9. <https://doi.org/10.1088/1468-6996/14/1/014208>
- [11] Song, T., & De Cooman, B. C. (2013). Effect of boron on the isothermal bainite transformation. *Metallurgical and Materials Transactions A: Physical Metallurgy and Materials Science*, 44(4), 1686–1705. <https://doi.org/10.1007/s11661-012-1522-9>
- [12] Morito, S., Huang, X., Furuhashi, T., Maki, T., & Hansen, N. (2006). The morphology and crystallography of lath martensite in alloy steels. *Acta Materialia*, 54(19), 5323–5331. <https://doi.org/10.1016/j.actamat.2006.07.009>
- [13] Krauss, G. (2003). Solidification , Segregation , and Banding in Carbon and Alloy Steels. *Metallurgical and Materials Transactions B*, 34B, 781–792.
- [14] Majka, T. E. D. F., Matlock, D. K., & Krauss, G. (2002). Development of Microstructural Banding in Low-Alloy Steel with Simulated Mn Segregation. *Metallurgical and Materials Transactions A*, 33A, 1627–1637. <https://doi.org/10.1007/s11661-002-0172-8>

- [15] Popovich, V., & Richardson, I. M. (2015). Fracture Toughness of Welded Thick Section High Strength Steels. *TMS 2015 144th Annual Meeting & Exhibition: Supplemental Proceedings.*, 1031–1038. <https://doi.org/10.1002/9781119093466.ch125>
- [16] Réger, M., Vero, B., & Józsa, R. (2014). Control of centerline segregation in slab casting. *Acta Polytechnica Hungarica*, 11(4), 119–137.
- [17] Beckermann, C. (2008). Macrosegregation. *ASM Handbook*, 15, 348–352. <https://doi.org/10.1361/asmhba0005216>
- [18] Forouzan, F., Borasi, L., Vuorinen, E., & Mücklich, F. (2019). Optimization of Quenching Temperature to Minimize the Micro Segregation Induced Banding Phenomena in Quenching and Partitioning (Q & P) Steels. *Steel*, 1800281, 1–6. <https://doi.org/10.1002/srin.201800281>
- [19] Feng, R., Li, S., Zhu, X., & Ao, Q. (2015). Microstructural characterization and formation mechanism of abnormal segregation band of hot rolled ferrite / pearlite steel. *Journal of Alloys and Compounds*, 646, 787–793. <https://doi.org/10.1016/j.jallcom.2015.05.128>
- [20] Guo, F., Wang, X., Wang, J., Misra, R. D. K., & Shang, C. (2020). The Significance of Central Segregation of Continuously Cast Billet on Banded Microstructure and Mechanical Properties of Section Steel. *Metals*, 10(76), 1–13. <https://doi.org/https://doi.org/10.3390/met10010076>
- [21] Nagode, A., Resnik, A., Vertnik, R., Bizjak, M., Kosec, B., & Goji, M. (2017). The development of a banded microstructure in S355J2 steel bar. *Kovove Mater.*, 55, 51–56. <https://doi.org/10.4149/km2017>
- [22] Wang, Q., Ye, Q., Wang, Z., Kan, L., & Wang, H. (2020). Thickness Effect on Microstructure, Strength, and Toughness of a Quenched and Tempered 178 mm Thickness Steel Plate. *Metals*, 10(5), 1–16. <https://doi.org/10.3390/met10050572>
- [23] Liu, H., Zhang, H., & Li, J. (2018). Thickness Dependence of Toughness in Ultra-Heavy Low-Alloyed Steel Plate after Quenching and Tempering. *Metals*, 8(628), 1–11. <https://doi.org/10.3390/met8080628>
- [24] Moore, P., Yordanova, B., Lu, Y., & Janin, Y. J. (2019). Influence of microstructural variation in thick section steels on the characterisation of fracture toughness using sub-size specimens. *Proceedings of the ASME 2019 38th International Conference on Ocean, Offshore and Arctic Engineering OMAE 2019*. <https://doi.org/10.1115/OMAE2019-96010>
- [25] Wang, Z., Shi, M., Tang, S., & Guodong Wang. (2017). Effect of Heat Input and M-A Constituent on Microstructure Evolution and Mechanical Properties of Heat Affected Zone in Low Carbon Steel. *Journal of Wuhan University of Technology, Materials Science Edition*, 32, 1163–1170. <https://doi.org/10.1007/s11595-017-1726-3>
- [26] Zerbst, U., Madia, M., Schork, B., Hensel, J., Kucharczyk, P., Ngoula, D., Tchuindjang, D., Bernhard, J., & Beckmann, C. (2019). *Fatigue and Fracture of Weldments: The IBESS Approach for the Determination of the Fatigue Life and Strength of Weldments by Fracture Mechanics Analysis*. <https://doi.org/10.1007/978-3-030-04073-4>
- [27] Corwin, W. R. (1994). *Heavy-Section Steel Irradiation Program*, Metals and Ceramics Division (tech. rep. No. 2).

- [28] Kim, B. C., Lee, S., Kim, N. J., & Lee, D. Y. (1991). Microstructure and local brittle zone phenomena in high-strength low-alloy steel welds. *Metallurgical Transactions A*, 22(2), 139–149.
- [29] Mohseni, P., Solberg, J. K., Karlsen, M., Akselsen, O. M., & Østby, E. (2012). Investigation of mechanism of cleavage fracture initiation in intercritically coarse grained heat affected zone of HSLA steel. *Materials Science and Technology*, 28(11), 1261–1268.
- [30] Lee, S., Kim, B. C., & Lee, D. Y. (1989). Fracture mechanism in coarse grained HAZ of HSLA steel welds. *Scripta Metallurgica*, 23(6), 995–1000. [https://doi.org/10.1016/0036-9748\(89\)90284-6](https://doi.org/10.1016/0036-9748(89)90284-6)
- [31] Davis, C. L., & King, J. E. (1994). Cleavage Initiation in the Intercritically Reheated Coarse-Grained Heat-Affected Zone : Part I . Fractographic Evidence. *Metallurgical and Materials Transactions A*, 25A, 563–573.
- [32] Lee, S. G., Kim, B., Sohn, S. S., Kim, W. G., Um, K. K., & Lee, S. (2019). Effects of local-brittle-zone (LBZ) microstructures on crack initiation and propagation in three Mo-added high-strength low-alloy (HSLA) steels. *Materials Science and Engineering A*, 760(June), 125–133. <https://doi.org/10.1016/j.msea.2019.05.120>
- [33] Yusof, F., & Jamaluddin, M. F. (2014). Welding Defects and Implications on Welded Assemblies. *Comprehensive Materials Processing*, 125–134. <https://doi.org/10.1016/B978-0-08-096532-1.00605-1>
- [34] Pirinen, M. (2013). *The Effects of Welding Heat Input on the Usability of High Strength Steels in Welded Structures* (Doctoral dissertation). Lappeenranta University of Technology.
- [35] Celin, R., Burja, J., & Kosec, G. (2016). A comparison of as-welded and simulated heat affected zone (HAZ) microstructures. *Materiali in Tehnologije*, 50(3), 455–460. <https://doi.org/10.17222/mit.2016.006>
- [36] Kucharczyk, P., Madia, M., Zerbst, U., Schork, B., Gerwien, P., & Münstermann, S. (2018). Fracture-mechanics based prediction of the fatigue strength of weldments. Material aspects. *Engineering Fracture Mechanics*, 198, 79–102. <https://doi.org/10.1016/j.engfracmech.2017.09.010>
- [37] Far, S. M. (2011). Influence of thermal simulated and real tandem submerged arc welding process on the microstructure and mechanical properties of the coarse-grained heat-affected zone. *Materials and Manufacturing Processes*, 26(11), 1423–1429. <https://doi.org/10.1080/10426914.2010.544827>
- [38] Chen, J. H., & Cao, R. (2015a). *Micromechanism of Cleavage Fracture of Metals*. Butterworth-Heinemann. <https://doi.org/10.1016/B978-0-12-800765-5.00003-4>
- [39] Morris Jr, J. W., Kinney, C., Pytlewski, K., & Adachi, Y. (2013b). Microstructure and cleavage in lath martensitic steels. *Science and Technology of Advanced Materials*, 14. <https://doi.org/10.1088/1468-6996/14/1/014208>
- [40] Pineau, A., Benzerga, A. A., & Pardoën, T. (2016). Failure of metals I : Brittle and ductile fracture. *Acta Materialia*, 107, 424–483.
- [41] Tu, M. Y., Wang, W. H., & Hsu, Y. F. (2006). On the Microstructure and Fracture Surface of Bainite in JIS SK5 Steel. *Solid State Phenomena*, 118, 451–456. <https://doi.org/10.4028/www.scientific.net/SSP118.451>

- [42] Briant, C. (1988). Intergranular Fracture in Metals. *Journal de Physique Colloques*, 49(C5), 3–23.
- [43] Ghosh, A. (2016). *Effect of Microstructure and Crystallographic Texture on Impact Toughness in Low Carbon Ferritic Steel* (Doctoral dissertation February). Indian Institute of Technology. <https://doi.org/10.13140/RG.2.1.5175.6562>
- [44] Curry, D. A., & Knott, J. F. (1978). Effects of microstructure on cleavage fracture stress in steel. *Metal Science*, 12(11), 511–514.
- [45] Chen, J. H., & Cao, R. (2015b). Chapter 1 - Introduction. In J. H. Chen & R. Cao (Eds.), *Micromechanism of cleavage fracture of metals* (pp. 1–54). Butterworth-Heinemann. <https://doi.org/10.1016/B978-0-12-800765-5.00001-0>
- [46] Gu, C., Lian, J., Bao, Y., & Münstermann, S. (2019). Microstructure-based fatigue modelling with residual stresses : Prediction of the microcrack initiation around inclusions. *Materials Science & Engineering A*, 751, 133–141. <https://doi.org/10.1016/j.msea.2019.02.058>
- [47] Li, X., Ma, X., Subramanian, S. V., Shang, C., & Misra, R. D. K. (2014). Influence of prior austenite grain size on martensite – austenite constituent and toughness in the heat affected zone of 700 MPa high strength linepipe steel. *Materials Science & Engineering A*, 616, 141–147. <https://doi.org/10.1016/j.msea.2014.07.100>
- [48] Zhou, M.-w., & Yu, H. (2012). Effects of precipitates and inclusions on the fracture toughness of hot rolling X70 pipeline steel plates. *International Journal of Minerals, Metallurgy and Materials*, 19(9), 805–811. <https://doi.org/10.1007/s12613-012-0632-0>
- [49] Guo, F., Wang, X., Liu, W., Shang, C., Misra, R. D. K., Wang, H., Zhao, T., & Peng, C. (2018). The Influence of Centerline Segregation on the Mechanical Performance and Microstructure of X70 Pipeline Steel. *Steel Research International*, 89(1800407), 1–8. <https://doi.org/10.1002/srin.201800407>
- [50] Ray, A., Sivaprasad, S., & Chakrabarti, D. (2019). A Critical Grain Size Concept to Predict the Impact Transition Temperature of Ti- Microalloyed Steels. *International Journal of Fracture*, 173(2), 215–222.
- [51] Knott, J. F. (1995). Micromechanisms of fracture and their structural significance. *Second Griffith Conference*.
- [52] Yang, Z., Liu, Z., He, X., Qiao, S., & Xie, C. (2018). Effect of microstructure on the impact toughness and temper embrittlement of SA508Gr . 4N steel for advanced pressure vessel materials. *Scientific Reports*, 8(207), 1–12. <https://doi.org/10.1038/s41598-017-18434-3>
- [53] Kim, H. J., Kim, Y. H., & Morris, J. W. (1998). Thermal mechanisms of grain and packet refinement in a lath martensitic steel. *ISIJ International*, 38(11), 1277–1285. <https://doi.org/10.2355/isijinternational.38.1277>
- [54] Song, R., Ponge, D., & Raabe, D. (2005). Mechanical properties of an ultra-fine grained C-Mn steel processed by warm deformation and annealing. *Acta Materialia*, 53(18), 4881–4892. <https://doi.org/10.1016/j.actamat.2005.07.009>
- [55] Morris Jr, J. W. (2001). The influence of grain size on the mechanical properties of steel. [https://doi.org/10.1016/S0965-9773\(97\)00137-2](https://doi.org/10.1016/S0965-9773(97)00137-2)

- [56] Park, M. H., Shibata, A., & Tsuji, N. (2020). Challenging Ultra Grain Refinement of Ferrite in Low-C Steel Only by Heat Treatment. *Frontiers in Materials*, 7(November), 1–10. <https://doi.org/10.3389/fmats.2020.604792>
- [57] Li, X., Zhao, J., Dong, L., Devesh Kumar Misra, R., Wang, X., Wang, X., & Shang, C. (2020). The significance of coherent transformation on grain refinement and consequent enhancement in toughness. *Materials*, 13(22), 1–15. <https://doi.org/10.3390/ma13225095>
- [58] Smoljan, B. (2004). An analysis of combined cyclic heat treatment performance. *Journal of Materials Processing Technology*, 155-156(1-3), 1704–1707. <https://doi.org/10.1016/j.jmatprotec.2004.04.121>
- [59] Hall, E. O. (1951). The deformation and ageing of mild steel: III Discussion of results. *Proceedings of the Physical Society. Section B*, 64(9), 747–753. <https://doi.org/10.1088/0370-1301/64/9/303>
- [60] Petch, N. (1953). The cleavage strength of polycrystals. *J. Iron Steel Inst.*, 174(25).
- [61] Inoue, T., Qiu, H., Ueji, R., & Kimura, Y. (2021). Ductile-to-brittle transition and brittle fracture stress of ultrafine-grained low-carbon steel. *Materials*, 14(1634), 1–14. <https://doi.org/10.3390/ma14071634>
- [62] Hanamura, T., Yin, F., & Nagai, K. (2004). Ductile-brittle transition temperature of ultrafine ferrite/cementite microstructure in a low carbon steel controlled by effective grain size. *ISIJ International*, 44(3), 610–617. <https://doi.org/10.2355/isijinternational.44.610>
- [63] Griffith, A. A. (1920). The Phenomena of Rupture and Flow in Solids. *Philosophical Transactions of the Royal Society A: Mathematical, Physical and Engineering Sciences*, 100, 163–198.
- [64] Lee, S., Kim, S., Hwang, B., Lee, B. S., & Lee, C. G. (2002). Effect of carbide distribution on the fracture toughness in the transition temperature region of an SA 508 steel. *Acta Materialia*, 50, 4755–4762.
- [65] Bordet, S. R., Karstensen, A. D., Knowles, D. M., & Wiesner, C. S. (2005). A new statistical local criterion for cleavage fracture in steel . Part II : application to an offshore structural steel. *Engineering Fracture Mechanics*, 72, 453–474. <https://doi.org/10.1016/j.engfracmech.2004.02.010>
- [66] Pacyna, J., & Witek, L. (1988). The effect of carbides on fracture toughness of steels of ferritic matrix. *Steel Research International*, 59, 68–74.
- [67] Lindley, T. C., Oates, G., & Richards, C. E. (1970). A CRITICAL APPRAISAL OF CARBIDE CRACKING FERRIDE/CARBIDE AGGREGATES. *Acta Metallurgica*, 18, 1127–1136.
- [68] Miao, P., & Knott, J. F. (2015). Effects of Inclusions and Their Surface Chemistry on Cleavage Fracture in a C- Mn Steel Weld Metal. *HSLA Steels 2015, Microalloying 2015 & Offshore Engineering Steels*, 1149–1161.
- [69] Fairchild, D. P., Howden, D. G., & Clark, W. A. T. (2000). The Mechanism of Brittle Fracture in a Microalloyed Steel : Part I . Inclusion-Induced Cleavage. *Metallurgical and Materials Transactions A*, 31A, 641–652.
- [70] Ghosh, A., Ray, A., Chakrabarti, D., & Davis, C. L. (2013). Cleavage initiation in steel : Competition between large grains and large particles. *Materials Science & Engineering A*, 561, 126–135. <https://doi.org/10.1016/j.msea.2012.11.019>

- [71] Garrison, W. M., & Wojcieszynski, A. L. (2007). A discussion of the effect of inclusion volume fraction on the toughness of steel. *Materials Science & Engineering A*, 464, 321–329. <https://doi.org/10.1016/j.msea.2007.02.015>
- [72] Ray, A., Paul, S. K., & Jha, S. (1995). Effect of Inclusions and Microstructural Characteristics on the Mechanical Properties and Fracture Behavior of a High-Strength Low-Alloy Steel. *Journal of Materials Engineering and Performance*, 4(6), 679–688.
- [73] Jia, T., Zhou, Y., Hia, X., & Wang, Z. (2017). Effects of Microstructure on CVN Impact Toughness in Thermomechanically Processed High Strength Microalloyed. *Metallurgical and Materials Transactions A*, 48(2), 685–696.
- [74] Laitinen, R. (2006). *Improvement of weld HAZ toughness at low heat input by controlling the distribution of M-A constituents* (Doctoral dissertation). University of Oulu.
- [75] Bayraktar, E., & Kaplan, D. (2004). Mechanical and metallurgical investigation of martensite-austenite constituents in simulated welding conditions. *Journal of Materials Processing Technology*, 153–154, 87–92. <https://doi.org/10.1016/j.jmatprotec.2004.04.021>
- [76] Kumar, S., & Nath, S. K. (2017). Effect of Weld Thermal Cycles on Microstructures and Mechanical Properties in Simulated Heat Affected Zone of a HY 85 Steel. *Transactions of the Indian Institute of Metals*, 70(1), 239–250. <https://doi.org/10.1007/s12666-016-0880-1>
- [77] Li, Y., & Baker, T. N. (2010). Effect of morphology of martensite-austenite phase on fracture of weld heat affected zone in vanadium and niobium microalloyed steels. *Materials Science and Technology*, 26(9), 1029–1040. <https://doi.org/10.1179/026708309X12512744154360>
- [78] Luo, X., Chen, X., Wang, T., Pan, S., & Wang, Z. (2018). Effect of morphologies of martensite-austenite constituents on impact toughness in intercritically reheated coarse-grained heat-affected zone of HSLA steel. *Materials Science and Engineering A*, 710(October 2017), 192–199. <https://doi.org/10.1016/j.msea.2017.10.079>
- [79] Wallin, K., Yamamoto, M., & Ehrnström, U. (2016). Location of initiation sites in fracture toughness testing specimens - the effect of size and side grooves. *ASME 2016*, 1–9.
- [80] Kyada, T., Shant, J. R., Goyal, R. K., & Kathayat, T. S. (2014). Understanding the Delamination and Its Effect on Charpy Impact Energy in Thick Wall Linepipe Steel. *Journal of Materials and Metallurgical Engineering*, 4(1), 31–39.
- [81] Mendoza, R., Alanis, M., Perez, R., & Gonzalez, C. (2002). On the processing of Fe-C-Mn-Nb steels to produce plates for pipelines with sour gas resistance. *Materials Science and Engineering A*, 337, 115–120.
- [82] Su, L., Li, H., Lu, C., Li, J., Fletcher, L., Simpson, I. A. N., Barbaro, F., Zheng, L. E. I., & Bai, M. (2016). Transverse and z-Direction CVN Impact Tests of X65 Line Pipe Steels of Two Centerline Segregation Ratings. *Metallurgical and Materials Transactions A*, 47A, 3919–3932. <https://doi.org/10.1007/s11661-016-3578-4>
- [83] Bhadeshia, H., & Honeycombe, R. (2017). *Steels : Microstructure and Properties* (4th ed.). Butterworth-Heinemann.
- [84] Lei, Y., Dowd, N. P. O., & Webster, G. A. (2000). Fracture mechanics analysis of a crack in a residual stress field. *International Journal of Fracture*, 106, 195–216.

- [85] Xu, W. G., & Burdekin, F. M. (1998). Effects of residual stresses on constraint and fracture behaviour of wide plates. *Proceedings of the Royal Society A*, 2505–2528.
- [86] Gao, X., & Jr, R. H. D. (2001). An engineering approach to assess constraint effects on cleavage fracture toughness. *Engineering Fracture Mechanics*, 68, 263–283.
- [87] Gu, C., Lian, J., Bao, Y., Xiao, W., & Münstermann, S. (2019). Numerical Study of the Effect of Inclusions on the Residual Stress Distribution in High-Strength Martensitic Steels During Cooling. *Applied Sciences*, 9(455), 1–13. <https://doi.org/10.3390/app9030455>
- [88] Murakami, Y., & Uchida, M. (1992). Effects of thermal residual stress and external stress on stress intensity factors for a penny-shaped crack emanating from an ellipsoidal nonmetallic inclusion. *Proceedings JSME Meeting*, 70(B), 239–241.
- [89] Nasir, N. S. M., Razab, M. K. A. A., Mamat, S., & Ahmad, M. I. (2016). Review on Welding Residual Stress. *ARPJ Journal of Engineering and Applied Sciences*, 11(9), 6166–6175.
- [90] Sule, J., Ganguly, S., Coules, H., & Pirling, T. (2015). Comparative Study of Evolution of Residual Stress State by Local Mechanical Tensioning and Laser Processing of Ferritic and Austenitic Structural Steel Welds. *Journal of Mechanical Engineering and Automation*, 5(1).

3

A COMPREHENSIVE QUANTITATIVE CHARACTERISATION OF THE MULTIPHASE MICROSTRUCTURE OF A THICK-SECTION HIGH STRENGTH STEEL

The through-thickness heterogeneous microstructure of thick-section high strength steels is responsible for the significant scatter of properties along the thickness. In this study, in order to identify the critical microstructural features in the fracture behaviour and allow for design optimisation and prediction of structural failure, the through-thickness microstructure of thick-section steels was extensively characterised and quantified. For this purpose, samples were extracted from the top quarter and middle thickness positions, and a combination of techniques including chemical composition analysis, dilatometry, and microscopy was used. The hardness variation through the thickness was analysed via micro-Vickers measurements and the local hardness variation in the middle section was studied via nanoindentation. The middle section presented larger prior austenite grain (PAG) sizes and larger sizes and area fraction of inclusions than the top section. Additionally, cubic inclusions were observed distributed as clusters in the middle, sometimes decorating PAG boundaries. Defects associated with the cubic inclusions or the interface between the matrix and the circular and cubic inclusions were observed in the mid-thickness. Moreover, the middle section presented long interfaces with the most significant hardness gradients due to the presence of hard centreline segregation bands. Hence, the microstructural and nanoindentation analyses indicated the middle section as the most likely area to have the lowest fracture toughness and, therefore, the most unfavourable section for fracture performance of the investigated S690QL high strength steel. The detrimental effect of the middle section was confirmed via CTOD tests where the middle presents lower fracture toughness than the top section.

This chapter is based on the scientific publication Bertolo, V., Jiang, Q., Scholl, S., Petrov, R. H., Hangen, U., Walters, C., Sietsma, J. & Popovich, V. (2022). A comprehensive quantitative characterisation of the multiphase microstructure of a thick-section high strength steel, *Journal of Materials Science*, 57, 7101-7126. <https://doi.org/10.1007/s10853-022-07121-y>

3.1. INTRODUCTION

The multiphase microstructure of high strength steels (HSSs), composed of multiple bcc microconstituents, carbides, and inclusions, is responsible for the attractive combination of strength and toughness, greatly valued for structural applications, such as components of highly loaded offshore lifting equipment. Supporting high loads is of utmost importance for these structures, and thick-section steel plates are required. The commonly found microstructural complexity of HSSs may become more pronounced when produced in thick sections due to the non-uniform cooling rates and deformation levels through the thickness experienced during the processing route (e.g., rolling and heat treatments such as quenching and tempering). As a result, different phases, grain sizes, inclusions, phase fractions, and the presence of elemental segregation may be observed from the outer surface of the steel plate towards its centre. Consequently, a considerable through-thickness variation of mechanical properties is observed [1–3]. Although HSSs display the desired properties for structural applications, harsh service conditions (e.g., temperature and loading levels) may make them prone to cleavage fracture leading the structure to fail catastrophically. Hence, to predict and control structural failure and optimise thick-section steel's design it is essential to accurately characterise the through-thickness microstructure and the resulting local variations of mechanical properties.

Several studies [1–5] have investigated the heterogeneous through-thickness microstructure and its effect on the mechanical properties of thick-section steel plates. However, the key microstructural features have not been thoroughly characterised and quantified for adequate experimental and modelling assessment of cleavage fracture. While macroscopic inhomogeneities of steels have been modelled at millimetre scale with bimodal methods in cleavage simulations [6, 7], the heterogeneous microstructures at a smaller scale have not been taken into account. The micromechanism-driven modelling of cleavage fracture typically accounts for the probability of failure based on the local stress (and sometimes strain) field, which is referred to as the local approach [8, 9]. On the grain scale and lower scale, multi-barrier theory has been proposed to represent the micromechanism of cleavage in local approaches (e.g., [10–13]). The application of a multi-barrier theory requires knowledge of the nucleating particle size distribution and the grain (packet) size distribution. Therefore, the required comprehensive assessment of the microstructural variation of thick-section HSSs that allows for identifying potential critical sites in fracture behaviour has not yet been performed.

However, correlating the microstructural heterogeneity and properties of HSSs requires extensive work due to the microstructural complexity of the steel plate analysed herein. For this purpose, different techniques and methods have to be used to obtain relevant microstructural information, making it possible to establish a clear processing-microstructure-properties relationship. Moreover, this study faces some challenges.

First, we face the difficulty to distinguish and quantify bcc microconstituents. The microstructure of quenched and tempered HSSs consists of a mixture of tempered bcc micro-constituents such as martensite and bainite [1]. Due to the similar structure and morphology of these constituents, it is a significant challenge to distinguish and quantify them by standard microscopy techniques. Alternatively, dilatometry is a technique used in phase transformation studies and may be useful to distinguish and quantify

phases formed under a given thermal cycle [14]. Furthermore, although all previously mentioned constituents are bcc-structured, the use of Electron Backscatter Diffraction (EBSD) can be valuable. Since each phase has its characteristics inherited from the phase transformation nature, their diffraction pattern may be different. Consequently, some parameters calculated from the EBSD data (e.g., image quality, kernel average misorientation, and grain orientation spread) can assist the characterisation and quantification of phases in a multi-bcc-phase microstructure. For instance, several studies unanimously use EBSD to differentiate bcc micro-constituents in steels [15, 16]. However, EBSD analysis may not lead to an accurate and conclusive analysis in bcc micro-constituents distinction, especially for tempered microstructures where the separation of martensite from other phases is difficult because the quality of the Kikuchi pattern is increasingly becoming more similar to the other phases [15, 16]. Another beneficial approach can be to perform the material characterisation in the reverse way where the local mechanical response of the bcc micro-constituents is used to distinguish them.

Recently, tests on the nanoscale allowed the measurement of properties of individual features. Chang et al. [17] observed that ferrite, bainite, and martensite have considerably different average nanohardness (3.8, 4.4, and 5.6 GPa, respectively) in a multiphase advanced high strength steel. This difference may assist their distinction along with other techniques. However, attention must be paid since the measurement scatter sometimes causes overlap between the results for several phases. Although this approach is promising to distinguish bcc micro-constituents, it may be challenging to apply it to tempered steels as the nanohardness values for the phases can become close and even overlap, making it difficult to distinguish between them [18].

Second, conventional microhardness measurement is insufficient to measure the local gradient of properties in detail due to its large indent size compared to the dimensions of microstructural features. Hence, investigation in the nanoscale is needed. Additionally, indentation hardness is also useful for investigating the effects of microstructural heterogeneities on properties since it has a direct relationship with other mechanical properties (e.g., elastic moduli, strength, and ductility) [19, 20]. Moreover, hardness analysis may indicate critical sites in fracture behaviour that can affect the global material performance. For instance, Hidalgo, Celada-Casero and Santofimia [21] reported that the significant hardness difference between Mn enriched areas and the surrounding matrix was responsible for generating brittle fracture mechanisms in a medium Mn quenching and partitioning steel. Another observation regarding the effect of hardness gradients in fracture was done by Lee et al. [22], where large hardness variations make the material more prone to interfacial separation between matrix and hard particles, thus lowering the fracture toughness [21, 22]. Hence, several studies reveal that hardness gradients may facilitate crack formation.

Therefore, this work aims to identify critical microstructural features for fracture in commercially available HSSs used in actual structures. Hence, the through-thickness microstructure of a commercially available thick-section quenched and tempered high strength steel is comprehensively investigated quantitatively. For this purpose, a combination of techniques involving chemical composition analysis, dilatometry, microscopy, and nanoindentation is used. The in-depth microstructural characterisation presented in this paper also represents a unique combination of microstructural parameters which

are necessary for understanding and modelling the continuum-level properties. The effects of the multiphase and heterogeneous microstructure on mechanical properties and the identification of critical sites for fracture behaviour are investigated in terms of hardness and fracture toughness measurements. Moreover, nanoindentation was used to distinguish and quantify tempered bcc micro-constituents. This research will be useful to assess fracture behaviour, including the modelling approaches, and also to optimize steel design [23].

3

3.2. MATERIALS AND METHODS

A commercially available 80 mm thick hot rolled, quenched, and tempered S690 high strength steel plate (designated as S690QL in accordance with EN 10025-6 [24]) of 80 x 1500 x 5000 mm³, used in offshore structural applications, with the limited toughness of the material as a critical factor, was studied. Out of the large commercial plate, smaller slabs (80x740x180 mm³) were cut for further investigation. The chemical composition along the thickness of the S690QL steel plate was measured by LECO combustion analysis (for C, N, and S) and X-ray fluorescence (XRF) (for other elements) (Table 3.1). All elements, including the ones referred to as “other”, are in accordance with the range determined by the standard EN 10025-6 (max wt.% of Mn=1.7, Ni=4.0, Cr=1.5, Nb=0.06, P=0.02, N=0.015, S=0.01 and B=0.005) [24]. In order to avoid any superficial layer that may affect the results, the samples’ surfaces were ground with coarse P180 aluminium oxide sanding paper. Elements can generally be considered homogeneously distributed through the plate thickness as average values are within the scatter except for C, which is higher in the top section.

Table 3.1: Through thickness chemical composition of S690QL (measured by XRF and LECO).

wt. (%)	Fe	C	Si	Al	Mo	Other
Top	Bal.	0.170 ± 0.001	0.29 ± 0.02	0.070 ± 0.005	0.30 ± 0.01	Mn, Ni, Cr, Nb, P, N, S, B
Middle	Bal.	0.160 ± 0.001	0.30 ± 0.03	0.08 ± 0.01	0.29 ± 0.02	

To characterise the material along the thickness, samples were taken from the top quarter (further referred to as top) and middle thickness positions. The investigation of these thickness sections is motivated by 1) the quarter section is the thickness position required to be tested according to some standard and rules (e.g., 10025-6 [24]) for quality control of this type of steel, and 2) the middle section is reported as the most detrimental region for the performance of thick-section steel plates [1–4]. The bottom quarter section was also characterised and found to be identical to the top quarter sections. As isotropy is expected in this material, only one plane was chosen to be studied. Figure 3.1 schematically represents the investigated thickness positions and the RDxND planes (hatched areas in top and middle thickness positions), in which 2-D characterisation and hardness analyses were carried out.

The through-thickness microstructure of the steel plate was etched with 5% Nital and analysed through conventional optical microscopy, optical Keyence digital microscopy, and scanning electron microscopy (SEM). The last two techniques mentioned were also used to quantify inclusions. The quantification of inclusions was performed according

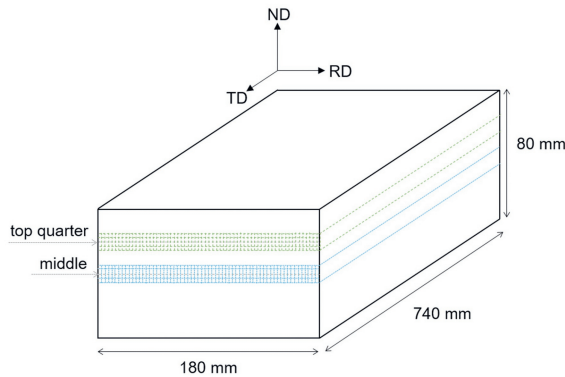


Figure 3.1: Schematic illustration of the investigated thickness positions. The 2D analyses were carried out in the hatched RD x ND plane.

to ASTM E1245-03:2016 [25]. In order to reveal the Prior Austenite Grain (PAG) boundaries and, for the cases in which it is more interesting to have the centreline segregation bands more distinguishable from the matrix, samples were swabbed etched with a solution of 100 ml of saturated aqueous picric acid solution and 0.5 g of sodium dodecylbenzene sulfonate for 5 minutes.

Chemical composition measurements of centreline segregation bands in the middle section of the S690QL high strength steel plate were performed by Electron Probe Microanalysis (EPMA) with a JEOL JXA 8900R microprobe using an electron beam with energy of 10 keV and beam current of 200 nA employing Wavelength Dispersive Spectrometry (WDS). Before EPMA measurements, the extremes of four segregation bands were identified by micro-indentations (HV_3) in an etched sample. Subsequently, the sample was polished again with 3 μm and 1 μm diamond solution and a colloidal silica solution (OPS). EPMA analysis was performed along a line of 300 μm in the thickness direction in increments of 2 μm . The line scan initiates and ends at points located outside the investigated segregation band, and both points are located approximately 150 μm from the centre of the band.

Dilatometry solid cylindrical specimens with dimensions of 10 mm x 4 mm (length x diameter) were placed in a Bähr 805A quench dilatometer (Bähr-Thermoanalyse GmbH, Germany), and induction heated and cooled using helium gas according to the industrial quenching thermal profile (Fig. 3.2). Note that for the middle section, a reduction in the cooling rate is observed from 200 $^{\circ}\text{C}$. However, this reduction caused instrumental disturbances in the dilatometry curve. As no phase transformation below 200 $^{\circ}\text{C}$ is expected and was not observed for the top section, the cooling profile for the middle section has been simplified to 5 $^{\circ}\text{C/s}$. Additionally, samples were analysed under a rapid quenching, 75 $^{\circ}\text{C/s}$, to define the start and finish martensite transformation temperatures to be used as a reference. The temperature was monitored using a thermocouple spot-welded to the centre of the sample. Only the quenching stage was studied in the dilatometric tests since the tempering stage (between 600 $^{\circ}\text{C}$ and 650 $^{\circ}\text{C}$ for a few minutes) only affects the carbide precipitation and not the phase composition, if no retained austenite is

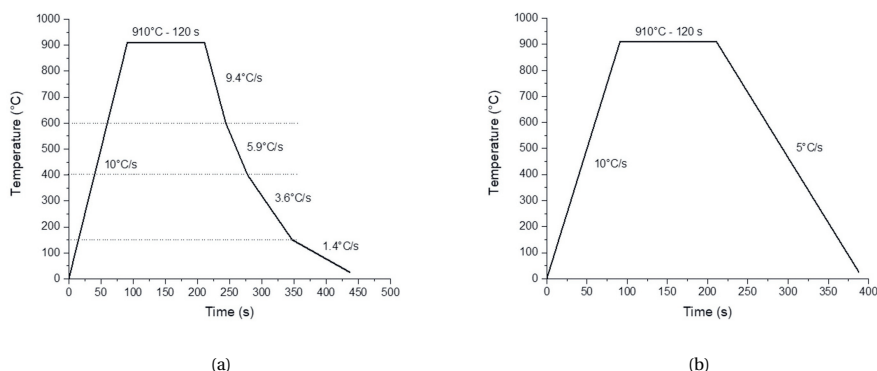


Figure 3.2: Schematic representation of the thermal profile applied in the dilatometer to (a) top and (b) middle sections of the S690QL steel plate.

present in the quenched material [26]. Consequently, no significant dilatometry signal can be expected. Afterward, the results obtained by dilatometric tests are compared to theoretical CCT diagrams calculated by the JMatPro 7.0 software [27].

EBSID data were acquired on a JEOL scanning electron microscope equipped with a Field Emission Gun (FEG-SEM) using 25 kV accelerating voltage, the working distance of 25 mm, tilt angle of 70°, and step size 0.2 μm by means of HKL Channel 5 software and post-processed with EDAX-TSL-OIM AnalysisTM software. Scan areas around 360 μm x 270 μm were randomly chosen from the top and middle sections (areas outside and including the segregation bands). Indentations (HV 3) were placed in the extremes of some segregation bands as previously explained to locate them. The initial EBSID post-processing step was the data clean-up. First, grain fit standardization with a grain tolerance angle of 5° and a minimum grain size of 4 pixels was applied, considering that grains contain multiple pixel rows. Secondly, the neighbour orientation correlation procedure with a grain tolerance angle of 5° and a minimum confidence index of 0.1 was used. Lastly, neighbour phase correlation with a minimum confidence index of 0.1 was applied. Afterward, grains were defined with a tolerance angle of 5° and a minimum size of 4 pixels. Prior austenite grains were reconstructed in automatic mode using quadruplets as the reconstruction method, with tolerance for parent grain nucleation and growth equal to 3° and 6° by the ARPGE software developed by Cayron [28]. Each reconstructed map was post-processed in the TSL-OIM Analysis v7 software for grain size measurements. Minor and major axis (i.e., width and length, respectively) distributions of PAG were obtained using the TSL-OIM software, and the weighted average values were post-processed. PAG and packet sizes and block widths were measured according to ASTM E112-13 through the Heyn lineal intercept procedure [29].

The hardness analysis was carried out at micro- and nanoscales. Micro-Vickers hardness testing at the minimum load produces indents with a dimension of around 8 μm , which are too large for most of the fine-scale features in the material. Although it would be possible to indent some particles and grains with dimensions larger than the minimum indent size, it would not be feasible to perform multiple indentations within indi-

vidual features to obtain a representative result. Nevertheless, micro-Vickers hardness can still be used to evaluate the microstructure-hardness gradients through the thickness of the steel plate. Since the microstructure is significantly inhomogeneous and measurements in single features are not possible at the micro-scale, hardness testing was performed through the thickness of the S690QL steel plate using a DuraScan 70 Emco with 30 N (indent size around 140 μm) to average out the local inhomogeneity and better understand how the bulk hardness varies in such thick quenched and tempered plates. Separate nanoindentation measurements were performed in a Hysitron TI 980 Triboindenter from Bruker (BNSM division, Aachen, Germany) in the accelerated property mapping (XPM) mode. A 200x200 indentation map was made, covering an area of approximately 320x320 μm^2 in the middle section of the S690QL steel plate. Shallow indents are performed to accommodate the high resolution. In this study, a preliminary analysis with different load levels and resultant indentation depths was made to identify the minimum load and depth in which the properties would become independent of the indentation depth to avoid indentation size effects (ISE) [30]. Therefore, the maximum load and resultant maximum indentation depth were defined as 1 mN and 70 nm. The indentations were made with a Berkovich indenter in load-controlled mode. In order to avoid overlapping of the indent's plastic zones, a distance of 1.6 μm was kept between the indents. Hardness and reduced modulus properties were obtained from the load-displacement curves through the method of Oliver and Pharr [31]. Afterward, EBSD scans using a step size of 0.07 μm were performed in the tested area to correlate the obtained properties with microstructural aspects such as phases.

To investigate the through-thickness microstructural inhomogeneity effect on cleavage fracture, sub-sized single edge-notched bending (SENB) specimens extracted from top and middle sections were tested by three-point bending similar to the ISO 12135 standard [32] at a deformation rate of 2 mm/s at $-100\text{ }^{\circ}\text{C}$ using a 350 kN MTS 858 servo hydraulic. The specimens are cooled down by immersion in liquid nitrogen until the heat exchange is over, approximately at $-196\text{ }^{\circ}\text{C}$ (liquid nitrogen's boiling temperature). This difference from the test temperature is to allow for thermal soaking and for more time to mount the sample in the set up. Afterwards, the specimens are placed in the machine, touching a thermal insulation material to avoid the fast heat exchange with the metallic parts. Then, when the test temperature is reached, the test is performed. The temperature applied in this work ($-100\text{ }^{\circ}\text{C}$) is to ensure that the test is performed in the brittle regime of the HSSs under study. The notch is oriented in T-L, parallel to the rolling direction, and the crack depth-width ratio (a/W) is equal to 0.5. Details on the specimen's dimensions and how they were extracted from the thick plate are given in Fig. 3.3.

3.3. RESULTS

3.3.1. THROUGH-THICKNESS MICROSTRUCTURAL CHARACTERISATION

The microscopic analysis of the as-received steel reveals a complex microstructure with different features interacting with each other. Figure 3.4 reasonably suggests that for both top and middle thickness positions, grains resemble tempered microconstituents,

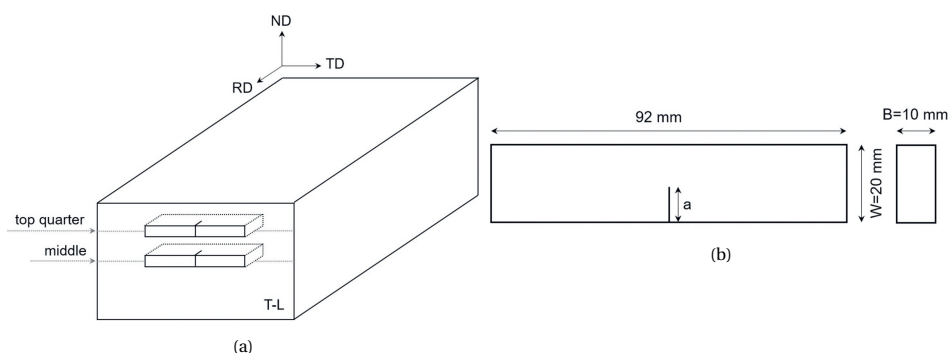


Figure 3.3: Schematic illustration showing (a) the extraction of the SENB specimens from the steel plate in terms of thickness position and notch orientation to the RD, and (b) the SENB specimen's dimensions. ND is the normal direction, RD is the rolling direction, and TD is the transverse direction.

including martensite (TM) – grains with carbides oriented in multiple directions within individual laths; bainite (TB) – grains with carbides, from the original bainite grain, aligned in a single orientation within individual laths that are barely affected during tempering; and ferrite (F) – grains with no substructure [33]. However, it should be acknowledged that the distinction of these constituents is challenging due to their morphological similarity. Hence, this procedure is of limited accuracy. For this reason, other methods (e.g., dilatometry, EBSD, and nanoindentation) to distinguish these bcc microconstituents will be applied and discussed herein.

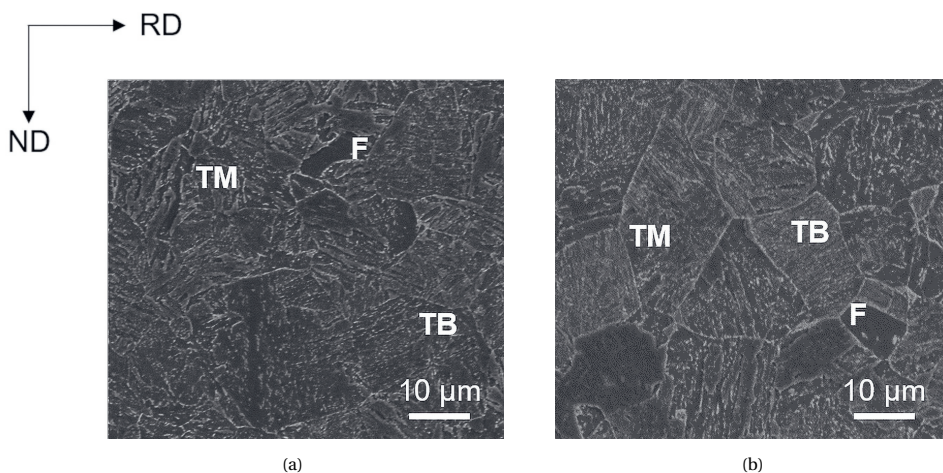


Figure 3.4: Representative SEM micrographs of (a) top and (b) middle sections of the S690QL steel plate. Grains identified as F, TB, and TM refer to ferrite, tempered bainite, and tempered martensite, respectively.

Dilatometry tests were performed for the top and middle sections. Under the quenching and tempering processing route, steels mainly transform during quenching,

while the tempering stage only causes carbide precipitation [26]. Thus, the investigated thickness sections were submitted to their respective quenching cooling routes to investigate the phase transformations that occur during the steel processing. The dilatometric curves and their derivatives are presented in Fig. 3.5. CCT diagrams for top and middle sections calculated with JMatPro software are shown in Fig. 3.6. This material's prior austenite grain size was observed to vary within a wide range, with its length between 5 to 70 μm , approximately, with a mean intercept value around 20 μm [3]. Hence, CCT curves for 5, 10, and 20 μm grain sizes are presented. Further grain size analysis and discussion will follow later in this study.

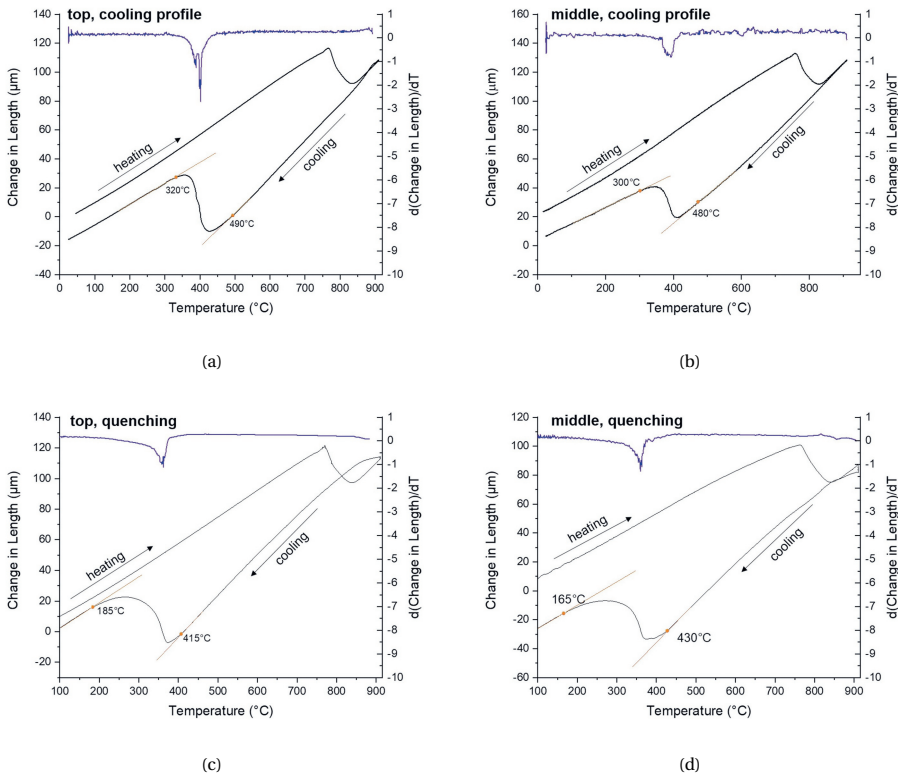


Figure 3.5: Dilatometric and cooling differential curves of (a), (c) top and (b), (d) middle samples following the cooling profile of the quenching process of the S690QL steel processing route (a), (b) and quenching (75°C/s) (c), (d), respectively.

The first deviation of the tangent from the dilatometric curves during cooling occurs in the temperature range of 480-490 $^{\circ}\text{C}$, indicating the beginning of a phase transformation, followed by a significant expansion completed between 300 $^{\circ}\text{C}$ and 320 $^{\circ}\text{C}$. The rapid quenching test performed by dilatometry indicates that the martensitic start and finish temperatures are around 415-430 $^{\circ}\text{C}$ and 165-185 $^{\circ}\text{C}$ (90% of martensite is formed at 255 $^{\circ}\text{C}$ calculated by the lever rule), respectively, for both positions in the thickness.

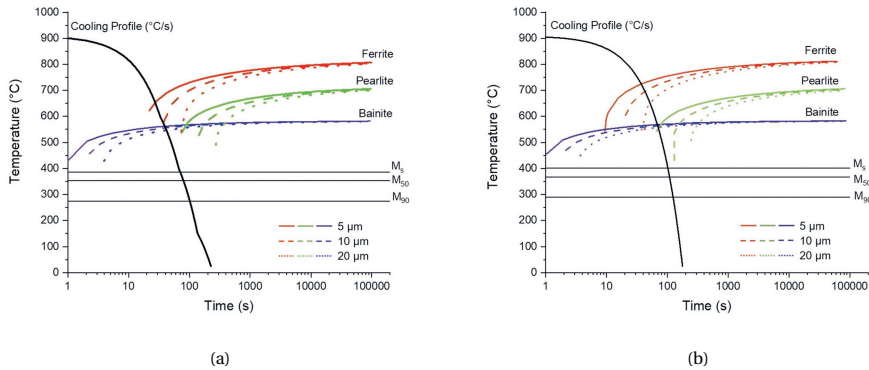


Figure 3.6: CCT diagrams calculated with JMatPro software for (a) top and (b) middle sections of the S690QL steel plate showing ferritic, pearlitic, and bainitic starting temperatures for various prior austenite grain diameters from 5 to 20 μm .

These temperatures have good agreement with the CCT diagrams (Fig. 3.6). Therefore, since the phase transformation under the cooling profile of the processing route begins and ends at temperatures above the start and finish martensitic temperatures, this transformation part likely results in another phase than martensite. According to the CCT diagrams, the most likely micro-constituent formed in this transformation temperature range is bainite. Figure 3.6 also shows that ferrite is prone to form under the quenching processing route depending on the prior austenite grain size. However, no significant dilatation was observed in the dilatometric curves that can be associated with ferrite formation.

Various inclusions are observed distributed through the matrix. Table 3.2 and Fig. 3.7 provide an overview of the most commonly found inclusions through the plate thickness. Most inclusions, regardless of the thickness position, have a complex chemical composition with mixtures of oxides, nitrides, sulphides, and carbonitrides.

The top and mid-thickness positions exhibit circular inclusions of similar sizes. However, larger cubic inclusions are observed in the middle, and they are present in larger area fractions than in the top. Furthermore, many of the inclusions in the middle section present important characteristics, as highlighted below. Firstly, middle-section inclusions have often been seen associated with defects (e.g., voids and cracking of both matrix/inclusion interface and inclusion cracking) as shown in Fig. 3.7(d) to 3.7(f). Secondly, cubic-shaped inclusions are often observed distributed as clusters. In some cases, these clusters are found decorating the PAG boundaries (Fig. 3.7(e)). Due to the proximity of the inclusions in the cluster, these inclusions may be viewed as a line of collinear inclusions, corresponding to a single large that can reach a length of up to 30 μm (Fig. 3.7(e) and 3.7(f)).

Moreover, centreline segregation bands formed during the solidification process and pancaked during the hot rolling step were observed in the mid-thickness and are shown in Fig. 3.8(a). The individually identified centreline segregation bands exhibit widths in the range of 40 to 210 μm that extend approximately 8 mm across the thickness of the

Table 3.2: Morphology, chemical composition, diameter, and area fraction of inclusions observed in the top and middle positions.

Position	Type of Inclusion	Composition	Diameter range (major axis), (μm)	Area fraction
Top	Circular	(Mg,Al,Ca)(O,N,S)	1 – 5	$5 \times 10^{-4} \pm 3 \times 10^{-4}$
		(Mg,Al,Ca,Ti)(O,N)	1 – 2.5	
	Cubic	(Nb,Ti)(C) (B,Ti,Nb)(N,C)	1 – 7	$7 \times 10^{-5} \pm 4 \times 10^{-5}$
Middle	Circular	(Mg,Al,Ca)(O) (Mg,Al,Ca,B)(N,S) (Mg,Al,Ca,Ti)(O,N)	1 – 5	$7 \times 10^{-4} \pm 3 \times 10^{-4}$
	Cubic	(Nb,Ti,Mg,Ca)(C,O,N) NbC (Nb,Ti)(C) (Nb,Ti)(C,N)	1 – 12	$2 \times 10^{-4} \pm 3 \times 10^{-5}$

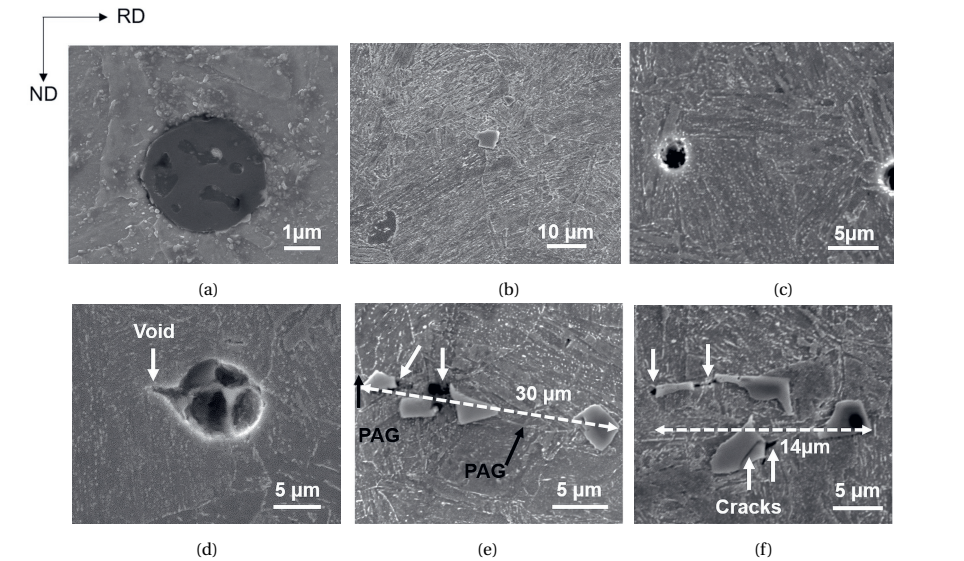


Figure 3.7: SEM micrographs of inclusions through the thickness of the S690QL steel plate showing (a) (Mg,Al,Ca)(O,N,S), (b) (Nb,Ti)(C) and (Nb,Ti)(C,N), and (c) (B)(N) inclusions for the top section; (d) (Mg,Al,Ca)(O,S), (e) (Nb, Ti) (C,N) and (f) NbC and (Nb,Ti)(N,C) inclusions for the middle section (Partially included in [3]).

plate. Then, this section of the material, layered with segregation bands, represents 10% of the material's volume. As shown in Fig. 3.8 (c), clusters of Nb-rich cubic inclusions are directly associated with these segregation bands and aligned with them. It should be mentioned that in the top section, cubic Nb-rich inclusions are often observed distributed individually. However, they can also be scarcely seen distributed as clusters and aligned similarly to the segregation bands.

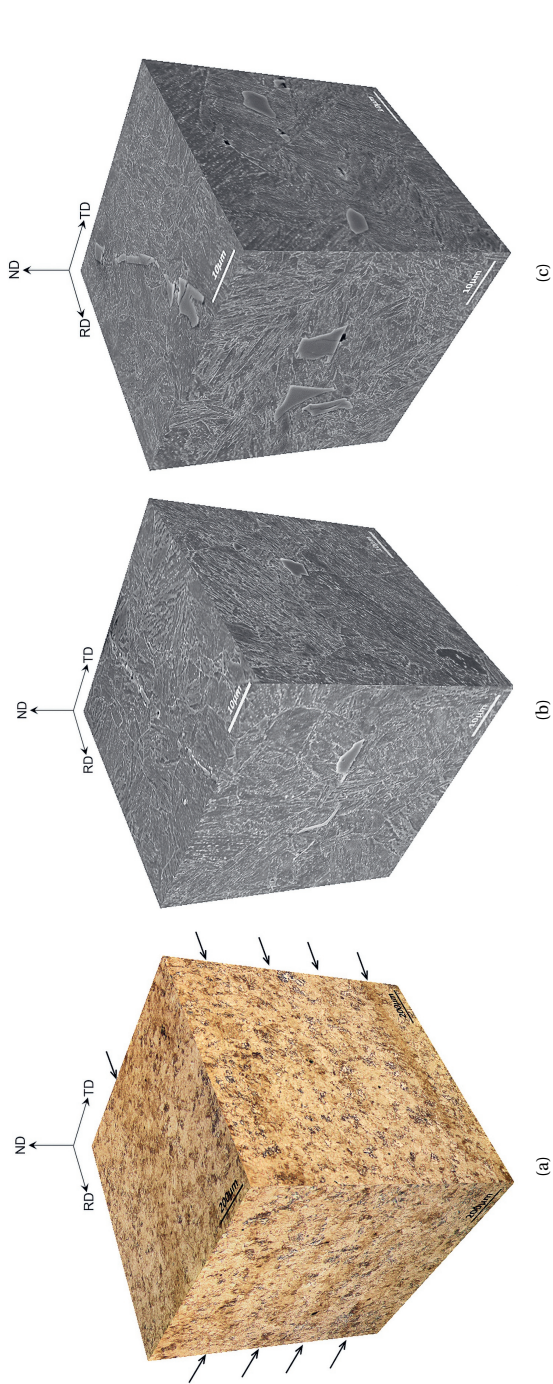


Figure 3.8: 3D-representation of (a) pancaked centreline segregation bands in the middle section by optical microscopy, and clusters of cubic inclusions distributed aligned to the segregation bands (indicated by black arrows) in the (b) top and (c) middle thickness positions of the S690QL steel plate by SEM. The scale bar in the SEM and optical images is 10 µm and 200 µm, respectively.

To characterise the chemical composition of segregation bands, EPMA line scan analyses were carried out from depleted through enriched areas. Elements including Mn, Cr, Mo, Si, Ni, and C were segregating in the bands. Figure 3.9 shows representative EPMA results for one of the analysed bands. The minimum and maximum elemental contents of each element averaged over the various line scans are shown in Table 3.3.

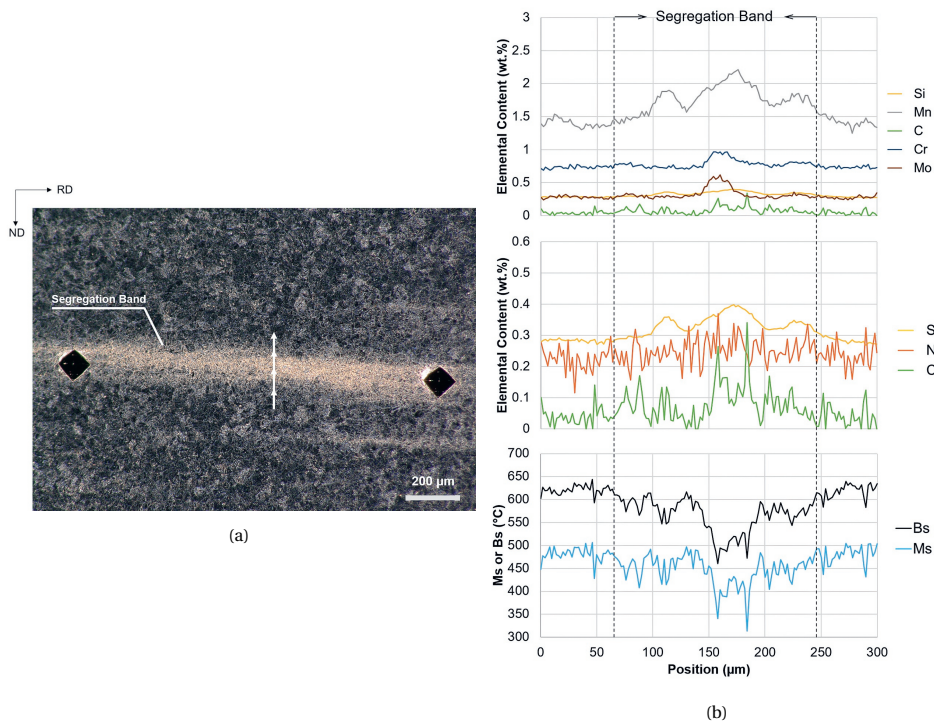


Figure 3.9: (a) Optical micrograph of the analysed segregation band. The white arrow shows the measurement start and end positions of the measurement as well as its direction. (b) Electron probe microanalysis results of the centreline segregation band. (c) Results for C, Ni, and Si in another scale are presented in a separate chart to show their trends clearly. (d) Bainite and martensite starting temperature charts as a function of the composition (per distance) are also included.

C is the element that stands out most in the segregation bands in the middle section of the S690QL steel plate, followed by Mo, as shown in Table 3.3. The content of these elements in the enriched regions reaches levels up to 29 and 4.5 times, respectively, that of the low-solute regions. The other elements – Mn, Cr, Si, and Ni – despite being present in smaller proportions compared to C and Mo, still stand out for reaching up to twice the concentration measured in depleted areas. Note that the contents of these elements also vary within the segregation band. Such elemental variation in the mid-thickness are reported to affect phase/micro-constituents transformation temperatures (e.g., bainite and martensite start temperature) and may lead to different microstructural compositions in the centreline segregation bands compared to the depleted areas and also within the bands at the same cooling rate [34–36].

Table 3.3: Average maximum and minimum values for Mn, Cr, Mo, Si, Ni, and C elements along with EPMA line scan.

Centreline Segregation Bands – Elemental Content (wt. %)						
	Mn	Cr	Mo	Si	Ni	C
Max	2 ± 0.3	1.1 ± 0.2	0.8 ± 0.3	0.40 ± 0.04	0.35 ± 0.04	0.29 ± 0.04
Min	1.10 ± 0.10	0.70 ± 0.01	0.20 ± 0.01	0.30 ± 0.01	0.10 ± 0.02	0.01 ± 0.02

The compositional dependence of theoretical bainite and martensite start temperature (B_s and M_s) is described by van Bohemen [36] and established by

$$B_s(^{\circ}\text{C}) = 839 - \sum_i P_i x_i - 270[1 - e^{(-1.33x_C)}] \quad (3.1)$$

$$M_s(^{\circ}\text{C}) = 565 - \sum_i K_i x_i - 600[1 - e^{(-0.96x_C)}] \quad (3.2)$$

where,

$$\sum_i P_i x_i = 86x_{Mn} + 23x_{Si} + 67x_{Cr} + 33x_{Ni} + 75x_{Mo};$$

$$\sum_i K_i x_i = 31x_{Mn} + 13x_{Si} + 10x_{Cr} + 18x_{Ni} + 12x_{Mo} \text{ and};$$

the concentration x_i is in wt.%, and the subscript i indicates the element (Mn, Si, Cr, Ni, and Mo).

Calculations for B_s and M_s temperatures based on both equations were performed along with the EPMA line scan and are shown in Fig. 3.9(c). According to the equations mentioned above, the higher the concentration of alloying elements, the lower the B_s and M_s temperatures. In the middle section of the steel plate under study, which presents an alternation of high-solute and low-solute bands, the difference between the highest and lowest B_s and M_s temperatures, considering all analysed segregation bands, can be up to 230 °C and 190 °C, respectively.

Visual inspection of prior austenite grains in the middle section (Fig. 3.10) suggests that this section presents a bimodal distribution of grains, with segregation bands featuring smaller grains than the areas outside these bands. The quantification of PAG and its substructure size is essential for establishing a microstructure-properties relationship and will be further presented along with the results obtained by the EBSD investigation.

The reconstructed PAGs, over the entire thickness of the steel plate, were found to have an elongated shape (Fig. 3.11). The PAG aspect ratio was around 0.43 for all investigated areas (Fig. 3.12(b)). Hence, grain sizes are measured with respect to their width and length. Figure 3.12 displays the distribution and average values of PAG's width and length. Table 3.4 shows the average PAG sizes for future comparison with the substructures size. The grain axis distribution of all sections presents a broad range of minor and major axis dimensions varying from 2 to 29 µm and 4 to 69 µm, respectively. However, a high asymmetry is noticeable where the most frequent data is concentrated on the low-dimension side. In general, for all analysed areas, most of the PAG width and length are lower than 10 µm and 23 µm, respectively.

The top section has a significantly smaller grain size than the middle section outside the segregation bands. Within the middle section, it is possible to identify a difference

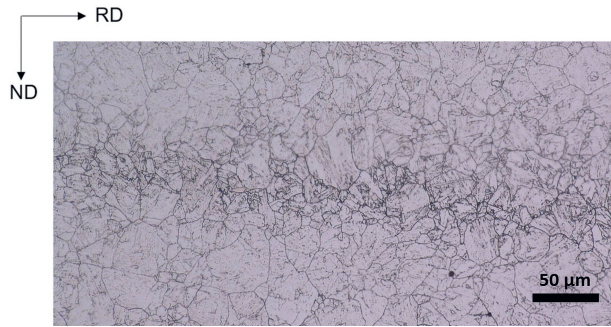


Figure 3.10: Prior austenite grain (PAG) distribution in the middle of the plate with the segregation band showing a reduction in PAG size in the region of the band configuring a bimodal distribution of PAG.

3

between average grain sizes of the areas outside the segregation bands and within the segregation bands (SB), characterising a bimodal distribution of grains in this section. The effect of the presence of segregation bands can be seen by the average values of the whole field (middle including SB), which is slightly smaller than the middle outside SB.

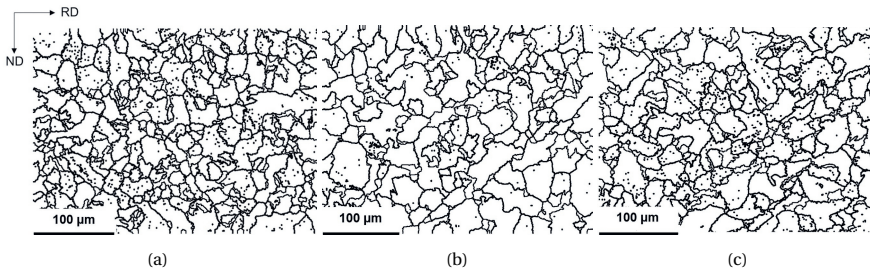


Figure 3.11: Reconstructed prior austenite grains for (a) top, (b) middle outside segregation bands, and (c) middle including segregation bands

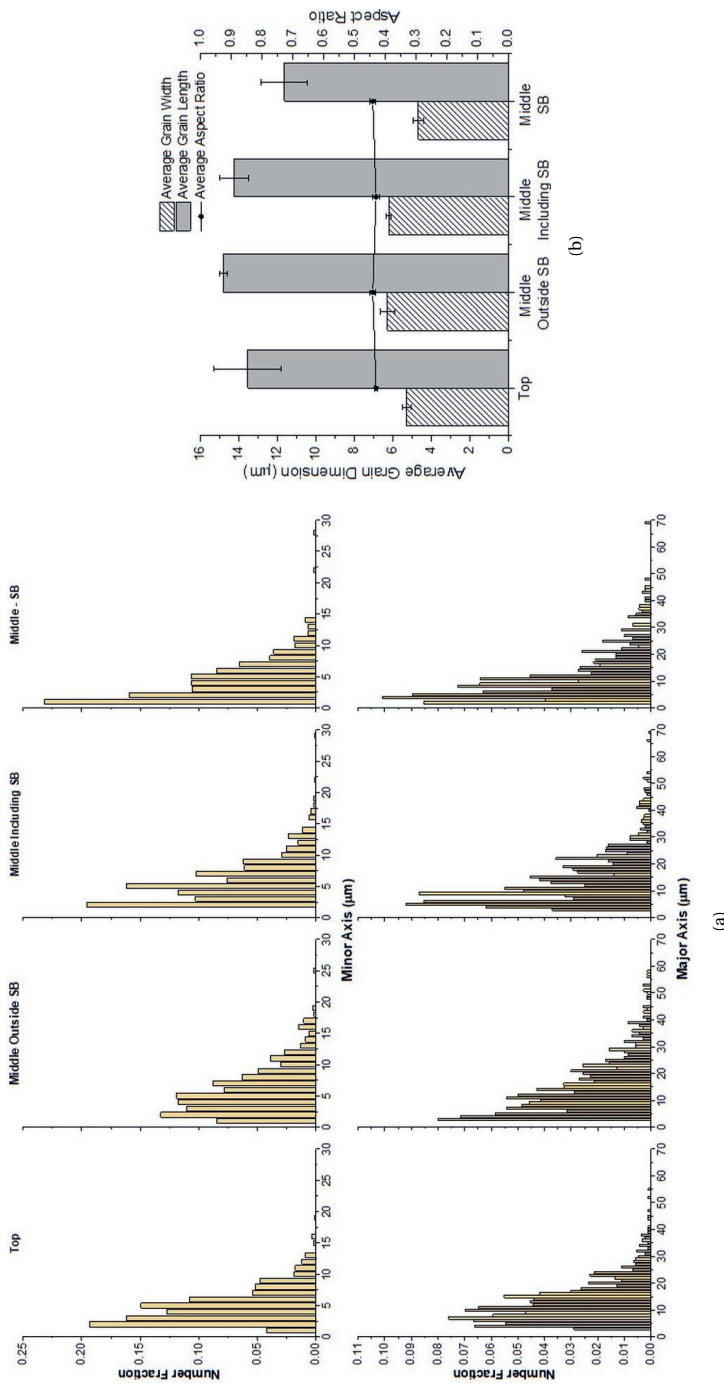


Figure 3.12: Prior austenite grain size investigation represented as (a) distributions of their width and length, and (b) average values and aspect ratio for top, middle outside segregation bands, middle including segregation bands, and middle only in the segregation bands.

Table 3.4: Average width, length, and intercept size of prior austenite grains and their substructures for the top, middle outside segregation bands, middle including segregation bands, and middle only in the segregation bands sections of the S690QL steel plate.

Area	Average PAG Width (μm)	Average PAG Length (μm)	Average Intercept Grain Size (μm)	Average Packet Size (μm)	Average Block Width (μm)
Top	5.3 ± 0.2	13.5 ± 1.8	19.2 ± 1.4	10.1 ± 2.8	2.0 ± 0.3
Middle Outside SB	6.3 ± 0.4	14.8 ± 0.2	23.5 ± 2.3	12.2 ± 3.5	3.0 ± 0.6
Middle Including SB	6.2 ± 0.1	14.2 ± 0.7	20.1 ± 2.8	10.6 ± 2.6	2.7 ± 0.9
Middle only within SB	4.7 ± 0.3	11.6 ± 1.2	19.1 ± 2.6	11.6 ± 2.6	2.4 ± 0.8

Lath martensitic and bainitic grains can be described as PAGs divided into distinguishable packets subdivided into blocks consisting of laths. From $\{100\}$ and $\{101\}$ pole figures for all analysed areas investigated in this work (Fig. 3.13), it is found that the crystallographic orientation relationship (OR) between the parent austenite phase and martensite or bainite for the S690QL steel being studied is the Kurdjumov-Sachs (K-S). The K-S OR has 24 variants, which are the different orientations that bcc phases can be formed within a single austenitic grain. These variants can be divided into four groups where each of these groups share the same $\{111\}_{\text{austenite}} // \{110\}_{\text{martensite/bainite}}$ parallel relation of close-packed planes (same habit plane) [37].

As packets consist of sets of laths that share the same habit plane, packets can be distinguished by identifying the K-S OR variants from each group. This procedure was followed for each PAG, and Fig. 3.13 shows one prior austenite grain as an example. Blocks within a packet present the same habit plane and thus have the same colour in Fig. 3.13. Different packets and different variant groups are coloured in red, blue, green, and yellow. Black lines represent grain boundaries with misorientation angles higher than 10° , defining blocks.

Between 5 and 15 individual PAGs were cut from the EBSD maps of each analysed areas (top, middle outside SB, and middle including SB) to distinguish the different packets and the different blocks allowing to measure their respective sizes. The average packet sizes and block widths are presented in Table 3.4. Slight variations are observed in the size of the packets when comparing the various investigated areas. However, all mean values are within the scatter. The same behaviour is observed for the measurement of the width of the blocks. No significant discrepancies were observed between regions.

EBSD may also help differentiate and quantify the bcc microconstituents through their unique microstructural characteristics (e.g., lattice distortion and dislocation density) originating from their respective phase transformation processes that may affect diffraction parameters such as the grain average image quality.

The grain average image quality (GAIQ) distributions were plotted in the TSL-OIM software, and no clear distinction between multiple peaks could be made (Figure 3.14(a), (d), and (g)). A method to fit three peaks was applied in these distributions to dissociate the GAIQ peak into the contributions of different phases. However, for the minority of cases in which it was possible to dissociate GAIQ data into a maximum of three peaks, regarding the possibly present phases, the peaks strongly overlap. Hence, this method does not help define the threshold GAIQ values to distinguish the phases.

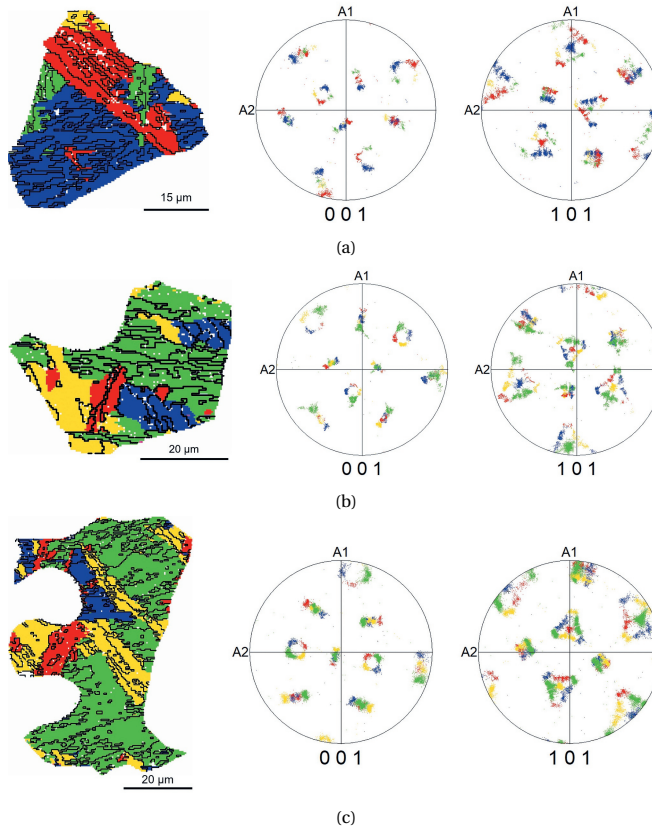


Figure 3.13: Prior austenite grains and (001) and (101) pole figures for (a) top, (b) middle outside segregation bands, and (c) middle including segregation bands in which different packets and variant groups, that share the same habit plane, are coloured in the same colour (red, blue, green, or yellow). Black lines represent grain boundaries with misorientation angles higher than 10°, defining blocks.

The TSL-OIM software indicates threshold values when generating color-coded GAIQ maps based on the user's number of colors. In order to confirm and, when necessary, improve the definition of these values, a comparison of the color-coded GAIQ map and the greyscale IQ map was performed.

EBSD areas for top and middle samples, outside the segregation bands, and including areas outside and inside the segregation bands (further referred to as "middle outside SB" and "middle including SB", respectively), were analysed. Figure 3.14 shows GAIQ maps, inverse pole figures, and reconstructed PAG maps for the top and middle sections. In the GAIQ maps, green was chosen to represent ferrite (highest GAIQ values), blue to bainite, and red to martensite (lowest GAIQ values). Phase fractions based on the GAIQ method for each analysed area are shown in Table 3.5.

Based on GAIQ, martensite content is found larger in the top, which is compensated by the lower contents of ferrite and bainite. Moving towards the centre of the plate, a

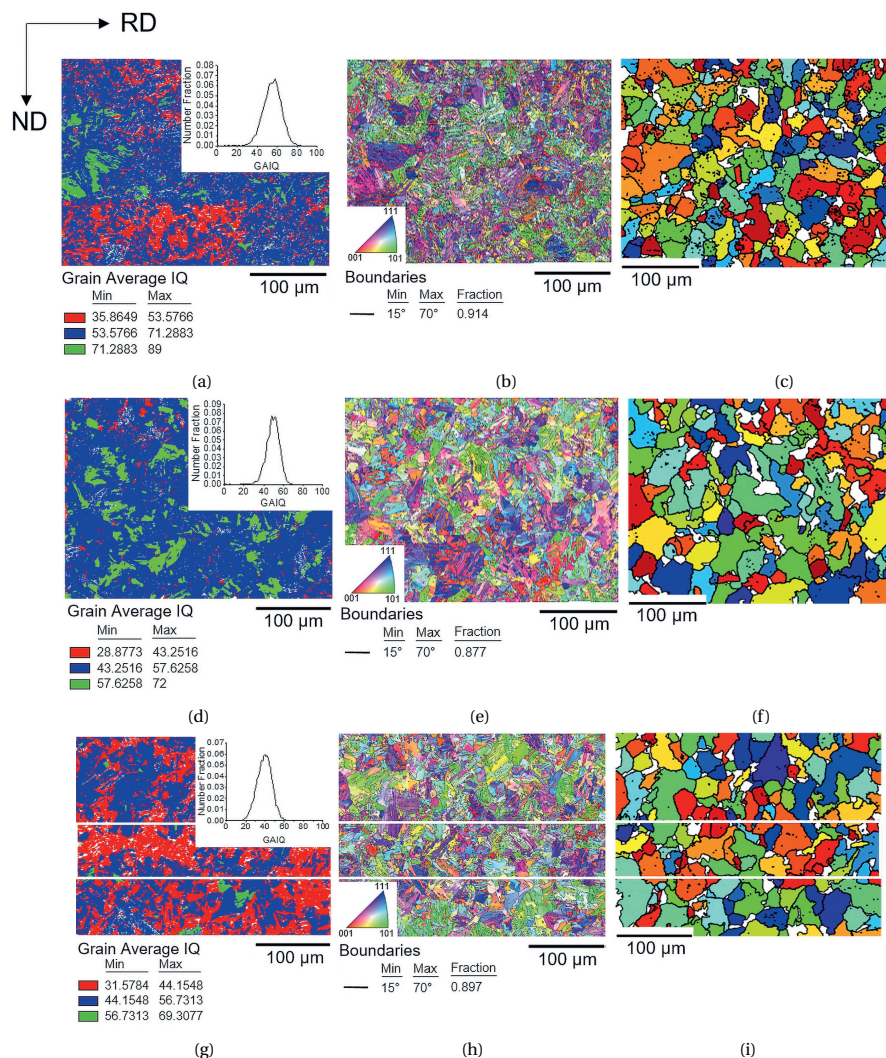


Figure 3.14: Respective coloured GAIQ maps, ND inverse pole figures, and unique grain colour PAG maps reconstructed by the ARPGE software for the (a),(b),(c) top; (d), (e), (f) middle outside the segregation band; and (g), (h), (i) middle including the segregation band which is shown by the white rectangle. Martensite is indicated in red, bainite in blue, and ferrite in green in GAIQ maps (a), (d) and (g). The white grains in (c), (f), and (i) correspond to non-reconstructed areas.

higher content of ferrite and bainite in the middle area outside segregation bands is observed. On the other hand, centreline segregation bands are observed to play a strong role in the middle section and stand out for presenting very much higher martensitic content – clearly banded structure in Fig. 3.14(g), which, in turn, increase the martensitic content and, consequently, decrease the ferrite content. Although the results obtained through the GAIQ parameter fit with what is expected from the theoretical back-

Table 3.5: Constituent's fractions for top, middle outside segregation band (SB), middle including areas outside and inside SB and exclusively in the SB based on the GAIQ method.

Microstructural Constituent	Phase Fraction (%)			
	Top	Middle Outside SB	Middle Including SB	Middle SB
Tempered Martensite	22 ± 4	7 ± 6	29 ± 2	14.0 ± 0.5
Tempered Bainite	68 ± 3	76 ± 3	64 ± 2	86 ± 3
Ferrite	6 ± 1	15 ± 3	3 ± 2	0.2 ± 0.1

ground and the results previously discussed, it is necessary to analyse the GAIQ maps more carefully, especially for tempered steel. For this, we will consider grain boundaries. According to the misorientation distribution of all grain boundaries, about 30%-50% are martensitic sub-structures boundaries (57-65°) while approximately 10%-20% are bainitic boundaries (48-55°) in all analysed samples [38].

To confirm an area as a ferrite, a comparison between the three maps (GAIQ, inverse pole figures, and reconstructed prior austenite grains) was made, and three criteria were used: 1) the grain should present a high GAIQ; 2) the grain morphology shown in the inverse pole figure must not be lath-like; 3) the grain orientation should be homogeneous inside the grain. The possible ferrite grains that meet these criteria were identified and then quantified. The results indicate that ferrite corresponds to 0.2% in the top section while the middle section outside the segregation bands and including the segregation bands contain approximately 0.4% and 0.1%, respectively.

Grain boundary misorientation angles can also bring relevant and helpful information regarding crack resistance through-thickness [4]. Figure 3.15 shows that the investigated areas display a very similar misorientation distribution, only differing in the intensity of some peaks. The smallest fraction of misorientation angles in the range between 28 and 33° are attributed to high mobility boundaries mainly represented by the prior austenite grain boundaries [39]. In this range, no significant difference in the number fraction was observed between the sections. On the other hand, a larger fraction of misorientation angles above 48° is present in the top section.

3.3.2. HARDNESS MEASUREMENTS

For a bulk analysis, the micro-Vickers hardness (HV₃) was performed and the result as a function of distance from the top of the 80 mm S690QL steel plate is presented in Fig. 3.16. The S690QL steel plate displays a clear hardness gradient across the thickness where the outer surfaces of the plate are harder than the centre. The hardness profile also shows that there is a peak of hardness exactly in the middle of the plate (at a distance of 40 mm from the top). It is observed that the scatter increases in the areas closer to the mid-thickness.

A nanoindentation map was determined in the middle section, which is the most complex region of the steel, over a large area (320 x 320 μm²) to cover the maximum different microstructural zones observed in the material. This map is presented in Figure 3.17. Figure 3.18 relates the nanohardness ranges for different areas within

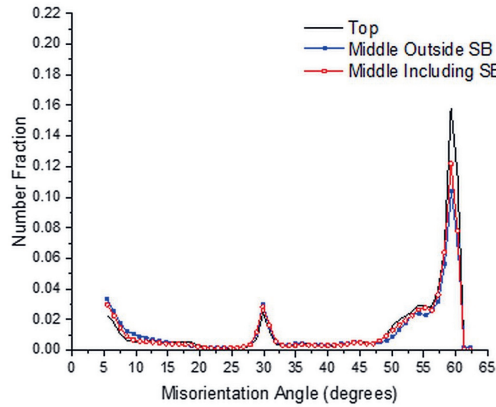


Figure 3.15: Number fraction of boundary misorientation angles for the top, middle outside segregation bands, and middle including segregation bands sections.

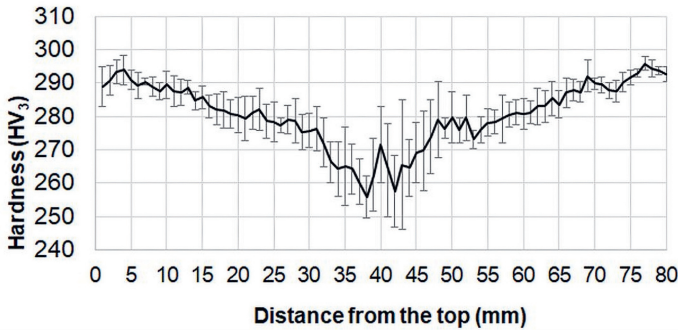


Figure 3.16: Through-thickness micro-Vickers hardness (HV_3) profile of the 80 mm S690QL steel plate. The error bars represent the standard deviation from the mean.

the map and presents their respective area fractions. The area fraction of zones with nanohardness of 7.33 – 8.62 GPa (red) and 8.62 – 9.75 GPa (dark red) area are so low that they do not appear in Fig. 3.18.

The contrasting microstructural areas located in the middle section have nanohardness values varying from 2.0 to 9.75 GPa. Blue, green, yellow, orange, red, and dark red zones correspond to the following hardness ranges: 2.00 – 2.80, 2.80 – 4.74, 4.74 – 5.55, 5.55 – 7.33, 7.33 – 8.62, and 8.62 – 9.75 GPa. The different zones will be further referred to by their colours. At first, what calls the most attention is how most of the harder zones (above 4.74 GPa) are densely concentrated and mainly distributed as horizontal lines parallel to the rolling direction at $y = 130, 200,$ and $270 \mu\text{m}$. These lines refer to the centreline segregation bands. Inside the segregation bands, orange, red and dark red zones with higher hardness are present while outside the segregation bands, a mixture of yellow, green, and blue areas is observed. Regarding the blue areas, less than 1% of the map has the lowest nanohardness, between 2 and 2.8 GPa.

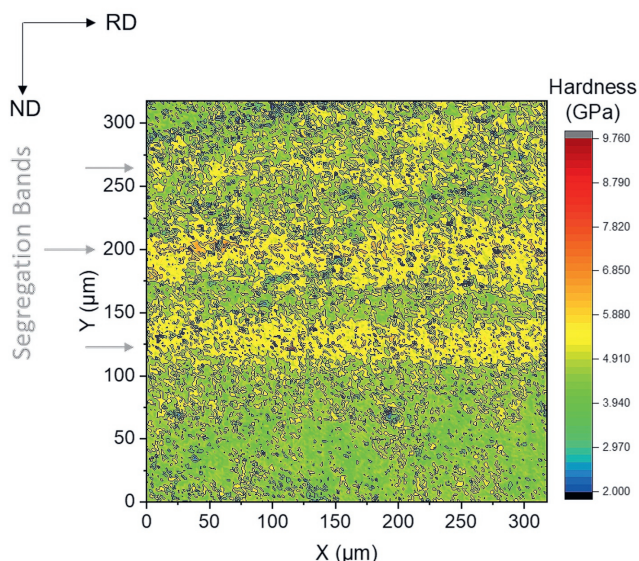


Figure 3.17: Through-thickness micro-Vickers hardness (HV_3) profile of the 80 mm S690QL steel plate. The error bars represent the standard deviation from the mean.

The areas of transition between blue and green colours and green and yellow colours have the largest mechanical heterogeneity. Nevertheless, the blue/green interfaces are small since the area fraction of the first represents 1% of the entire map while the green/yellow is extensive due to the segregation bands planes.

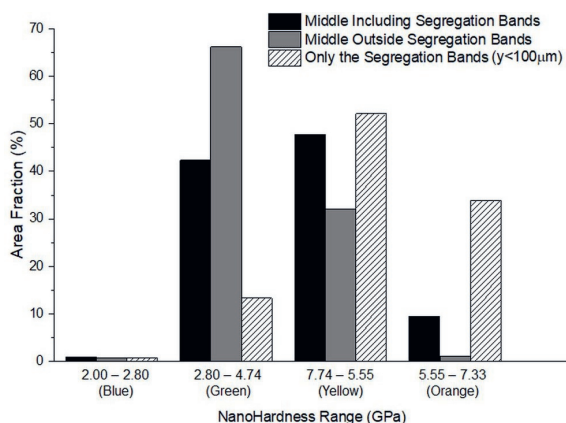


Figure 3.18: Nanohardness ranges and their respective area fractions for each investigated zone in the map of Fig. 3.17. The area fraction of zones with nanohardness of 7.33 – 8.62 GPa (red) and 8.62 – 9.75 GPa (dark red) area significantly lower than the others (maximum of 0.1%) and, therefore, are not able to be presented at this scale.

In an attempt to correlate the different hardness areas with the different microstructural zones, helping to distinguish the different BCC constituents, EBSD and SEM analysis were performed on the indentation map. Regarding EBSD, no correlation was found. Therefore, despite providing a rough estimate and indicating potential critical fracture zones, EBSD and nanoindentation cannot be used to accurately distinguish between BCC structural constituents for the quenched and tempered S690 high strength steel studied herein. In the case of SEM analysis, two main problems were observed that prevented the analysis of the etched nanoindentation map to be carried out. The first one is that, during EBSD analysis, the areas where the electron beam makes contact with the surface to acquire the diffraction patterns, a contamination layer is built. Due to the presence of this layer, the etchant has no effect and the material remains unetched in the previously analysed EBSD areas. The second problem is that, due to the small depth of the indents (around 70 nm), the etching procedure completely removed the residual imprint of the indentation, not being able to locate the indents afterwards.

3.3.3. THROUGH-THICKNESS FRACTURE BEHAVIOUR

Three-point bending tests were performed at $-100\text{ }^{\circ}\text{C}$ in the top and middle sections of the S690QT steel plate. The minimum, maximum, and average CTOD results including their standard deviation from the average values are shown in Table 3.6. As can be seen, the middle section presents a lower fracture toughness and a lower scatter than the top section.

Table 3.6: CTOD results for top and middle thickness positions in T-L orientation tested at $-100\text{ }^{\circ}\text{C}$.

Thickness Position	Minimum CTOD [mm]	Maximum CTOD [mm]	Average CTOD (mm)
Top	0.022	0.074	0.048 ± 0.019
Middle	0.010	0.020	0.012 ± 0.004

3.4. DISCUSSION

3.4.1. THROUGH THICKNESS MICROSTRUCTURAL INHOMOGENEITY

In this study, the comprehensive microstructural characterisation of the S690 HSS demonstrated that the microstructure significantly varies through the thickness. Through the processing route, the steel plate experiences uneven strain levels and cooling rates. Consequently, the top and middle sections present distinctly different microstructural composition.

In terms of bcc microconstituents distinction and quantification, different techniques were used: dilatometry, microscopy and nanoindentation. The dilatometric analysis suggests the presence of martensite and bainite after quenching, while the microscopic investigation indicates the presence of grains that resemble tempered bainite, tempered martensite, and ferrite, as also predicted by the CCT diagrams. Ferrite grains were quantified from the SEM micrographs and the results show that each

position in the thickness contains around 0.2% of ferrite. Consequently, this phase is present in a too small fraction to be detected by the dilatometric curve. EBSD was also used through the analysis of GAIQ maps in an attempt to assist the distinction of bcc microconstituents. However, in the case of tempered steels such as the currently investigated steel, the use of GAIQ for phase distinction may be less effective, since during the heat treatment, the saturated carbon in solid solution, specifically for martensitic grains, diffuses out and possibly forms carbides, the dislocation density is reduced, and the residual stress in the crystal is relieved. Consequently, the phase's diffraction pattern is sharpened, leading to an approximation, and possible overlap, of the GAIQ values. As a result, it is difficult to define the threshold GAIQ values. Hence, an estimation may be made, but an accurate analysis is not possible. According to the analysis via GAIQ maps, the martensitic fraction is larger in the top section while the ferritic and bainitic fractions are larger in the middle outside of the segregation band. This result is in line with the expectation where a faster cooling during the quenching process occurs in the outer surface of the steel plate, as can be seen in Fig. 3.2(a). Moreover, the middle section was observed to have a clear banded structure – centreline segregation bands – with grains of very low GAIQ. As presented in the EPMA results and M_s and B_s transformation temperatures in Fig 3.9, the segregated alloying elements (e.g., Mo, Cr, and Mn) facilitate the formation of martensite, resulting in a greater fraction. During cooling, the bainitic transformation occurs initially in areas with lower solute content due to higher B_s temperature, rejecting carbon to areas recognised as high-solution regions, enriching them even more. It is known that the alloying elements that identify segregation in the bands slow down the transformation kinetics (e.g., austenite to ferrite), shifting the CCT curve (Fig. 3.6) to longer times and, thus, increasing steel's hardenability [40, 41]. Hence, at the same cooling rate at the central part of the plate (5 °C/s) as the regions with lower content of alloying elements, where the microstructure is composed of a mixture of ferrite, bainite, and martensite, greater martensite and lower or zero ferrite fractions are expected in the segregation bands. Nevertheless, it is worth mentioning that the elemental segregation by itself may cause distortion in the lattice and contribute to the low GAIQ in the segregation bands. The discussion on the use of nanoindentation to distinguish bcc microconstituents by their local properties will be presented in section 3.4.2.

The misorientation distribution of martensitic and bainitic grain boundaries were also analysed. Contrary to the phase fraction measured by the GAIQ values, the misorientation values at grain boundaries indicate that martensite is present in a larger fraction than bainite. Moreover, it also suggests that areas identified as bainite by the GAIQ map not only refer to bainite but also to martensite, which, when tempered, has its diffraction pattern improved, approaching image quality values close to that of bainite, which, as a result, leads to a misidentification as bainite.

For the ferritic quantification based on the GAIQ values, it was observed that grains mistakenly indexed as ferrite in Fig. 3.14 may be tempered bainite or low-carbon tempered martensite. The regions corresponding only to the segregation bands do not contain ferrite grains. These fractions are per the quantification made based on the micrographs obtained by SEM and also in accordance with the theoretical background discussed above.

Therefore, although the GAIQ method gives a rough estimation of phase fractions and distribution of these bcc phases in different sections, it is still necessary to propose other methods to differentiate and accurately quantify them. For this purpose, we propose a correlative approach by using a combination of techniques which include nanoindentation measurements.

Most inclusions through the thickness of the plate have a complex chemical composition. This complexity is due to the fact that pre-existing inclusions serve as a site for nucleation and subsequent growth of other inclusions such as titanium nitrides (TiN) on the surface of oxide inclusions, niobium carbides (NbC) on the surface of TiN, and manganese sulphide (MnS) on oxides ($\text{Al}_2\text{O}_3\cdot\text{MgO}$) as observed by [1, 42, 43]. Oxide inclusions were found to be of the same size and area fraction in the top and middle sections while Nb-rich inclusions were found in a greater area fraction and larger sizes in the middle section. This can be attributed to their different nucleation/growth steps in the steelmaking process. The nucleation of oxides and sulphides occur during the secondary metallurgy (e.g., in the alloying addition) and are homogeneously distributed afterwards in the liquid steel. During solidification, these inclusions are captured by growing dendrites and are homogeneously distributed through the thickness along the solidification process. For the Nb-rich inclusions that nucleate and grow in the liquid state during casting, the cooling gradient through the thickness and the elemental segregation in the middle section have a major effect. In thick slabs, the temperature in the central part of the slab takes longer to dissipate and the centre of the slab remains as a liquid while the solidification process in the outer surface of the slab had already started. Consequently, the inclusion nucleation and growth processes continue, resulting in larger content and sizes of inclusions in the middle section. The elemental segregation in the middle of the slab also leads to larger chance of reaching the solubility limits of the elements in the liquid, increasing the probability to form these inclusions in the middle section. Moreover, defects were observed in middle-section inclusions as shown in Fig. 3.7(d) to 3.7(f). These defects may have originated during the rolling process due to a combination of factors such as the rolling stress and the brittle nature of such inclusions. Nevertheless, the sample preparation procedure, already known for breaking or tearing inclusions out of the matrix, should also be considered as influencing the formation of defects. Da Costa e Silva [44] reports the effect of hot rolling deformation on different inclusions. Usually, brittle inclusions are more likely to crack or break under rolling stress. Moreover, the interfacial strength between the inclusion and the matrix is low, which causes the interface to act as a source of microvoid and crack formation [45]. In the case of coarse and irregular-shaped inclusions, such as those found in the presently studied S690QL steel, the consequences can be more severe since a high stress concentration is generated in the sharp interfacial corners, and cracks can nucleate and grow at the interfaces of the inclusions under the rolling load, even in steels of which the matrix has a relatively high ductility [45].

Several authors report the effects of PAG size of lath martensitic and lath bainitic grains and their microstructural units that present high-angle boundaries (e.g., packets and blocks) on strength, toughness, and crack propagation [37, 46–50]. Therefore, the grain sizes in the top and middle sections were measured and compared. In the top section of the steel plate, the PAG are slightly smaller than the ones in the middle sec-

tion outside the segregation bands (Fig. 3.12(b)). This agrees with expectations that high strain values are reached in the surface and decrease through the thickness during rolling [51] and as a result, more defect energy, determining recrystallization, is stored by the material close to the surface than in the centre of the plate. Hence, the austenite recrystallization during hot rolling tends to lead to a more refined grain structure in the outer part of the slab. Within the middle section, the average PAG sizes in the areas outside the segregation bands and within the segregation bands (SB) are different (Fig. 3.12 (b)) and, characterise a bimodal distribution of grain sizes. The smaller grain sizes found in the segregation bands may be explained by the solute drag effect where segregated elements retard the grain boundary migration and slow down the grain growth, and also the Nb-rich cubic inclusions observed along the PAG boundaries (Fig. 3.7(e)) pinning grain boundaries [52]. Moreover, Reiter, Bernhard, and Presslinger [53] reported, through a study of the austenite grain size during casting, that the equivalent carbon content ($c_p = x_C - 0.14x_{Si} + 0.04 x_{Mn}$, where x_i is the weight percentage of element i) can influence the grain size [55]. According to the authors, when c_p is larger than 0.17 %, the grain size decreases with increasing c_p value [53]. The parameter c_p was calculated based on the EPMA line scans through the segregation bands. The results show that a significant fraction of the segregation band width has $c_p > 0.17$ %. Furthermore, c_p may reach values up to 0.37 %, where the bands with smaller widths have a higher number of areas with c_p values > 0.17 %. Therefore, narrower segregation bands might present smaller PAG and larger relative frequency of small grains. Regarding the PAG substructures (e.g., packets and blocks), as the prior austenite grain sizes (Table 3.4) of the analysed regions do not present major differences, large variations in the size of PAG substructures are not detected. No significant discrepancies were observed between the investigated regions.

3.4.2. MICROSTRUCTURE – HARDNESS RELATIONSHIP

The hardness gradient through the 80 mm thickness of the S690QL HSS plate reflects the different microstructural composition of the top and middle sections in terms of the fraction of microconstituents and prior austenite grain sizes. The lower fraction of hard martensite and larger PAG sizes in the centre lead to a lower hardness compared to the top section. The peak of hardness in the central part of the plate can be attributed to the presence of centreline segregation bands which are likely to have higher hardness due to the solute segregation that serve as barriers to dislocations during plastic deformation, larger content of martensite, the cluster of brittle Nb-rich inclusions and smaller prior austenite grain size than the surrounding areas. Through the middle section, a large scatter in the hardness measurements in the middle section is due to the mixture of transformation products with different hardness, banded microstructure with interspersed enriched and depleted zones with different hardness, PAG sizes, and brittle inclusions distribution.

From the micro-Vickers hardness measurements, it was shown that the micro-scale hardness measurements cannot be used to accurately evaluate the microstructural variations and single microstructural features that exist in fine-structured multiphase steels like the S690QL steel under study. Therefore, nanoindentation analyses are essential to bring a more in-depth knowledge regarding local microstructural and property in-

homogeneities, individual behaviours, and their combined effect on mechanical properties and fracture behaviour. The segregation bands were observed to be the harder area in the steel plate. Their hardness reach values up to 2.4 times that of surrounding areas, which is likely to affect the material's crack resistance and mechanical and fracture performance. As already discussed, the largest hardness in segregation bands is due to the combined effect of solute segregation, the predominantly martensitic structure, smaller PAG size than the surrounding areas, and the presence of Nb-rich brittle inclusions. Inside of the segregation bands, some areas present higher hardness than the average value for the band. Areas with hardness varying from 5.55 to 7.33 GPa (orange areas in the hardness map of Fig. 3.17) are present in a large area fraction (34%) and thus it is unrealistic to consider them clusters of brittle inclusions, but they may be representing high-carbon martensite grains. Areas with the highest hardness level, 7.33 – 9.75 GPa (red and dark red zones in Fig. 3.17) exist in an area fraction similar to that estimated for brittle inclusions within these areas by optical microscopy, suggesting that these second-phase particles can be responsible for the largest hardness. Outside the segregation bands, the material presents hardness varying from 2.8 to 5.55 GPa (yellow and green areas in Fig. 3.17) which is likely to be representing tempered bainite and tempered low-carbon martensite. Within this area, the hardness is constantly alternating at a distance less than a typical PAG size, showing a certain degree of heterogeneity inside lath grains attributed to their substructures [17]. Only a few areas (1%) present a hardness range of 2.00 – 2.80 GPa (blue areas in Fig. 3.17). These values agree with the ones reported in the literature for ferrite after tempering [18, 54]. Although a comparison with other studies can be made, the testing parameters used herein may differ from other research, and the direct comparison is uncertain. The area fraction of ferrite estimated from the nanoindentation results are within the estimated value from SEM and EBSD analysis.

Therefore, from the nanoindentation measurements, the local properties variation provides indications about the different phases, but it was not possible to distinguish them precisely. Due to the tempering process, the nanohardness values for different phases come closer together with an overlap. Consequently, the accurate distinction of the phases through their properties is not possible.

3.4.3. POTENTIAL MICROSTRUCTURAL ASPECTS AFFECTING FRACTURE TOUGHNESS

The through-thickness microstructural analyses and the hardness measurements pointed out the differences between the top and middle sections that can significantly influence the fracture behaviour of the steel under study. Hence, these results provide evidence of the through-thickness potential critical sites for fracture and the most detrimental thickness section in the steel plate.

The top and middle sections differ microstructurally mainly by characteristics of inclusions, the size of the PAG and their distribution of misorientation at grain boundaries. The middle section presents a larger volume fraction of inclusions, mainly the cubic-shaped ones, which are known for acting as cleavage crack nucleation sites [55]. Hence, more potential initiation sites are present in the middle section. These inclusions are

also present in larger sizes, which means that once the fracture process is initiated inside them, the initial crack will have a larger size in the middle than the top section. As a consequence, the fracture stress is lower in the middle [56]. This initial crack length can be even larger when cubic inclusions are dispersed close to each other in clusters, being considered as one single large inclusion, as discussed in section 3.3.1, further reducing the required stress to fracture. Furthermore, inclusions, mostly cubic, in the middle section were also usually associated with defects in themselves and at the interface inclusion/matrix. In this case, these inclusions potentially characterise an easy path for crack propagation. Regarding the grain size and the distribution of misorientation at grain boundaries, both parameters can affect the propagation of fracture micromechanism affecting fracture toughness [57]. The middle section presents the larger grain sizes and smaller fraction of high-angle grain boundaries than the top, which reduces the stress needed for fracture and the crack resistance, respectively.

In terms of hardness variation, the nanoindentation map highlights the microstructural variation and its effects on nanohardness in the middle section. Due to the significant nanohardness difference between the segregation bands and the matrix, their interface would be preferential sites for crack formation due to the high probability of interfacial separation and can be responsible for fracture toughness reduction [21, 22].

The three-point bending tests at $-100\text{ }^{\circ}\text{C}$ show that, in line with the microstructural and hardness analyses performed by the comprehensive quantitative characterisation, the middle section has lower cleavage fracture toughness and, therefore, is more detrimental than the top. Another important aspect is that the lower standard deviation for the middle may indicate that, even though the through-thickness microstructure of the material is inhomogeneous, the microstructure of the middle section as a whole is more brittle and critical than the top. A continuation of this work will focus on investigating the fracture surfaces of tested CTOD specimens to identify the weak microstructural features and to study the initiation and propagation micromechanisms of cleavage failure in the 80 mm thick quenched and tempered S690 high strength steel.

3.5. CONCLUSIONS

In order to identify the potential weak microstructural sites on fracture at low-temperature applications, a correlative approach was proposed to characterise and quantify the through-thickness complex and heterogeneous microstructure of the 80 mm thick quenched and tempered S690 high strength steel plate. The study resulted in the following conclusions:

1. The combined analysis via dilatometry, CCT diagrams and SEM showed that a mixed tempered microstructure including ferrite, bainite and martensite is present through the entire thickness, where ferrite represents less than 1% of the phases. However, microstructural variations were observed in terms of grain size, inclusion content, and elemental segregation.
2. The PAG size slightly increases as it approaches the centre of the plate, except for the centreline segregation bands found in the middle section. The middle section exhibits a bimodal grain size distribution where grains outside the segregation

bands are slightly larger than the top section, but PAG inside segregation bands are smaller than the top. Nevertheless, there was no significant difference in packet size and block width over thickness. This is due to the slight variation in the grain size of the prior austenite between the sections.

3. In terms of inclusions, the most commonly observed particles have spherical and cubic morphologies and complex chemical compositions of oxides, carbides, and nitrides throughout the thickness. Although the analysed thickness positions have circular inclusions of the same size range, the middle of the plate presents larger cubic inclusions that are often distributed as clusters, a greater amount of spherical and cubic particles than the top. Note that these clusters of cubic inclusions may be considered a line of collinear inclusions reaching sizes larger than 4 times the size of cubic inclusions in the top. Additionally, defects in the interface inclusion/matrix and the inclusion itself were observed in the middle.
4. The chemical composition analysis through the centreline segregation bands indicates that Mo, Mn, Cr, Si, Ni, and C are the elements that segregate in these areas. By calculating the transformation temperatures for bainite and martensite based on the chemical composition variation through the bands, it is clear that elemental segregation affects the microstructural transformation and, consequently, the phase fractions found in these areas. Hence, greater martensite and lower or no ferrite fractions are expected in the segregation bands.
5. For the S690QL high strength steel studied herein, the EBSD analysis does not accurately distinguish bcc micro-constituents based on the GAIQ and boundary misorientation angles. The misorientation distribution of martensitic and bainitic boundaries shows that some areas, identified as bainite from the GAIQ method, refer to martensite, which had their image quality improved during the tempering process. Additionally, some lath grains were mistakenly indexed as ferrite due to their high image quality values. Nevertheless, it gives a rough estimation of the micro-constituents and their fraction in the material. The GAIQ procedure indicates higher martensitic and lower ferritic content in the top section, which is a consequence of the faster cooling process in the outer part of the plate compared to the mid-thickness during the quenching process. On the other hand, centreline segregation bands present a higher martensitic content than the middle outside the segregation band due to the elemental segregation, which, in turn, scale up the martensitic content. Moreover, EBSD data allowed the investigation of misorientation boundary distribution in all sections, indicating that the top section has the largest fraction of high-angle grain boundaries ($>15^\circ$) and the middle section has the largest fraction of low-angle grain boundaries ($<15^\circ$).
6. Micro-Vickers measurements showed a clear bulk hardness gradient through the thickness, where the harder areas belong to the outer surfaces of the plate. This result is directly related to the microstructural observations regarding the area fraction of micro-constituents and PAG sizes. On the one hand, the top section has a larger area fraction of martensite and smaller PAG sizes, which increase their hardness. On the other hand, in the general middle section, the martensitic fraction is

lower, and the grains are larger, which reduces their hardness. However, a peak of hardness right in the central part of the plate is attributed to the presence of segregation bands with a larger area fraction of martensite than the middle outside the segregation bands, the smallest grain sizes of the entire thickness, the presence of clusters of hard inclusions, and solute segregation act as barriers for dislocation movements.

7. In the nanoscale, the dense and large nanoindentation map in the middle section – the most complex area of the material – shows that the centreline segregation bands are the hardest zones reaching values up to 2.4 times higher than the hardness of surrounding areas. The highest hardness gradient was observed in the interface between the matrix and the segregation bands. Consequently, this would be the preferential site for crack formation due to the high chance of interfacial separation and the reduction of fracture toughness. Regarding the phase distinction through properties, although the local properties variation indicates different phases, it was not possible to distinguish them accurately. Due to the tempering process, the nanohardness values overlap for the different phases, making their distinction difficult. Additionally, although the use of EBSD and nanoindentation provide a rough estimate of constituents' fraction and indication of potential critical fracture zones, they cannot be used to accurately distinguish between BCC structural constituents for the S690QL high strength steel under study.
8. The top section of the HSSs plate displays a higher fracture toughness than the middle section. Moreover, a high scatter in the CTOD values is observed for the top section, while in the middle it is very low. This behaviour can be explained by the more detrimental microstructure present in the middle section (e.g., clusters of Nb-rich inclusions, larger Nb-rich inclusions and long interfaces with large hardness gradients) than in the top, as suggested by the quantitative microstructural characterisation.

Therefore, the comprehensive microstructural characterisation and quantification of this high strength steel suggests that the plate's middle section is the most critical area in mechanical and fracture behaviours, being likely to affect the global material performance and the reliability of structural components. This unfavourability of the middle section is attributed to its larger prior austenite grain sizes, larger sizes and area fraction of inclusions, the presence of defects associated with the circular and cubic inclusions and with their interface with the matrix, clusters of cubic inclusions that may also be distributed along the PAG boundaries, and the long interfaces with the largest hardness gradients. All these factors make the middle section more prone to crack initiation and more likely to present the lowest fracture toughness of the S690QL high strength steel. Future work will focus on investigating the impact of the presented microstructural inhomogeneities on cleavage fracture toughness and damage micromechanisms of the commercially available 80 mm thick quenched and tempered S690 high strength steel allowing the confirmation of the weak microstructural features. This will be done through both modelling and experimental approaches.

REFERENCES

- [1] Popovich, V., & Richardson, I. M. (2015). Fracture Toughness of Welded Thick Section High Strength Steels. *TMS 2015 144th Annual Meeting & Exhibition: Supplemental Proceedings.*, 1031–1038. <https://doi.org/10.1002/9781119093466.ch125>
- [2] Wang, Q., Ye, Q., Wang, Z., Kan, L., & Wang, H. (2020). Thickness Effect on Microstructure, Strength, and Toughness of a Quenched and Tempered 178 mm Thickness Steel Plate. *Metals*, 10(5), 1–16. <https://doi.org/10.3390/met10050572>
- [3] Bertolo, V. M., Jiang, Q., Walters, C. L., & Popovich, V. A. (2020). Effect of microstructure on cleavage fracture of thick-section quenched and tempered S690 high-strength steel. *Characterization of Minerals, Metals and Materials 2020*, 155–168. <https://doi.org/https://doi.org/10.1007/978-3-030-36628-5\15>
- [4] Liu, H., Zhang, H., & Li, J. (2018). Thickness Dependence of Toughness in Ultra-Heavy Low-Alloyed Steel Plate after Quenching and Tempering. *Metals*, 8(628), 1–11. <https://doi.org/10.3390/met8080628>
- [5] Moore, P., Yordanova, B., Lu, Y., & Janin, Y. J. (2019). Influence of microstructural variation in thick section steels on the characterisation of fracture toughness using sub-size specimens. *Proceedings of the ASME 2019 38th International Conference on Ocean, Offshore and Arctic Engineering OMAE 2019*. <https://doi.org/10.1115/OMAE2019-96010>
- [6] Wallin, K. (2015). Master Curve Analysis of Ductile to Brittle Transition Region Fracture Toughness Round Robin Data. The " EURO " fracture toughness curve.
- [7] Andrieu, A., Pineau, A., Besson, J., Ryckelynck, D., & Bouaziz, O. (2012). Beremin model: Methodology and application to the prediction of the Euro toughness data set. *Engineering Fracture Mechanics*, 95, 102–117. <https://doi.org/10.1016/J.ENGFRACMECH.2011.10.019>
- [8] Pineau, A. (2006). Development of the Local Approach to Fracture over the Past 25 years: Theory and Applications. *International Journal of Fracture*, 138(1), 139–166. <https://doi.org/10.1007/s10704-006-0035-1>
- [9] Jiang, Q., Bertolo, V. M., Popovich, V. A., & Walters, C. L. (2019). Recent Developments and Challenges of Cleavage Fracture Modelling in Steels: Aspects on Microstructural Mechanics and Local Approach Methods. *Proceedings of the ASME 2019 38th International Conference on Ocean, Offshore and Arctic Engineering OMAE 2019*. <https://doi.org/https://doi.org/10.1115/OMAE2019-95464>
- [10] Lin, T., Evans, A. G., & Ritchie, R. O. (1986). A statistical model of brittle fracture by transgranular cleavage. *Journal of the Mechanics and Physics of Solids*, 34(5), 477–497. [https://doi.org/10.1016/0022-5096\(86\)90013-X](https://doi.org/10.1016/0022-5096(86)90013-X)
- [11] Martín-Meizoso, A., Ocaña-Arizcorreta, I., Gil-Sevillano, J., & Fuentes-Pérez, M. (1994). Modelling cleavage fracture of bainitic steels. *Acta Metallurgica et Materialia*, 42(6), 2057–2068. [https://doi.org/10.1016/0956-7151\(94\)90031-0](https://doi.org/10.1016/0956-7151(94)90031-0)
- [12] Kroon, M., & Faleskog, J. (2005). Micromechanics of cleavage fracture initiation in ferritic steels by carbide cracking. *Journal of the Mechanics and Physics of Solids*, 53(1), 171–196. <https://doi.org/10.1016/j.jmps.2004.05.008>

- [13] Chen, J. H., Li, G., Cao, R., & Fang, X. Y. (2010). Micromechanism of cleavage fracture at the lower shelf transition temperatures of a C – Mn steel. *Materials Science & Engineering A*, 527, 5044–5054. <https://doi.org/10.1016/j.msea.2010.04.063>
- [14] Navarro-López, A., Hidalgo, J., Sietsma, J., & Santofimia, M. J. (2017). Characterization of bainitic/martensitic structures formed in isothermal treatments below the Ms temperature. *Materials Characterization*, 128(January), 248–256. <https://doi.org/10.1016/j.matchar.2017.04.007>
- [15] Papaefthymiou, S., Banis, A., Bouzouni, M., & Petrov, R. H. (2019). Effect of Ultra-Fast Heat Treatment on the Subsequent Formation of Mixed Martensitic / Bainitic Microstructure with Carbides in a CrMo Medium. *Metals*, 9(312), 1–14. <https://doi.org/10.3390/met9030312>
- [16] Petrov, R., Kestens, L., Wasilkowska, A., & Houbaert, Y. (2007). Microstructure and texture of a lightly deformed TRIP-assisted steel characterized by means of the EBSD technique. *Materials Science and Engineering A*, 447, 285–297. <https://doi.org/10.1016/j.msea.2006.10.023>
- [17] Chang, Y., Lin, M., Hangen, U., Richter, S., Haase, C., & Bleck, W. (2021). Revealing the relation between microstructural heterogeneities and local mechanical properties of complex-phase steel by correlative electron microscopy and nanoindentation characterization. *Materials and Design*, 203(109620). <https://doi.org/10.1016/j.matdes.2021.109620>
- [18] Baltazar Hernandez, V. H., Panda, S. K., Kuntz, M. L., & Zhou, Y. (2010). Nanoin-dentation and microstructure analysis of resistance spot welded dual phase steel. *Materials Letters*, 64(2), 207–210. <https://doi.org/10.1016/j.matlet.2009.10.040>
- [19] Busby, J. T., Hash, M. C., & Was, G. S. (2005). The relationship between hardness and yield stress in irradiated austenitic and ferritic steels. *Journal of Nuclear Materials*, 336, 267–278. <https://doi.org/10.1016/j.jnucmat.2004.09.024>
- [20] Ariza-Echeverri, E. A., Masoumi, M., Nishikawa, A. S., Mesa, D. H., Marquez-Rossy, A. E., & Tschiptschin, A. P. (2020). Development of a new generation of quench and partitioning steels: Influence of processing parameters on texture, nanoin-dentation, and mechanical properties. *Materials and Design*, 186(108329). <https://doi.org/10.1016/j.matdes.2019.108329>
- [21] Hidalgo, J., Celada-Casero, C., & Santofimia, M. J. (2019). Fracture mechanisms and microstructure in a medium Mn quenching and partitioning steel exhibiting macrosegregation. *Materials Science and Engineering A*, 754(January), 766–777. <https://doi.org/10.1016/j.msea.2019.03.055>
- [22] Lee, S. G., Kim, B., Sohn, S. S., Kim, W. G., Um, K. K., & Lee, S. (2019). Effects of local-brittle-zone (LBZ) microstructures on crack initiation and propagation in three Mo-added high-strength low-alloy (HSLA) steels. *Materials Science and Engineering A*, 760(June), 125–133. <https://doi.org/10.1016/j.msea.2019.05.120>
- [23] Jiang, Q., Bertolo, V. M., Popovich, V. A., Sietsma, J., & Walters, C. L. (2021). Relating matrix stress to local stress on a hard microstructural inclusion for understanding cleavage fracture in high strength steel. *International Journal of Fracture*, 232, 1–21. <https://doi.org/10.1007/s10704-021-00587-y>

- [24] CEN. (2019). NEN-EN 10025-6: Hot rolled products of structural steels - Part 6: Technical delivery conditions for flat products of high yield strength structural steels in the quenched and tempered condition.
- [25] ASTM International. (2016). ASTM E1245-03: Standard Practice for Determining the Inclusion or Second-Phase Constituent Content of Metals by Automatic Image Analysis. <https://doi.org/10.1520/E1245-03R08.2>
- [26] Hesamodin Talebi, S., Ghasemi-Nanesa, H., Jahazi, M., & Melkonyan, H. (2017). In situ study of phase transformations during non-isothermal tempering of bainitic and martensitic microstructures. *Metals*, 7(9), 1–13. <https://doi.org/10.3390/met7090346>
- [27] Sente Software. (n.d.). JMatPro® API.
- [28] Cayron, C. (2007). ARPGE : a computer program to automatically reconstruct the parent grains from electron backscatter diffraction data. *Journal of Applied Crystallography*, 40, 1183–1188. <https://doi.org/10.1107/S0021889807048777>
- [29] ASTM International. (2012). ASTM E112-13 Standard Test Methods for Determining Average Grain Size. <https://doi.org/10.1520/E0112-13.1.4>
- [30] Rodríguez, R., & Gutierrez, I. (2003). Correlation between nanoindentation and tensile properties Influence of the indentation size effect. *Materials Science and Engineering*, 361, 377–384. [https://doi.org/10.1016/S0921-5093\(03\)00563-X](https://doi.org/10.1016/S0921-5093(03)00563-X)
- [31] Oliver, W. C., & Pharr, G. M. (1992). An Improved Technique for Determining Hardness and Elastic Modulus Using Load and Displacement Sensing Indentation Experiments. *J. Mater. Res*, 7(6). <https://doi.org/10.1557/JMR.1992.1564>
- [32] ISO. (2018). ISO 12135: Metallic materials - Unified method of test for the determination of quasistatic fracture toughness. 2016.
- [33] Canale, L. C. F., Vatauvuk, J., & Totten, G. E. (2014). 12.02 - Introduction to Steel Heat Treatment. In S. Hashmi, G. F. Batalha, C. J. Van Tyne, & B. Yilbas (Eds.), *Comprehensive materials processing* (pp. 3–37). Elsevier. <https://doi.org/10.1016/B978-0-08-096532-1.01202-4>
- [34] Feng, R., Li, S., Zhu, X., & Ao, Q. (2015). Microstructural characterization and formation mechanism of abnormal segregation band of hot rolled ferrite / pearlite steel. *Journal of Alloys and Compounds*, 646, 787–793. <https://doi.org/10.1016/j.jallcom.2015.05.128>
- [35] Guo, F., Liu, W., Wang, X., Misra, R. D. K., & Shang, C. (2019). Controlling Variability in Mechanical Properties of Plates by Reducing Centerline Segregation to Meet Strain-Based Design of Pipeline Steel. *Metals*, 9(7:749). <https://doi.org/10.3390/met9070749>
- [36] van Bohemen, S. (2012). Bainite and martensite start temperature calculated with exponential carbon dependence. *Materials Science and Technology*, 28(4), 487–495. <https://doi.org/10.1179/1743284711Y.0000000097>
- [37] Takayama, N., Miyamoto, G., & Furuhashi, T. (2012). Effects of transformation temperature on variant pairing of bainitic ferrite in low carbon steel. *Acta Materialia*, 60(5), 2387–2396. <https://doi.org/10.1016/j.actamat.2011.12.018>
- [38] Papaefthymiou, S., Bouzouni, M., & Petrov, R. H. (2018). Study of Carbide Dissolution and Austenite Formation during Ultra-Fast Heating in Medium Carbon

- Chromium Molybdenum Steel. *Metals*, 8(646). <https://doi.org/10.3390/met8080646>
- [39] Tsuchiyama, T., Natori, M., Nakada, N., & Takaki, S. (2010). Conditions for Grain Boundary Bulging During Tempering of Lath Martensite in Ultra-Low Carbon Steel. *ISIJ International*, 50(5), 771–773. <https://doi.org/10.2355/isijinternational.50.771>
- [40] Bhadeshia, H., & Honeycombe, R. (2017). *Steels : Microstructure and Properties* (4th ed.). Butterworth-Heinemann.
- [41] Nagode, A., Resnik, A., Vertnik, R., Bizjak, M., Kosec, B., & Goji, M. (2017). The development of a banded microstructure in S355J2 steel bar. *Kovove Mater.*, 55, 51–56. <https://doi.org/10.4149/km2017>
- [42] Choi, W., Matsuura, H., & Tsukihashi, F. (2013). Effect of Nitrogen on the Formation and Evolution of Non-Metallic Inclusions in Fe–Al–Ti–N Alloy. *ISIJ International*, 53(11), 2007–2012. <https://doi.org/10.2355/isijinternational.53.2007>
- [43] Subramanian, S., Xiaoping, M., Wenjin, N., & Xiaobing, Z. (2015). Application of Nano-scale Precipitate Engineering of TiN-NbC Composite in 32mm K60-E2 Grade Plate Rolling. *HSLA Steels 2015, Microalloying 2015 & Offshore Engineering Steels*, 211–221. https://doi.org/10.1007/978-3-319-48767-0{_}21
- [44] da Costa e Silva, A. L. V. (2019). The effects of non-metallic inclusions on properties relevant to the performance of steel in structural and mechanical applications. *Journal of Materials Research and Technology*, 8(2), 2408–2422. <https://doi.org/10.1016/j.jmrt.2019.01.009>
- [45] Mandal, S. K. (2015). *Steel Metallurgy - Properties, Specifications, Applications*. McGraw-Hill.
- [46] Morris Jr, J. W. (2001). The influence of grain size on the mechanical properties of steel. [https://doi.org/10.1016/S0965-9773\(97\)00137-2](https://doi.org/10.1016/S0965-9773(97)00137-2)
- [47] Morris Jr, J. W., Kinney, C., Pytlewski, K., & Adachi, Y. (2013). Microstructure and cleavage in lath martensitic steels. *Science and Technology of Advanced Materials*, 14. <https://doi.org/10.1088/1468-6996/14/1/014208>
- [48] Prawoto, Y., Jasmawati, N., & Sumeru, K. (2012). Effect of Prior Austenite Grain Size on the Morphology and Mechanical Properties of Martensite in Medium Carbon Steel. *Journal of Materials Science and Technology*, 28(5), 461–466. [https://doi.org/10.1016/S1005-0302\(12\)60083-8](https://doi.org/10.1016/S1005-0302(12)60083-8)
- [49] Rancel, L., Gómez, M., Medina, S. F., & Gutierrez, I. (2011). Measurement of bainite packet size and its influence on cleavage fracture in a medium carbon bainitic steel. *Materials Science and Engineering A*, 530(1), 21–27. <https://doi.org/10.1016/j.msea.2011.09.001>
- [50] Wang, C., Wang, M., Shi, J., Hui, W., & Dong, H. (2007). Effect of microstructure refinement on the strength and toughness of low alloy martensitic steel. *Journal of Materials Science and Technology*, 23(5), 659–664.
- [51] Wang, Y., Wang, Q., Liu, L., & Xu, W. (2015). Fracture mode of martensite-austenite constituents containing multiphase steel controlled by microstructural and micromechanical aspects. *Mechanics of Advanced Materials and Structures*, 22(7), 591–596. <https://doi.org/10.1080/15376494.2013.828808>

- [52] Cahn, J. W. (1962). The Impurity-Drag Effect in Grain Boundary Motion. *Acta Metallurgica*, 10, 789–798.
- [53] Reiter, J., Bernhard, C., & Presslinger, H. (2008). Austenite grain size in the continuous casting process: Metallographic methods and evaluation. *Materials Characterization*, 59(6), 737–746. <https://doi.org/10.1016/j.matchar.2007.06.003>
- [54] Li, X., Ma, X., Subramanian, S. V., Misra, R. D. K., & Shang, C. (2015). Structure–Property–Fracture Mechanism Correlation in Heat-Affected Zone of X100 FerriteBainite Pipeline Steel. *Metallurgical and Materials Transactions E*, 2(1), 1–11. <https://doi.org/10.1007/s40553-014-0036-3>
- [55] Chen, J. H., & Cao, R. (2015). *Micromechanism of Cleavage Fracture of Metals*. Butterworth-Heinemann. <https://doi.org/10.1016/B978-0-12-800765-5.00003-4>
- [56] Griffith, A. A. (1920). The Phenomena of Rupture and Flow in Solids. *Philosophical Transactions of the Royal Society A: Mathematical, Physical and Engineering Sciences*, 100, 163–198.
- [57] Ghosh, A., Ray, A., Chakrabarti, D., & Davis, C. L. (2013). Cleavage initiation in steel : Competition between large grains and large particles. *Materials Science & Engineering A*, 561, 126–135. <https://doi.org/10.1016/j.msea.2012.11.019>

4

CLEAVAGE FRACTURE MICROMECHANISMS IN THICK-SECTION QUENCHED AND TEMPERED S690 HIGH STRENGTH STEELS

For structural assessment and optimal design of thick-section high strength steels in applications under harsh service conditions, it is essential to understand the cleavage fracture micromechanisms. In this study, we assess the effects of through-thickness microstructure of an 80 mm thick quenched and tempered S690 high strength steel, notch orientation, and crack tip constraint in cleavage nucleation and propagation via sub-sized crack tip opening displacement (CTOD) testing at $-100\text{ }^{\circ}\text{C}$. The notch was placed parallel and perpendicular to the rolling direction, and the crack tip constraint was analysed by varying the a/W ratio: 0.5, 0.25, and 0.1. The notch orientation does not play a role, and the material is considered isotropic in-plane. Nb-rich inclusions were observed to act as the weak microstructural link in the steel, triggering fracture in specimens with the lowest CTOD values. While shallow-cracked specimens from the top section present larger critical CTOD values than deep-cracked ones due to stress relief ahead of the crack tip, the constraint does not have a significant influence in the middle due to the very detrimental microstructure in the presence of Nb-rich inclusions. Some specimens show areas of intergranular fracture due to the combined effect of C, Cr, Mn, Ni, and P segregation along with precipitation of Nb-rich inclusions clusters on the grain boundaries. Several crack deflections at high-angle grain boundaries were observed where the neighbouring substructure has different Bain axes.

This chapter is based on the scientific publication Bertolo, V., Jiang, Q., Tiringer, U., Walters, C., Sietsma, J. & Popovich, V. (2022). Cleavage fracture micromechanisms in thick-section quenched and tempered S690 high-strength steels, *Journal of Materials Science*, 57, 20033-20055. <https://doi.org/10.1007/s10853-022-07841-1>

4.1. INTRODUCTION

Cleavage fracture, the most dangerous form of fracture, raises concern in structural components under harsh operating conditions. Although high-performance materials with an optimal combination of strength and toughness, such as high strength steels (HSSs), are often selected for structural applications, severe operating conditions can make them susceptible to brittle fracture [1–3]. For example, thick-section HSSs are applied in offshore structures, including equipment necessary for installing green energy farms and decommissioning old structures that had been used for the exploitation of oil and gas. In such applications, the service environments account for the presence of high stresses and the potential of very low temperatures. As body-centred cubic (BCC) HSSs are known to transition from ductile to brittle when the temperature is reduced or high strain rates are applied, the potential for catastrophic cleavage fracture exists. Cleavage is the governing micromechanism in the ductile-to-brittle transition region and the lower shelf [4]. Hence, for integrity assessment and optimal material design of these structures, including modelling approaches, the investigation of cleavage initiation and propagation micromechanisms of thick-section HSSs is required. The influence of microstructural factors on cleavage fracture toughness and micromechanisms has been investigated in the literature [5–10]. However, there are still some knowledge gaps to be filled.

First, from the microstructural point of view, thick-section HSSs display complex and multiphase microstructures with a significant degree of inhomogeneity through the thickness (e.g., grain size, inclusions, and phase fractions) [5, 11, 12]. Consequently, a considerable scatter of mechanical and fracture properties is observed along the thickness [5, 6, 12, 13], resulting in great consequences for accurate structural integrity evaluation and definition of structural design specifications. To assess cleavage fracture for such steel plates, many experimental studies found in the literature use Charpy testing, which has limitations regarding specimen plastic constraint – blunt notch instead of a sharp crack –, strain rate – dynamic loading instead of quasi-static loading –, and specimen size and size-dependent property – relatively small, not representing metallurgical structural variations and material true property [5, 12, 13]. Another limitation of these studies is that they are mostly focused on modified or experimental steels that are not used in industrial practice. Thus, they do not necessarily have the actual heterogeneous microstructures observed in operating structural components [12, 13]. Moreover, they lack sufficiently detailed material characterisation to allow for an accurate and comprehensive analysis of cleavage fracture [5, 6, 12, 14]. Hence, these studies do not provide a representative understanding of the involved fracture micromechanisms, crack initiation and propagation, in structures. For instance, Pallasपुरi et al. [13] carry out a similar study where a comprehensive and statistical microstructural characterisation is provided. However, the steel is experimental, where material from different positions is separately hot rolled and heat treated, resulting in a different microstructure and mechanical and fracture properties representative of real commercial steels. Liu, Zhang and Li, and Wang et al. [5, 12] also investigated the scatter of properties through the thickness of thick-section steels connecting it with microstructural features. These studies were carried out in steels that are not commercial but are subjected to similar industrial

processing routes. However, the authors do not provide sufficient statistical microstructural information for the assessment of various microstructural features on the onset and propagation of cleavage cracks. Moreover, fracture is evaluated in terms of impact toughness via Charpy tests.

Studies related to micromechanism-driven modelling of cleavage fracture share this knowledge gap. In a multi-barrier theory, cleavage fracture of ferritic steels is regarded as the result of the successive occurrence of three microscale events: nucleation of a slip-induced crack at a brittle second-phase particle (i.e. carbides in steels) or inclusion; propagation of the microcrack across the particle/matrix interface under the local stress state; and propagation of the grain-sized crack to neighbouring grains across the grain boundary under the local stress state [15–18]. Hence, the use of a multi-barrier theory requires an understanding of the relationship between representative and statistical microstructure, local properties, and failure micromechanisms. Bimodal methods in cleavage simulations of steels have modelled macroscopic microstructural inhomogeneities at the millimetre scale [19, 20]. However, microstructural inhomogeneities below the millimetre scale have not yet been considered.

Second, from the experimental perspective, fracture toughness testing and assessment are standardized, e.g., [21, 22]. However, there are some variables in the fracture toughness testing that may have a significant effect on the resulting toughness values. For instance, research has shown that the orientation of the notch may affect the toughness, reflecting an anisotropic behaviour of the material and indicating the most critical crack orientation in the structure [7, 23]. The crack tip constraint and its effect on fracture toughness are also extensively studied in the literature [8, 9, 24–26]. The crack tip constraint is related to the stresses at the crack tip. In standard fracture assessments, deep-cracked specimens ($0.45 \leq a/W \leq 0.55$), where a is the nominal crack length and W is the specimen width) are used to restrict the plastic zone near the crack tip, resulting in very small plastic zones compared to the specimen dimensions. Hence, a high degree of stress triaxiality (constraint) in the crack-tip is ensured. This procedure follows a conservative approach and measures a lower-bound value for the material's fracture toughness. However, structural components may contain initial surface (shallow) cracks originating from welding and corrosion processes. In this case, when the material is loaded, the plastic deformation at the crack tip may expand to the nearest free surface, relaxing the stresses at the crack tip and reducing the constraint. Consequently, shallow-cracked specimens are likely to have higher fracture toughness than deep-cracked specimens [9, 10, 26, 27]. Sorem, Dodds, and Rolfe [10] reported that shallow-cracked specimens ($a/W=0.15$) of a low-strength structural steel have critical CTOD values: 2.5 times higher than deep-cracked specimens ($a/W=0.5$) within the lower transition region. Also, the crack tip constraint was observed to affect the toughness-temperature relationship, which is important for BCC steels [26, 27]. As stresses ahead of the crack tip are relieved with the loss of constraint in the shallow-cracked specimens, larger far-field stresses need to be reached for brittle fracture to occur and cleavage is delayed in relation to the deep-cracked specimens. A difference of 20 °C in the transition temperature between deep- and shallow-notched specimens for a low-strength structural steel was observed by Sorem, Dodds, and Rolfe [26]. Thus, standard procedures may be considered too conservative for actual structures with shallow cracks, and the material fracture behaviour

with shallow defects is worth investigating for a realistic practical fracture integrity assessment. As discussed, extensive research has been done to address the impact of crack depth and plastic constraint on fracture toughness. Nevertheless, the influence of the material microstructure on the plastic constraint effect in HSSs still needs to be investigated.

Therefore, the effects of through-thickness microstructural inhomogeneity on cleavage fracture toughness are comprehensively investigated to identify the microstructural features governing cleavage fracture in HSSs. Bertolo et al. [11] extensively and statistically characterised the through-thickness microstructure of the steel studied herein. In the present work, the cleavage fracture toughness of the investigated high strength steel is assessed via three-point bend crack tip opening displacement (CTOD) tests on a commercially available 80 mm thick S690QL HSS plate at $-100\text{ }^{\circ}\text{C}$, to evaluate the material on the lower-shelf. Three macroscopic variables were considered in the CTOD tests for further examination: (1) crack orientation with respect to the rolling direction to analyse whether the material presents anisotropic behaviour, (2) crack depth to understand the constraint effects on toughness in the present material/microstructure under study, and (3) through-thickness position to understand through-thickness homogeneity. Afterwards, fracture surfaces and their transversal planes were analysed, providing an extensive statistical analysis of cleavage initiation sites, showing the direct effect of different initiation sites on fracture toughness and the preferential propagation paths. The outcome of this research along with the work carried out in [11] represents a unique data set that relates the micro and macro scales relevant for understanding cleavage fracture in HSSs and modelling it using the multi-barrier theory.

4.2. MATERIALS AND METHODS

4.2.1. MATERIAL

The investigated materials were taken from the top quarter (further referred to as top) and middle thickness sections of a commercially available 80 mm thick quenched and tempered (S690QL according to EN 10025-6 [28]) high strength steel plate. The chemical composition of these sections, measured by X-ray Fluorescence (XRF) and LECO combustion analysis, is given in Table 4.1. The elemental content of this steel is in accordance with the standard EN 10025-6, including for the ones under “other” (max wt.% of Mn=1.7, Ni=4.0, Cr=1.5, Nb=0.06, P=0.02, N=0.015, S=0.01 and B=0.005) [28]. The tensile and micro-Vickers hardness properties for the top and middle sections at room temperature and $-100\text{ }^{\circ}\text{C}$ are presented in Table 4.2. The material was measured to have an isotropic in-plane behaviour.

Table 4.1: Chemical composition of S690QL at two through-thickness locations.

wt. (%)	Fe	C	Si	Al	Mo	Other
Top	Bal.	0.170 ± 0.001	0.29 ± 0.02	0.070 ± 0.005	0.30 ± 0.01	Mn, Ni, Cr, Nb, P, N, S, B
Middle	Bal.	0.160 ± 0.001	0.30 ± 0.03	0.08 ± 0.01	0.29 ± 0.02	

An in-depth microstructural characterisation of both thickness positions was per-

Table 4.2: Tensile and Micro-Vickers hardness properties of the top and middle sections at -100°C and room temperature (RT).

Thickness Position	Yield Strength (MPa)		Tensile Strength (MPa)		Micro-Vickers Hardness (HV ₃)
	RT	-100°C	RT	-100°C	RT
Top	811 ± 4	974 ± 13	931 ± 4	1078 ± 14	280 ± 5
Middle	739 ± 11	895 ± 12	861 ± 12	1013 ± 13	272 ± 11

formed and is discussed in detail in [11]. Figure 4.1 exemplifies the microstructure and inclusions found in the through-thickness of the S690QL high strength steel. Table 4.3 summarises the main microstructural characteristics. The through-thickness microstructural matrix of the HSS plate under study is a mixture of tempered (between 600°C and 650°C for a few minutes) microconstituents ferrite (F), bainite (TB), and martensite (TM). Additionally, centreline segregation bands (SB) were observed in the mid-thickness section, with different phase fractions of the middle section outside SB. Based on the grain average image quality (GAIQ) analysis, the phase fraction of F, TB and TM is: 6%, 68%, and 22% (top); 15%, 76%, and 7% (middle section outside SB); and 0.2%, 86% and 14% (middle section inside SB). Prior austenite grains (PAG) are larger in the middle section than in the top section, except for the segregation bands where PAG are smaller within the middle and comparable to the grains in the top section. In general, the top and middle sections display spherical and cubic inclusions with complex chemical compositions with a mixture of oxides, carbides, and nitrides (e.g., (Mg, Ca, Al, Ti)(O, N) and (Nb, Ti)(N, C)). Nb-rich cubic inclusions are often observed distributed as clusters and associated with defects (e.g., cracks in the inclusions themselves and voids in the interface inclusion/matrix). These inclusions were quantified, and their sizes were measured. It was observed that bigger – spherical and cubic – inclusions are presented in a larger area fraction in the central part of the steel plate than on the outer surface [11]. A distinct hardness gradient is observed through the plate's thickness. The top section shows higher hardness than the middle section. However, a hardness maximum, comparable to the value in the top section, right in the centre of the plate is observed. This is related to the area fraction of martensite and PAG sizes. The top section, as well as the segregation bands, have a larger area fraction of martensite and smaller PAG sizes than the middle section outside the segregation bands, resulting in higher hardness. Moreover, the segregation bands also present clusters of brittle inclusions which explains their nanohardness being up to 2.4 times higher than in the surrounding areas in the middle section.

Table 4.3: Summary of microstructural quantitative characteristics for the S690QL high strength steel under study reported in [11]. SB stands for segregation bands.

Thickness Position	Average PAG size (Intercept) (μm)	Inclusions				
		Shape	Range (μm)	Area Fraction	Fraction (%)	Fraction of Clustered Inclusions (%)
Top	19.2 ± 1.4	Oxide-circular	1 – 5	$5 \times 10^{-4} \pm 3 \times 10^{-4}$	88 ± 1	-
		Nb-cubic	1 – 7	$7 \times 10^{-5} \pm 4 \times 10^{-5}$	12 ± 1	47
Middle	Outside SB 23.5 ± 2.3	Oxide-circular	1 – 5	$7 \times 10^{-4} \pm 3 \times 10^{-4}$	76 ± 6	-
	Inside SB 19.1 ± 2.6	Nb-cubic	1 – 12	$2 \times 10^{-4} \pm 3 \times 10^{-5}$	24 ± 6	74

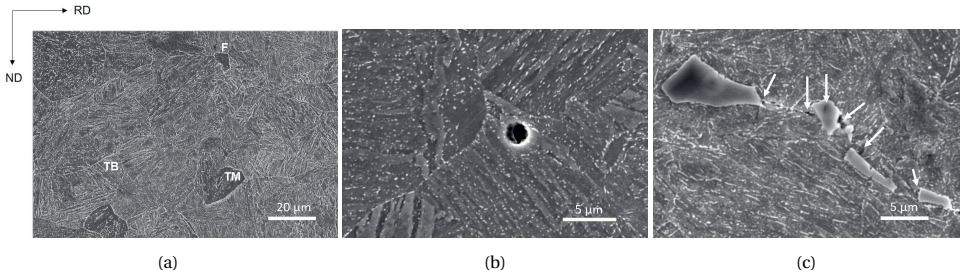


Figure 4.1: SEM micrographs of the (a) tempered microconstituents, ferrite, bainite, and martensite, and (b) (Mg, Al, Ca)(O, S) and (c) (Nb, Ti)(C) inclusions that constitute the through-thickness microstructure of the S690QL steel. Defects associated with inclusions and the interface inclusion/matrix are indicated by the white arrows (Partially included in [29]).

4

4.2.2. METHODS

4.2.2.1. CHARACTERISATION OF FRACTURE PROPERTIES

Three-point bending tests using sub-sized single edge-notched bending (SENB) specimens from the top and middle sections were carried out similar to the ISO 12135 standard [21] at $-100\text{ }^{\circ}\text{C}$ and a deformation rate of 2 mm/s using a 350 kN MTS 858 servo-hydraulic test rig. First of all, a thermocouple is spot welded to the specimen to monitor the temperature during cooling and testing. Next, the specimen is cooled down by immersion in liquid nitrogen until, approximately $-196\text{ }^{\circ}\text{C}$ (liquid nitrogen's boiling temperature). The temperature difference between the minimum cooling temperature and the test temperature is to allow for thermal soaking and to ensure there is enough time to mount the specimen in the setup. Subsequently, the specimen is placed on the machine, touching a thermal insulation material placed next to the rollers (at a larger height) of the three-point bending setup. The aim is to avoid the specimen to touch the metallic rollers before that test and avoid the fast heat exchange. Finally, a pre-load is applied to make contact between rollers-specimen and when the specimen reaches $-100\text{ }^{\circ}\text{C}$, the test is performed. This test temperature ($-100\text{ }^{\circ}\text{C}$) is much lower than the temperatures experienced in offshore and maritime applications as the aim is to perform tests in the cleavage fracture regime. Although the studied S690QL steel fully satisfies the design requirements for offshore and maritime applications, it may exhibit weaknesses under these more severe test conditions which impact its performance.

Different experimental conditions were taken into account regarding crack orientation, T-L (parallel to the rolling direction) and L-T (perpendicular to the rolling direction), and crack depth (a/W), 0.5, 0.25 and 0.1 to vary the crack tip constraint from high to low conditions (Fig. 4.2). Specimens with $a/W=0.5$ will be referred to as high-constraint; $a/W=0.25$ will be referred to as mid-constraint; $a/W=0.1$ will be referred to as low-constraint. Details on the specimen's dimensions and conditions are given in Fig. 4.2. The dashed grey semi-circles represent the three-point bending rollers.

The CTOD results for shallow notches, $a/W=0.1$ and 0.25, were calculated according to the ISO 12135 standard [21]. CTOD fracture toughness tests are based on the plastic

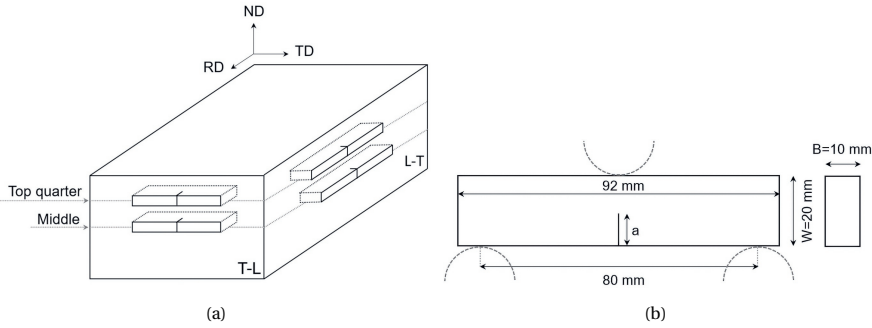


Figure 4.2: Schematic illustration showing how SENB specimens were extracted from the steel plate in terms of thickness position and notch orientation to the RD, and SENB specimen's dimensions. The dashed grey semi-circles represent the three-point bending rollers. ND is the normal direction, RD is and rolling direction and TD is the transverse direction (Adapted from [11]).

hinge model. For the shallow-cracked specimens, the plastic hinge point location in the unnotched ligament ahead of the crack tip can be shifted due to the smaller a/W ratio than in the conventional deep-cracked specimens. Some studies reported a significantly lower value of the rotational factor (r_p) for the shallow-cracked specimens compared to the 0.4 used in the standards for deep-cracked specimens [21]. For instance, it was estimated at 0.2 for $a/W=0.1$ [30, 31]. Hence, it is essential to determine the r_p values for shallow cracked specimens for an accurate fracture toughness measurement of structures having surface defects. The values of r_p for a/W of 0.1 and 0.25 were determined through finite element analyses by [32]. The shallow-cracked specimens were modelled in three dimensions with appropriate boundary conditions reproducing the experimental setup. For a/W of 0.1, the total initial crack length used was 2 mm, which includes a 0.6 mm long notch and a 1.4 mm long pre-fatigued crack. For a/W of 0.25, the total initial crack length used was 5 mm, which includes a 3.5 mm long notch and a 1.5 mm long pre-fatigued crack. The crack tip was modelled with an initial blunted opening with a radius of 0.005 mm. The finite element models were loaded by a displacement ramp imposed on the loading point through a rigid roller. The plastic rotational factor, r_p , is calculated from its relationship with CTOD and crack mouth opening displacement (CMOD):

$$\delta_p = \frac{(r_p(W - a)V_p)}{(r_p(W - a) + a)} \quad (4.1)$$

where δ_p is the plastic CTOD component and V_p is the plastic CMOD measured from the finite element model. As a result of the finite element analyses, r_p values were calculated as 0.24 and 0.31 for a/W of 0.1 and 0.25, respectively.

The failure probability of a specimen was calculated as a rank probability:

$$\text{Failure probability} = \frac{(i - 0.3)}{(N + 0.4)} \quad (4.2)$$

where i is the rank number in terms of CTOD and N is the total number of experiments.

4.2.2.2. CHARACTERISATION OF FRACTURE SURFACE AND PROFILE

SENB fractured surfaces were investigated to study the fracture micromechanisms (e.g., crack initiation and propagation). First, the direct examination of fracture surfaces via scanning electron microscopy (SEM) equipped with electron dispersive spectroscopy (EDS) provided information on the mode of failure and identification of initiation sites. Second, to identify the cleavage micromechanisms involved in the crack propagation process of the S690QT high strength steel, the transverse section of the fractured surface of SENB specimens (hatched area in Fig. 4.3 (b)) tested at $-100\text{ }^{\circ}\text{C}$ was analysed by SEM and Electron Backscattered Diffraction (EBSD). Specimens from the top and middle sections with the notch oriented parallel to the rolling direction (T-L) and with the lowest CTOD values (0.02 and 0.01 mm, respectively) were selected for this investigation to study the worst-case scenario. The preparation of the transverse section of the fractured surfaces was done according to the following steps:

1. The distance from the external surface (edge) of the CTOD specimen and the initiation site was measured;
2. The CTOD specimen was mounted in conductive resin to ensure a final flat and well-polished sample where the external cross-section surface of the specimen was the one exposed for metallographic preparation and subsequent analysis;
3. The mounted sample was ground using P80 SiC grinding paper to reduce the sample thickness at a distance mentioned in step 1 (Fig. 4.3 (a)). Thus, the fracture profile to be analysed would be close to the initiation site and, consequently, represent an area tested under a triaxial stress state (hatched area in Fig. 4.3 (b)). The surface was further ground with SiC sanding papers of P180, P320, P800, and P1200. Subsequently, samples were polished with $3\text{ }\mu\text{m}$ and $1\text{ }\mu\text{m}$ diamond solution for 25 minutes per step followed by OPS polishing with $0.25\text{ }\mu\text{m}$ for 1 hour. The appearance of the cross-section of the fracture surface is shown in Fig. 4.3 (c).
4. The sample was then removed from the resin to avoid drift during the EBSD scans. The analysed areas in the transversal section of the fractured surfaces were located close to the pre-crack tip, where initiation sites were usually located, and where the crack has propagated without considerably changing its path and has also deflected significantly. Then, it is possible to identify microstructural characteristics that have a weak and strong influence on the crack propagation under triaxial stress state.

EBSD data was acquired on a ThermoFisher Helios™ UXe G4 PFIB scanning electron microscope equipped with a Field Emission Gun (FEG-SEM) using 20 kV accelerating voltage, 3.2 nA current, tilt angle 70° , and step size $0.1\text{ }\mu\text{m}$ using Team™ software and post-processed with EDAX-TSL-OIM Analysis™ software. The initial post-processing step was the data clean-up. First, grain fit standardization with a grain tolerance angle of 5° and minimum grain size of 4 pixels was applied considering that grains contain multiple pixel rows. Secondly, the neighbour orientation correlation procedure with a grain tolerance angle of 5° and a minimum confidence index of 0.1 was used. Lastly,

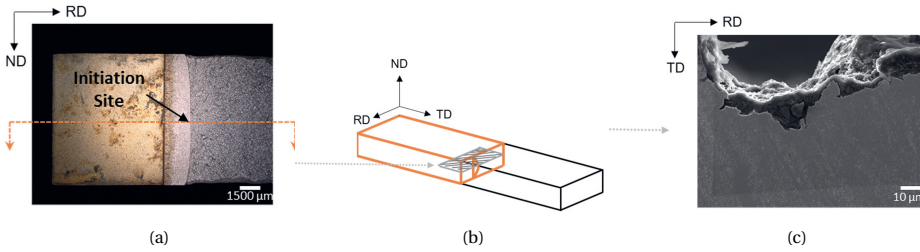


Figure 4.3: Schematics of the T-L sample preparation for fractographic profile investigation showing (a) the sample's distance ground to analyse the crack propagation path in an area fractured in triaxial stress state, (b) an illustration of the specimen's plane which was metallographically prepared, and (c) the polished fracture profile.

neighbour phase correlation with a minimum confidence index of 0.1 was applied. Afterwards, the final grain definition was done with a tolerance angle of 5° and a minimum size of 4 pixels.

In order to further investigate the regions of the middle section that fractured in an intergranular manner and inspect whether the alloying segregation at the grain boundary is playing a role, a preliminary chemical composition line scan analysis was carried out via Scanning Auger Microprobe (SAM). A PHI-650 SAM, equipped with a cylindrical mirror analyser (CMA) and operated with an energy resolution $\Delta E/E$ of 0.6%, was used. An electron beam of 5 kV and 150 nA at an angle of incidence of 30° with respect to the sample surface normal was applied. At these experimental conditions, the lateral resolution was approximately 0.3 to 0.4 μm , and the low pressure in the main chamber was about 7×10^{-8} Pa. Each line scan, consisting of 256 scan points for the elements C, Mn, Cr, Mo, P, Ni, and Si, was made through intergranular facets of the specimen, crossing the grain boundaries. These elements were selected for this analysis, as they were identified to be enriched in the segregation bands or for being frequently reported in the literature as the main elements responsible for grain boundary embrittlement in steels, such as P including the case of temper embrittlement in the references [11, 33–35].

4.3. RESULTS AND DISCUSSION

Three variables were analysed in the CTOD tests: thickness position, notch orientation, and crack tip constraint. SENB specimens were extracted from the top and middle sections of the S690QL steel plate and the notches were machined in T-L and L-T orientations. Initially, two notch depths were considered to investigate the constraint (crack depth) effects: $a/W=0.5$ and 0.1. These different notch depths allowed the analysis of high- and low-constraint conditions, respectively. Figure 4.4 presents the failure probability as a function of CTOD for the top and middle sections, in T-L and L-T orientations and $a/W=0.5$ and 0.1. Note that sub-sized SENB specimens were proven to be suitable only for cleavage-controlled fractured specimens, meaning that valid CTOD values should be below 0.2 mm [36]. Hence, specimens with CTOD values greater than 0.2 mm, presenting extensive plastic deformation, as confirmed by visual inspection, were disre-

garded in the following discussions made in this study.

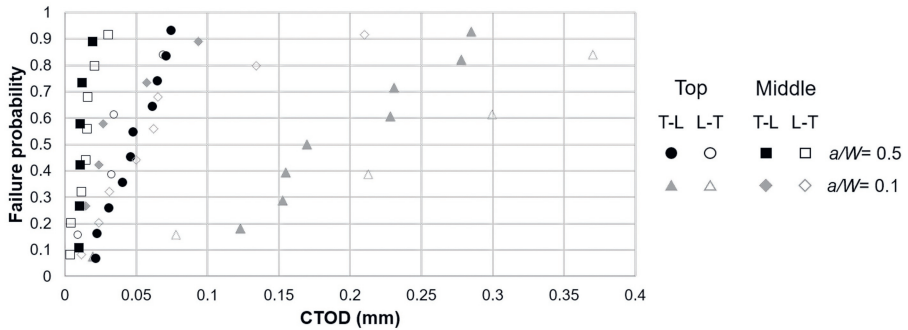


Figure 4.4: Rank failure probability vs. CTOD of the experimental fracture tests at $-100\text{ }^{\circ}\text{C}$, top and middle sections, T-L and L-T orientations, and $a/W = 0.5$ and 0.1 .

4.3.1. EFFECT OF NOTCH ORIENTATION AND CONSTRAINT

As can be seen in Fig. 4.4, most of the top, low-constraint specimens, in both notch orientations, present CTOD values higher than 0.2 mm and show mixed-mode fracture characteristics. These specimens represent more than 50% of the tested specimens in this condition. Thus, the a/W ratio of 0.1 does not provide representative CTOD results for further discussion of cleavage fracture in the top section. However, the effect of notch orientation can be investigated for the high-constraint and low-constraint middle specimens. Moreover, no significant difference in the CTOD values between T-L and L-T orientations was observed either for the top or middle. This behaviour is expected since the S690QL plate does not have a preferential crystallographic orientation – texture – through the thickness [11]. Therefore, the material is considered isotropic in-plane.

As many of the low-constraint tests were not valid and, therefore, not included in the analysis (most of the specimens in the top position with an a/W ratio of 0.1 present critical CTOD values greater than 0.2 mm), a mid-constraint ($a/W=0.25$) condition was included in the test matrix. As the notch orientation does not play a role, the CTOD results (Fig. 4.4) for T-L and L-T orientations were added up for the high- and low-constraint conditions ($a/W=0.5$ and 0.1), and mid-constraint specimens ($a/W=0.25$) were only tested in T-L orientation.

Figure 4.5 (a) shows the failure probability as a function of CTOD for the top and middle sections and $a/W=0.5$, 0.25 , and 0.1 . Figure 4.5 (b) shows the relationship between the average CTOD values and the a/W ratio for the top and middle sections. On one hand, a considerable increase in CTOD values with the crack depth reduction is seen for the top section, primarily for the $a/W=0.1$ condition. On the other hand, the a/W influence on CTOD is minor for the middle section, even for $a/W=0.1$.

In general, the lower the a/W ratio the larger the CTOD [10, 26, 27]. This correlation is associated with the specimen's plastic zone and the resultant stress state ahead of the crack tip when varying the crack depth. Sorem, Dodds, and Rolfe [10, 26] performed

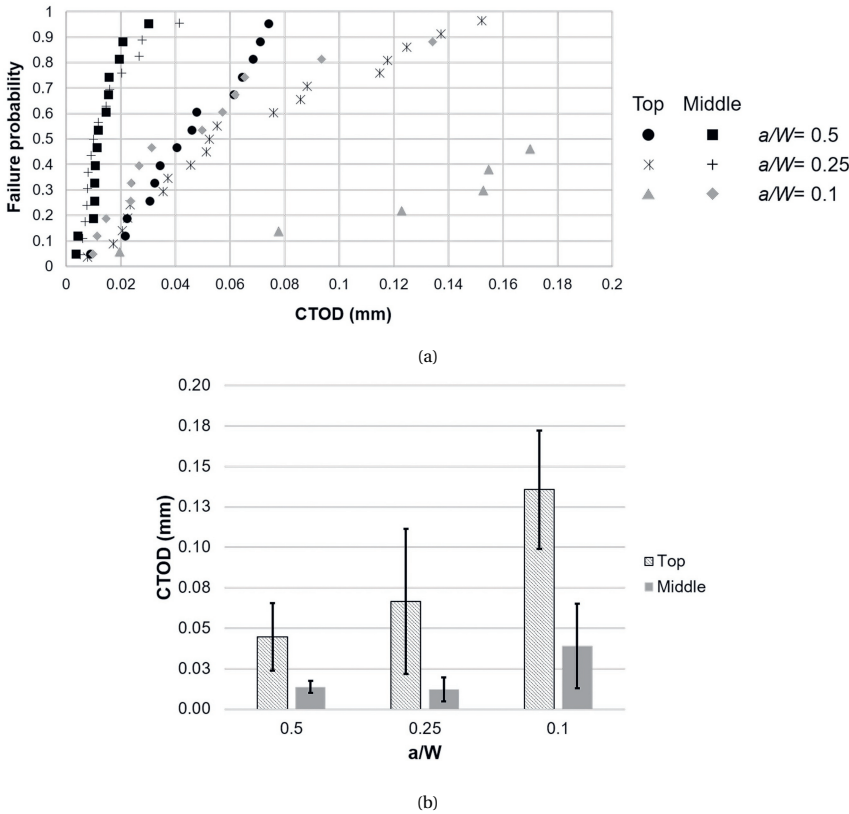


Figure 4.5: Experimental CTOD data presented as (a) rank failure probability and (b) average values and standard deviation from the average for the top and middle sections and $a/W = 0.5, 0.25$, and 0.1 . The data includes the combined T-L and L-T CTOD results for $a/W = 0.5$ and 0.1 , and T-L CTOD for $a/W = 0.25$

studies comparing the behaviour of shallow- and deep-cracked CTOD specimens of A36 steel. The authors observed that, when the material is in a linear-elastic regime (e.g., the lower shelf of the ductile-brittle transition curve, where the material failure is controlled by cleavage), shallow and deep-cracked specimens present the same stress ahead of the crack tip for the same CTOD value. In other words, fracture toughness is independent of a/W values. On the other hand, in the elastic-plastic regime, at the same CTOD level, stresses vary ahead of the crack tip for shallow- and deep-cracked specimens. Furthermore, they [10] observed that when a CTOD specimen with $a/W = 0.05$ or 0.1 is loaded, the plastic zone ahead of the crack tip interacts with the nearest free surface before a plastic hinge forms, which would cause the specimen to be invalid. For the investigated level of loading, the authors observed that at $a/W = 0.15$, the formation of a plastic hinge coincides with the interaction of the plastic zone with the nearest specimen's free surface. At $a/W = 0.2$, the plastic hinge developed long before the plastic zone interacted with the free surface. Finally, at $a/W = 0.5$, the plastic zone was limited to a small region ahead of the crack tip without expanding to the free surface. Hence, for the A36 steel, the boundary

between shallow and deep cracks was found to be around $a/W=0.15$. However, this number may vary with the loading, specimen size, and material hardening behaviour. For instance, materials that have a considerable strain hardening may have larger a/W transition values as the hardening expands the plastic zone to the free surface [26]. Hence, although the shallow- and deep-cracked specimens are submitted to the same loading conditions and, consequently, would present similar stress levels ahead of the crack tip, the expanded plastic zone in shallow-cracked specimens relieves the stress, reducing the triaxiality, and also the constraint. Then, shallow-cracked specimens need to be deformed further to reach the critical stress for failure, leading to a larger CTOD [26]. This resultant larger strains experienced by the low-constraint specimens before fracture may involve the crack tip blunting [26].

To simulate the stress distribution near the crack tip (Fig. 3.6) for $a/W = 0.5, 0.25$, and 0.1 , a finite element analysis (FEA) is performed in Abaqus 2017. The specimen is modelled as a 3D deformable solid with 20-noded hexahedral elements. The supports and load roller are modelled as frictionless rigid surfaces. The initial pre-fatigued crack tip is modelled as a finite notch that is 0.005 mm in radius with the smallest element having the dimensions $0.001 \times 0.005 \times 0.067$ mm³. A full Newton-Raphson algorithm is used to solve the geometric and material nonlinearity in an implicit method. The stress-strain relationship of the steel is characterised by Ludwik's law, defined with the flow stress (σ) and the effective plastic strain (ϵ_p) as:

$$\sigma = \sigma_y + K \epsilon_p^{(n_L)} \quad (4.3)$$

where σ_y is yield strength, K and n_L are material parameters fitted from tensile tests.

The experimental tensile true stress-strain curves and the fitting curves with Eq. 4.3 for the top and middle sections (tensile test curves are plotted until the maximum stress) are presented in our previous work [32]. Figure 4.6 displays the normal stress distribution in front of the crack tip for the top and middle sections and the three tested a/W , 0.5 , 0.25 , and 0.1 . The figure corresponds to CTOD = 0.05 mm for all the cases. It can be seen that, for both top and middle sections, a smaller a/W ratio implies a lower normal stress ahead of the crack. This explains the very different CTOD values between high- and low-constraint conditions observed for the top section at -100 °C. However, for the middle section, such a difference is not observed. Moreover, the normal stress in the top section is higher than in the middle section for the same a/W ratio due to the difference in yield strength. However, the middle section still exhibits lower fracture toughness than the top section.

The weak dependence of the fracture toughness on the a/W ratio in the middle section relative to the top may be explained by the ductile-to-brittle transition behaviour. First, for shallow-cracked specimens, the material experiences fracture at a different temperature relative to the reference temperature because constraint is known to affect the ductile-to-brittle transition temperature. Shallow-cracked specimens need more deformation to reach the fracture stress to fail, resulting in larger CTOD. It means that the transition for low-constraint specimens occurs at a lower temperature than for high-constraint specimens. Hence, at the same test temperature, the material under different constraints may be tested in different regimes of the ductile-to-brittle transition curve. Second, the reference temperature (T_0) for each thickness section was calculated based

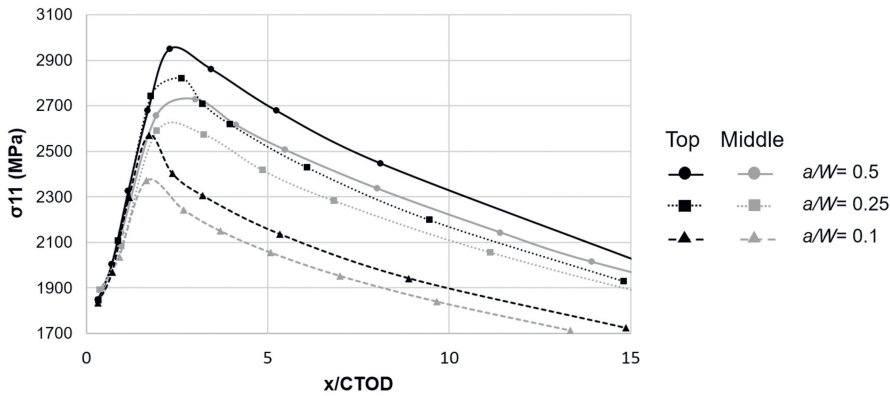


Figure 4.6: Normal stress (σ_{11}) at the specimens' mid-plane and distance x mm from the crack tip (undeformed configuration).

on the master curve method using the ASTM E1921 [37]. For the top and middle sections, T_0 is -101 °C and -41 °C, respectively. It means that, while the fracture behaviour of the top section is being assessed near T_0 and closer to the ductile-to-brittle transition, for the middle section the test temperature is further from T_0 and the toughness therefore near or at the lower shelf due to its embrittled microstructure, as discussed in [11]. In this case, even with the shift of the ductile-to-brittle transition curve for the shallow-cracked specimens, the middle section remains at the lower transition part of the ductile-brittle transition curve, where less plasticity is involved, while the top section is near the upper part of the transition. Hence, the fracture toughness differences between high- and low-constraint specimens in the middle section are considerably smaller than for the top section.

The different behaviour between the top and middle sections in low-constraint conditions may be explained by fracture surface analysis. The fracture surface of low-constraint specimens shows that different damage characteristics for top and middle samples may occur even having the same initiation site type, an Nb-rich inclusion. Figure 4.7(a) shows that for the top section, the fatigue pre-crack is followed by a stretch zone – characteristic of plastic deformation as a consequence of crack tip blunting – and a flat transgranular cleavage surface (mixed-mode fracture usually observed in the ductile-to-brittle transition region of the ductile-brittle curve, but still represents a cleavage-controlled fracture). As previously explained, the lack of constraint causes the material to experience larger deformation to compensate for stress relief. Then, the crack blunts before reaching the critical stress to failure, resulting in a stretch zone just after the pre-fatigue crack tip and before the cleavage surface. For the same constraint condition, the fracture surface of middle specimens either does not show any or presents only a small stretch zone compared to the top, as shown in Fig. 4.7(b), reflecting the limited crack-tip plasticity resultant from the detrimentally brittle microstructure. The presence of the stretch zone and its width may be related to the type of initiation site and its distance far from the pre-crack tip.

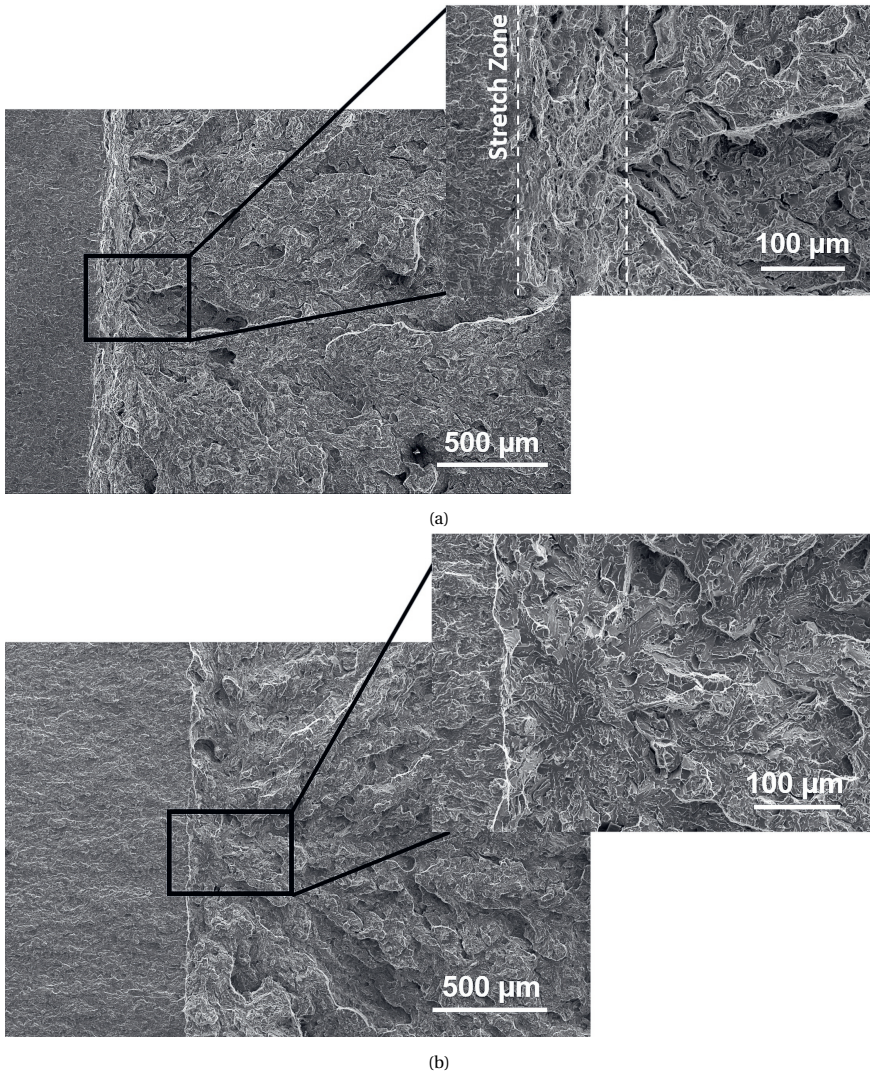


Figure 4.7: SEM micrographs of fracture surfaces of low-constraint specimens ($a/W=0.1$) tested at $-100\text{ }^{\circ}\text{C}$ from (a) top, with a critical CTOD of 0.12 mm showing a fatigue pre-crack, stretch zone, and cleavage area, and (b) middle, with a critical CTOD of 0.02 mm showing a fatigue pre-crack and cleavage area.

4.3.2. MICROSTRUCTURAL FACTORS CONTROLLING CLEAVAGE CRACK INITIATION

Figure 4.8 (b) shows the average CTOD and the standard deviation from the average for all analysed constraint conditions. The distinct difference in fracture toughness between

the top and middle sections is notable, where the top shows the highest CTOD values. The adverse microstructure of the middle section in thick-section steel plates in terms of fracture behaviour was already pointed out before [5, 6, 12, 14, 29], including for the high strength steel investigated in this study [11]. According to Bertolo et al. [11], the unfavourable microstructure of the middle section compared to the top section of the 80 mm thick quenched and tempered S690QL steel plate includes “larger prior austenite grain sizes, larger sizes and area fraction of inclusions, the presence of defects associated with the circular and cubic inclusions and with their interface with the matrix, clusters of cubic inclusions that may also be distributed along the PAG boundaries, and the long interfaces with the largest hardness gradients”. To investigate which microstructural features are involved in the cleavage initiation responsible for the difference in fracture behaviour, the CTOD fracture surfaces were analysed by SEM based on the river lines that lead to the initiation site.

Fracture surfaces of 32 Single Edge Notched Bending (SENB) specimens tested at $-100\text{ }^{\circ}\text{C}$ including high- and low-constraint conditions ($a/W = 0.5$ and 0.1 , respectively), and T-L and L-T orientations extracted from the top and middle sections of the plate were investigated. In 63% of all surfaces, it was possible to identify microstructural features triggering the fracture. In the other 37% of samples, it was not possible to identify the initiation site because fracture surfaces did not show clear river lines or the river lines did not converge.

Figure 4.8 (a) shows the number fraction of each type of initiation site that was observed in the top and middle section, with no distinction between notch orientation and constraint. For the top section, initiation sites were identified for 11 fracture surfaces, 9 from high-constraint and 2 from low-constraint samples. The (Mg, Al, Ca)(O, S) inclusions, which in some cases also include traces of Ti, B, C, and N, are the most common initiation sites, being present in 73% of the identified cases (7 high-constraint and 1 low-constraint). The remaining 27% of the specimens had their fracture process triggered by Nb-rich inclusions (2 high-constraint and 1 low-constraint). Within the 27%, more than 2/3 presented the lowest CTOD values of their categories (constraint and orientation conditions) showing a more detrimental effect of Nb-rich than of oxide inclusions, as shown in Fig. 4.8(b). Hence, cleavage initiation from Nb-rich inclusions represents the worst-case scenario. Note that the points without a scatter bar refer to initiation sites observed in only one specimen. Figure 4.9 shows an example of a fracture surface where an (Mg, Al, Ti)(O, C, N) inclusion was observed to be a cleavage initiation site in a high-constraint, top quarter, L-T specimen.

In specimens extracted from the middle section of the plate, initiation sites were identified for 9 fracture surfaces, 3 from high-constraint and 6 from low-constraint. The Nb-rich inclusions were observed to be responsible for triggering the fracture process in 78% of the identified cases (3 high-constraint and 4 low-constraint), even though oxides are the majority, 76% (Table 4.3). This is likely to be mainly attributed to the larger sizes and clustering of Nb-rich inclusions. These inclusions were found in the initiation site both single and distributed as clusters. Additionally, oxides were observed in 22% of the identified initiation sites (2 low-constraint) which had the highest CTOD values within their categories (constraint and orientation condition). Figure 4.10 shows an example of a fracture surface of a low-constraint, middle, T-L specimen where an Nb-inclusion can

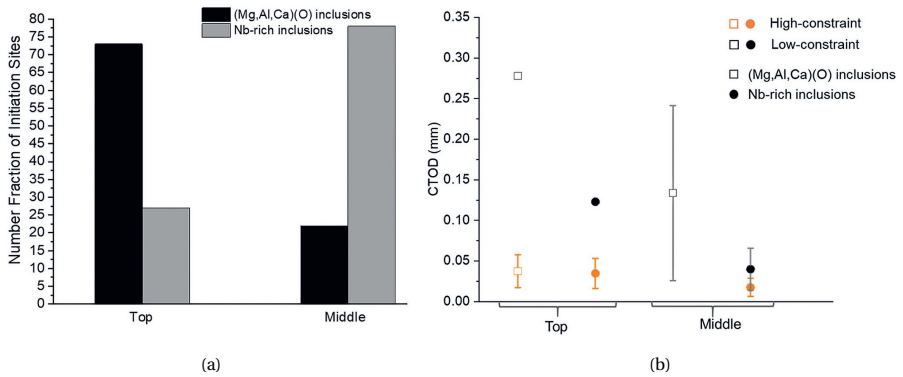


Figure 4.8: Summary of the fracture surface analysis and CTOD tests showing the (a) number fraction of each type of initiation sites that were observed in specimens from the top and middle section, with no distinction between T-L and L-T, and high- and low-constraint specimens and (b) the CTOD values for high- and low-constraint specimens (represented in orange and black colours, respectively) varying the type of initiation site. The points without a scatter bar refer to initiation sites observed in only one specimen.

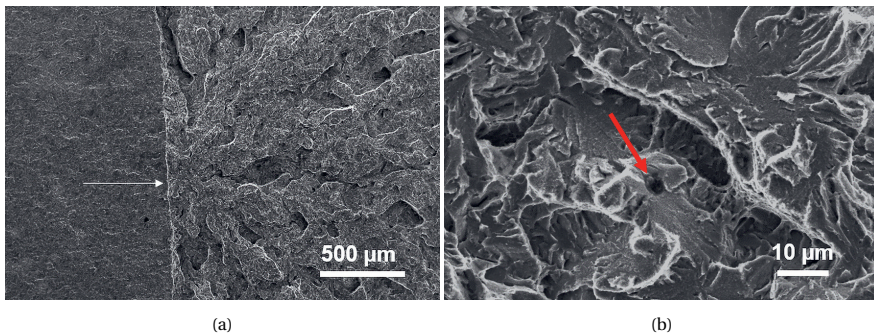


Figure 4.9: SEM micrographs showing (a) river lines and a white arrow indicating the cleavage initiation site in high-constraint, top, L-T specimen fractured at -100°C with CTOD equal to 0.01 mm and (b) an (Mg, Al,Ti)(O, C, N) inclusion (indicated by the red arrow) as a likely initiation site.

be recognised as a cleavage initiator.

The detrimental effect of Nb-rich inclusions can be explained by the microstructural observations reported by Bertolo et al. [11] for this S690QL steel. First, compared to the oxide inclusions, Nb-rich inclusions tend to be larger and distributed in clusters. When distributed as clusters, Nb-rich inclusions may be considered as a single larger inclusion due to their proximity, through which the cluster, represents an easy propagation path. As both inclusion types were observed acting as crack initiators, it indicates that the initial crack length in the fracture process is the size of these inclusions. According to Griffith's theory [38], the larger the crack, the lower the fracture stress. Hence, Nb-rich inclusions represent the weakest microstructural link for fracture. Lastly, cubic-shaped inclusions, as a result of their sharp edges, present larger residual stresses in the interface with the steel matrix originated from the steel processing and act as stress concentrators,

raising stress more effectively than circular inclusions [39]. Along with the intrinsic detrimental effect of Nb-rich inclusions, the pre-existence of cracks in the inclusions themselves and in the interface inclusion/matrix, most often for the Nb-rich inclusions, may also explain the lower fracture toughness in the middle section. Nucleation in a hard particle and the unstable crack propagation across the particle/matrix interface and the matrix are the steps of cleavage fracture [3]. However, the existing crack associated with these inclusions may serve as a Griffith crack. Hence, the crack propagation into the matrix is the only likely remaining stage in the fracture process in the middle section, while in the top section, both nucleation and propagation are necessary for fracture to occur.

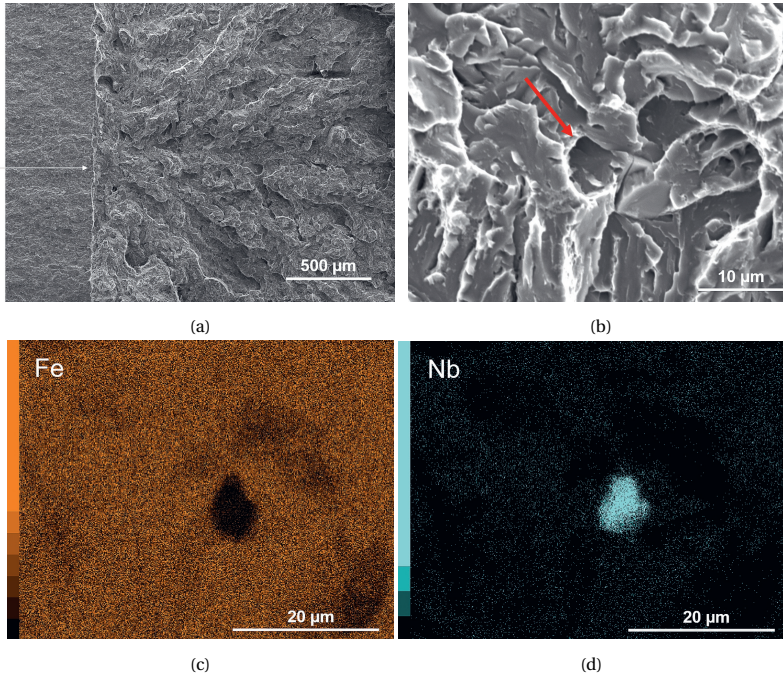


Figure 4.10: SEM micrographs and EDS mapping showing (a) river lines and a white arrow indicating the cleavage initiation site in low-constraint, middle, T-L specimen fractured at -100°C with CTOD equal to 0.015 mm and (b) an Nb-rich inclusion (indicated by the red arrow) located in the cleavage initiation site (c) and (d) EDS mapping of Fig. 4.10(b) showing Fe and Nb maps, respectively, for the matrix and Nb-rich inclusion.

4.3.3. MICROSTRUCTURAL FACTORS AFFECTING CLEAVAGE CRACK PROPAGATION

In general, cleavage crack propagation mode is transgranular and is governed by crystallographic microstructural characteristics [3, 40–42]. For instance, the cleavage crack path is affected by high-angle grain boundaries (e.g., prior austenite, packet, and block boundaries) and cracks preferentially propagate through planes with the lowest surface

energy, $\{001\}$ and $\{011\}$ [42]. According to Morris [40], in cleavage fracture, the laths inside a block share the same cleavage plane and cleavage as a unit. This is expected as lath boundaries are low-angle grain boundaries and, therefore, not able to deflect the crack. Therefore, laths are ineffective in deflecting or hindering a cleavage crack and are not the focus of this work. Furthermore, the complex crystallographic structure of lath martensite and lath bainite is observed to influence the local changes in the crack path [40, 41, 43]. Hence, the transverse section of CTOD fracture surfaces was analysed by EBSD to investigate the correlation between crack propagation path and microstructural crystallographic features, and, therefore, establish the mechanism of failure of the S690QL high strength steel. Figures 4.11 and 4.12 show the inverse pole figures (IPF), kernel average misorientation (KAM) maps of the fracture surface profile, and individual prior austenite grains involved in the propagation process for the specimens extracted from the top and middle thickness position in T-L orientation, respectively.

It can be seen that the cleavage crack propagation micromechanism is transgranular, where the crack propagates through the PAGs. Along the propagation path, it is clear that the IPF presents dense zones of poorly indexed points. As a dislocation-pileup-driven process, cleavage is preceded by microplasticity [3]. Hence, the poorly indexed points might be associated with plastic deformation during the fracture process. The KAM, obtained via EBSD data, is a measure of the average misorientation angle between a central point and all points at the perimeter (its neighbours) and it has been reported to be dependent on the geometrically necessary dislocations (GND) density [44]. Consequently, it is frequently used as a measure of plastic deformation. Figures 4.11 (b) and 4.12 (b) are KAM maps for the 3rd neighbour. By comparing the IPF and KAM maps (Fig. 4.11 (a) with 4.11 (b) and 4.12 (a) with 4.12 (b)), it can be seen that the KAM areas with maximum misorientation (red) match with the IPF areas with poor indexation. Thus, plastic deformation is involved in the cleavage fracture process leading to a significant density of dislocations and, consequently, to a poor indexation of points in EBSD maps in the sub-surface of the fracture plane. Nevertheless, these specific areas do not provide accurate and reliable data for analysis of the propagation micromechanism and, consequently, are not considered in further discussion.

The 3D crystal lattice cubes in Fig. 4.11 (a) and 4.12 (a) indicate the crystal orientations of the grain sub-structures directly below the fracture surface. Green, red and blue circles are used to respectively highlight when $\{100\}$, $\{110\}$, and $\{310\}$ plane traces under the fracture surface are aligned parallel (tolerance misorientation of 10°) to the fracture plane. For almost the entire analysed length (around 95%) of the fracture surface, the cleavage crack propagates through the $\{100\}$ and $\{110\}$ planes in the top and middle sections, where both families of planes have a similar contribution. Less than 10% of the cleavage planes seem to be aligned to the $\{310\}$ planes, also observed to be involved in the cleavage process of other bcc steel [45]. Hence, the most favourable cleavage planes in the S690QL steel under study are the $\{110\}$ and $\{001\}$ planes.

The contribution of crystallographic grain structures in crack propagation is also acknowledged in the literature [40, 41, 46]. However, there is no consensus on cleavage crack propagation mechanisms across PAG in tempered lath martensite and lath bainite. Ideally, in lath microstructures, individual PAG are divided into four distinguishable packets that share the same planes of the parent austenite. In other words, have

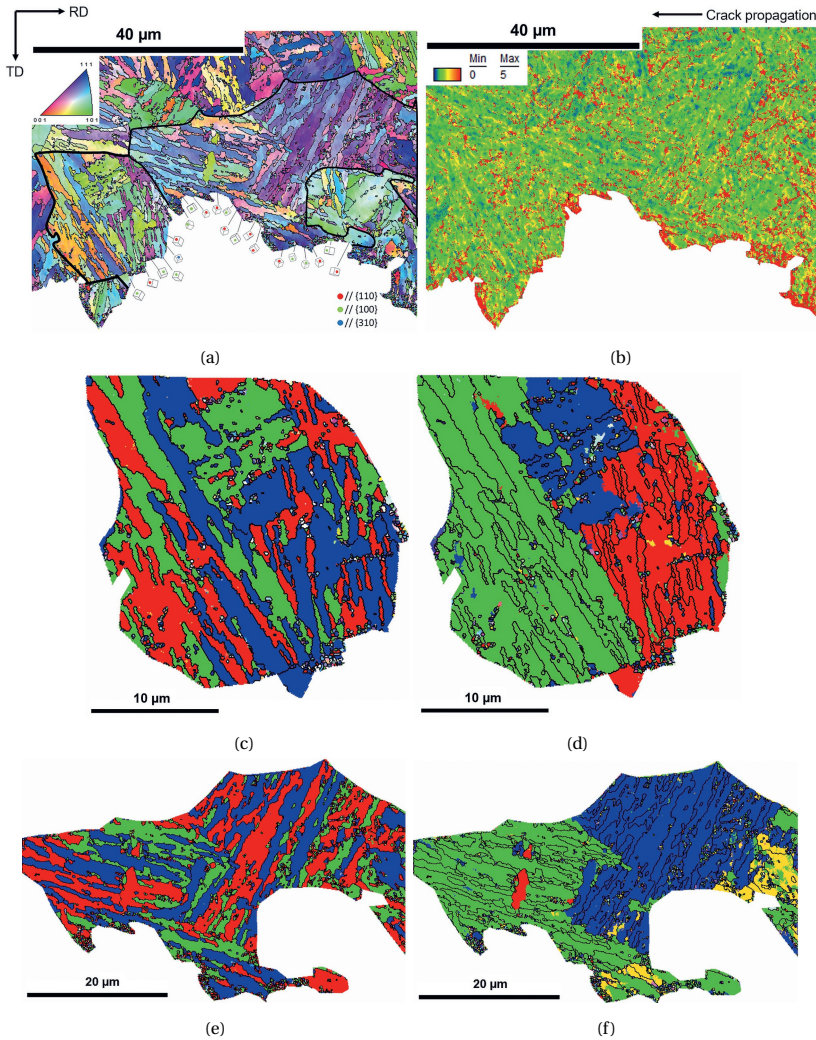


Figure 4.11: Fractographic profile of a CTOD specimen extracted from the top, high-constraint, T-L presented as (a) Inverse Pole Figure, (b) Kernel Average Misorientation map, (c) and (d) are an individual PAG located at the left-hand side of (a), and (e) and (f) an individual PAG located at the right-hand side of (a). The colours in (c) and (e) represent different Bain variants, while the colours in (d) and (f) represent the different K-S variants). Thin black lines are high-angle ($>15^\circ$) grain boundaries and the thick black contour in (a) is the PAG boundary.

the same Kurdjumov-Sachs (K-S) variant (according to Bertolo et al. [11], this steel has a K-S crystallographic relation to the parent austenite). Each packet is composed of three blocks of different Bain variants [40]. Hence, Bain (Fig. 4.11 and 4.12 (c) and (e)) and K-S (Fig. 4.11 and 4.12 (d) and (f)) variant maps were generated for individual PAG grains of top and middle sections, where different colours correspond to different Bain or K-S

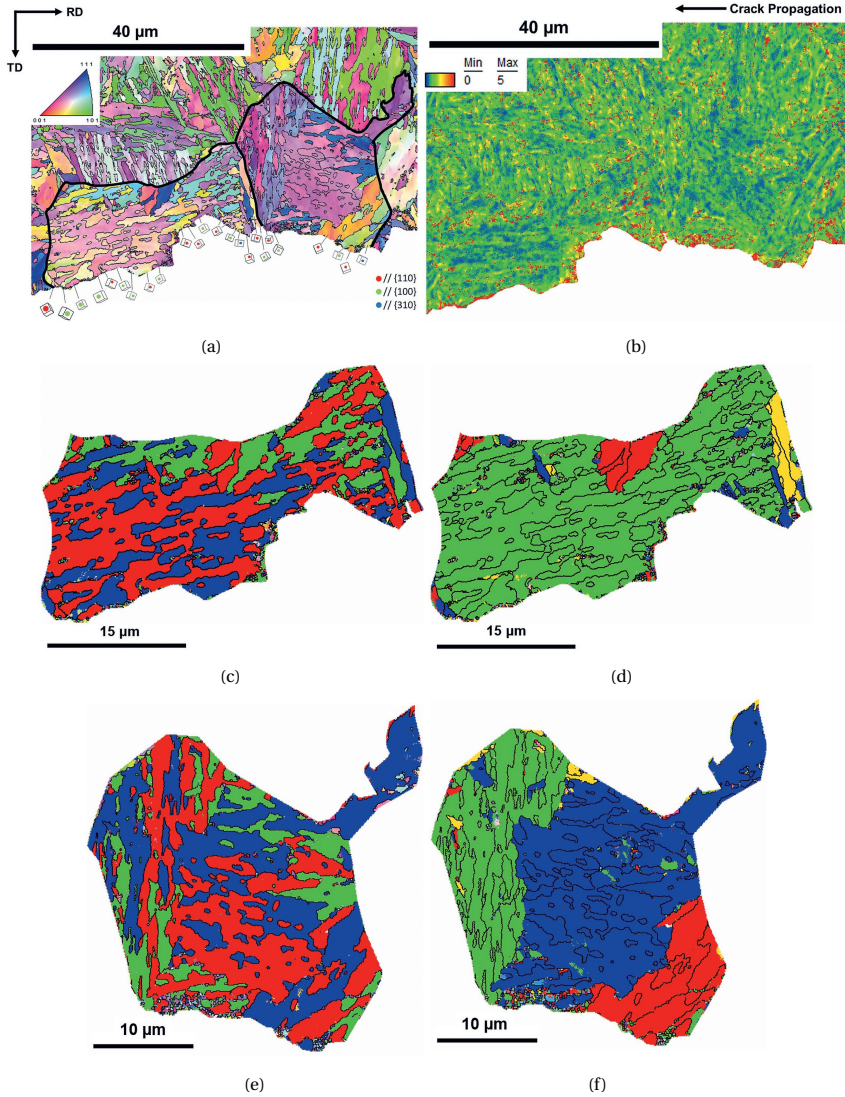


Figure 4.12: Fractographic profile of a CTOD specimen extracted from the middle, high-constraint, T-L presented as (a) Inverse Pole Figure, (b) Kernel Average Misorientation map, (c) and (d) are an individual PAG located at the left-hand side of (a), and (e) and (f) an individual PAG located at the right-hand side of (a). The colours in (c) and (e) represent different Bain variants, while the colours in (d) and (f) represent the different K-S variants). Thin black lines are high-angle ($>15^\circ$) grain boundaries and the thick black contour in (a) is the PAG boundary.

groups. In general, it can be seen that the PAG grains follow the previously explained ideal hierarchical lath structure: each PAG has four packets and each of them has three Bain variants. In the cases where there are not four packets, it can be the case that another packet is part of the other half of the fracture surface. When the packet does not

contain three Bain variants, it might be that the packet is relatively small. In both top and middle thickness positions, the crack is observed to significantly deflect from its path in PAG, packets, and block boundaries mostly where the neighbouring sub-structure has a different Bain axis. However, in a few boundaries with different Bain axis of the middle section, only slight deflections were observed. This could be attributed to the thickness of the Bain area, as also observed by Wang et al. [41]. It is also important to mention that some areas could not be analysed as only a small remaining part of the other specimen's half was present not leading to a clear and reliable conclusion. Thus, the investigation of the transverse section of the fracture surfaces shows that despite the differences/classification of sub-structures into PAG, packets, and block boundaries, the Bain zone is the effective crystallographic microstructural characteristic in deflecting the cleavage crack. This is in agreement with what was found for heat affected zones of an offshore engineering steel tested by Charpy [41].

Although one of the characteristics of cleavage fracture is the transgranular mode, 36% of the studied fracture surfaces presented zones of intergranular fracture. The intergranular fracture was observed locally in some samples, while in others these regions extended over a significant part of the fracture surface. Figure 4.13 shows SEM micrographs of a fracture surface with extensive intergranular fracture and EDS maps along this area. It should be noted that this extensive intergranular fracture region does not start from the initiation site, which is shown in the insert image 1 of Fig. 4.13. Hence, the intergranular fracture is mainly affecting the propagation micromechanism. In image 1, it is possible to observe the presence of cleavage facets and Nb-rich inclusions, responsible for triggering fracture. Ahead of this area, in image 2, the region of intergranular fracture begins, which resembles a corridor-like path composed of smooth facets that are arranged in a straight line, in the presence of Nb-rich inclusions. From this area, it is possible to observe the presence of several Nb-rich inclusions decorating the grain boundaries which are directly related to the grain boundary embrittlement and lead to unexpected intergranular fracture.

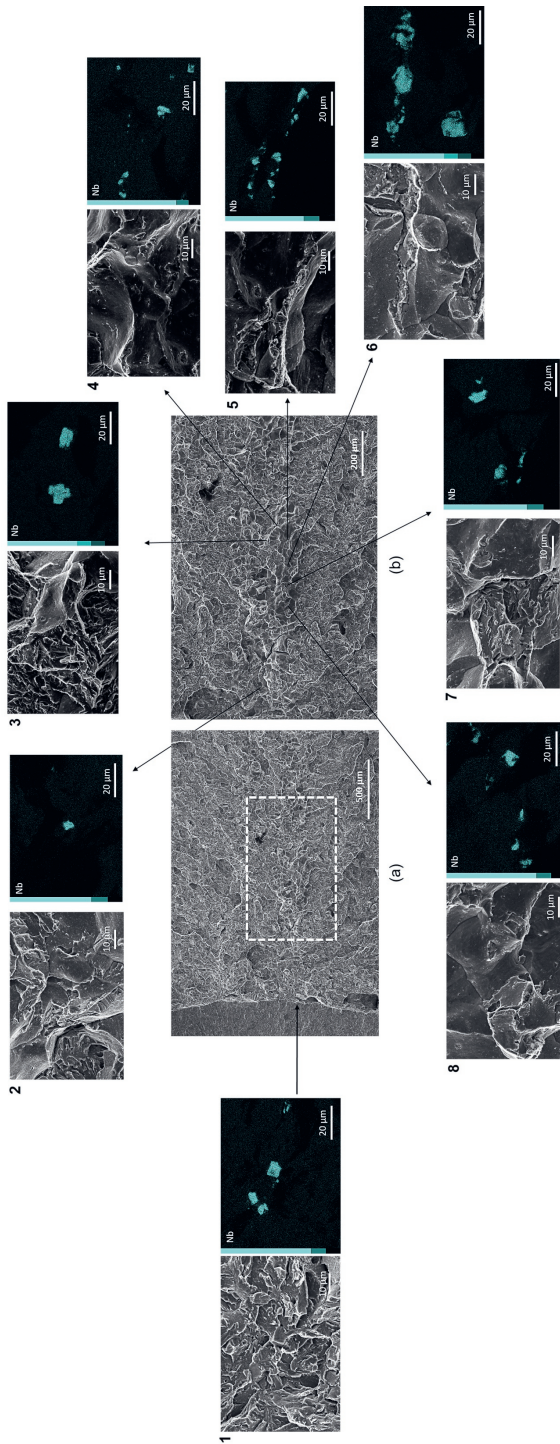


Figure 4.13: SEM micrographs of the fracture surface in a low-constraint, middle, T-L specimen fractured at -100°C with CTOD equal to 0.03 mm showing (a) river lines indicating the cleavage initiation site and a linear zone of intergranular fracture (inside the dashed rectangle) and (b) higher-magnification image of the area highlighted by the white rectangle in (a). SEM images and Nb EDS maps numbered from 1 to 8 show, in greater magnification, areas of (a) and (b) such as the cleavage initiation site and areas along the line of intergranular fracture where Nb-rich inclusions were observed.

Like in the specimen analysed in Fig. 4.13, some other samples showed characteristics of intergranular fracture where Nb-rich inclusions were not present or distributed throughout the region along PAG boundaries. It means that, in some regions, the intergranular fracture was not associated with these particles. Therefore, it may be that there is an additional microstructural contribution to the grain boundary embrittlement in the central part of the plate, such as the segregation of alloying elements.

For several years, researchers have been studying the effect of alloying segregation in the boundaries of PAG. Many authors report that, along with the inclusions and precipitates, the segregation of elements along the PAG boundaries can reduce the boundary cohesion, embrittling them and, consequently, making them prone to intergranular fracture [33, 47]. This segregation can take place during casting, which gives rise to segregation bands in the centre of steel plates. Elements such as Mo, C, Mn, Cr, Si, Ni were observed to segregate in the middle section of the S690QL steel studied herein, and their content was quantified by EPMA [11]. P is acknowledged as a significant embrittling element in steel, especially if Si and Mn, which are often responsible for reducing the cohesion of grain boundaries, are present in high content [35, 48, 49]. Unfortunately, the degree of segregation of P in the segregation bands cannot be analysed by EPMA due to the low P concentration in the S690QL steel (0.009 wt.%), as the EPMA detection limit is equal to 0.1 wt.%. However, the segregation of P should not be ruled out. Mn and Si were also observed to segregate in the bands of the middle section and are highly likely elements responsible for embrittling the PAG boundaries. Thus, for a more precise and detailed understanding of the grain boundary embrittlement due to the alloying segregation, Auger Electron Spectroscopy analyses (AES) are required. AES is the most used technique in the study of element segregation in the grain boundaries on fracture surfaces [50, 51].

Figure 4.14 shows an SEM micrograph of a large region, including areas 3, 4, 5, and 6 of Fig. 4.13, that fractured in an intergranular manner in a CTOD specimen from the middle section. The location of Nb-rich inclusions in these areas is also shown. The line scan results via AES are presented in Fig. 4.15. An intergranular fracture surface is known for its shiny and flat surface, and straight edges of the grain (grain boundaries). As prior austenite grains have different orientations, the facets aligned in different angles to the normal direction make the grain boundaries distinguishable from the SEM image and they can be located along the Auger line scan. The great majority of the peaks of all elements are located in the prior austenite grain boundaries present in the intergranular areas. Hence, these boundaries are enriched with C, Cr, Mn, Mo, Si, P, and Ni. However, the elemental spectrum shows that part of the line scans that cross transgranular areas also shows peaks of the previously mentioned elements. This observation suggests that the degree of grain boundary segregation may be not sufficient in certain areas to individually cause grain boundary embrittlement and lead the crack to propagate through the grain boundaries. These areas are probably located in the segregation bands due to the presence of the main segregated elements according to the EPMA analysis [11]. One possible explanation for this behaviour is a competition between elements that increase the grain boundary cohesion, such as C, and elements that reduce the grain boundary cohesion, such as Mn, and P [33, 52]. Therefore, the presence of Nb-rich inclusions decorating the PAG boundaries is a necessary condition to sufficiently weaken the grain

boundaries for the intergranular fracture to occur in areas where the grain boundaries are not sufficiently weakened by the elemental segregation.

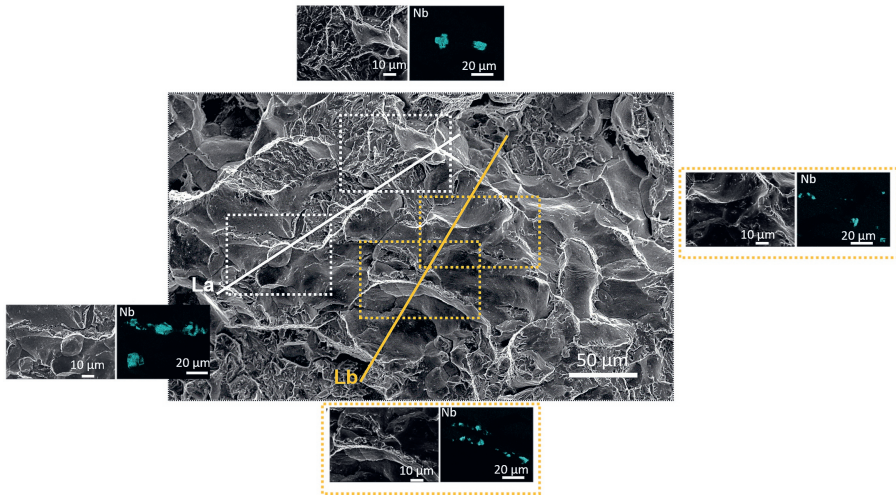


Figure 4.14: SEM micrographs showing the line scans, La and Lb, measured by SAM as well as the locations of Nb-rich inclusions along this selected intergranular fracture area.

4.3.4. CONCLUSIONS

The studied thick-section S690QL high strength steel presents through-thickness microstructural variations. In general, larger size and area fraction of inclusions as well as larger PAG sizes are found in the middle section compared to the top. Additionally, Nb-rich cubic inclusions, observed in higher densities in the middle section, are often distributed as clusters and may be found decorating the PAG boundaries. These inclusions are associated with defects such as cracks in the inclusions themselves and voids at the inclusion/matrix interface. Hence, to identify the weak microstructural links, an investigation on the microstructural contribution to cleavage fracture initiation and propagation micromechanisms has been carried out on thick-section high strength S690QL steel. Furthermore, the effect of notch orientation, through-thickness location, and crack tip constraint on fracture toughness was analysed. The following key conclusions can be drawn from this study:

1. Large Nb-rich inclusions, some of which are distributed as clusters, act as weak microstructural links in the studied S690QL high strength steel. For the middle section, Nb-rich inclusions are found to initiate fracture in 78% of specimens and are responsible for the worse cleavage fracture performance. For the top section, (Mg,Al,Ca)(O,S) inclusions trigger fracture in 73% of the specimens and the rest is attributed to Nb-rich inclusions. In both top and middle sections, the highest CTOD values were associated with fracture process initiated by oxide inclusions, while the lowest CTOD values were mainly found to be related to the fracture pro-

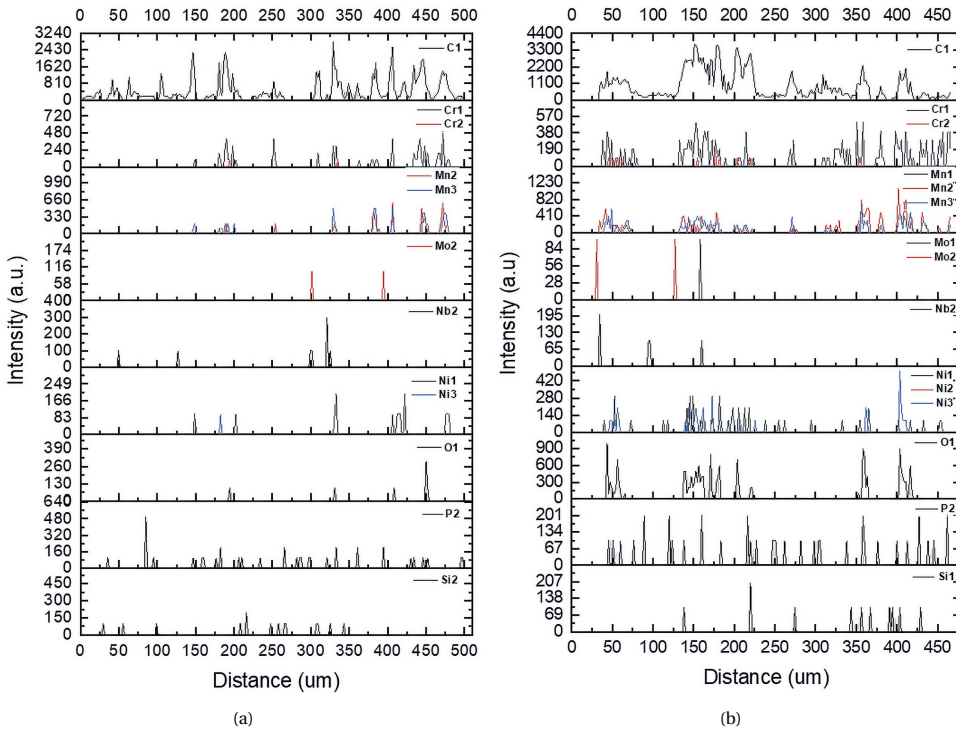


Figure 4.15: Elemental spectrum results from the Scanning Auger Microprobe line scan analysis for (a) line a and (b) line b identified in Fig. 4.14.

- cess initiated from Nb-rich inclusions. This confirms the detrimental effect of the Nb-rich particles.
- The pre-existing cracks in the Nb-rich inclusions themselves and/or in their interface with the matrix may serve as Griffith cracks. In this case, the crack propagation from the inclusion into the matrix is the dominant fracture step in the middle section, also contributing to lower fracture toughness.
 - Very detrimental microstructural features are observed to influence the material's fracture response to plastic constraint, also affecting the fracture micromechanisms. Contrary to the expected increase of fracture toughness with the reduction of plastic constraint (lower a/W) as observed for the top section, the CTOD values of shallow-cracked specimens extracted from the middle section remained very low. Due to the significant detrimental effect of Nb-rich inclusions, T_0 is -41°C for the middle and -101°C for the top. In other words, the middle section is near or at the lower shelf area of the ductile-to-brittle transition, while the top section is around the transition region. In this case, less plasticity is involved in fracture process of the middle section and the influence of the constraint in the fracture toughness is much lower than for the top section. Hence, in embrittled microstructures,

where plasticity is limited, the low constraint at the crack tip has no considerable contribution to fracture toughness.

4. Although fracture is predominantly transgranular, 36% of specimens showed areas of intergranular fracture affecting the propagation step. PAG boundaries in intergranularly fractured areas were found to be enriched with elements such as C, Cr, Mn, Ni, and P. However, these elements were also measured in the transgranular areas located around the intergranular ones. This may suggest that, in areas where the elemental segregation at PAG boundaries is not sufficient to embrittle the grain boundaries, the presence of Nb-rich inclusions decorating the PAG boundaries is a necessary and most likely a sufficient condition to weaken the grain boundaries, leading to intergranular fracture.
5. Fractographic profile investigation showed that the transgranular fracture for the material under study occurred in the most favourable cleavage planes $\{001\}$ and $\{110\}$. It was also observed that some plastic deformation took place in the cleavage fracture process, resulting in poor indexation of points in the EBSD maps due to the considerable dislocation density. These areas could not be properly analysed as they do not provide accurate data. The crack was observed to be significantly deflected at high-angle grain boundaries, prior austenite grain, packet, and block boundaries, mostly where the neighbouring sub-structure presents a different Bain axis.

This work provides new knowledge on the effect of microstructural and experimental factors on fracture toughness and cleavage micromechanisms in a thick-section quenched and tempered S690 high strength steel. The results obtained in this study will contribute to modelling predictions and control of structural failure as well as provide insights on microstructural design optimisation of thick-section steels assuring structural reliability to cleavage fracture. Future work will be focused on investigating the simulated coarse grained and intercritically reheated coarse grained heat affected zones in this S690QL high strength steel. This work is aimed at gaining fundamental understanding of the most detrimental cleavage micromechanisms in welded structures.

REFERENCES

- [1] Taylor, J., Mehmanparast, A., Kulka, R., Moore, P., Xu, L., & Farrahi, G. H. (2020). Experimental study of the relationship between fracture initiation toughness and brittle crack arrest toughness predicted from small-scale testing. *Theoretical and Applied Fracture Mechanics*, 110, 102799. <https://doi.org/10.1016/J.TAFMEC.2020.102799>
- [2] Burdekin, F. M., Zhao, W., Tkach, Y., Wiesner, C., & Xu, W. (2004). *The effects of dynamic loading on structural integrity assessments - Health & Executive Research Report 208* (tech. rep.). Health & Safety Executive.
- [3] Chen, J. H., & Cao, R. (2015). *Micromechanism of Cleavage Fracture of Metals*. Butterworth-Heinemann. <https://doi.org/10.1016/B978-0-12-800765-5.00003-4>
- [4] Morris Jr., J. W. (1993). *Steels: For low temperature applications* (H. D. McPherson, Ed.). Pergamon Press.
- [5] Liu, H., Zhang, H., & Li, J. (2018). Thickness Dependence of Toughness in Ultra-Heavy Low-Alloyed Steel Plate after Quenching and Tempering. *Metals*, 8(628), 1–11. <https://doi.org/10.3390/met8080628>
- [6] Popovich, V., & Richardson, I. M. (2015). Fracture Toughness of Welded Thick Section High Strength Steels. *TMS 2015 144th Annual Meeting & Exhibition: Supplemental Proceedings*, 1031–1038. <https://doi.org/10.1002/9781119093466.ch125>
- [7] Joo, M. S., Suh, D. W., Bae, J. H., Sanchez Mouriño, N., Petrov, R., Kestens, L. A., & Bhadeshia, H. K. (2012). Experiments to separate the effect of texture on anisotropy of pipeline steel. *Materials Science and Engineering: A*, 556, 601–606. <https://doi.org/10.1016/J.MSEA.2012.07.033>
- [8] Xu, J., & Fan, Y. (2011). Effects of temperature and crack tip constraint on cleavage fracture toughness in the weld thermal simulated X80 pipeline steels. *Advanced Materials Research*, 197–198, 1595–1598. <https://doi.org/10.4028/www.scientific.net/AMR.197-198.1595>
- [9] Matsoukas, G., Cotterell, B., & Mai, Y. W. (1986). Hydrostatic stress and crack opening displacement in three-point bend specimens with shallow cracks. *Journal of the Mechanics and Physics of Solids*, 34(5), 499–510. [https://doi.org/10.1016/0022-5096\(86\)90014-1](https://doi.org/10.1016/0022-5096(86)90014-1)
- [10] Sorem, W. A., Dodds, R. H., & Rolfe, S. T. (1990). An analytical comparison of short crack and deep crack CTOD fracture specimens of an A36 steel. *ASTM Special Technical Publication*, (1074), 3–23. <https://doi.org/10.1520/stp18986s>
- [11] Bertolo, V., Jiang, Q., Scholl, S., Petrov, R., Hangen, U., Walters, C., Sietsma, J., & Popovich, V. (2022). A Comprehensive Quantitative Characterisation of the Multiphase Microstructure of a Thick-Section High Strength Steel. *Journal of Materials Science*, 57, 7101–7126. <https://doi.org/https://doi.org/10.1007/s10853-022-07121-y>
- [12] Wang, Q., Ye, Q., Wang, Z., Kan, L., & Wang, H. (2020). Thickness Effect on Microstructure, Strength, and Toughness of a Quenched and Tempered 178 mm Thickness Steel Plate. *Metals*, 10(5), 1–16. <https://doi.org/10.3390/met10050572>
- [13] Pallaspuuro, S., Mehtonen, S., Kömi, J., Zhang, Z., & Porter, D. (2019). Effects of local grain size and inclusions on the low-temperature toughness of low-carbon

- as-quenched martensite. *Materials Science & Engineering A*, 743, 611–622. <https://doi.org/10.1016/j.msea.2018.11.105>
- [14] Moore, P., Yordanova, B., Lu, Y., & Janin, Y. J. (2019). Influence of microstructural variation in thick section steels on the characterisation of fracture toughness using sub-size specimens. *Proceedings of the ASME 2019 38th International Conference on Ocean, Offshore and Arctic Engineering OMAE 2019*. <https://doi.org/10.1115/OMAE2019-96010>
- [15] Lin, T., Evans, A. G., & Ritchie, R. O. (1986). A statistical model of brittle fracture by transgranular cleavage. *Journal of the Mechanics and Physics of Solids*, 34(5), 477–497. [https://doi.org/10.1016/0022-5096\(86\)90013-X](https://doi.org/10.1016/0022-5096(86)90013-X)
- [16] Martín-Meizoso, A., Ocaña-Arizcorreta, I., Gil-Sevillano, J., & Fuentes-Pérez, M. (1994). Modelling cleavage fracture of bainitic steels. *Acta Metallurgica et Materialia*, 42(6), 2057–2068. [https://doi.org/10.1016/0956-7151\(94\)90031-0](https://doi.org/10.1016/0956-7151(94)90031-0)
- [17] Chen, J. H., Li, G., Cao, R., & Fang, X. Y. (2010). Micromechanism of cleavage fracture at the lower shelf transition temperatures of a C – Mn steel. *Materials Science & Engineering A*, 527, 5044–5054. <https://doi.org/10.1016/j.msea.2010.04.063>
- [18] Kroon, M., & Faleskog, J. (2005). Micromechanics of cleavage fracture initiation in ferritic steels by carbide cracking. *Journal of the Mechanics and Physics of Solids*, 53(1), 171–196. <https://doi.org/10.1016/J.JMPS.2004.05.008>
- [19] Wallin, K., Nevasmaa, P., Laukkanen, A., & Planman, T. (2004). Master Curve analysis of inhomogeneous ferritic steels. *Engineering Fracture Mechanics*, 71(16-17), 2329–2346. <https://doi.org/10.1016/J.ENGFRACMECH.2004.01.010>
- [20] Andrieu, A., Pineau, A., Besson, J., Ryckelynck, D., & Bouaziz, O. (2012). Bimodal Beremin-type model for brittle fracture of inhomogeneous ferritic steels: Theory and applications. *Engineering Fracture Mechanics*, 95, 84–101. <https://doi.org/10.1016/j.engfracmech.2011.10.016>
- [21] ISO. (2018). ISO 12135: Metallic materials - Unified method of test for the determination of quasistatic fracture toughness. 2016.
- [22] ASTM International. (2020). *E1820: Standard Test Method for Measurement of Fracture Toughness* (tech. rep.). <https://doi.org/10.1520/E1820-20B>
- [23] Kyada, T., Shant, J. R., Goyal, R. K., & Kathayat, T. S. (2014). Understanding the Delamination and Its Effect on Charpy Impact Energy in Thick Wall Linepipe Steel. *Journal of Materials and Metallurgical Engineering*, 4(1), 31–39.
- [24] Ruggieri, C. (2010). A micromechanics approach to assess effects of constraint on cleavage fracture toughness: A weibull stress model. *Journal of the Brazilian Society of Mechanical Sciences and Engineering*, 32(4), 475–488. <https://doi.org/10.1590/S1678-58782010000400010>
- [25] Francois, D., & Pineau, A. (2001). Fracture of Metals Part I : Cleavage Fracture. In E. Bouchaud, D. Jeulin, C. Prioul, & S. Roux (Eds.), *Physical aspects of fracture* (pp. 15–33). Kluwer Academic. <https://doi.org/https://doi.org/10.1007/978-94-010-0656-9>
- [26] Sorem, W. A., Dodds, R. H., & Rolfe, S. T. (1991). Effects of crack depth on elastic-plastic fracture toughness. *International Journal of Fracture*, 47(2), 105–126. <https://doi.org/10.1007/BF00032572>

- [27] Smith, J., & Rolfe, S. (1994). The Effect of Crack Depth (a) and Crack Depth to Width Ratio (a/W) on the Fracture Toughness of A553-B Steel. *Journal of Pressure Vessel Technology*, 116:2, 115–121. <https://doi.org/https://doi.org/10.1115/1.2929564>
- [28] CEN. (2019). NEN-EN 10025-6: Hot rolled products of structural steels - Part 6: Technical delivery conditions for flat products of high yield strength structural steels in the quenched and tempered condition.
- [29] Bertolo, V. M., Jiang, Q., Walters, C. L., & Popovich, V. A. (2020). Effect of microstructure on cleavage fracture of thick-section quenched and tempered S690 high-strength steel. *Characterization of Minerals, Metals and Materials 2020*, 155–168. [https://doi.org/https://doi.org/10.1007/978-3-030-36628-5\(_ \)15](https://doi.org/https://doi.org/10.1007/978-3-030-36628-5(_)15)
- [30] Dawes, M. G., & Cho, G. (1992). Shallow Crack Fracture Mechanics Toughness Tests and Applications: First International Conference. Elsevier Science & Technology.
- [31] Rak, I. (2016). CTOD Toughness Evaluation of Hyperbaric Repair Welds Made Under Severe Conditions. *Structural Integrity and Life*, 16(3), 171–178.
- [32] Jiang, Q., Bertolo, V. M., Popovich, V. A., Sietsma, J., & Walters, C. L. (2022). Microstructure-informed statistical modelling of cleavage fracture in high strength steels considering through-thickness inhomogeneities. *Engineering Fracture Mechanics*, 267(108432). <https://doi.org/https://doi.org/10.1016/j.engfracmech.2022.108432>
- [33] Doig, P., Lonsdale, D., & Flewitt, P. E. J. (1982). Segregation of embrittling elements to prior austenite grain boundaries in 2 · 25Cr – 1 Mo steel. *Metal Science*, 16(7), 335–344. <https://doi.org/10.1179/030634582790427488>
- [34] Lemblé, P., Pineau, A., Castagne, J. L., Dumoulin, P., Lemble, P., Pineau, A., & Castagne, J. L. (1979). Temper embrittlement in 12 % Cr martensitic steel. *Metal Science*, 13(8), 496–502. <https://doi.org/10.1179/030634579790438381>
- [35] Nasim, M., Edwards, B. C., & Wilson, E. A. (2000). A study of grain boundary embrittlement in an Fe – 8 % Mn alloy. *Materials Science and Engineering A*, 281, 56–67. [https://doi.org/https://doi.org/10.1016/S0921-5093\(99\)00734-0](https://doi.org/https://doi.org/10.1016/S0921-5093(99)00734-0)
- [36] Walters, C. L., Voormeeren, L. O., Janssen, M., & Wallin, K. (2013). Validation of the acceptability of 10x20 mm specimens for fracture toughness determination of high-strength steels. *Proceedings of the ASME 2013 32nd International Conference on Ocean, Offshore and Arctic Engineering*, 1–9.
- [37] ASTM International. (n.d.). E1921-11a: Standard Test Method for Determination of Reference Temperature, T₀, for ferritic Steels in the Transition Range. *ASTM Book of Standards*. <https://doi.org/10.1520/E1921-05>
- [38] Griffith, A. A. (1920). The Phenomena of Rupture and Flow in Solids. *Philosophical Transactions of the Royal Society A: Mathematical, Physical and Engineering Sciences*, 100, 163–198.
- [39] Gu, C., Lian, J., Bao, Y., & Münstermann, S. (2019). Microstructure-based fatigue modelling with residual stresses : Prediction of the microcrack initiation around inclusions. *Materials Science & Engineering A*, 751, 133–141. <https://doi.org/10.1016/j.msea.2019.02.058>
- [40] Morris Jr, J. W., Kinney, C., Pytlewski, K., & Adachi, Y. (2013). Microstructure and cleavage in lath martensitic steels. *Science and Technology of Advanced Materials*, 14(014208), 1–9. <https://doi.org/10.1088/1468-6996/14/1/014208>

- [41] Wang, X., Wang, Z., Xie, Z., Ma, X., Subramanian, S., Shang, C., Li, X., & Wang, J. (2019). Combined effect of M/A constituent and grain boundary on the impact toughness of CGHAZ and ICCGAZ of E550 grade offshore engineering steel. *Mathematical Biosciences and Engineering*, 16(6), 7494–7509. <https://doi.org/10.3934/mbe.2019376>
- [42] Davies, P. A., & Randle, V. (2001). Combined application of electron backscatter diffraction and stereo-photogrammetry in fractography studies. *Journal of Microscopy*, 204(1), 29–38. <https://doi.org/10.1046/j.1365-2818.2001.00922.x>
- [43] Bhadeshia, H. K. (2001). *Bainite in Steels: Transformations, Microstructure and Properties* (2nd). IOM Communications.
- [44] Calcagnotto, M., Ponge, D., Demir, E., & Raabe, D. (2010). Orientation gradients and geometrically necessary dislocations in ultrafine grained dual-phase steels studied by 2D and 3D EBSD. *Materials Science and Engineering A*, 527(10–11), 2738–2746. <https://doi.org/10.1016/j.msea.2010.01.004>
- [45] Mohseni, P., Solberg, J. K., Karlsen, M., Akselsen, O. M., & Østby, E. (2013). Application of combined EBSD and 3D-SEM technique on crystallographic facet analysis of steel at low temperature. *Journal of Microscopy*, 251(1), 45–56. <https://doi.org/10.1111/jmi.12041>
- [46] Wang, C., Wang, M., Shi, J., Hui, W., & Dong, H. (2008). Effect of microstructural refinement on the toughness of low carbon martensitic steel. *Scripta Materialia*, 58(6), 492–495. <https://doi.org/10.1016/j.scriptamat.2007.10.053>
- [47] Seah, M. (1976). Segregation and the strength of grain boundaries. *Proceedings of the Royal Society A*, 349, 535–554.
- [48] Ding, R. G., Rong, T. S., & Knott, J. (2005). Grain boundary segregation of phosphorus and molybdenum in A533B steel. *Institute of Materials, Minerals and Mining*, 21(11), 1255–1260. <https://doi.org/10.1179/174328405X63953>
- [49] Archie, F., Li, X., & Zae, S. (2017). Micro-damage initiation in ferrite-martensite DP microstructures : A statistical characterization of crystallographic and chemical parameters. *Materials Science & Engineering A*, 701(June), 302–313. <https://doi.org/10.1016/j.msea.2017.06.094>
- [50] Menyhard, M., Jr, C. J. M., & Yoshioka, Y. (1987). A high resolution Auger electron spectroscopy study of the intergranular fracture of a temper embrittled steel. *Journal of Vacuum Science & Technology A*, 5(1158). <https://doi.org/10.1116/1.574626>
- [51] Papworth, A. J., & Williams, D. B. (2000). Segregation to prior austenite grain boundaries in low-alloy steels. *Scripta Materialia*, 42, 1107–1112. [https://doi.org/10.1016/S1359-6462\(00\)00335-3](https://doi.org/10.1016/S1359-6462(00)00335-3)
- [52] Messmer, R. P., & Briant, C. L. (1982). The role of chemical bonding in grain boundary embrittlement. *Acta Metallurgica*, 30(2), 457–467. [https://doi.org/10.1016/0001-6160\(82\)90226-7](https://doi.org/10.1016/0001-6160(82)90226-7)

5

CLEAVAGE FRACTURE MICROMECHANISMS IN SIMULATED HEAT AFFECTED ZONES OF S690 HIGH STRENGTH STEELS

High strength steels are widely used for structural applications, where a combination of excellent strength and ductile-to-brittle transition (DBT) properties are required. However, such a combination of high strength and toughness can be deteriorated in the heat affected zone (HAZ) after welding. This work aims to develop a relationship between microstructure and cleavage fracture in the most brittle areas of welded S690 high strength structures: coarse-grained and intercritically reheated coarse-grained HAZ (CGHAZ and ICCGHAZ). Gleeble thermal simulations were performed to generate three microstructures: CGHAZ and ICCGHAZ at 750 and 800 °C intercritical peak temperatures. Their microstructures were characterised, and the tensile and fracture properties were investigated at -40 °C, where cleavage is dominant. Results show that despite the larger area fraction of martensite-austenite (M-A) constituents in ICCGHAZ 750 °C, the CGHAZ is the zone with the lowest fracture toughness. Although M-A constituents are responsible for triggering fracture, their small size (less than 1 µm) results in local stress that is insufficient for fracture. Crack propagation is found to be the crucial fracture step. Consequently, the harder auto-tempered matrix of CGHAZ leads to the lowest fracture toughness. The main crack propagates transgranularly, along {100} and {110} planes, and neither the necklace structure at prior austenite grain boundaries of ICCGHAZs nor M-A constituents are observed as preferential sites for crack growth. The fracture profile shows that prior austenite grain boundaries and other high-angle grain boundaries (e.g., packet and block) with different neighbouring Bain axes can effectively divert the cleavage crack. Moreover, M-A constituents with internal sub-structures, which have high kernel average misorientation and high-angle boundaries, are observed to deflect and arrest the secondary cracks. As a result, multiple pop-ins in load-displacement curves during bending tests are observed for the investigated HAZs.

This chapter is based on the scientific publication Bertolo, V., Jiang, Q., Terol Sanchez, M., Riemsлаг, T., Walters, C., Sietsma, J. & Popovich, V. (2023). Cleavage Fracture Micromechanisms in Simulated Heat Affected Zones of S690 High Strength Steels, *Materials Science and Engineering A*, 868, 144762. <https://doi.org/10.1016/j.msea.2023.144762>

5.1. INTRODUCTION

The balance between high strength and high fracture toughness required for structural applications, such as for components in heavy lifting equipment and wind farms, is found in high strength steels even at such low temperatures as -60°C (e.g., in the Arctic). However, this balance usually is compromised by welding processes used for connecting structural components. The welding thermal input modifies the base material microstructure and generates heat-affected zones (HAZ) with complex microstructures and potentially poor toughness. For single- and multi-pass welding – needed for thick-section steel plates –, the coarse-grained heat affected zone (CGHAZ) and the intercritically reheated coarse-grained heat affected zone (ICCGHAZ) are the areas with the lowest toughness as a consequence of preferential failure sites. Due to the formation of brittle zones, the ductile-to-brittle transition temperature of high strength steels is shifted as a result of welding from around -80°C to approximately -30°C , raising concern in terms of cleavage fracture [1].

Many authors [2–5] have reported that the degradation of fracture properties of CGHAZ and ICCGHAZ are related to the coarsening of austenite grains and the formation of martensite-austenite (M-A) constituents. Extensive investigation on the effect of different M-A parameters, such as size, volume fraction and morphology, on toughness, has also been carried out [6–10]. It is well established that the larger the size and volume fraction of M-A constituents, the lower the fracture toughness [6–8]. On the other hand, there is no consensus on the morphological effect of M-A constituents on toughness. The two most detrimental M-A morphologies are blocky (or massive) and slender (or elongated). While Bayraktar and Kaplan [6], Kumar and Nath [7], and Li and Baker [10] observed that the blocky M-A constituents are more detrimental than the slender ones, Kim et al. [8] and Luo et al. [9] have found that the slender M-A has a more negative impact than the blocky ones. Hence, the knowledge available in the literature regarding the morphological effect of M-A constituents on fracture toughness does not allow us to understand the cleavage behaviour and micromechanisms in CGHAZ and ICCGHAZ in high strength steels.

Furthermore, the effects of the microstructural features of the base material on the fracture toughness of HAZ are barely discussed in the literature. Although the discussions involving the degradation of the mechanical and fracture properties of HAZ are mostly related to M-A constituents, microstructural features in HAZ inherited from the base material, such as brittle inclusions, may also play a role. In previous work by the present authors [11], Nb-rich inclusions were recognised as the most deleterious microstructural feature of a base S690QL high strength steel. In general, Nb-rich inclusions have higher nanohardness than M-A constituents (in the range of 20 to 25 GPa and 4 to 11 GPa, respectively), which causes them to be more prone to fracture than M-A constituents [12–14]. Nevertheless, parameters such as size, area fraction and spatial distribution can also influence the criticality of the brittle particles, and it is currently unknown which of these features act as the weakest microstructural sites. Some authors [10, 15] analysed steels containing pre-existing carbides and brittle inclusions in the base material that could trigger the fracture process in HAZ. Li and Baker [10] analysed a V and Nb microalloyed steel in which, compared to M-A constituents, pre-existing

carbides and aluminium oxide inclusions did not have a significant impact on the toughness of ICCGHAZ. In this case, the carbides were present as thin particles and one order of magnitude smaller than M-A constituents, behaving as isolated particles and not having a major effect on toughness, while the number density of inclusions was quantified as significantly lower than the M-A density. In contrast, pre-existing TiN inclusions in an ultra-low carbon bainitic steel studied by Vassilaros [15] were observed to trigger cleavage fracture in the thermally simulated CGHAZ instead of M-A constituents. It is thus clear that no clear trend has been identified on the cleavage initiation micromechanism in welded steels with different types of brittle particles. Therefore, it needs to be further analysed in order to fully understand the cleavage micromechanisms involved in a multi-phase steel such as S690 high strength steel.

In the present study, thermal welding simulations via Gleeble were carried out to create large sections of CGHAZ and of ICCGHAZ with peak temperatures of 750 °C and 800 °C. The simulated microstructures were analysed and quantified using different techniques that include local chemical composition analysis, microscopy and hardness. The cleavage fracture toughness of the generated CGHAZ and ICCGHAZs was obtained through three-point bending tests at the lower shelf of their ductile-to-brittle transition curve. Afterward, the fracture surfaces and their cross-sections were analysed to investigate the cleavage initiation and propagation micromechanisms and identify the most critical microstructural features. Therefore, this work establishes the relationship between microstructure, fracture toughness and cleavage micromechanisms in the most critical HAZs of an S690 high strength steel. As a result, a microstructure-based failure criterion for the CGHAZ and ICCGHAZ is developed, allowing the prediction of their fracture behaviour at low-temperature applications concerning structural safety. Moreover, the comprehensive qualitative and quantitative microstructural and fracture data presented in this paper represents the required data for modelling the continuum-level properties of welded structures. Thus, this work can assist in the prediction of fracture behaviour of actual welded structures of high strength steels.

5.1.1. MATERIALS AND METHODS

The commercially available 80 mm thick quenched and tempered S690 high strength steel used in this study was previously comprehensively characterised in terms of microstructure and cleavage fracture behaviour [11, 16]. The mid-thickness of this steel plate was found to represent the lowest cleavage fracture toughness and, therefore, was chosen for further investigation of welded heat-affected zones. The chemical composition of the middle section of the S690QL high strength steel plate is given in Table 5.1. The content range of elements referred as “Other” are in accordance with the standard EN 10025-6 (maximum wt.% of Mn: 1.7, Ni: 4.0, Cr: 1.5, Nb: 0.06, P: 0.02, N: 0.015, S: 0.01, and B: 0.005) [17].

The microstructures of CGHAZ and ICCGHAZ were created via Gleeble-1500 thermo-mechanical simulator. The thermal profile to simulate the CGHAZ was experimentally obtained from an actual gas metal arc welding (GMAW) procedure with a heat input of 2.2 kJ/mm. First, the material is heated at 210 °C/s up to 1300 °C and held for 2 seconds. Subsequently, the material is cooled down at 25 °C/s from 1300 to 800 °C, 17 °C/s from

Table 5.1: Chemical composition of mid-thickness S690QL.

wt. (%)					
Fe	C	Si	Al	Mo	Other
Bal.	0.160 ± 0.001	0.30 ± 0.03	0.080 ± 0.011	0.29 ± 0.02	Mn, Ni, Cr, Nb, P, N, S, B

800 to 500 °C, and 6 °C/s to room temperature (Fig. 5.1 (a)). The same heating and cooling conditions were used for the subsequent thermal cycle of the ICCGHAZ at peak temperatures of 750 °C and 800 °C (Fig. 5.1 (b)). The temperatures of start (Ac_1) and finish (Ac_3) of austenite formation were determined by dilatometry as 750 °C and 910 °C, respectively, under the heating rate of 210 °C/s. These thermal profiles were used to perform Gleeble thermal treatments on samples for microstructural characterisation, tensile and fracture testing.

Samples for microstructural characterisation, 80 mm long – parallel to the rolling direction – with 6 mm diameter, were heat treated with the schedules of Fig. 5.1. Subsequently, the samples were prepared metallographically and etched with Nital 5% for microstructural analysis. Microstructures were observed via scanning electron microscopy (SEM), energy dispersive spectroscopy (EDS) and electron backscatter diffraction (EBSD). In order to accurately identify and quantify M-A constituents, EBSD analysis was used. EBSD data was acquired on a Helios G4 PFIB SEM using a current of 3.2 nA and accelerating voltage of 30 kV, a tilt angle of 70° using TEAM EDAX software, and was post-processed with EDAX-TSL-OIM Analysis™ v7 software. High and low magnifications were used for M-A characterisation and quantification (step size 0.025 µm) and for prior austenite grain size measurement (step size 1 µm), respectively. In the EBSD scans for the M-A study, the retained austenite was distinguished from the matrix by its FCC crystal structure, while martensite was identified by its clusters of randomly indexed points in the inverse pole figures (IPF) due to its low image quality (IQ), resultant from the high density of defects and the lattice distortion. In this case, the poor indexation is used to identify and quantify the M-A constituents. Therefore, no clean up procedure was performed. To quantify the M-A constituents, the first post-processing step for EBSD data is, for each analysed area, to generate a new data set with the points from the original data set that deviate more than 5° from their neighbours – the randomly indexed points. However, one should be aware that falsely indexed points from the uncertainties in the Kikuchi pattern may be present (e.g., overlapping patterns at grain boundaries) and may lead to inaccurate M-A identification and quantification. These two, randomly (from martensite) and falsely indexed points, can be distinguished by their image quality (IQ). While martensitic areas have lattice distortions and, consequently, low IQ, falsely indexed points do not have a low IQ. Then, points with high IQ were excluded. The threshold between low and high IQ was defined by comparing the grey-scale representation of IQ and the IPF. Afterwards, the maps with martensitic areas were overlapped with the phase maps, allowing for the quantification of M-A constituents. For the prior austenite grain (PAG) size measurement, the PAGs were reconstructed via ARPG software [18], in automatic mode using quadruplets with tolerance for parent grain nucleation and growth of 3° and 6°, respectively. The reconstructed data was post-processed in the TSL-OIM Analysis™ software v7 software

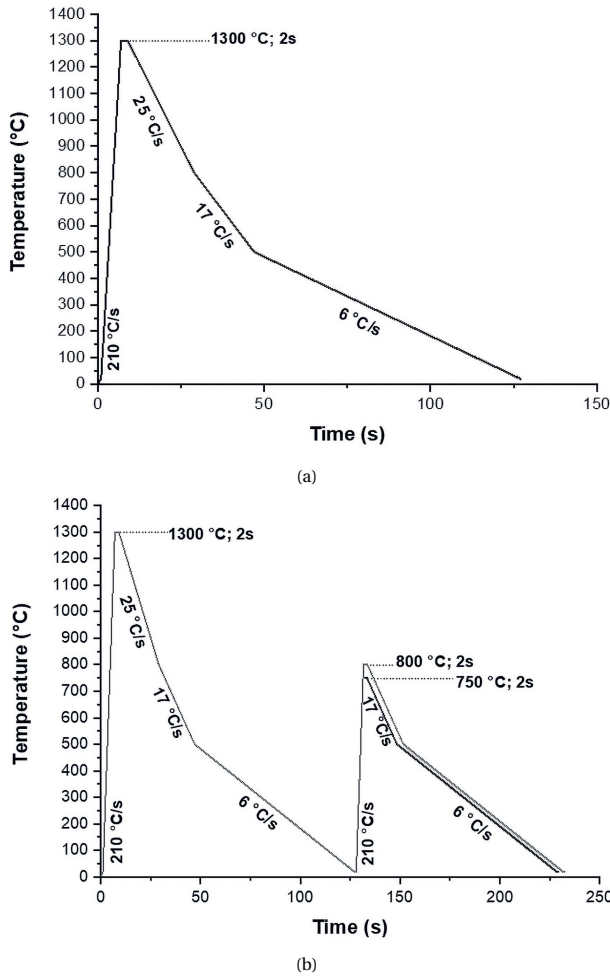


Figure 5.1: Gleeble thermal profiles for (a) CGHAZ and (b) ICCGAZ 750 °C and 800 °C.

where the distribution of minor (width) and major (length) axis was acquired and the weighted average grain dimensions were calculated.

To measure the chemical composition of segregation bands Electron Probe Micro Analysis (EPMA) with a JEOL JXA 8900R microprobe was used, with an electron beam with energy of 10 keV and beam current of 200 nA employing Wavelength Dispersive Spectrometry (WDS). The measurements were done through line scans along a 300 μm line in increments of 3 μm . The line scan initiates and ends at points located outside the investigated segregation band, and both points are chosen approximately 150 μm from the centre of the band. Micro-Vickers hardness measurements, loads of 3 kgf (30 N) and 0.025 kgf (0.25 N), were performed for the different studied HAZ, providing overall hardness and individual hardness of the most predominant phase present in each HAZ,

respectively.

Tensile specimens (Fig. 5.2) perpendicular to the rolling direction were heat treated, and a homogeneous simulated microstructure was obtained along 10 mm of the gauge length. Then, the cross section of the original tensile specimen was reduced by 50% (Fig. 5.2) to achieve the highest stress in this length and, consequently, ensure that the failure occurs within the simulated material. A set of three specimens per heat treatment were tested under a crosshead displacement of 0.2 mm/s and at room temperature using an Instron 100 kN tensile rig. Afterward, the properties were converted to $-40\text{ }^{\circ}\text{C}$ according to the BS7910:2013+A1:2015 standard [19].

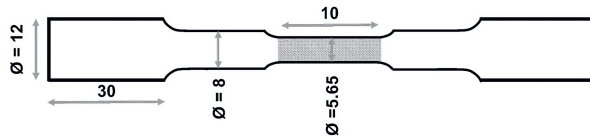


Figure 5.2: Tensile specimen of HAZs simulated material. The homogeneous heat-treated area is represented in grey. All dimensions are in mm.

The fracture toughness was assessed via three-point bending tests using sub-sized single edge-notched bending (SENB) specimens (Fig. 5.3). Between 5 to 10 SENB, T-L (crack propagation direction parallel to the rolling direction (RD)) specimens were heat treated via Gleeble resulting in a homogeneous microstructure along 5 mm of the specimen's centre. Next, the notch was machined by electrical discharge machining in the specimen's centre. The crack/width ratio (a/W) of all specimens is 0.5, and the tests were carried out according to ISO 12135 standard [20]. The crack tip opening displacement (CTOD) parameter was used in this study as a measure of toughness. As the scope of this project is to study cleavage fracture, it is of interest to perform the tests at a temperature below the lower transition region of the ductile-to-brittle transition. The tests were performed at $-40\text{ }^{\circ}\text{C}$, a temperature at which the cleavage fracture is dominant for all analysed simulated HAZ, by immersing the specimen in liquid nitrogen, at a displacement rate of 2 mm/s using a 350 kN MTS 858 servo-hydraulic test rig. During the test, the crack mouth opening displacement (CMOD) was measured by means of a clip gauge. Note that specimens were initially immersed in liquid nitrogen at $-196\text{ }^{\circ}\text{C}$ and then placed between the anvils of the hydraulic test machine, allowing it to warm up slowly, as monitored by a mounted thermocouple. At reaching the test temperature, the load application was triggered. Afterwards, to identify the microstructural features playing a role affecting cleavage initiation and propagation micromechanisms, the fracture surfaces were investigated via SEM/EDS and their transverse section by SEM and EBSD, respectively. Note that the analysed transverse section is near the initiation position and, therefore, the area with highest stress. Detailed information on the preparation of the transverse section of fracture surfaces for EBSD analysis is described in [16].

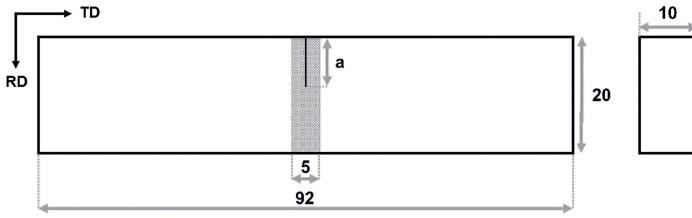


Figure 5.3: Dimensions of sub-sized SENB specimens used in fracture toughness tests. The 5 mm homogeneously heat treated region is represented in grey. All dimensions are in mm. RD stands for rolling direction and TD for transverse direction.

5.2. RESULTS

5.2.1. MICROSTRUCTURAL CHARACTERISATION OF HAZs

Figures 5.4, 5.5, and 5.6 show the microstructures of the simulated CGHAZ, ICCGHAZ 750 °C, and ICCGHAZ 800 °C, respectively. As can be seen, all investigated HAZs have a complex microstructure composed of a mixture of phases. The CGHAZ is composed of fresh martensite (M), auto-tempered martensite (ATM), and coalesced martensite [21] (indicated by white arrows). For both ICCGHAZ 750 °C and ICCGHAZ 800 °C, the microstructure includes fresh martensite (M), auto-tempered martensite (ATM), bainitic ferrite (BF), granular bainite (GB), and polygonal ferrite (PF). Furthermore, a necklace structure at the prior austenite grain (PAG) boundaries is observed in the ICCGHAZ 750 °C and 800 °C (Fig. 5.5(a) and Fig. 5.6(a)). The same structure is also often observed inside the PAG. From SEM investigation, this fine structure is characterised as being composed of auto-tempered martensite.

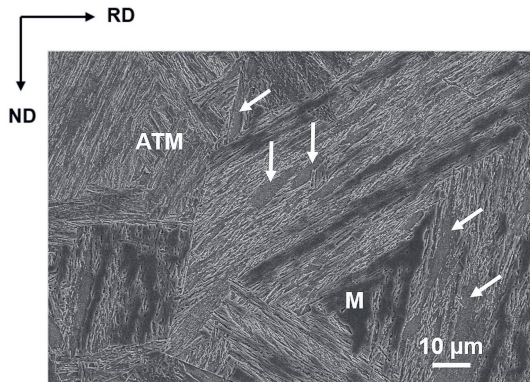


Figure 5.4: SEM micrographs of CGHAZ showing fresh martensite (M) and auto-tempered martensite (ATM). The white arrows indicate areas of coalesced martensite. ND stands for normal direction.

Figure 5.7 exhibits the phase fractions for the base material and the HAZs. Bertolo et al. [11] reported the presence of tempered martensite (TM), tempered bainite (TB)

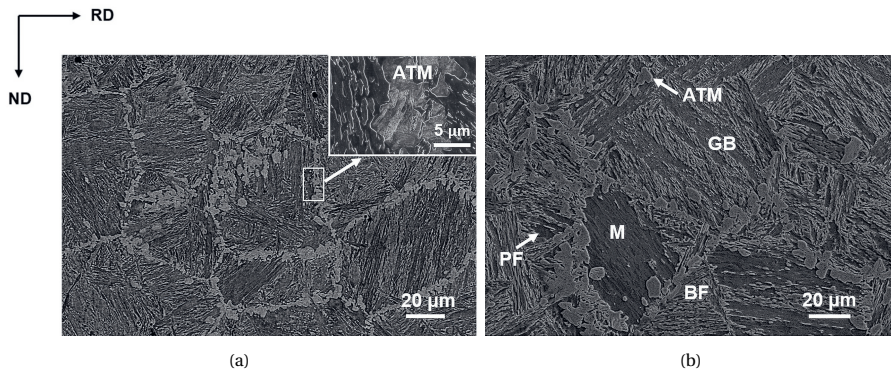


Figure 5.5: SEM micrographs of the ICCGHAZ 750 °C showing (a) the necklace structure at prior austenite grain boundaries mainly composed of auto-tempered martensite (ATM) and (b) the presence of fresh martensite (M), auto-tempered martensite (ATM), granular bainite (GB), bainitic ferrite (BF), and polygonal ferrite (PF).

5

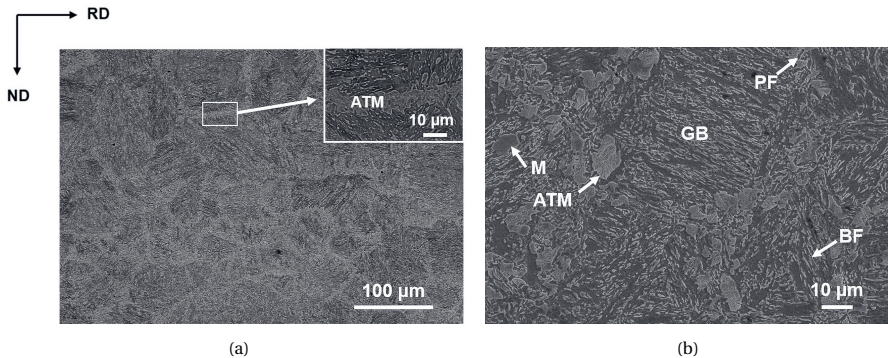


Figure 5.6: SEM micrographs of the ICCGHAZ 800 °C showing (a) the necklace structure at prior austenite grain boundaries mainly composed of auto-tempered martensite (ATM) and (b) the presence of fresh martensite (M), auto-tempered martensite (ATM), granular bainite (GB), bainitic ferrite (BF), and polygonal ferrite (PF).

and ferrite (F) in the base material, with TB representing the majority, followed by TM. Nanohardness measurements showed that tempered martensite and tempered bainite, which make up more than 90% of the base material, present similar properties [11]. For the HAZs, the phases that are found in the majority are auto-tempered martensite for the CGHAZ, 90%, and granular bainite for the ICCGHAZ 750 °C and ICCGHAZ 800 °C, 70% and 80%, respectively.

Furthermore, the material subjected to different thermal profiles retained the centre-line segregation bands parallel to the rolling direction, which was previously observed in the middle section of the base material [11]. Table 5.2 shows the maximum elemental content measured by EPMA inside the segregation bands for the base material and the CGHAZ, ICCGHAZ 750 °C, and ICCGHAZ 800 °C. It should be noted that contrary to

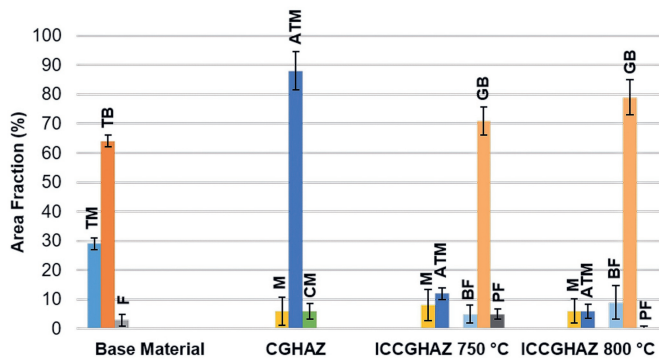


Figure 5.7: Phase fractions for the base material, CGHAZ, ICCGHAZ 750 °C, and ICCGHAZ 800 °C. TM stands for tempered martensite, TB for tempered bainite, F for ferrite, M for martensite, ATM for auto-tempered martensite, CM for coalesced martensite, BF for bainitic ferrite, GB for granular bainite, and PF for polygonal ferrite.

5

the base material where microstructural differences (e.g., grain size) were observed inside and outside the segregation bands, no significant microstructural differences were found in the different HAZs related to the presence of segregation bands. This is possibly related to the decreased degree of segregation of Mn, Cr, and Mo after the thermal cycles in the simulated HAZs, except for the ICCGHAZ 750 °C where the Mo content was slightly increased. In the base material, these were the elements that most strongly segregated in the bands [11]. Therefore, the results presented in this work will not make a distinction between outside and inside segregation bands and will be representative of the overall material, including the segregation bands.

Table 5.2: Maximum elemental content (wt.%) measured by EPMA inside the segregation bands for the base material and the CGHAZ, ICCGHAZ 750 °C, and ICCGHAZ 800 °C.

Condition	Maximum Elemental Content (wt.%)					
	Mn	Cr	Mo	Si	Ni	C
As-received	2.2 ± 0.3	1.1 ± 0.2	0.8 ± 0.3	0.40 ± 0.04	0.35 ± 0.04	0.29 ± 0.04
CGHAZ	1.64 ± 0.04	0.821 ± 0.002	0.56 ± 0.05	0.37 ± 0.01	0.31 ± 0.04	0.24 ± 0.05
ICCGHAZ 750 °C	1.9 ± 0.4	1.10 ± 0.05	1.01 ± 0.15	0.4 ± 0.1	0.3 ± 0.1	0.42 ± 0.05
ICCGHAZ 800 °C	1.9 ± 0.4	1.0 ± 0.2	0.7 ± 0.3	0.45 ± 0.07	0.39 ± 0.04	0.28 ± 0.04

Inclusions pre-existing in the base material [11] were also observed in the simulated HAZ. No difference was found in terms of chemical composition, size, and area fraction between the as-received commercial S690QL steel and the simulated CGHAZ, ICCGHAZ 750 °C, and ICCGHAZ 800 °C microstructures. Spherical inclusions – (Mg,Al,Ca)(O), (Mg,Al,Ca)(O,S), and (Mg,Al,Ca,Ti)(O,N) – with a major-axis (diameter) range of 1 to 5 µm were present in an area fraction around 3.3×10^{-4} . Cubic inclusions – (Nb,Ti,Mg,Ca)(O,C), (Nb,Ti)(C), (Nb,Ti)(C,N), and NbC – with a major-axis (length) range of 1 to 12 µm were present in all HAZs, with an area fraction around 2.0×10^{-4} . Thermodynamic simulations by ThermoCalc predict dissolution temperatures of 1161 °C for Nb–Ti carbonitrides and of 1754 °C for Al oxides. Although the peak temperature of the simulated thermal profiles

is 1300 °C, the Nb-Ti carbonitrides are not affected. This is because the thermodynamic simulations consider equilibrium conditions for the calculations, while the welding thermal profiles comprise fast heating, short holding time, and fast cooling, which prevent the system from reaching the equilibrium. Hence, the dissolution temperature predicted by ThermoCalc is not effective for this heat treatment. Figure 5.8 shows representative examples of spherical and cubic inclusions in the ICCGHAZ 800 °C, also found in the other samples. Note that typical clusters of cubic inclusions and cracks associated with the inclusions themselves and in the inclusion/matrix interface, which were observed in the base material [11], are also present in the HAZ microstructures.

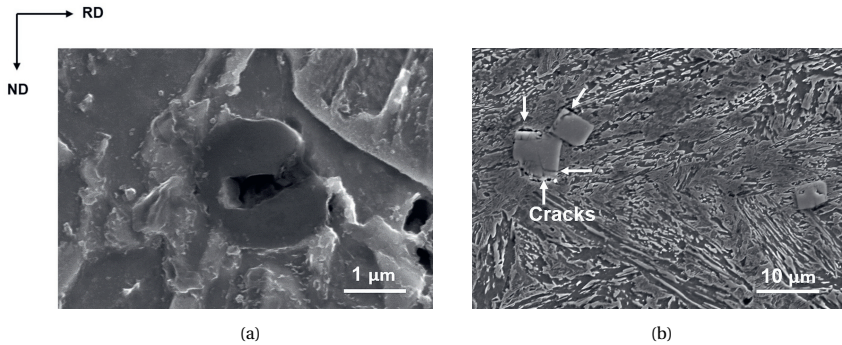


Figure 5.8: Representative examples of (a) (Mg,Al,Ca)(O) and (b) (Nb,Ti)(C) and NbC inclusions found in the ICCGHAZ 800 °C. These images are also representative of inclusions found in other simulated HAZs.

M-A constituents and PAG size, as key microstructural features in HAZ notably contributing to the reduction of fracture toughness, were analysed and quantified. Figure 5.9 (a) – (c) illustrate the special distribution, size, and morphology of M-A constituents in the simulated HAZs. Areas that refer to M-A constituents are the ones with austenitic (green) and martensitic regions (dark grey in the image quality map). Austenitic areas not associated with dark grey areas of the image quality map may be misindexed points (e.g., grain boundaries). Moreover, Fig. 5.9 (d) – (f) show the Kernel Average Misorientation (KAM) maps for the 3rd neighbour, where the blue and red coloured areas are the ones with the lowest and highest KAM levels, respectively. Misorientations within a grain can be attributed to geometrically necessary dislocations (GND) as they contribute to lattice curvature [22]. The larger the KAM value, the larger the density of GND and, therefore, the larger the plastic strain that has occurred during martensite formation [23]. As M-A constituents are also often observed decorating PAG boundaries, EBSD analysis was carried out for accurate characterisation of the necklace structure at PAG of the ICCGHAZs (Fig. 5.10).

As can be seen, M-A constituents are present in different amounts, shapes and sizes through the different HAZs. Regarding the presence of M-A constituents within the necklace structures of ICCGHAZs, austenite is associated with low image quality areas, likely to be martensite, distributed in their necklace structures at the PAG boundaries (Fig. 5.10). Hence, the necklace structure at the PAG boundaries in these conditions is composed of auto-tempered martensite and M-A constituents. Furthermore, the KAM

maps show that the M-A constituents are areas of high GND density and, consequently, high degree of plastic strain (Fig 5.9 (d) – (f)). Nevertheless, note that the KAM level, and consequently, the GND density and the degree of plastic strain, varies depending on M-A morphology. Some M-A constituents have no internal sub-structure (grain boundaries) and the austenitic part is dense (highlighted by yellow ellipses in Fig. 5.9 (b), (c), and (f)). In this case, the KAM level is low (mostly green colour). On the other hand, there are M-A constituents with internal sub-structures and sparsely distributed austenite (highlighted by black rectangles in Fig. 5.9 (b),(c), (e), and (f)). For this morphology, the KAM is high (red colour) and the highest values are associated predominantly with the austenitic areas. The presented morphological differences of M-A and their resultant KAM can be clearly seen for the ICCGHAZs.

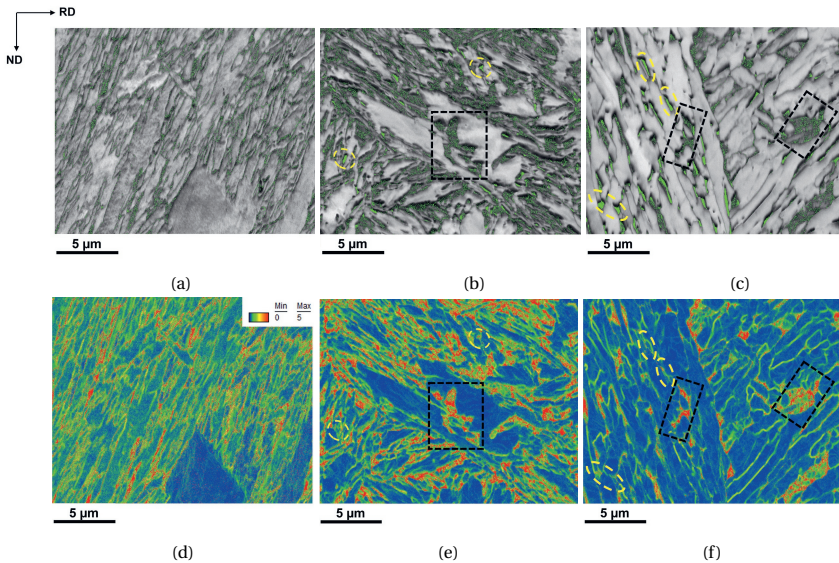


Figure 5.9: Combined grey scale image quality map with coloured phase map showing austenite in green and KAM maps for (a,d) CGHAZ, (b,e) ICCGHAZ 750 °C, and (c,f) ICCGHAZ 800 °C. Areas that refer to M-A constituents are the ones with the combined austenitic and martensitic regions (dark grey in image quality map).

Table 5.3 summarises the area fraction of M-A constituents for each HAZ, their respective average M-A length, and their number fraction of slender and small M-A constituents. The remainder represents blocky and large M-A constituents, respectively. An M-A constituent is considered slender if the aspect ratio is larger than 4. Else, it is considered blocky. Regarding the size, it is considered small if the M-A length is smaller than 1 µm. Else, it is considered large. These values were defined based on the distribution of morphologies and sizes for all investigated areas. Figure 5.11 displays the distribution of major axis length and aspect ratio for the CGHAZ as an example. The ICCGHAZs also had similar distributions. The distributions have a considerable fraction drop at 1 µm and 4, respectively, which suggest the threshold values for the morphological and size definition.

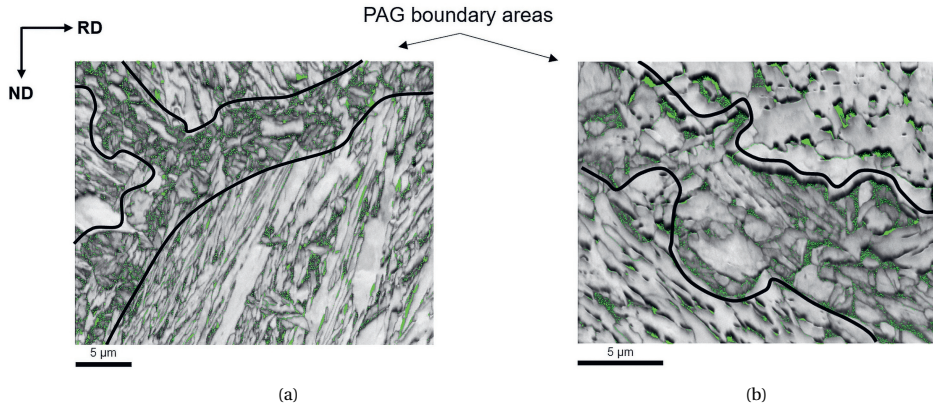


Figure 5.10: Combined grey scale image quality map with coloured phase map showing austenite in green for (a) ICCGHAZ 750 °C and (b) ICCGHAZ 800 °C. The black lines delineate the necklace structure found in PAG boundaries.

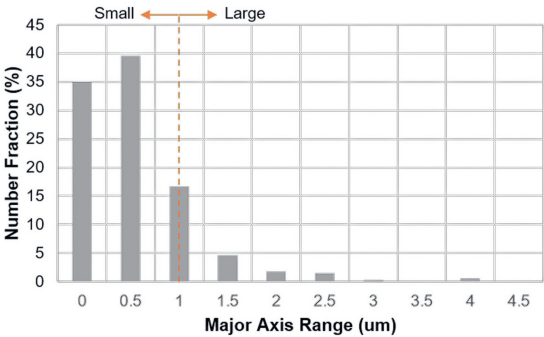
5

Table 5.3: Total area fraction of M-A constituent, average M-A length, and the fraction of slender and small M-A for simulated CGHAZ, ICCGHAZ 750 °C, and ICCGHAZ 800 °C.

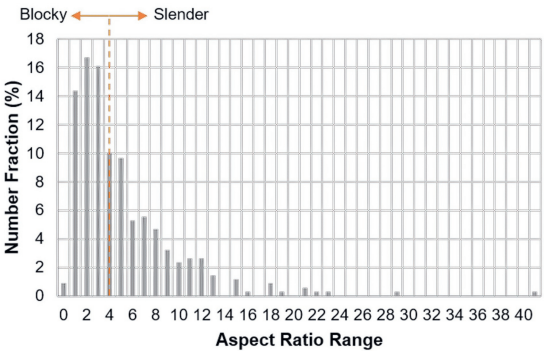
Condition	Area Fraction of M-A (%)	Morphology (%)	Size (%)	Average M-A Length (µm)
		Slender (aspect ratio >4)	Small (length <1 µm)	
CGHAZ	4 ± 1	53 ± 4	75 ± 5	0.79 ± 0.11
ICCGHAZ 750 °C	14 ± 2	42 ± 10	72 ± 6	0.83 ± 0.04
ICCGHAZ 800 °C	6 ± 1	30 ± 12	75 ± 10	0.74 ± 0.13

The quantitative analysis (Table 5.3) indicates that the ICCGHAZ 750 °C stands out with the highest volume fraction of M-A, 14%, followed by the ICCGHAZ 800 °C, 6%, and the CGHAZ with the lowest area fraction, 4%. The CGHAZ has similar fractions of slender and blocky M-A constituents, while for the ICCGHAZs, the majority is blocky. In terms of size, all materials have a majority of small M-A constituents with average M-A length smaller than 0.9 µm.

The reconstructed PAGs for the simulated HAZ show non-equiaxed grain morphology. For the HAZs, the average ratio of the minor-axis length and the major-axis length ranges from 0.43 to 0.48, similarly to the observations for the PAG of the base material [11]. Figure 5.12 shows the average grain width and length for the base material and the investigated HAZs. The results indicate that the HAZs have larger PAG size than the base material. Among the HAZs, the CGHAZ has smaller PAG size than the ICCGHAZ 750 °C and ICCGHAZ 800 °C. However, the large scatter present in the ICCGHAZs measurements demonstrates that there is a heterogeneous distribution of grain sizes within the samples, which is not expected to be generated by the intercritical cycle, which is the difference between CGHAZ and ICCGHAZs processing. Therefore, the large scatter indicates that the larger PAG sizes in the ICCGHAZs may be due to a sampling effect, being statistically insufficient for an accurate comparison.



(a)



(b)

Figure 5.11: Distribution of (a) major axis range and (b) aspect ratio range for M-A constituents in the CGHAZ.

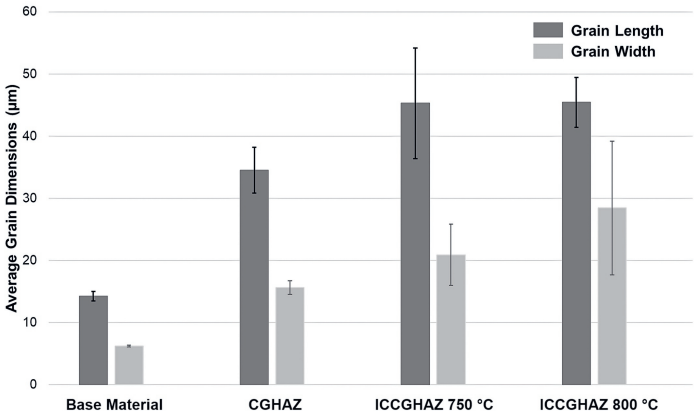


Figure 5.12: Average grain width and length of PAG and their standard deviation from the mean for base material and simulated CGHAZ, ICCGHAZ 750 °C, and ICCGHAZ 800 °C.

An additional important grain parameter for fracture propagation is the misorientation angle [24]. The misorientation angle distribution for the investigated HAZs is shown in Fig. 5.13. It can be seen that the curves do not differ through almost the entire angle range, with the exception of certain ranges of misorientation angles (notably $48^\circ - 57^\circ$). Hence, misorientation angles are not expected to cause significant differences for the different HAZs.

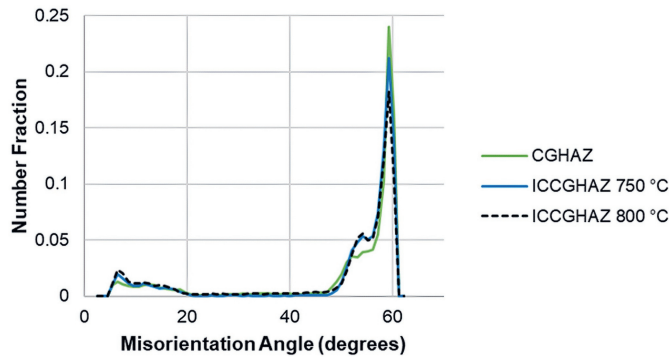


Figure 5.13: Misorientation angle distribution for the simulated CGHAZ, ICCGHAZ 750 °C, and ICCGHAZ 800 °C.

5.2.2. MECHANICAL BEHAVIOUR OF SIMULATED HAZS

The micro-Vickers hardness (HV_3) and tensile properties for the simulated CGHAZ, ICCGHAZ 750 °C, and ICCGHAZ 800 °C are presented in Table 5.4 for room temperature (RT) and -40°C . The properties of the base material are included for comparison [16]. Note that tensile tests from the base material used standard specimens, without the cross-section reduction as in specimens from the HAZs. As can be seen, the hardness and yield strength are proportional, as expected. In descending order of strength, the HAZs are sorted as CGHAZ, ICCGHAZ 750 °C, and ICCGHAZ 800 °C. To better correlate the overall behaviour of the HAZs and their microstructure, the hardness of the predominant phases of each HAZ was measured ($HV_{0.025}$). The dominant phase in CGHAZ, auto-tempered martensite, is much harder than the dominant granular bainite in the ICCGHAZs.

Figure 5.14 (a) displays the average CTOD and the standard deviation from the average for the base material and simulated CGHAZ, ICCGHAZ 750 °C, and ICCGHAZ 800 °C tested at -40°C . For context, with a yield strength of 1000 MPa (representative of CGHAZ at -40°C), a CTOD of 0.02 mm and 0.10 mm correspond to a K_{Ic} of approximately 60 and 130 $\text{MPa}\cdot\text{m}^{1/2}$, respectively. As expected, the HAZs have lower fracture toughness than the base material. The fracture toughness difference between the CGHAZ and ICCGHAZs 750 °C and 800 °C is significant. The CGHAZ shows the lowest CTOD values, followed by the ICCGHAZ 800 °C and the ICCGHAZ 750 °C, where the latter two have similar toughness. Note that the calculation of the CTOD values is influenced by the

Table 5.4: Micro-Vickers hardness (HV₃ and HV_{0.025}) and tensile properties of the base material and the simulated CGHAZ, ICCGHAZ 750 °C, and ICCGHAZ 800 °C at room temperature (RT) and –40 °C. Hardness measurements are presented for the bulk material and for the HAZdominant phases of each HAZ.

Condition	Micro-Vickers Hardness		Yield Strength		Tensile Strength	
	(Overall: HV ₃		(MPa)		(MPa)	
	Predominant Phase: HV _{0.025})					
	RT		RT	–40 °C	RT	–40 °C
Base Material	Bulk	270 ± 10	730 ± 5	780 ± 5	850 ± 10	930 ± 10
CGHAZ	Bulk	380 ± 15	950 ± 20	1000 ± 30	1350 ± 50	1470 ± 50
	Auto-tempered martensite	440 ± 50	-			
ICCGHAZ 750 °C	Bulk	315 ± 5	690 ± 20	740 ± 20	1130 ± 50	1240 ± 50
	Granular bainite	330 ± 30	-			
ICCGHAZ 800 °C	Bulk	230 ± 5	660 ± 10	710 ± 10	1060 ± 30	1160 ± 30
	Granular bainite	330 ± 10	-			

occurrence of pop-ins in the load-displacement curves. Contrary to the base material, multiple pop-in behaviour was observed in the CGHAZ and ICCGHAZs in the bending tests (86%, 17 out of 22 SENB specimens, showed multiple pop-ins). Pop-ins are seen in load-displacement curves as discontinuities as a consequence of a sudden load drop accompanied by an increase in displacement, followed by an increase in load. Figure 5.14 (b) shows one load-displacement curve for each HAZ as examples of the multiple pop-in behaviour. The curve for the base material is added for comparison. The perception on the significance of the pop-ins in the determination of fracture toughness, CTOD, varies in literature. The significance of a pop-in can be quantified by a parameter P , which represents the cumulative increase in crack size and compliance due to prior pop-ins and the pop-in being analysed and can be directly determined from the experimental data. Knowing that the compliance is the inverse of stiffness, P_n of the n^{th} pop-in can be determined by

$$P_n = 1 - \frac{(S_n^l)}{(S_1^u)} \quad (5.1)$$

where, S_1^u is the stiffness of the material at the first pop-in considering the upper force value, and S_n^l is the stiffness at the n^{th} pop-in considering the lower force value. More details on P and its calculation can be found in the ISO 12135 [20] standard.

On the one hand, according to the ISO 12135 [20] standard, a pop-in should be taken as critical CTOD point (point which the data is considered as maximum force and displacement for CTOD calculation) if the ratio between the force drop and the maximum force at the pop-in is smaller than P . On the other hand, the ASTM E-1820 [25] considers the pop-in as the critical CTOD point if P is larger than 5%. In the present study we follow the ASTM E-1820 [25] standard and evaluate the significance of a pop-in as $P > 5\%$, since the ISO 12135 standard [20] would result in an overly conservative analysis. In the majority of the specimens, all pop-ins exceeded 5%, where 90% presented $P > 20\%$.

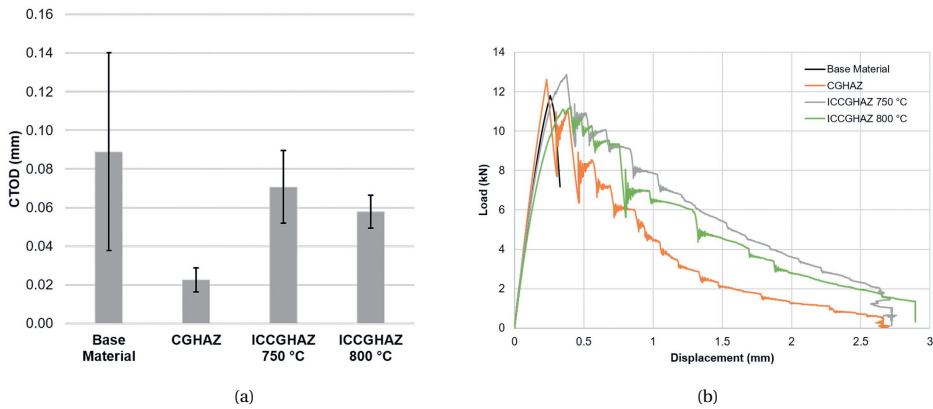


Figure 5.14: Plots of (a) CTOD results and their standard deviation from the mean at -40°C for the base material and the simulated CGHAZ, ICCGHAZ 750°C , and ICCGHAZ 800°C and (b) load vs. displacement curve for the base material, CGHAZ, ICCGHAZ 750°C , and ICCGHAZ 800°C showing the multiple pop-in behaviour observed in the simulated HAZs.

5

5.2.3. MICROSTRUCTURAL FEATURES AFFECTING CLEAVAGE FRACTURE IN HAZS

5.2.3.1. CLEAVAGE INITIATION

Contrary to the base material, clear river lines were not observed on the fracture surface of HAZs. This suggests the presence of multiple initiation sites. As a result, the identification of the initiation sites was challenging, and the fractography at most indicates likely initiation sites. Figures 5.15, 5.16, and 5.17 show representative fractographic images of the CGHAZ, ICCGHAZ 750°C , and ICCGHAZ 800°C . As can be seen, particles that resemble M-A constituents are present at cleavage facets where river lines appear to be converging.

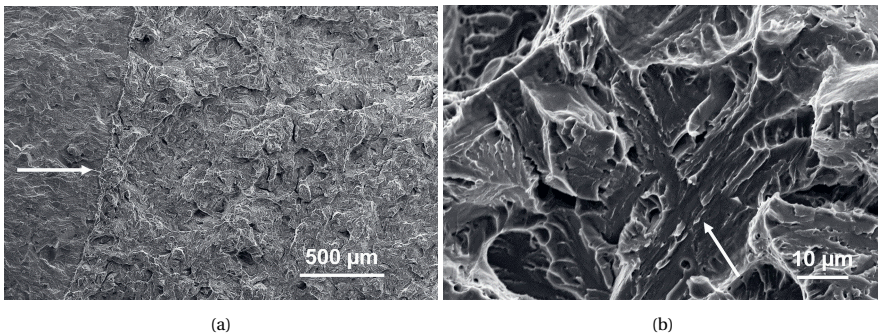


Figure 5.15: Fractographic SEM image showing (a) local river lines indicating a likely initiation site in a CGHAZ specimen fractured at -40°C (CTOD = 0.02 mm) and (b) is a zoom-in of (a) showing a cleavage facet where particles that resemble M-A constituents, pointed out by a white arrow, are likely to have triggered fracture.

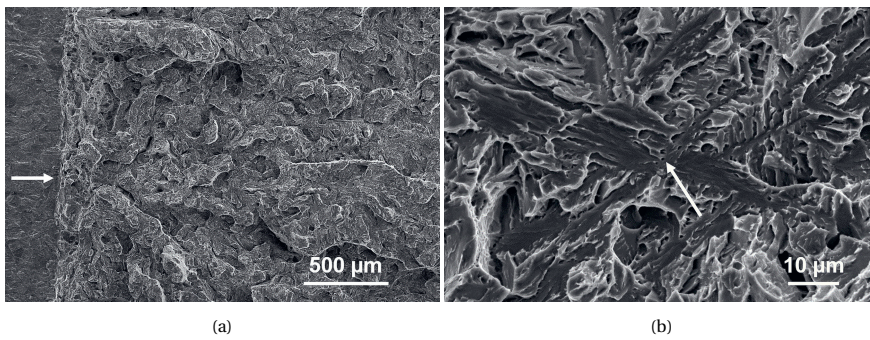


Figure 5.16: Fractographic SEM image showing (a) local river lines indicating a likely initiation site in a ICCGHAZ 750 °C specimen fractured at -40°C (CTOD = 0.01 mm) and (b) is a zoom-in of (a) showing a cleavage facet where a particle that resembles a M-A constituent, pointed out by a white arrow, is likely to have triggered fracture.

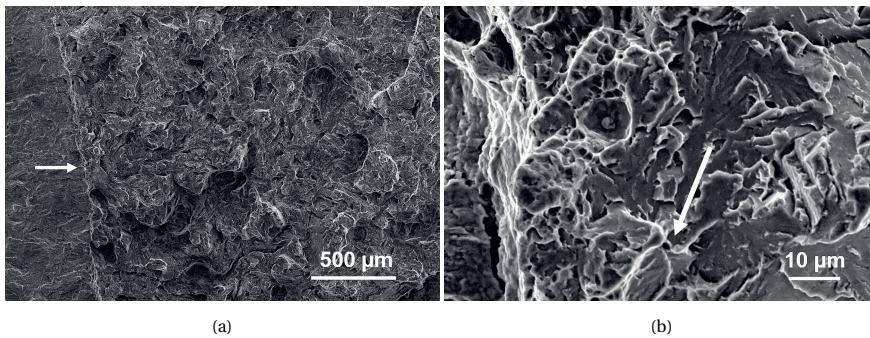


Figure 5.17: Fractographic SEM image showing (a) local river lines indicating a likely initiation site in a ICCGHAZ 800 °C specimen fractured at -40°C (CTOD = 0.05 mm) and (b) is a zoom-in of (a) showing a cleavage facet where particles that resemble M-A constituents, pointed out by a white arrow, are likely to have triggered fracture.

5.2.3.2. CLEAVAGE PROPAGATION

The cleavage crack propagation of CGHAZ, ICGHAZ 750 °C, and ICGHAZ 800 °C was investigated through SEM directly on the fracture surface and by SEM and EBSD on their transverse section. All simulated HAZs presented the same propagation characteristics. Figure 5.18 (a) shows the inverse pole figure (IPF) of the fracture surface profile of an SENB specimen of the simulated CGHAZ as an example. Additionally, prior austenite grains involved in the propagation process are individually analysed (Fig. 5.18 (b) – (g)). The prior austenite and the martensite phases for the HAZs follow the Kurdjumov-Sachs (K-S) crystallographic orientation relationship. The K-S orientation relationship has 24 variants that can be separated into four groups where variants in each group share the same habit plane and form a packet [26]. Packets consist of blocks that share the same habit plane. The different colours in Fig. 5.18 (c), (e), and (g) represent different variant

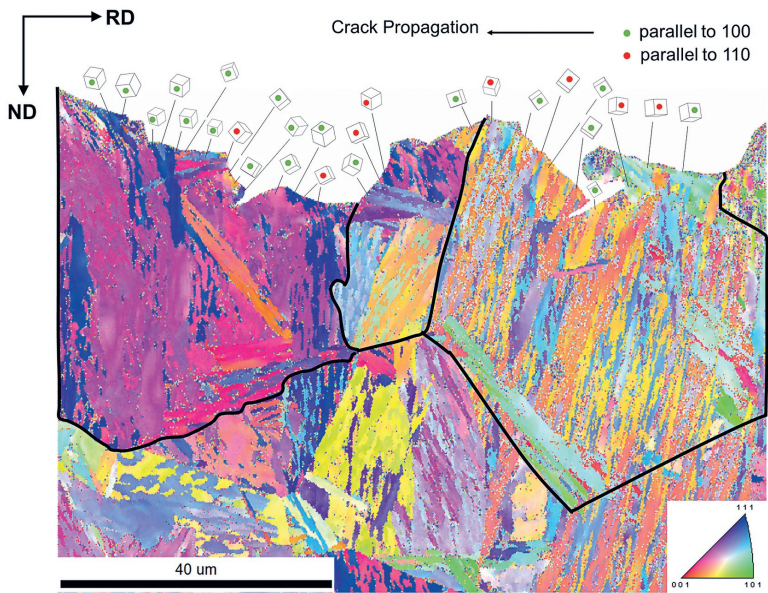
groups and, therefore, also represent different packets. Each packet is composed of three blocks of different Bain variants. The Bain axis is the cube axis in which austenite was compressed to be transformed into martensite [26]. The colours in Fig. 5.18 (b), (d), and (f) represent the Bain variants.

The cleavage fracture in the studied HAZs was found to be transgranular. Note that transgranular fracture was also observed in the ICCGHAZs, meaning that the crack does not progress exclusively through the necklace structure at PAG boundaries. Moreover, the IPF contains evidence of microplasticity due to the presence of dense areas of poorly indexed points along the propagation path as pointed out by Bertolo et al. [16]. Note that accurate data cannot be acquired from these areas. Hence, they are not considered further. Along with the IPF in Fig. 5.18 (a), 3D crystal lattice cubes are used to analyse the crystal orientations underneath the fracture surface and identify the preferential cleavage crack propagation planes. When determining which plane is parallel to the fracture surface, a tolerance angle of 10° is applied. Green and red circles inside the 3D cubes indicate that $\{100\}$ and $\{110\}$ planes are aligned parallel to the fracture plane, respectively. As can be seen, the study of the fracture profile shows that 100 and 110 are the most favourable cleavage planes in the CGHAZ. The same is observed for the ICCGHAZ 750 °C and ICCGHAZ 800 °C. Similarly to the base material [16], high-angle grain boundaries, such as PAG boundaries, are observed to deflect the crack, and packets and blocks also play a strong role in diverting the crack when the neighbouring sub-structure has a different Bain axis. However, in some cases, different neighbouring Bain axes cause no or slight crack deflections. Wang [27] explained that this can be related to the thickness of the Bain area (regions of constant colour in Fig. 5.18 (b), (d), (f)), where thin Bain areas have minor effects on the crack path.

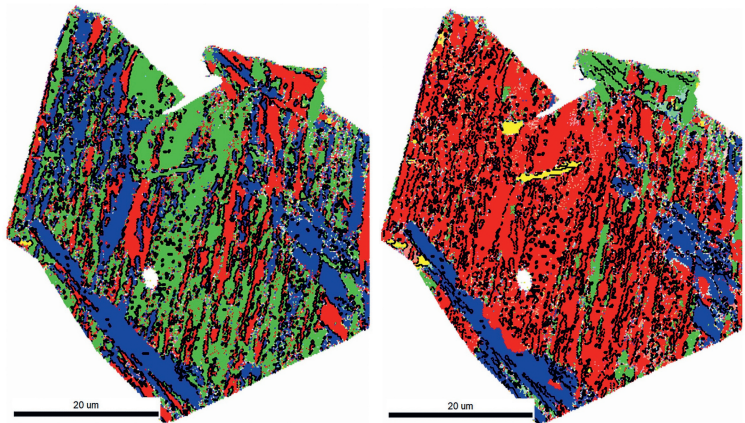
To investigate the role of the M-A constituents in crack propagation, higher magnification EBSD near the crack propagation path was carried out for the investigated HAZs. Figure 5.19 shows the image quality map combined with the colour phase map (austenite in green) and the KAM map for the CGHAZ as an example. This area is part of Fig. 5.18 (a) and refers to the area within the dashed rectangle. The white arrows in Fig. 5.19 (a) are pointing at some M-A constituents present on the surface. As can be seen, only one M-A constituent is observed to interact with the main crack path. This indicates that M-A constituents do not act as dominant weak links for crack propagation.

5.3. DISCUSSION

The M-A presence of the CGHAZ, ICCGHAZ 750 °C, and ICCGHAZ 800 °C through thermal welding simulations via Gleeble is in good agreement with other studies [6, 27]. In the CGHAZ, the material is heated to very high peak temperatures (above A_{c3}). Then, the higher the temperature, the higher the degree of carbon homogenisation, and the less stable austenite is at room temperature. On the other hand, in the ICCGHAZs, the material is intercritically reheated, between A_{c1} and A_{c3} , and partially transformed to austenite, which is enriched with carbon. During cooling, it partially transforms into martensite and it is partially retained at room temperature. Nevertheless, the higher the peak temperature, the less the probability of retaining austenite at room temperature. This is because the equilibrium carbon concentration in austenite decreases with



(a)



(b)

(c)

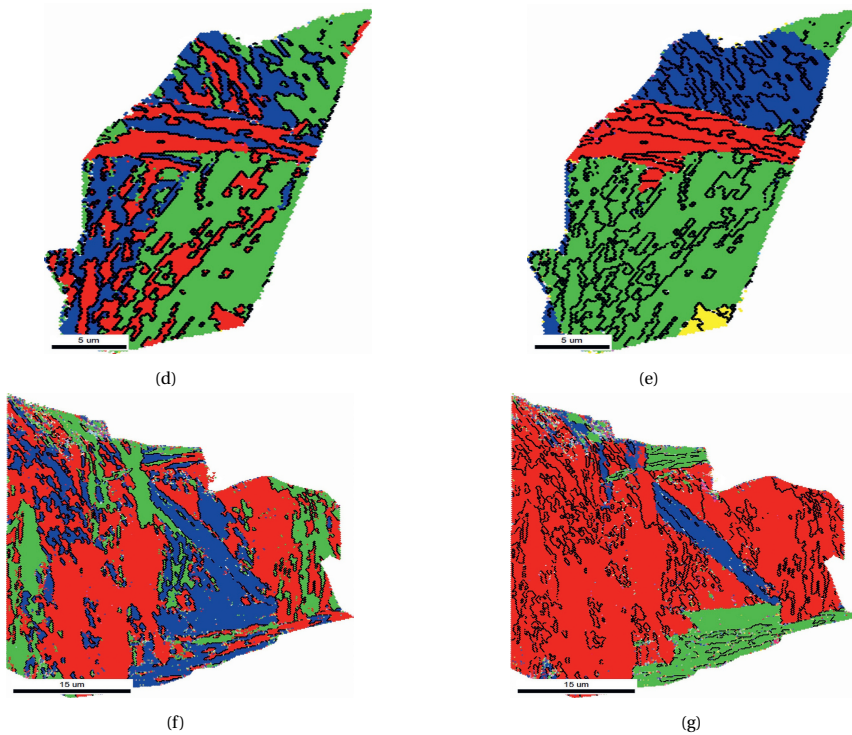


Figure 5.18: Fractographic profile of the fractured CTOD specimen of the simulated CGHAZ presented as (a) Inverse Pole Figure, (b) and (c) are an individual PAG located at the right-hand side of (a), (d) and (e) an individual PAG located at the centre of (a), and (f) and (g) an individual grain located at the left-hand side of (a). The colours in (b), (d), and (f) represent different Bain variants, while the colours in (c), (e), and (g) represent the different groups of K-S variants. Thin black lines are high-angle (misorientation larger than 15°) grain boundaries and the thick black contour in (a) is the PAG boundary.

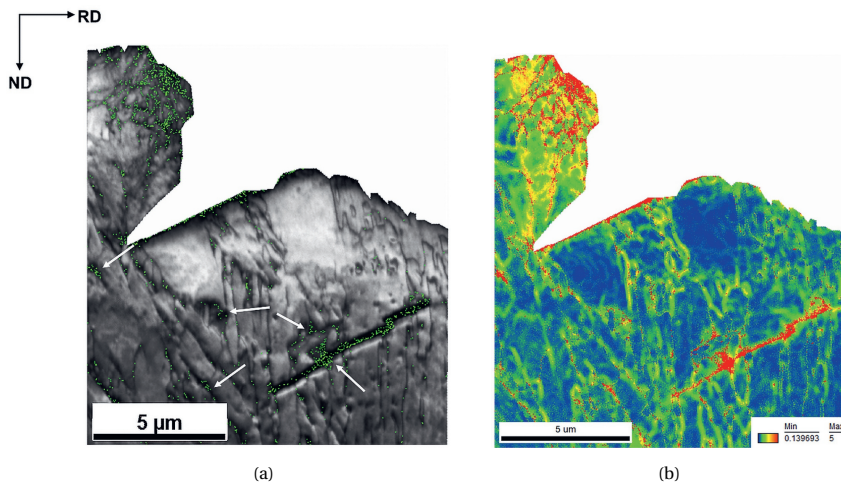


Figure 5.19: Fractographic profile of a simulated CGHAZ CTOD specimen presented as (a) combined grey image quality map and coloured phase map where austenite is represented as green and (b) Kernel average misorientation (KAM) map. The white arrows in (a) are pointing out to some M-A constituents present on the surface.

increasing temperature. Then, the maximum fraction of M-A constituent content is usually formed at a temperature around A_{c1} and then it decreases at higher temperatures. This explains the largest area fraction of M-A constituent present in the ICCGHAZ 750 °C, 14%; followed by the ICCGHAZ 800 °C, which have less than half of this fraction, 6%; and the CGHAZ, 4%. The necklace structure observed at the PAG boundaries of the ICCGHAZs is formed upon heating above A_{c1} , where austenite preferentially nucleates at PAG boundaries. During the subsequent cooling, austenite is partially retained and the rest is transformed to martensite and auto-tempered due to high martensitic start temperature [28]. Another microstructural change observed in the simulated HAZs compared to the base material is the prior austenite grain coarsening, widely reported in the literature [29, 30].

According to many authors [5, 31, 32], the ICCGHAZs present lower toughness than the CGHAZ. They attribute the main loss of toughness in the intercritically reheated zones to M-A constituents, that are present in a larger size, higher fraction, and also along PAG boundaries in a necklace-like form. Moreover, phases such as bainitic ferrite and granular bainite, often observed in ICCGHAZs, are also indicated as unfavourable microstructure constituents as they have low toughness [5]. The abovementioned microstructural characteristics that differentiate CGHAZ from ICCGHAZ and make the latter more prone to brittle fracture are also observed in the HAZs of the present study. However, in the present work, the CGHAZ exhibits the lowest fracture toughness. To understand the differences between the HAZs, the fracture surfaces of the CTOD specimens were analysed. Contrary to the base material (plate's mid-thickness) – tested at –100 °C at different a/W ratios, which covers the lower transition and lower shelf regimes of the ductile-to-brittle transition curves [16] – where cubic Nb-rich and oxide inclu-

sions are observed as cleavage crack initiators, the fracture surface analyses of the HAZs indicate that the microstructural feature triggering fracture is likely to be M-A. This happens despite Nb-rich and oxide inclusions being larger, which increases vulnerability to fracture, and Nb-rich inclusions being harder, which makes it more brittle and prone to fracture than M-A constituents. According to the KAM maps, the M-A constituents are the areas with the highest KAM values, indicating a high dislocation density and formation of dislocation pile-ups. Consequently, high stresses are induced in M-A constituents [33]. Under the combined applied stress on the structure and the phase-transformation-induced stresses during the heat treatment, M-A constituents are more readily cracked than Nb-rich inclusions. Note that residual stresses between the Nb-rich inclusions and the steel matrix are also usually present in steel plates due to thermal expansion [34]. Nevertheless, these residual stresses are probably relieved in the welding thermal cycles. Still, if the difference in fracture behaviour between CGHAZ and ICCGHAZs would be caused by crack initiation in M-A constituents, the ICCGHAZ 750 °C would represent the worst case as it has the largest M-A fraction and, therefore, a higher density of sites to locally initiate cracks. Instead, the ICCGHAZ 750 °C represents the HAZ with the highest fracture toughness in this study. This is related to the dimensions of M-A constituents. According to the Griffith criterion [35], the critical cleavage fracture stress is inversely proportional to the square root of the crack length. In this work, as M-A constituents are observed as crack initiators, the crack length can be assumed equal to the M-A constituent size. Hence, if the M-A size is at least equivalent to the length required for the critical event, the crack propagates in an unstable manner until final fracture. Otherwise, the crack would propagate stably until reaching the size of the critical crack through the particle/matrix interface, into the matrix and across the matrix/matrix interface [34, 37]. In the present study, the M-A constituents are predominantly small (70 – 75% is smaller than 1 µm in all HAZs), which is likely not sufficient to attain the local cleavage fracture stress. Hence, the matrix and its properties also influence the fracture toughness due to the crack propagation step. This explains the tougher behaviour of ICCGHAZs compared to the CGHAZ. The highest hardness and tensile properties of the CGHAZ are due to the auto-tempered martensite along with the smallest PAG dimensions. Due to the fast welding thermal cycles, the degree of auto-tempering is very limited and the auto-tempered martensite has properties comparable to fresh martensite rather than to significantly tempered martensite. For instance, the CGHAZ is harder and stronger than the base material composed of tempered martensite and tempered bainite. The ICCGHAZs, in turn, have lower hardness and tensile properties than the CGHAZ as a result of their predominant microstructure of granular bainite and larger PAG dimensions. The higher hardness and tensile properties of ICCGHAZ 750 °C compared to the ICCGHAZ 800 °C are likely due to the difference in the M-A constituent content, 14%, and 6%, respectively. Therefore, contrary to the findings in the literature [2–5], the microstructural composition of the HAZ matrix plays a more important role in fracture behaviour than M-A constituents.

The propagation micromechanisms are similar to the ones observed in the base material where cracks propagate in a transgranular manner and the PAG boundaries and packet and block boundaries with different neighbouring Bain axes are the microstructural characteristics effectively diverting the cleavage crack. It is also seen that different

from the studies in the literature [36, 37], the necklace structure of tempered martensite and M-A constituents at PAG boundaries are not preferential sites for crack propagation. M-A constituents are also not observed along the crack path of the fracture profile, an indication that they are not playing a significant role in the crack path. This is also supported by the observation that the crack propagates along the {100} and {110} planes, known as preferential cleavage planes in BCC steels [38].

It should however be noted that, contrary to the base material, the HAZs exhibit distinct pop-ins in the load-displacement curves, indicating multiple crack initiations and arrests (Fig. 5.14(b) and Fig. 5.20(g) – (i)). According to the literature [39–41], a pop-in is a discontinuity in the load-displacement curve resulting from local unstable crack growth which is subsequently arrested. A crack can be arrested, for instance, by surrounding tougher material or by the initiation of cracks perpendicular to the plane of the initial crack, also called delamination or splitting, and of secondary cracks [39–42]. Usually, the region of the arrested crack can be seen on the fracture surface as well as delamination/splitting. Figure 5.20 shows macrographs of the fracture surface, micrographs of the fracture surface at the initiation site indicated by the white arrow (the area where the river lines are converging), and the load-displacement curves for the CGHAZ (a, d, g), ICCGHAZ 750 °C (b, e, h), and ICCGHAZ 800 °C (c, f, j), respectively. As can be seen from the macro- and micrographs, there is no sign of delamination/splitting on the fracture surface. The transverse section of the fracture surfaces were also investigated. However, very few secondary cracks were observed, which would not justify the multiple pop-ins. Hence, the surrounding microstructure should be the cause for this behaviour.

To identify potential microstructural features responsible for reducing the crack energy and arresting the crack, EBSD analysis was carried out on secondary cracks on the transverse section of the fracture surface underneath the crack path (Fig. 5.21). As can be seen, M-A constituents are found along the propagation path of secondary cracks. In some cases, for instance in Fig. 5.21 (a) point 1, (c) points 1 and 2, and (e) point 1, some M-A constituents are observed to deflect the crack. Note that point 1 in Fig. 5.21 (e) resembles an M-A constituent, but it is too small compared to the crack width to accurately identify it. Moreover, points 2 and 3 in (e) show a crack initiation and crack arrest in M-A constituents. On the other hand, there are cases where M-A constituents do not influence the crack propagation path, as pointed out by point 3 in Fig. 5.21 (c). The M-A influence on the crack path is attributed to the different KAM distributions. KAM gives semi-quantitative information on geometrically necessary dislocations and, therefore, deformation localizations [23]. The strain located in M-A constituents is a consequence of the residual stresses induced during phase transformation to martensite and the retention of austenite during cooling. As an FCC crystal lattice is more closely packed than BCC, body centered cubic, and BCT, body cubic tetragonal, lattices, compressive stresses are generated in the surrounding matrix material during the transformation from austenite to martensite as a result of volume expansion [4]. Note that the residual stresses developed in actual welds are not present in thermally simulated welds. Then, their possible effect on the stress distribution inside M-A constituents is not considered here. From our observations, M-A constituents present different KAM distributions, depending on their morphology. The M-A constituents with internal substructures and sparse austenitic areas have higher KAM values than M-A constituents with small parts of martensite and

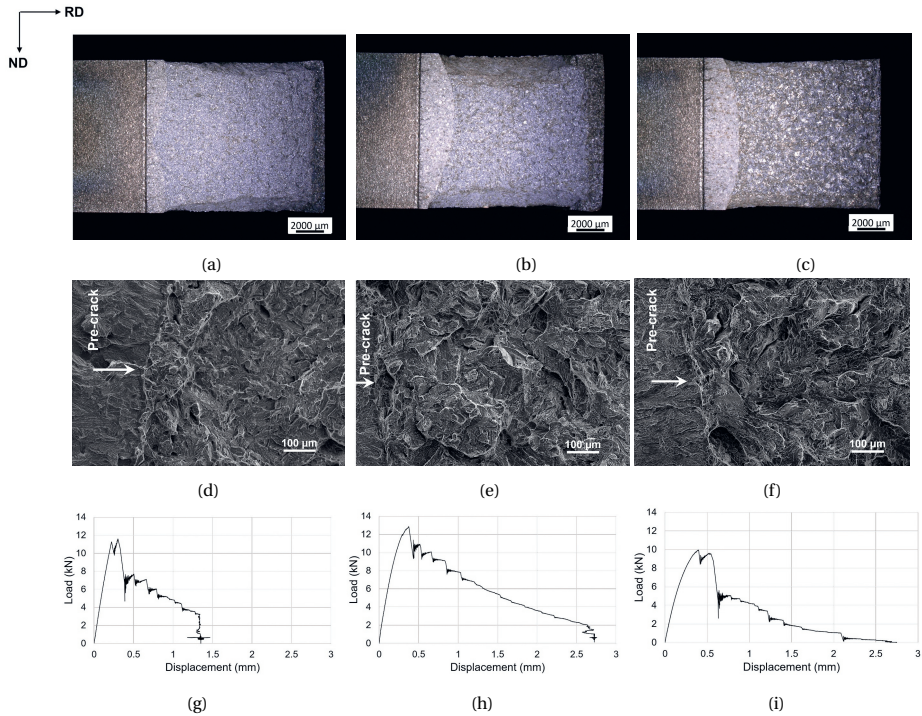


Figure 5.20: Macrographs and micrographs of the fracture surface and respective load-displacement curves of (a,d,g) CGHAZ, (b,e,h) ICCGHAZ 750 °C, and (c,f,i) ICCGHAZ 800 °C. The white arrows in the micrographs (d,e,f) are pointing out to the location of the initiation site.

dense areas of austenite. These observations are in good agreement with the literature [43]. Hence, when a crack interacts with M-A constituents with high KAM, the compressive stresses at M-A constituents affect the crack tip stress state, reducing the stress intensity and, therefore, its criticality. The reduction of crack-tip stresses due to the interaction of the crack with compressive stresses explains the crack deflections and also the crack arrest events. Furthermore, the literature also shows that the internal sub-structures of M-A constituents include high-angle boundaries, which can also change the direction of a crack or hinder it [43]. As a consequence, M-A constituents with internal sub-structures are potential microstructural features to be responsible for multiple pop-in behaviour. Therefore, it can be concluded that besides high-angle grain boundaries and Bain axes, M-A constituents with internal sub-structures and high KAM are important for the cleavage micromechanisms of HAZs of high strength steels. Moreover, for macroscopic fracture, when the first pop-in within many, such as for the HAZs under study, is taken as the point of critical CTOD, the result underestimates the material's fracture toughness.

In summary, the fracture process is triggered by M-A constituents, which are too small (less than 1 µm) to reach the stress for unstable crack growth. Then, the crack continues to grow through the matrix until it reaches the critical size. Thus, the ma-

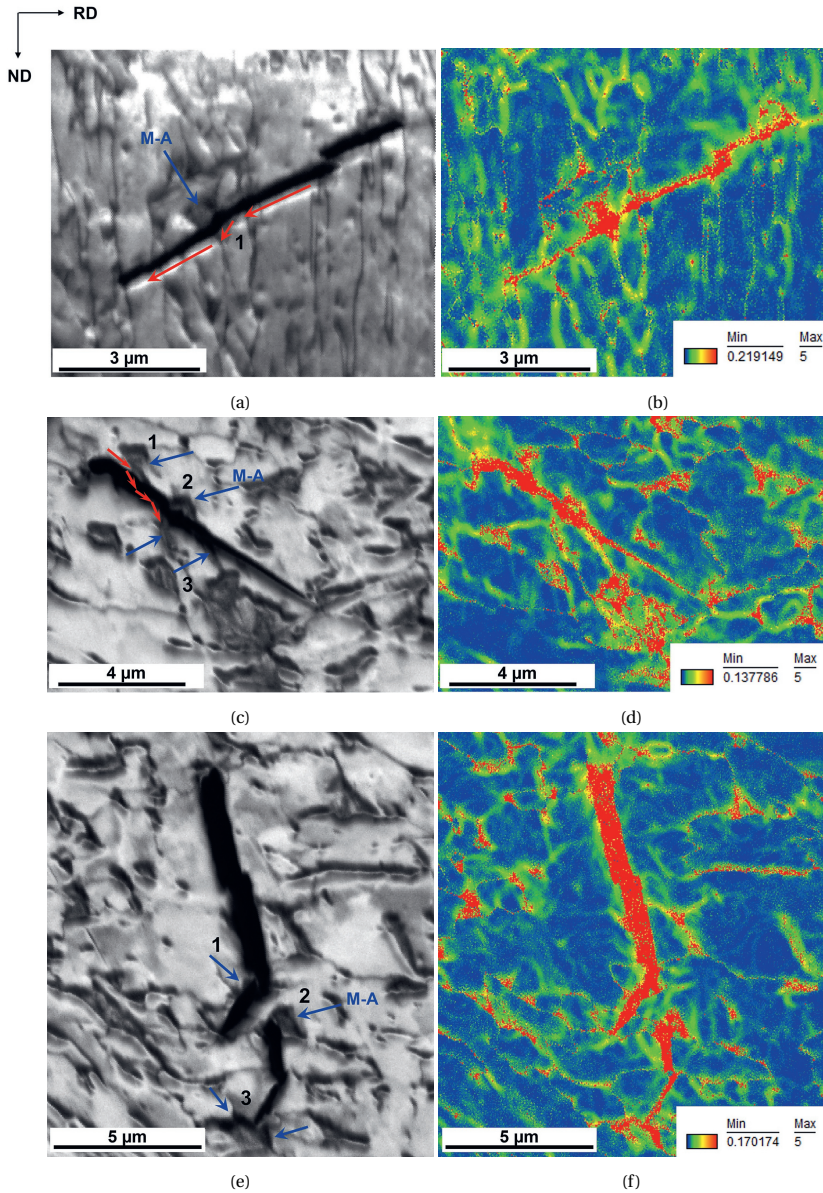


Figure 5.21: Image quality and KAM maps of secondary cracks on the transverse section of the fracture surface of (a,b) CGHAZ and (c,d,e,f) ICCGHAZ 800 °C. Blue arrows in (a,c,e) point out to M-A constituents interacting with secondary cracks. The red arrows in (a,c) are used to highlight the crack deflection.

trix and its properties strongly influence the fracture toughness. Moreover, M-A constituents, besides acting as crack initiators, are also observed to influence the propagation step. Although they are not preferential crack paths, M-A constituents with internal

sub-structures can still deflect and arrest the crack, influencing the crack propagation path. Other features such as PAG boundaries, and packets and block boundaries with different Bain axes are also observed to deflect the crack.

5.4. CONCLUSIONS

The influence of microstructure on cleavage fracture toughness and micromechanisms of fracture in CGHAZ and ICCGHAZs of quenched and tempered S690 high strength steels was studied in this work. The microstructure of CGHAZ, ICCGHAZ 750 °C, and ICCGHAZ 800 °C were studied via different techniques and the fracture behaviour was studied through three-point bending tests at -40 °C. The following conclusions can be made:

1. The ICCGHAZ 750 °C has the highest volume fraction of M-A, 14%, followed by the ICCGHAZ 800 °C, 6%, and the CGHAZ, 4%. In terms of morphology, M-A constituents are found in the form of dense austenitic areas along with a small portion of martensite on one side and with internal sub-structures where austenite is sparsely distributed. The latter presents the highest KAM, meaning that these M-A constituents have high geometrically necessary dislocation density (plastic strain) and compressive stress.
2. M-A constituents are found to trigger the fracture in CGHAZ and ICCGHAZs. However, due to their size (smaller than 1 µm), main cracks initiated from M-A constituents are likely not representing the critical crack length for unstable crack and final fracture. Hence, the matrix also contributes to the crack-growth step. The tougher behaviour of ICCGHAZs compared to the CGHAZ is associated with the matrix and its properties. The highest hardness and tensile properties of the CGHAZ are due to the auto-tempered martensite along with the smallest PAG. The ICCGHAZs, in turn, have lower hardness and tensile properties as a result of their microstructure of granular bainite and larger PAG dimensions.
3. The main crack propagates in a transgranular manner in all investigated HAZs and, therefore, the necklace structure at PAG boundaries of ICCGHAZs is not a preferential propagation path. Likewise, M-A constituents are rarely observed in the main crack path, meaning that these brittle particles do not act as favourable routes for propagation. This is also supported by the observation that the main crack propagates along the {100} and {110} planes. The PAG boundaries and packet and block boundaries with different neighbouring Bain axes are found to effectively divert the cleavage crack.
4. Multiple pop-ins are observed in the load-displacement curves of all investigated HAZs. The analysis of secondary cracks indicates that the M-A constituents with internal sub-structures have high KAM and are able to deflect and arrest secondary cracks. This is related to the reduction of crack-tip stresses due to the compressive stresses inside the M-A constituents and the high-angle boundaries of sub-structures. Hence, M-A constituents with these characteristics are potential features responsible for the multiple pop-in behaviour.

From a statistical and quantitative analysis of the microstructure and the fracture process, this research establishes the role of different microstructural features and parameters on the cleavage fracture micromechanisms of complex, multi-phase CGHAZ and ICCGH AZs of an S690QL high strength steel. Thus, a quantitative and statistical relationship between microstructure and cleavage fracture behaviour is defined, contributing to modelling predictions and, ultimately, the development of a microstructure-based failure criterion. Furthermore, this study brings insight into the microstructural aspects of HAZs to be considered when designing welded joints, which can improve low-temperature toughness of CGHAZ and ICCGH AZs, such as the size and morphology of M-A constituents (smaller than 1 μm and blocky with internal sub-structures) and matrix toughness.

REFERENCES

- [1] Popovich, V., & Richardson, I. M. (2015). Fracture Toughness of Welded Thick Section High Strength Steels. *TMS 2015 144th Annual Meeting & Exhibition: Supplemental Proceedings.*, 1031–1038. <https://doi.org/10.1002/9781119093466.ch125>
- [2] Lee, S., Kim, B. C., & Lee, D. Y. (1989). Fracture mechanism in coarse grained HAZ of HSLA steel welds. *Scripta Metallurgica*, 23(6), 995–1000. [https://doi.org/10.1016/0036-9748\(89\)90284-6](https://doi.org/10.1016/0036-9748(89)90284-6)
- [3] Mohseni, P., Solberg, J. K., Karlsen, M., Akselsen, O. M., & Østby, E. (2012). Investigation of mechanism of cleavage fracture initiation in intercritically coarse grained heat affected zone of HSLA steel. *Materials Science and Technology*, 28(11), 1261–1268.
- [4] Davis, C. L., & King, J. E. (1994). Cleavage Initiation in the Intercritically Reheated Coarse-Grained Heat-Affected Zone : Part I . Fractographic Evidence. *Metallurgical and Materials Transactions A*, 25A, 563–573.
- [5] Lee, S. G., Kim, B., Sohn, S. S., Kim, W. G., Um, K. K., & Lee, S. (2019). Effects of local-brittle-zone (LBZ) microstructures on crack initiation and propagation in three Mo-added high-strength low-alloy (HSLA) steels. *Materials Science and Engineering A*, 760(June), 125–133. <https://doi.org/10.1016/j.msea.2019.05.120>
- [6] Bayraktar, E., & Kaplan, D. (2004). Mechanical and metallurgical investigation of martensite-austenite constituents in simulated welding conditions. *Journal of Materials Processing Technology*, 153-154, 87–92. <https://doi.org/10.1016/j.jmatprotec.2004.04.021>
- [7] Kumar, S., & Nath, S. K. (2017). Effect of Weld Thermal Cycles on Microstructures and Mechanical Properties in Simulated Heat Affected Zone of a HY 85 Steel. *Transactions of the Indian Institute of Metals*, 70(1), 239–250. <https://doi.org/10.1007/s12666-016-0880-1>
- [8] Kim, B. C., Lee, S., Kim, N. J., & Lee, D. Y. (1991). Microstructure and local brittle zone phenomena in high-strength low-alloy steel welds. *Metallurgical Transactions A*, 22(2), 139–149.
- [9] Luo, X., Chen, X., Wang, T., Pan, S., & Wang, Z. (2018). Effect of morphologies of martensite–austenite constituents on impact toughness in intercritically reheated coarse-grained heat-affected zone of HSLA steel. *Materials Science and Engineering A*, 710(October 2017), 192–199. <https://doi.org/10.1016/j.msea.2017.10.079>
- [10] Li, Y., & Baker, T. N. (2010). Effect of morphology of martensite-austenite phase on fracture of weld heat affected zone in vanadium and niobium microalloyed steels. *Materials Science and Technology*, 26(9), 1029–1040. <https://doi.org/10.1179/026708309X12512744154360>
- [11] Bertolo, V., Jiang, Q., Scholl, S., Petrov, R., Hangen, U., Walters, C., Sietsma, J., & Popovich, V. (2022). A Comprehensive Quantitative Characterisation of the Multiphase Microstructure of a Thick-Section High Strength Steel. *Journal of Materials Science*, 57, 7101–7126. <https://doi.org/https://doi.org/10.1007/s10853-022-07121-y>
- [12] Penagos, J. J., Pereira, J. I., Machado, P. C., Albertin, E., & Sinatora, A. (2017). Synergetic effect of niobium and molybdenum on abrasion resistance of high

- chromium cast irons. *Wear*, 376-377, 983–992. <https://doi.org/10.1016/j.wear.2017.01.103>
- [13] Wang, Y., Wang, Q., Liu, L., & Xu, W. (2015). Fracture mode of martensite-austenite constituents containing multiphase steel controlled by microstructural and micromechanical aspects. *Mechanics of Advanced Materials and Structures*, 22(7), 591–596. <https://doi.org/10.1080/15376494.2013.828808>
- [14] Huda, N. (2018). *Effect of Martensite-Austenite (MA) on Mechanical Properties of X80 Linepipe Steel* (Doctoral dissertation). University of Waterloo. <https://www.sciencedirect.com/science/article/abs/pii/S0921509319310871>
- [15] Vassilaros, M. G. (1990). *Fracture Behavior of Ultra-Low-Carbon Steel Plate and Heat-Affected Zone* (tech. rep.). David Taylor Research Center.
- [16] Bertolo, V., Jiang, Q., Tiringer, U., Walters, C. L., Sietsma, J., & Popovich, V. (2022). Cleavage Fracture Micromechanisms in Thick-Section Quenched and Tempered S690 High-Strength Steels. *Journal of Materials Science*, 57, 20033–20055. <https://doi.org/10.2139/ssrn.4055055>
- [17] CEN. (2019). NEN-EN 10025-6: Hot rolled products of structural steels - Part 6: Technical delivery conditions for flat products of high yield strength structural steels in the quenched and tempered condition.
- [18] Cayron, C. (2007). ARPGE : a computer program to automatically reconstruct the parent grains from electron backscatter diffraction data. *Journal of Applied Crystallography*, 40, 1183–1188. <https://doi.org/10.1107/S0021889807048777>
- [19] BSI. (2015). *BS7910:2013+A1:2015 Guide to methods for assessing the acceptability of flaws in metallic structures* (tech. rep. UK).
- [20] ISO. (2016). INTERNATIONAL STANDARD Metallic materials — Unified method of test for the determination of quasistatic fracture toughness.
- [21] Pous-Romero, H., & Bhadeshia, H. (2014). Coalesced martensite in pressure vessel steels. *Journal of Pressure Vessel Technology, Transactions of the ASME*, 136(3), 1–6. <https://doi.org/10.1115/1.4026192>
- [22] Jiang, J., Britton, T. B., & Wilkinson, A. J. (2013). Measurement of geometrically necessary dislocation density with high resolution electron backscatter diffraction: Effects of detector binning and step size. *Ultramicroscopy*, 125, 1–9. <https://doi.org/10.1016/j.ultramic.2012.11.003>
- [23] Calcagnotto, M., Ponge, D., Demir, E., & Raabe, D. (2010). Orientation gradients and geometrically necessary dislocations in ultrafine grained dual-phase steels studied by 2D and 3D EBSD. *Materials Science and Engineering A*, 527(10-11), 2738–2746. <https://doi.org/10.1016/j.msea.2010.01.004>
- [24] Liu, H., Zhang, H., & Li, J. (2018). Thickness Dependence of Toughness in Ultra-Heavy Low-Alloyed Steel Plate after Quenching and Tempering. *Metals*, 8(628), 1–11. <https://doi.org/10.3390/met8080628>
- [25] ASTM International. (2020). *E1820: Standard Test Method for Measurement of Fracture Toughness* (tech. rep.). <https://doi.org/10.1520/E1820-20B>
- [26] Morris Jr, J. W., Kinney, C., Pytlewski, K., & Adachi, Y. (2013). Microstructure and cleavage in lath martensitic steels. *Science and Technology of Advanced Materials*, 14. <https://doi.org/10.1088/1468-6996/14/1/014208>

- [27] Bonnevie, E., Ferrière, G., Ikhlef, A., Kaplan, D., & Orain, J. M. (2004). Morphological aspects of martensite–austenite constituents in intercritical and coarse grain heat affected zones of structural steels. *Materials Science and Engineering: A*, 385(1-2), 352–358. <https://doi.org/10.1016/J.MSEA.2004.06.033>
- [28] Wang, Z., Shi, M., Tang, S., & Guodong Wang. (2017). Effect of Heat Input and M-A Constituent on Microstructure Evolution and Mechanical Properties of Heat Affected Zone in Low Carbon Steel. *Journal of Wuhan University of Technology, Materials Science Edition*, 32, 1163–1170. <https://doi.org/10.1007/s11595-017-1726-3>
- [29] Shome, M., Gupta, O. P., & Mohanty, O. N. (2004). Effect of simulated thermal cycles on the microstructure of the heat-affected zone in HSLA-80 and HSLA-100 steel plates. *Metallurgical and Materials Transactions A: Physical Metallurgy and Materials Science*, 35(13), 985–996. <https://doi.org/10.1007/s11661-004-1002-y>
- [30] Zhang, J., Xin, W., Luo, G., Wang, R., & Meng, Q. (2020). Significant Influence of Welding Heat Input on the Microstructural Characteristics and Mechanical Properties of the Simulated CGHAZ in High Nitrogen V-Alloyed Steel. *High Temperature Materials and Processes*, 39(1), 33–44. <https://doi.org/10.1515/htmp-2020-0003>
- [31] Zhu, Z., Kuzmnikova, L., Li, H., & Barbaro, F. (2014). Effect of inter-critically reheating temperaure on microstructure and properties of simulated inter-critically reheated coarse grained heat affected zone in X70 steel. *Materials Science & Engineering A*, 605, 8–13.
- [32] Fu, C., Li, X., Li, H., Han, T., Han, B., & Wang, Y. (2022). Influence of ICCGHAZ on the Low-Temperature Toughness in HAZ of Heavy-Wall X80 Pipeline Steel. *Metals*, 12(6), 907. <https://doi.org/10.3390/met12060907>
- [33] Chen, J. H., & Cao, R. (2015). *Micromechanism of Cleavage Fracture of Metals*. Butterworth-Heinemann. <https://doi.org/10.1016/B978-0-12-800765-5.00003-4>
- [34] Gu, C., Lian, J., Bao, Y., Xiao, W., & Münstermann, S. (2019). Numerical Study of the Effect of Inclusions on the Residual Stress Distribution in High-Strength Martensitic Steels During Cooling. *Applied Sciences*, 9(455), 1–13. <https://doi.org/10.3390/app9030455>
- [35] Griffith, A. A. (1920). The Phenomena of Rupture and Flow in Solids. *Philosophical Transactions of the Royal Society A: Mathematical, Physical and Engineering Sciences*, 100, 163–198.
- [36] Li, X., Ma, X., Subramanian, S. V., Misra, R. D. K., & Shang, C. (2015). Structure–Property–Fracture Mechanism Correlation in Heat-Affected Zone of X100 FerriteBainite Pipeline Steel. *Metallurgical and Materials Transactions E*, 2(1), 1–11. <https://doi.org/10.1007/s40553-014-0036-3>
- [37] Wang, X. L., Nan, Y. R., Xie, Z. J., Tsai, Y. T., Yang, J. R., & Shang, C. J. (2017). Influence of welding pass on microstructure and toughness in the reheated zone of multi-pass weld metal of 550 MPa offshore engineering steel. *Materials Science and Engineering A*, 702(April), 196–205. <https://doi.org/10.1016/j.msea.2017.06.081>
- [38] Tyson, W. R., Ayres, R. A., & Stein, D. F. (1973). Anisotropy of cleavage in B.C.C. transition metals. *Acta Metallurgica*, 21(5), 621–627. [https://doi.org/10.1016/0001-6160\(73\)90071-0](https://doi.org/10.1016/0001-6160(73)90071-0)

- [39] Berejnoi, C., Perez Ipiña, J., & Llorente, C. (2000). Reproducibility of pop-ins in laboratory testing of welded joints. *Materials Research*, 3(4), 139–146. <https://doi.org/10.1590/s1516-14392000000400008>
- [40] Pisarski, H. G., Hammond, R., & Watt, K. (2008). Significance of splits and pop-ins observed during fracture toughness testing of line pipe steel. *Proceedings of the IPC 2008, 7th International Pipeline Conference*. <https://doi.org/10.1115/IPC2008-64676>
- [41] Kyada, T., Shant, J. R., Goyal, R. K., & Kathayat, T. S. (2014). Understanding the Delamination and Its Effect on Charpy Impact Energy in Thick Wall Linepipe Steel. *Journal of Materials and Metallurgical Engineering*, 4(1), 31–39.
- [42] Neimitz, A., Galkiewicz, J., & Dzioba, I. (2010). The ductile-to-cleavage transition in ferritic Cr-Mo-V steel: A detailed microscopic and numerical analysis. *Engineering Fracture Mechanics*, 77(13), 2504–2526. <https://doi.org/10.1016/j.engfracmech.2010.06.003>
- [43] Ramachandran, D. C., Kim, S. D., Moon, J., Lee, C. H., Chung, J. H., Biro, E., & Park, Y. D. (2020). Classification of martensite-austenite constituents according to its internal morphology in high-strength low alloy steel. *Materials Letters*, 278(128422), 1–5. <https://doi.org/10.1016/j.matlet.2020.128422>

6

GRAIN REFINEMENT BY RAPID CYCLIC HEATING AND ITS EFFECT ON CLEAVAGE FRACTURE BEHAVIOUR OF AN S690 HIGH STRENGTH STEEL

The simultaneous improvement of strength and toughness with grain refinement is widely known. However, the literature lacks studies on the grain refinement effect on cleavage fracture toughness in multiphase steels containing detrimental brittle inclusions. Understanding whether the grain refinement can effectively improve fracture toughness of such steels will allow for the improvement of their design. Therefore, a quenched and tempered S690QL high strength steel with Nb-rich and oxide inclusions was subjected to a rapid cyclic heating (RCH) treatment aimed at grain refinement, followed by quenching and tempering to produce a microstructure equivalent to the as-received steel. The microstructure was investigated via scanning electron microscopy (SEM), energy-dispersive X-ray spectroscopy (EDS), and electron backscatter diffraction (EBSD). The resultant cleavage fracture toughness was measured via three-point bending tests at $-100\text{ }^{\circ}\text{C}$. The RCH effectively reduced the prior austenite grain size by 55%. However, other microstructural changes occurred. The elongated, parallel-aligned block sub-structure of martensitic/bainitic grains changed to rounded, randomly distributed blocks. Also, the ferritic content increased and martensite and cementite clusters were formed. The concurrent effects of microstructural modifications and grain refinement explain the very minor improvements in hardness and tensile properties. The grain refinement, theoretically responsible for decreasing the ductile-to-brittle transition temperature, improved the fracture toughness up to a factor of 2.5 and 8.6 when Nb-rich and oxide inclusions trigger fracture, respectively. The microstructural changes have minor effects on fracture toughness. Therefore, the proposed RCH treatment is effective in reducing the grain size and improving cleavage fracture toughness in steels containing brittle inclusions.

This chapter is based on the scientific publication Bertolo, V., Vilasi, L., Jiang, Q., Riemsdag, T., Scott, S., Walters, C., Sietsma, J. & Popovich, V. (2023). Grain Refinement by Rapid Cyclic Heating and its Effect on Cleavage Fracture Behaviour of an S690 High Strength Steel, *Journal of Materials Research and Technology*, 23, 1919-1933. <https://doi.org/10.1016/j.jmrt.2023.01.164>

6.1. INTRODUCTION

The concept that grain refinement simultaneously allows enhancement of the strength and toughness of metals has been extensively discussed over the years [1–6]. The Hall-Petch law [7, 8] is widely known for relating grain size with strength and hardness, where both are inversely proportional to the square root of the grain size. These correlations extend to cleavage stress and the ductile-to-brittle transition temperature (DBTT) [3, 9, 10]. Smaller grain size causes a higher cleavage stress and a lower DBTT [3, 9, 10]. Consequently, toughness is improved. Hence, for materials that exhibit ductile-to-brittle transition with temperature reduction (e.g., high strength bcc steels), grain refinement may be strongly valued for structural low-temperature applications. However, these relationships are generic and may be considered oversimplified in the case of multiphase materials, such as high strength steels, that contain brittle second-phase particles which are responsible for triggering fracture and reducing the steel's fracture toughness [11, 12]. The publications on the effect of grain refinement on toughness [3, 9, 10, 13] do not report the presence of brittle particles in the researched materials. Then, the question is raised whether the presence of brittle particles would negate the favourable effect of grain refinement. Therefore, it is essential to understand the interplay between grain refinement and brittle second-phase particles and their effects on cleavage fracture toughness.

6

Grain refinement can be achieved by various methods, the most popular being thermomechanical routes involving deformation and heat treatments purely involving variations in temperature [2, 14–19]. Heat treatments have some advantages over thermomechanical routes, such as the possibility of being performed on thick-section plates and welds [1]. This is of great interest for industrial applications that use thick-section high strength steels to support high loads and use welding processes to connect various structural components (e.g., highly loaded offshore lifting equipment). One type of heat treatment widely acknowledged as efficient for reducing grain size is the rapid cyclic heating (RCH) method [4, 6, 18–20]. For instance, Grange [18], in one of the first publications related to RCH, reports the significant reduction of prior austenite grain size in various steel types after applying the RCH. Furthermore, the author also shows further grain size reduction by increasing the number of cycles [18]. In a recent publication, Park, Tibata and Tsuji [4] observed a decrease in the austenite grain size from 244 μm to 36 μm after the first cycle, and a final austenite grain size of 11.9 μm after four cycles in a 2Mn-0.1C (wt.%) steel. Other researchers investigated the effect of grain size reduction via thermal cyclic heat treatment on toughness [20, 21]. Aweda, Orhadahwe, and Ohijeagbon [20] observed an increase of 10% and 30% in energy absorbed before fracture after 6% and 20% grain size reduction, obtained by 1 and 4 cycles, respectively, in a mild steel. Lv, Ren, Li et al. [21] reported a maximum Charpy-U notch impact absorbing energy after 3 cycles where the grain size was reduced by 30% and the Charpy energy increased by 100% in a Ti-V microalloyed steel. Nevertheless, the authors [21] explain that such an effect is not the exclusive result of grain refinement, but also due to a microstructural effect of pro-eutectoid ferrite.

On the contrary, brittle inclusions are known to initiate cleavage cracks in high strength steels and their presence in steel decreases their toughness at low temperatures

[11, 12, 22]. Some of these inclusions are more detrimental than others due to characteristics such as hardness and morphology (e.g., cubic vs. spherical). For instance, both Nb-rich and oxide inclusions are present in the high strength steel investigated in this study, and, in another study by the present authors [11], it has been reported that specimens that have fracture initiated from Nb-rich inclusions show the lowest fracture toughness. This effect is attributed to the higher hardness, sharp edges that act as stress concentrators, and larger sizes of Nb-rich inclusions compared to the oxide ones. Moreover, Nb-rich inclusions embrittle the steel so much that in the condition of low crack-tip plastic constraint the fracture toughness remains low [11]. These results show the detrimental effect of such type of inclusion. Hence, it is of interest to know ways to improve the low-temperature toughness of these steels. Nevertheless, it is not yet reported in the literature if the presence of such detrimental inclusions can counterbalance or overcome the positive effects of grain refinement. Moreover, although several studies related to grain refinement on toughness can be found in the literature, a small part being related to thermal cyclic heat treatments, research investigating grain refinement and its effect on microstructure of inhomogeneous high strength steels and the resulting cleavage fracture micromechanisms are not available.

In this study, we research the possibility and efficiency of RCH in reducing the grain size of a quenched and tempered S690QL high strength steel and investigate the combined effect of grain refinement and brittle inclusions on the cleavage fracture toughness. For this purpose, the steel was first subjected to the RCH and then to the same quenching and tempering treatment as the as-received material. The thermal route proposed in this study aims for grain refinement but an otherwise equivalent final microstructure between the as-received and the heat treated material. Then, the grain refinement would be the only factor affecting the fracture toughness of the as-received material, allowing for the study of the grain refinement effect. After the heat treatment, the final microstructure was characterised, tensile properties measured and the cleavage fracture toughness investigated via three-point bending tests at $-100\text{ }^{\circ}\text{C}$, a temperature at which cleavage is dominant. To elucidate the fracture micromechanisms in the heat treated material, the fracture surface was examined. This work experimentally assesses the possibility and analyses the effectiveness of using a simple heat treatment route to improve cleavage fracture of multiphase high strength steels that contain detrimental brittle particles, allowing for the improvement of high strength steel's design. Moreover, the quantitative data presented herein can be used as a validation of cleavage modelling methods, assessing whether the models can quantitatively predict the influence of grain size. Also, this study provides insight into the determination of model parameters to account for changes in prior austenite grain sub-structures (e.g., packets and blocks).

6.2. MATERIALS AND METHODS

The material used in this work is a commercial 80 mm thick quenched and tempered S690 high strength steel. Previous studies [11, 23] characterised the microstructure and fracture behaviour of this steel in-depth and concluded that the middle section of the plate (40 mm from the surface) has the least favourable microstructure for cleavage fracture. Thus, this research is focused on the middle section of the S690QL steel

plate, as it represents the most critical part of this material. The chemical composition of the middle section of the plate is 0.16 ± 0.001 C, 0.30 ± 0.03 Si, 0.080 ± 0.011 Al, 0.29 ± 0.02 Mo wt.%, and other elements such as Mn, Ni, Cr, Nb, and B in low concentrations. The elemental content range of the alloying elements is in accordance with the EN10025-6 standard [24].

The grain refinement heat treatment was carried out in a Gleeble-1500 thermo-mechanical simulator. The thermal profile consists of two sequential steps: 1) RCH and 2) quenching and tempering. The RCH is the step responsible for grain refinement. The following quenching and tempering steps follow the same profile as for the as-received steel to have equivalent microstructures in both materials. Then, it will be possible to directly compare the as-received and heat treated materials and analyse the effect of grain refinement on the material performance. The thermal profile performed in the Gleeble is shown in Fig. 6.1. The peak temperature range for the tempering step is between 600 °C and 650 °C. This is represented by the hatched area in Fig. 6.1. As a consequence, two curves are seen in the cooling part of the tempering process meaning that the cooling process takes place within this range, depending on the peak temperature. The RCH method consists of rapidly heating the material to a temperature in the range between Ac_1 and Ac_3 (start and end temperature of the austenite formation, respectively) or slightly above Ac_3 . Then, the material is held at this temperature to ensure a homogeneous temperature distribution throughout the sample. These first two steps minimize the austenite grain growth. Subsequently, the material is quickly cooled in order to transform austenite to lath martensite. As a result of the diffusionless shear transformation and the hierarchical substructures of lath martensite, a high dislocation density and a high density of high-angle grain boundaries (e.g., prior austenite grain, packets, and block boundaries) are generated. Both dislocations and high-angle grain boundaries serve as nucleation sites for austenite [4]. Therefore, after the first cycle (from an initial martensitic microstructure), the already refined (transformed) microstructure provides more austenitic nucleation sites for the next cycle. Consequently, consecutive heat treatment cycles allow for a progressive reduction in grain size. Note that the greatest grain refinement takes place in the first cycle if the initial microstructure is a fine aggregate (e.g., martensite and tempered martensite). In cases where the initial microstructure is different from these, an initial cycle is performed to first transform the as-received microstructure into martensite [18]. In subsequent cycles, the grain size only slightly reduces, and after a certain number of cycles (usually around 4) almost no additional reduction in grain size is observed [4, 21]. The reason is that, packets and blocks are also refined in each cycle and, as the austenite grains become smaller, only prior austenite grain (PAG) boundaries serve as nucleation sites for austenite upon heating. Hence, after a certain number of cycles, a balance between refinement by nucleation and grain growth after austenitisation is reached, leading to a limitation in grain refinement [4, 18]. Note that the thermal profile used in this work includes only one cycle of the RCH. Initial trials were performed with 1 and 2 cycles, and no significant grain refinement was observed after the first cycle. This is probably related to the already small prior austenite grains (average around 20 μm [22]) of the as-received material. Hence, it was decided to further continue heat treating with only one cycle. It should be mentioned that, due to the focus of this study on the presence

of brittle inclusions, thermodynamic simulations in Thermo-Calc® were performed to estimate the dissolution temperature of pre-existing inclusions.

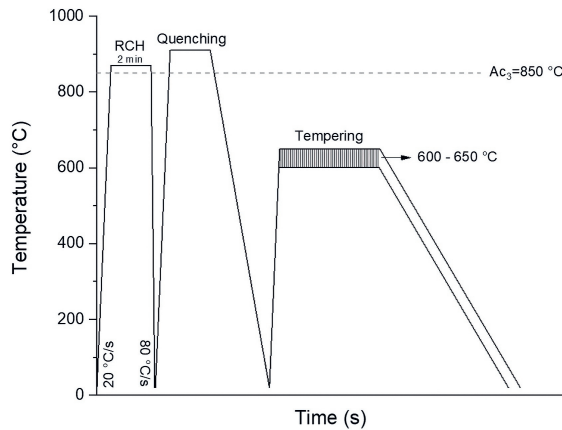


Figure 6.1: Proposed thermal profile aimed at grain refinement (RCH step) followed by quenching and tempering steps equivalent to the profile applied for the as-received steel. The hatched area corresponds to the peak temperature range that is reached during the tempering step.

Three cylindrical samples, 80 mm x 6 mm (length along rolling direction x diameter) were heat treated and used further for microstructural characterisation. The temperature was measured to be homogeneous in a 6 mm long region at the centre of the specimen. The samples were metallographically prepared following grinding and polishing steps and then etched with Nital 5%. Scanning electron microscope with energy-dispersive X-ray spectroscopy (SEM/EDS) and electron backscatter diffraction (EBSD) were used for microstructural investigation within the homogeneously heat-treated volume. Inclusions were qualified and quantified via SEM according to ASTM 1245-03:2016 [25]. For EBSD analysis, 6 representative areas were scanned: 3 outside the segregation bands and 3 including segregation bands. To identify the segregation bands, the sample was etched prior to the final polishing step for EBSD, and micro-Vickers indentations (HV_3) were performed in two points through the length of some bands to be used as landmarks. After polishing, the indentation imprints were still present. EBSD data was acquired on a Helios G4 PFIB SEM using a current of 3.2 nA and 30 kV accelerating voltage, a tilt angle of 70° using TEAM EDAX software, a step size of 0.15 μm , and post-processed with EDAX-TSL-OIM Analysis™ v7 software. Afterwards, the following clean-up procedure was applied: 1) Grain fit standardisation with a grain tolerance angle of 5° and minimum grain size of 4 pixels, considering that grains contain multiple pixel rows; 2) Neighbour orientation correlation with a grain tolerance angle of 5° and a minimum confidence index of 0.1; 3) Neighbour phase correlation with a minimum confidence index of 0.1. Grains were defined with a tolerance angle of 5° and a minimum size of 4 pixels. By using the grain orientation provided by EBSD, the PAGs were reconstructed by means of ARPGE software [26] in automatic mode. Afterwards, the PAG data was post-processed in the EDAX-TSL-OIM Analysis™ v7 software and the grain aspect ratio, major axis (length) and minor axis (width) distributions were ob-

tained. The elemental segregation in the bands was quantified by Electron Microprobe Analysis (EPMA) with a JEOL JXA 8900R microprobe using an electron beam with energy of 10 keV and beam current of 200 nA employing Wavelength Dispersive Spectrometry (WDS). Line scans were performed in 3 μm increments with start and end points 150 μm below and above the centres of the segregation bands. The grain refinement effect on the microstructure was also evaluated via micro-Vickers hardness measurements using a load of 3 kgf.

To evaluate the effect of grain refinement on mechanical properties, uniaxial tensile tests were performed at room temperature at a cross-head displacement of 0.2 mm/s using an Instron 5500R 100 kN machine. From these tests, the yield ($R_{0.2\%}$) and tensile strength (R_m) at -100°C , a temperature at which the material is in a cleavage fracture regime, were calculated by

$$R_{0.2\%(T)} = R_{0.2\%(T_R)} + \frac{10^5}{(491 + 1.8T)} - 189 \quad (6.1)$$

$$R_m(T) = R_m(T_R) + (0.7857 + 0.2423 \exp(\frac{-T}{170.646})) \quad (6.2)$$

where T is the assessment temperature and T_R is room temperature in degrees Celsius. These equations are defined in the BS7910:2013+A1:2015 standard [27].

A set of three tensile specimens with a gauge length of 40 mm, aligned to the rolling direction, and a diameter of 8 mm were heat treated following the thermal profile in Fig. 6.1. A homogeneously heat-treated gauge length of 10 mm was produced. In order to obtain the properties of the refined microstructure, the cross-section was reduced by 50% within the homogeneously heat-treated gauge length to ensure higher stresses in this zone. Figure 6.2 (a) illustrates the dimensions of the specimen after the cross-section reduction.

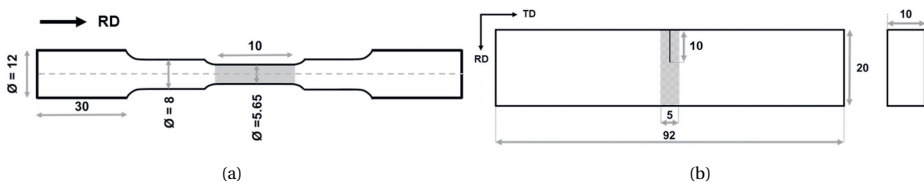


Figure 6.2: Dimensions of heat treated (a) tensile and (b) sub-sized SENB specimens. The homogeneously heat-treated area is coloured grey. All dimensions are in mm (Adapted from [28])

A total of eight sub-sized single edge-notched bending (SENB) specimens (Fig. 6.2(b)) were heat treated according to the profile described in Fig. 6.1, creating a homogeneous microstructure along 5 mm of the specimen's centre. Subsequently, a notch was machined in the centre of the specimen parallel to the rolling direction. The crack/width ratio (a/W) of all specimens is 0.5. The fracture toughness of the grain-refined material was measured through three-point bending tests, following a similar procedure to the ISO 12135 standard [29], at a displacement rate of 2 mm/s, at -100°C , using a 350 kN MTS 858 servo-hydraulic test rig. The fracture surfaces were

examined under SEM/EDS to identify the microstructural features associated with the fracture initiation event and to compare the fracture appearance with the as-received material.

6.3. RESULTS

Figure 6.3 displays the microstructures of the as-received and the heat treated S690QL steel. By visual inspection at the same magnification (Fig. 6.3 (a) and (b)) it can be noticed that the PAG size was considerably reduced following the heat treatment. The PAG size was quantified and will be presented and discussed in detail later. It should be noted that other features of the microstructure of the as-received S690QL were also modified during the heat treatments, as seen in Fig. 6.3 (c) and (d). The phases observed in the as-received steel, such as ferrite (F), tempered bainite (TB), and tempered martensite (TM), are also present in the heat treated material. However, the internal sub-structures of martensitic and bainitic grains, featuring elongated blocks densely aligned parallel to each other, which was observed in the as-received material, are clearly changed. Moreover, the content of ferrite is increased considerably and fresh martensite (M) is formed. Additionally, carbide distribution is found to be inhomogeneous, where the carbide content is found reduced in the matrix and concentrated as clusters in some areas (indicated by a red arrow in Fig. 6.3 (d) after the heat treatment). A cluster of cementite is presented in more detail and indicated by white arrows in Fig. 6.3 (e).

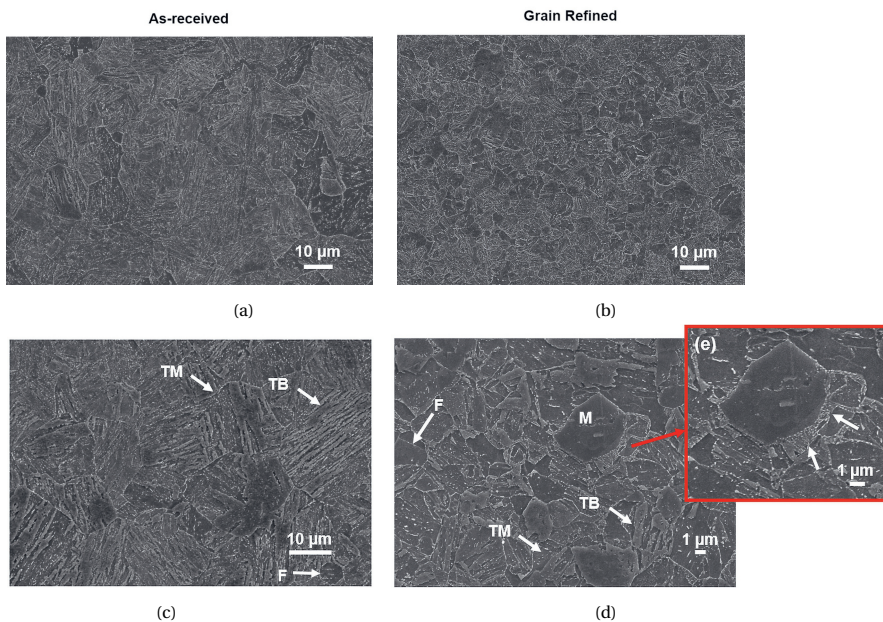


Figure 6.3: SEM micrographs of the (a),(c) as-received and the (b),(d) heat treated S690QL for the grain refinement study. The red arrow in (d) indicates a cluster of cementite formed during the heat treatment.

These clusters are presented in more detail in (e) where they are indicated by white arrows.

Inclusions have been found to strongly affect the cleavage fracture of the as-received steel [11]. Hence, inclusions were characterised and quantified after the heat treatment to investigate whether any changes took place that could affect the fracture behaviour of the heat treated material. Minor differences were observed in terms of chemical composition, size, and area fraction between the as-received [23] and the heat treated steel (Table 6.1). Figures 6.4 (a) and (b) exemplify the spherical and cubic inclusions found after the heat treatment. The differences are likely related to sampling effects as the formation of oxide inclusions takes place during the second metallurgy step of the steelmaking process [23]. The performed heat treatment is not expected to cause nucleation and growth of inclusions, since thermodynamic simulations via ThermoCalc give dissolution temperatures of 1161 °C for Nb–Ti carbonitrides, 1330 °C for Ti carbonitrides and 1754 °C for Al oxides (Fig. 6.4(c)). The maximum temperature reached during the heat treatment, 870 °C, is distinctly lower than the dissolution temperature of inclusions present in the as-received steel. The equilibrium fraction of cubic (Nb, Ti)(C, N) decreases according to the thermodynamic simulations, but this was not observed in the inclusion quantification analysis. Therefore, as observed, the differences between the as-received and heat treated material are minor and are not expected to be related to the performed heat treatment. The cracks observed in the cubic inclusions themselves and in the interface inclusion/matrix in the as-received material due to the rolling step [23] remain present after the heat treatment (Fig. 6.4 (b)) which is also evidence that these inclusions do not dissolve by the grain refinement heat treatment.

Table 6.1: Chemical composition, major axis range, and area fraction of spherical and cubic inclusions observed in the as-received steel and the material after the grain refinement heat treatment.

Material	Composition	Major Axis Range (µm)	Area Fraction (x10 ⁻⁴)
Spherical Inclusions			
As-received	(Mg,Al,Ca)(O) (Mg,Al,Ca,B)(N,S) (Mg,Al,Ca,Ti)(O,N)	1 – 5	7 ± 3
Grain Refinement HT	(Mg,Al,Ca)(O) (Mg,Al,Ca)(O,S) (Mg,Al,Ca,Ti)(O,N) (Mg,Al,Ca,B)(O,N)	1 – 7	2 ± 1
Cubic Inclusions			
As-received	(Nb,Ti,Mg,Ca)(C,O,N) NbC (Nb,Ti)(C) (Nb,Ti)(C,N)	1 – 12	2.0 ± 0.3
Grain Refinement HT	(Nb,Ti,Mg,Ca)(O,C) (Nb,Ti)(C) (Nb,Ti)(C,N) NbC	1 – 8	3 ± 1

Segregation bands parallel to the rolling direction, present in the as-received steel and observed to affect the local microstructure (e.g., grain size and phase distribution) [23], were retained in the heat treatment. In order to characterise elemental diffusion under influence of temperature and time, the chemical composition of segregation bands

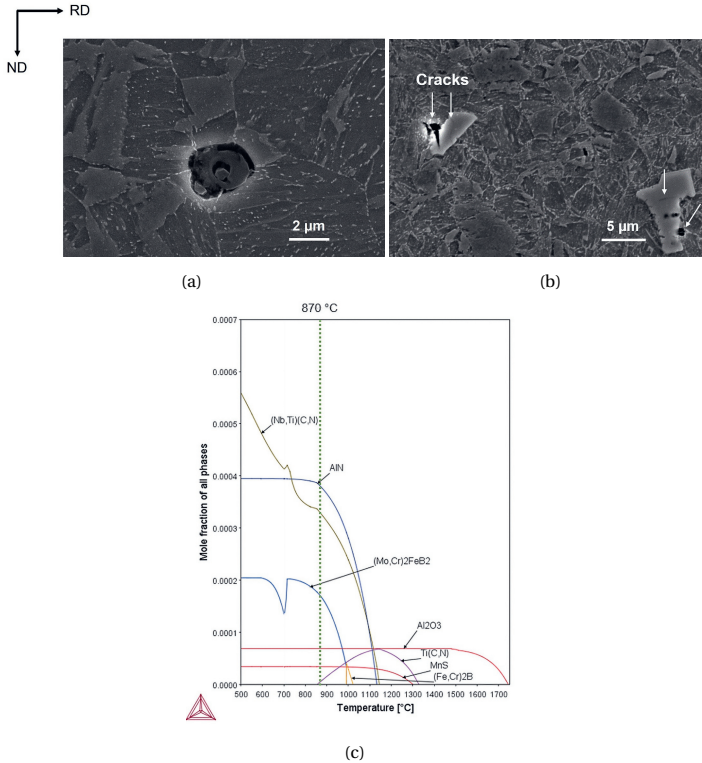


Figure 6.4: SEM micrographs of (a) spherical (Mg, Al, Ca) (O, N, S) and (b) cubic NbC inclusions. The white arrows in (b) indicate defects associated with the cubic inclusions. The equilibrium fractions of second-phase particles for the steel under study predicted via Thermo-Calc® thermodynamic simulations are presented in (c).

in the heat treated material was measured by EPMA and compared with the as-received material. Figure 6.5 presents an optical micrograph of the retained segregation bands after the heat treatment and displays the maximum elemental content in the bands for the as-received S690QL steel and the steel after the grain refinement heat treatment. The EPMA result shows that there are no significant changes in the maximum elemental content of the segregation bands of the as-received material after the heat treatment.

The as-received quenched and tempered S690 high strength steel did not have significant texture [23]. Likewise, since the material is only submitted to thermal cycles, the grains continue to be randomly oriented after the heat treatment. Information regarding low and high misorientation angles was retrieved and their distribution was determined by EBSD (Fig. 6.6). It follows from Fig. 6.6 that there are two main peaks, at 54° and 60°, of which the lower one shifts to lower angles after the heat treatment considering the areas including segregation bands. Additionally, increased density in the range of 30° and 45° is observed for these areas with segregation bands. However, the observed differences between the as-received and heat treated materials are not significant.

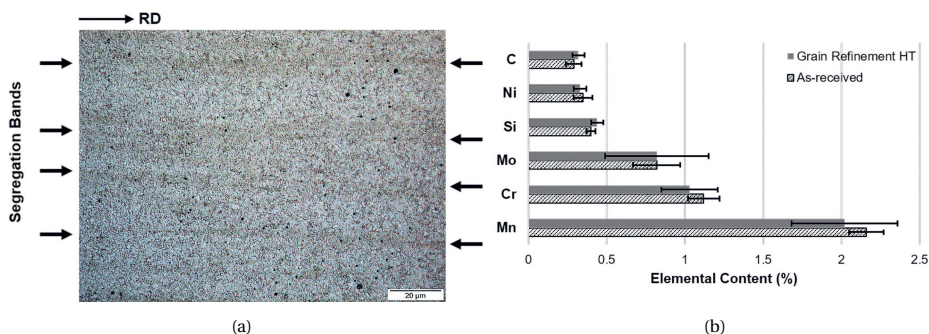


Figure 6.5: (a) Optical micrograph of the grain refined steel showing the retained segregation bands and (b) average maximum elemental content (wt.%) of segregation bands measured by EPMA for the as-received and grain-refined S690QL steel.

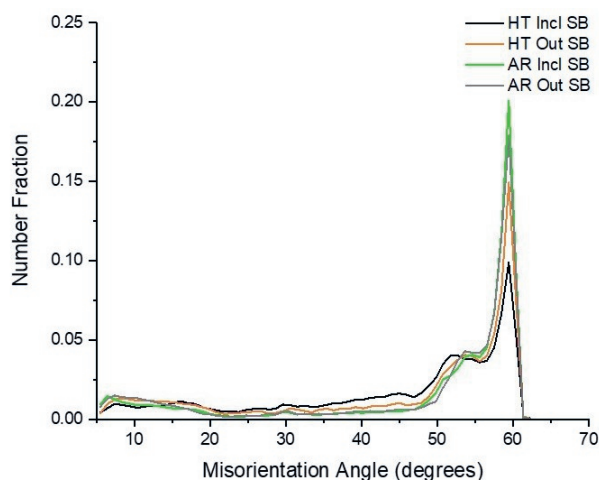


Figure 6.6: Grain boundary misorientation distribution for the as-received (AR) and heat treated (HT) S690QL steel in areas outside and including segregation bands (SB).

The reconstructed PAGs after the heat treatment are non-equiaxed having an average aspect ratio of 0.48, similar to the as-received S690QL steel. Due to their non-equiaxed shape, the PAG grain size was quantified with respect to their width and length. Figure 6.7 shows the PAG width and length distribution and reconstructed PAG average values for areas outside, including, and in the segregation bands. The data from the base material is added for comparison. As can be seen, the as-received material has a PAG width and length of up to 25 and 70 μm, respectively. After the heat treatment, these values are reduced to 8 and 20 μm, respectively. Through the heat treatment, a relative average grain size reduction of around 55% is achieved in all areas (outside and inside the segregation bands) (Fig. 6.8). It also means that, as observed for the as-received material [23], segregation bands keep their smaller grain sizes compared to the surrounding matrix areas.

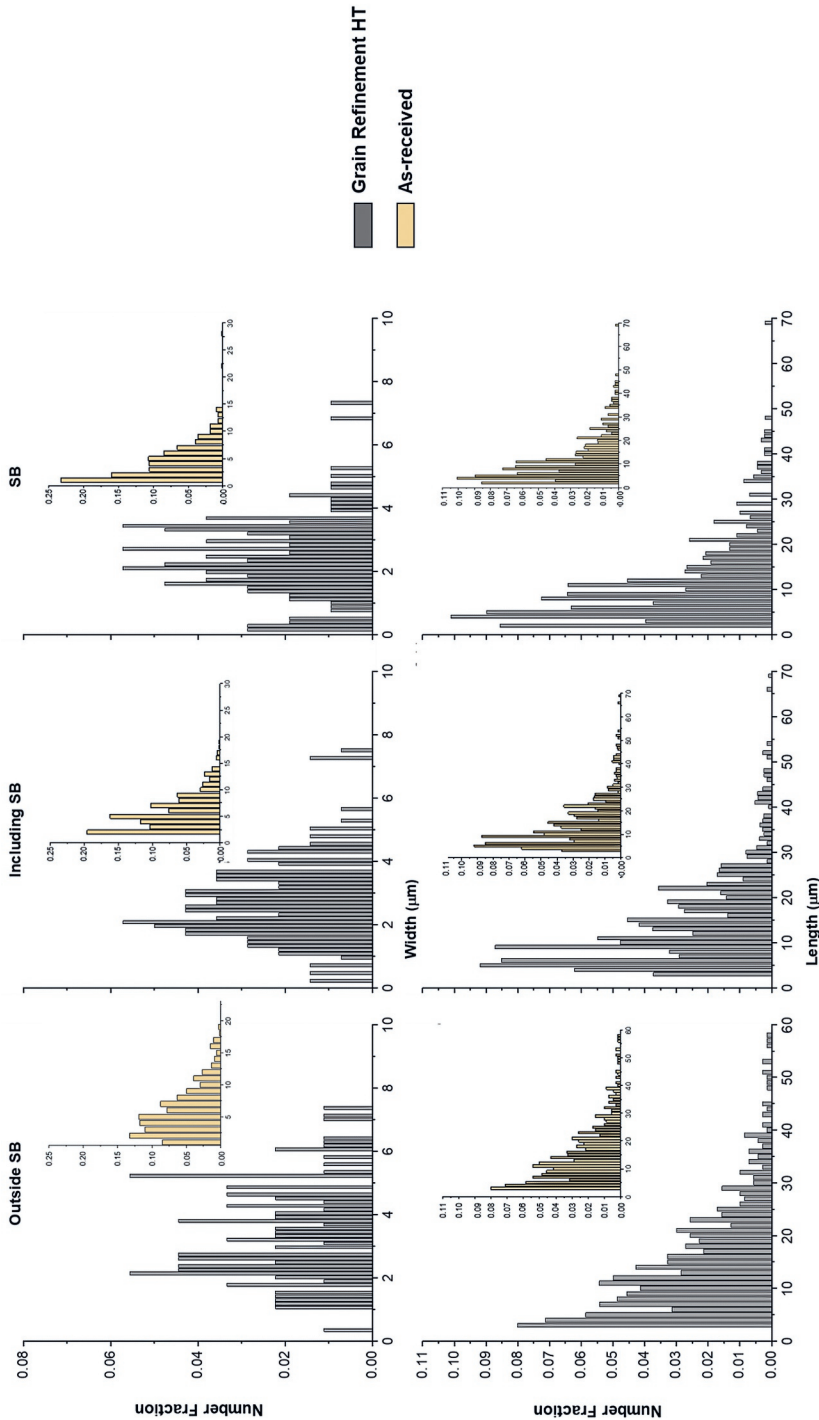


Figure 6.7: Prior austenite grain size represented as distributions of their width and length for the as-received and heat treated S690QL high strength steel outside, including, and inside segregation bands.

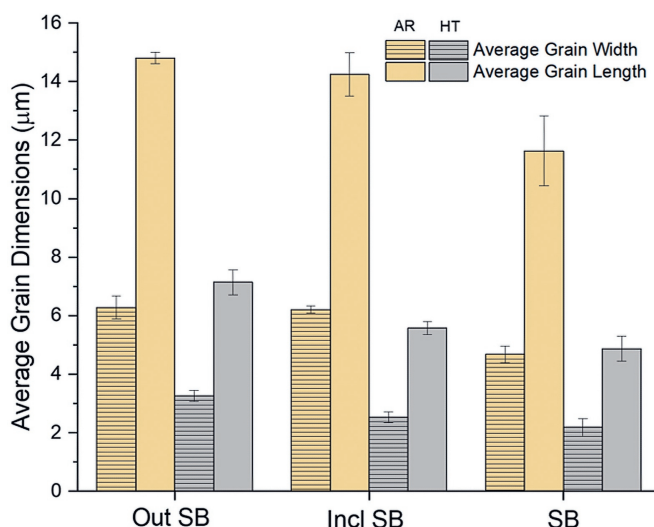


Figure 6.8: Average PAG width and length and their standard deviation from the mean for the as-received and heat-treated S690QL high strength steel for areas outside, including and inside segregation bands.

6

To evaluate the effect of the heat treatment (grain refinement and microstructural changes) on the mechanical properties of the as-received steel, the tensile properties and micro-Vickers hardness of the as-received and heat-treated S690QL steel at room temperature and $-100\text{ }^{\circ}\text{C}$ are presented in Table 6.2. Note that for the as-received steel, tensile tests were carried out on standard specimens and the cross-head displacement was 1.2 mm/s to be proportional to the gauge length (six times larger than for the heat treated specimens). Minor increases of less than 10% in tensile properties and hardness were achieved with a PAG size reduction of 55%.

Table 6.2: Tensile and Micro-Vickers hardness properties of middle sections of the as-received and heat treated S690QL at $-100\text{ }^{\circ}\text{C}$ and room temperature (RT).

Material	Hardness (HV3)	Yield Strength (MPa)		Tensile Strength (MPa)	
	RT	RT	$-100\text{ }^{\circ}\text{C}$	RT	$-100\text{ }^{\circ}\text{C}$
As-received	272 ± 11	739 ± 11	895 ± 12	861 ± 12	1013 ± 13
Grain Refinement HT	280 ± 15	810 ± 24	942 ± 24	875 ± 17	1068 ± 20

In contrast, the fracture behaviour changes significantly after the grain refinement heat treatment. In total, 10 and 8 sub-sized SENB specimens of the as-received and heat treated material, respectively, were tested at $-100\text{ }^{\circ}\text{C}$. As can be seen in Fig. 6.9, after the heat treatment, the material displays a considerably larger scatter, accompanied by an increase in the average crack tip opening displacement (CTOD) value. Considering the lower and upper bound, the heat treated material shows increase by a factor 2.5 and 8.6, respectively, in fracture toughness compared to the as-received S690QL steel. In terms of the average CTOD value, the increase is by a factor 6.

In order to differentiate between the fracture behaviour of the material before and af-

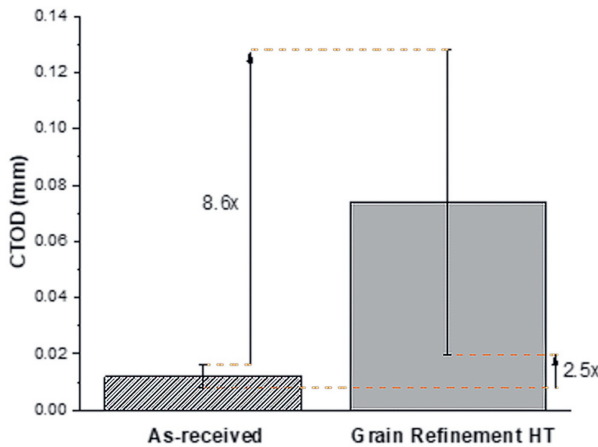


Figure 6.9: CTOD and standard deviation from the mean at $-100\text{ }^{\circ}\text{C}$ of the as-received and heat treated S690QL steel.

ter the grain refinement heat treatment, the fracture surfaces were analysed. A detailed discussion on the fracture micromechanisms of the as-received material is presented in [11]. The lowest CTOD values were found to be associated with fracture initiation from Nb-rich inclusions, as shown in Fig. 6.10. On the other hand, the largest CTOD values were either associated with oxide inclusions, as shown in Fig. 6.11, or an initiation site that was not identified, meaning that other features such as carbides could also be involved in the process. This is contrary to the as-received material where all tested specimens have fracture triggered by Nb-rich inclusions.

6.4. DISCUSSION

6.4.1. MICROSTRUCTURAL TRANSFORMATIONS DUE TO GRAIN REFINEMENT

The microstructure of the S690QL high strength steel was changed after the RCH. This shows that being subsequently submitted to the same quenching and tempering routes of the as-received material does not annihilate the microstructural changes in the RCH cycle. Differences such as the martensitic and bainitic block arrangement, cementite distribution, including cluster formation, larger ferritic fraction, and the formation of fresh martensite were observed. These aspects are related to PAG refinement.

The morphological change of martensitic and bainitic grains as a result of PAG refinement is reported in the literature [1, 19, 30]. Besides having the packet size and block width reduced with the PAG size refinement, the number of Kurdjumov-Sachs (K-S) variants is also reduced [19, 30]. Furthermore, as a result of RCH, the parallel alignment of

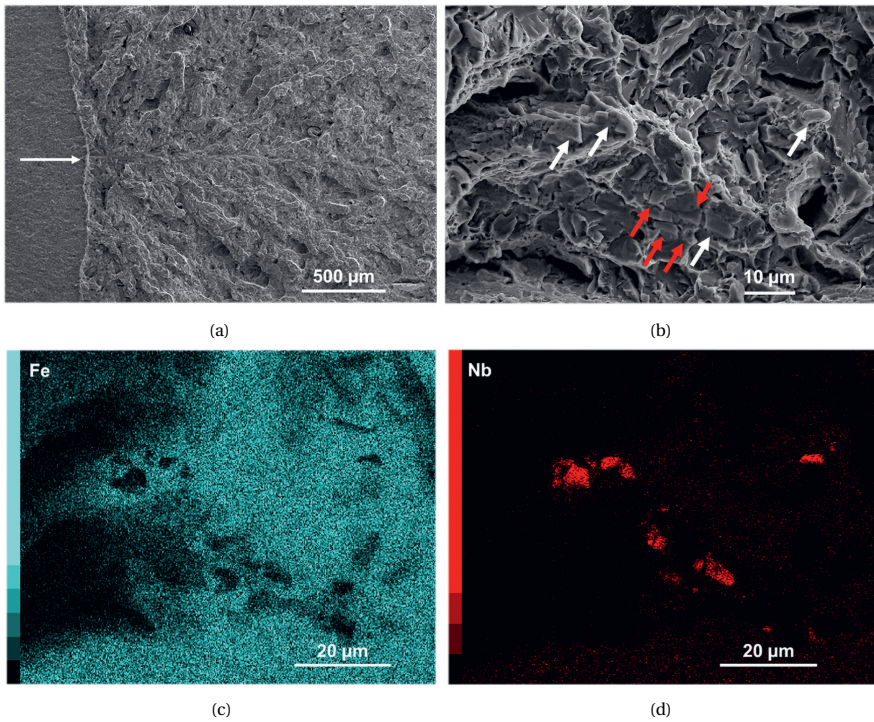


Figure 6.10: Fractographic SEM image showing (a) local river lines indicating the initiation in a specimen fractured at $-100\text{ }^{\circ}\text{C}$ ($\text{CTOD} = 0.03\text{ mm}$) and (b) a cleavage facet with Nb-rich particles, highlighted by white and red arrows identified by EDS mapping (Fe (c) and Nb (d)). The red arrows in (b) indicate the Nb-rich inclusions that were located in the cleavage facet and were directly contributed to the fracture initiation process.

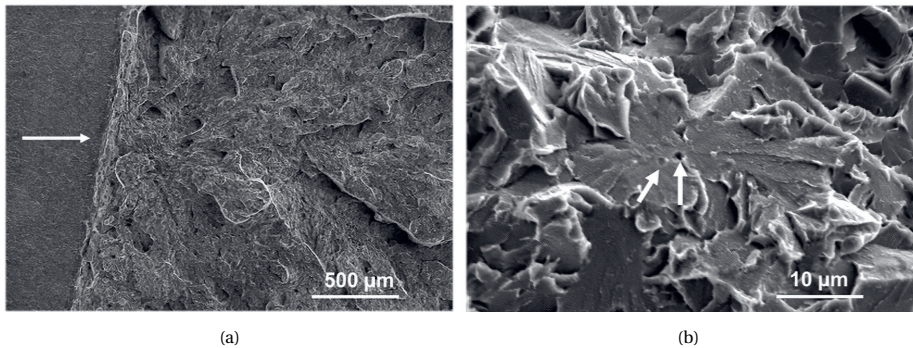


Figure 6.11: Fractographic SEM image showing (a) local river lines indicating a likely initiation site in a specimen fractured at $-100\text{ }^{\circ}\text{C}$ ($\text{CTOD} = 0.1\text{ mm}$) and (b) a cleavage facet where $(\text{Mg,Ca})(\text{O})$ and $(\text{Mg,Al,Ca,B})(\text{O,N})$ inclusions, indicated by white arrows, triggered fracture.

elongated blocks inside the PAGs is observed to be broken up and replaced by rounded blocks [1, 19]. Figure 6.12 (a) presents the martensite/bainite packet size and block widths for the as-received [23] and the grain-refined S690QL steel in areas outside, including and inside segregation bands. The average packet size and block width are reduced by around 60% and 40%, respectively. Figures 6.12 (b) – (e) show, as an example, single PAGs for the as-received and grain-refined S690L steel outside segregation bands and their (001) and (101) pole figures, where each colour represents packets that share the same habit plane. As can be seen, the dense arrangement of elongated, parallel blocks present in the as-received material is replaced by rounded, randomly distributed blocks. The number of packets inside the martensitic/bainitic grains is also reduced. Additionally, the number of K-S variants transformed during the cyclic heat treatment is decreased, and this is very distinct from the differences in the density of points in the pole figures (Fig. 6.12(c) and (e)), where the as-received material has denser clusters of points. Note that the K-S variants are represented in the pole figures by the different colours [31].

Another significant difference between the material prior to and after the RCH was the carbide distribution. The distribution of carbides after the heat treatment is related to the increase in dislocation density during grain refinement. According to Hidalgo and Santofimia [19] and Kennett, Krauss, and Findley [32], the dislocation density from the diffusionless austenite-martensite transformation increases with reducing the PAG size. A smaller grain size causes a larger high-angle grain-boundary fraction which serves as effective barrier to dislocation movement. Then, the dislocation density in the heat-treated steel is larger than in the as-received condition. Also, it has been reported that carbon preferentially diffuses to dislocations, getting segregated, rather than to other features such as lath boundaries [33]. Thus, solute carbon in the austenite lattice is likely to segregate more in the heat-treated steel due to a larger dislocation density than in the as-received steel. Consequently, carbides are found inhomogeneously distributed in the heat treated material, where the presence of carbide clusters is related to areas of carbon-rich dislocations. For instance, Morsdorf et al. [34] associate simultaneous carbon cluster dissolution and cementite precipitation during tempering with carbon-enriched dislocations.

The grain size is also observed to affect austenite decomposition. The reduction in grain size results in a larger grain boundary area density. Consequently, more nucleation sites are available, accelerating the phase transformation from austenite to ferrite [35]. Hence, a larger ferrite fraction is expected after the grain refinement heat treatment. The martensitic transformation is also affected by the PAG size. The grain refinement is known to lower the martensite start temperature (M_s) [36]. This would reduce the degree of auto-tempering of martensite during quenching. Then, the lower M_s along with the slower cementite precipitation kinetics may explain the presence of fresh martensite after tempering in the heat treated material.

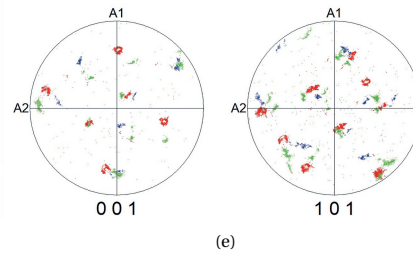
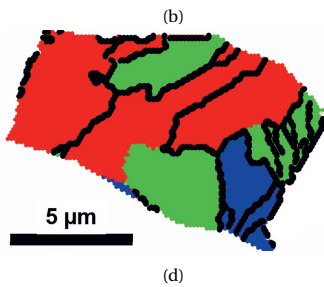
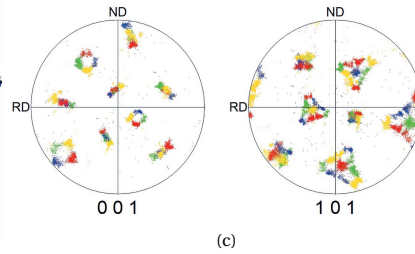
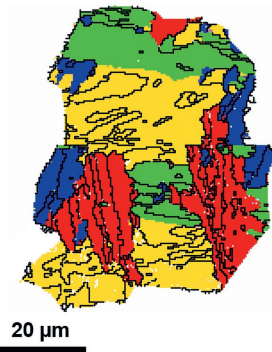
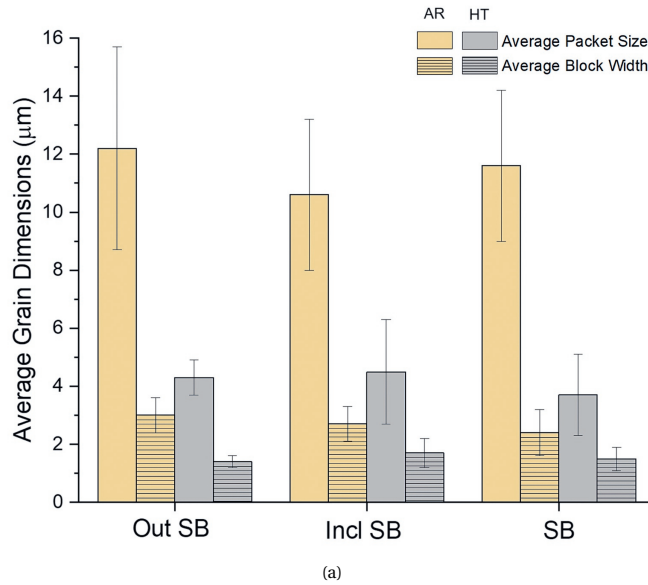


Figure 6.12: Martensite/bainite Packet size and block width and their standard deviation from the mean for the as-received (AR) and heat treated (HT) S690QL high strength steel in areas outside, inside, and including segregation bands. (b,d) cropped prior austenite grains and (c,e) (001) and (101) pole figures of the (b, c) as-received and (d,e) grain refined S690QL high strength steel outside the segregation bands. Each colour represents different packets and variants that share the same habit plane. The black lines in (b) and (d) are high-angle grain boundaries ($>15^\circ$).

6.4.2. GRAIN REFINEMENT EFFECT ON MECHANICAL AND FRACTURE BEHAVIOUR

The influence of grain size on hardness and yield strength is well established and is expressed via the Hall-Petch equations [7, 8]. A smaller grain size yields a higher hardness and yield strength. However, in this study, although a grain refinement of 55% has been achieved via the RCH, only minor increases in hardness and yield strength have been observed. As discussed in the previous section, the microstructure of the as-received steel has been modified after the proposed thermal profile – cyclic heat treatment followed by quenching and tempering. Hence, it is not feasible to separate the individual effect of the grain size reduction. Microstructural aspects such as the larger ferrite content and the lower fraction of cementite in the matrix induce a softening effect that opposes the hardening effect of grain refinement, segregation of carbon in dislocations, and fresh martensite.

With regard to the fracture behaviour, the reduction of grain size leads to an increase in cleavage fracture stress that is significantly larger than the increase in yield strength [3]. The CTOD is directly related to the cleavage stress and inversely related to the yield strength. Then, a smaller grain size leads to a larger CTOD at a given temperature. Consequently, the ductile-to-brittle transition temperature is shifted and, as already reported in other studies [3, 9, 10], the DBTT is reduced. This response explains the significant increase in fracture toughness at $-100\text{ }^{\circ}\text{C}$ after grain refinement. The modified microstructure after the heat treatment is not expected to play such a significant role in fracture toughness improvement. First, hardness and tensile properties that depend on the material matrix microstructure were not significantly changed. Second, the fracture toughness behaviour of the as-received material was observed to be strongly influenced by the initiation sites that were inclusions rather than the propagation step dependent on the matrix [11]. Figure 6.13 shows a schematic representation of the effect of grain refinement on the ductile-to-brittle transition curve and the cleavage initiation sites observed for the lower shelf and lower transition areas and the cleavage initiation micromechanisms. While the as-received steel at $-100\text{ }^{\circ}\text{C}$ is in the lower shelf regime, the decrease in the DBTT seems to bring the heat-treated steel to the lower transition regime or ductile-to-brittle transition region. The increase in CTOD values as well as the large scatter are indications of this shift. Furthermore, from the observations made in this study, the nature of crack nucleation sites may change when the material fracture behaviour shifts from lower shelf to lower transition. On the one hand, Nb-rich inclusions were found to trigger fracture in the as-received steel at $-100\text{ }^{\circ}\text{C}$. On the other hand, in the heat-treated steel, in addition to Nb-rich inclusions, oxide and likely carbides inclusions initiate cracks. Differences in CTOD results are also seen to depend on the initiation sites. Fracture processes initiating from Nb-rich inclusions result in the lowest CTOD values, while initiation from oxide inclusions results in the largest CTOD values. A detailed discussion on the reasons for Nb-rich inclusions being more detrimental can be found elsewhere [11]. The same trend has been observed for the as-received steel [11]. Under a high triaxial stress state, the as-received material is tested on the lower shelf at $-100\text{ }^{\circ}\text{C}$, where Nb-rich inclusions are the dominant initiation sites. However, under a lower stress state in front of the crack, a shift in the ductile to brittle transition is expected

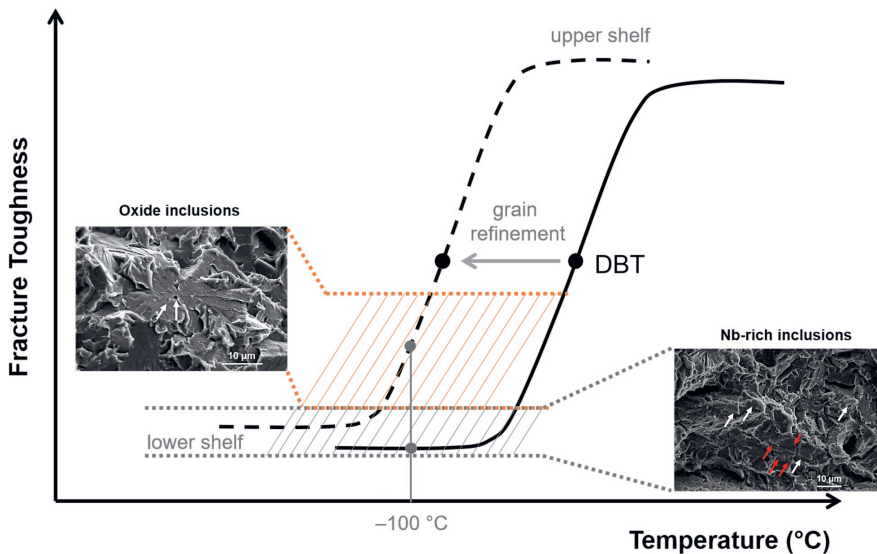


Figure 6.13: Illustration of the effect of grain refinement on the ductile-to-brittle transition curve and the cleavage initiation micromechanisms

6

and oxide inclusions start playing a role in the fracture initiation.

Figure 6.14 shows fracture surfaces from grain-refined specimens where the fracture was triggered from Nb-rich inclusions (Fig. 6.14(a)) and oxide inclusions (e.g., (Mg, Ca)(O)) (Fig. 6.14(b)). As can be seen, both specimens have a stretch zone (i.e., initial stable crack extension) just behind the fatigue pre-crack and right in front of the transgranular cleavage surface. This is evidence of the shift to the lower transition regime as the grain-refined material presents a mixed-mode fracture while the as-received material showed a full cleavage fracture [11]. Furthermore, it has been observed that, when more plasticity is involved in the fracture process, e.g., fracture behaviour shifts from the lower shelf to the lower transition regime, oxide inclusions are activated as cleavage initiation sites with the initial crack extension. This is attributed to the lack of very detrimental inclusion, such as Nb-rich inclusions, ahead of the pre-crack tip. Then, the crack extends stably, and the plastic zone ahead of the crack tip increases as the crack grows (stretch zone) and thus a larger volume of the material is sampled. Hence, there is a larger probability of involving microstructural features in the fracture process that were not present in the previous fracture step [37, 38].

Table 6.3 outlines the effectiveness of the heat treatment by presenting the improvement in mechanical properties and fracture toughness relative to the as-received material, along with the degree of grain size reduction. In summary, the RCH method was shown to be effective in significantly reducing the grain size (55%) of the quenched and tempered S690QL high strength steel. Moreover, even with the presence of very detrimental inclusions such as Nb-rich inclusions, which are responsible for the lowest CTOD values, the grain refinement seems to lead to a shift in the ductile-to-brittle transition

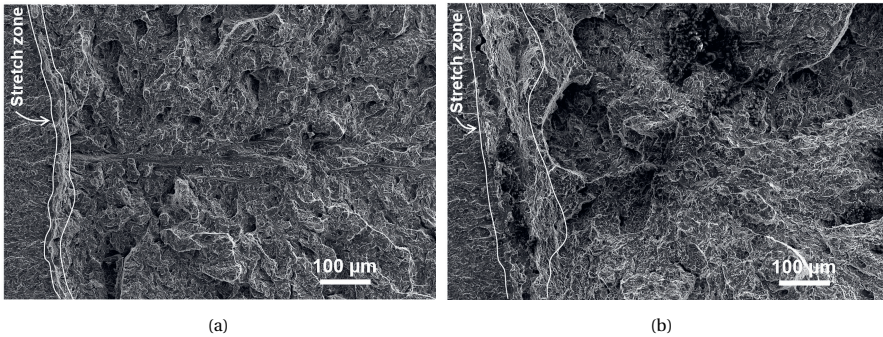


Figure 6.14: Fracture surfaces of grain refined S690QL steel tested at $-100\text{ }^{\circ}\text{C}$ where the fracture was triggered at (a) Nb-rich inclusions (CTOD = 0.03 mm) and (b) oxide inclusions (CTOD=0.1 mm). The stretch zone area is highlighted by the white lines.

Table 6.3: Grain size reduction and properties improvement relative to the as-received material, at room temperature (RT) and $-100\text{ }^{\circ}\text{C}$ after the RCH for grain refinement

Grain Refinement (%)	Properties Improvement Relative to the As-received Material (%)					
	Hardness	Yield Stress		Tensile Stress		Fracture Toughness
	RT	RT	$-100\text{ }^{\circ}\text{C}$	RT	$-100\text{ }^{\circ}\text{C}$	$-100\text{ }^{\circ}\text{C}$
55	3	10	5	2	5	Lower bound: 260
						Upper bound: 850

temperature and improves the fracture toughness at $-100\text{ }^{\circ}\text{C}$ by a factor of 2.5 (lower bound – initiated from Nb-rich inclusions) and a factor of 8.6 (upper bound – initiated from oxide inclusions).

6.5. CONCLUSIONS

Rapid Cyclic Heating (RCH), aimed at refining the steel grain size, followed by quenching and tempering was performed on a quenched and tempered S690QL high strength steel. Then, the effect of grain size reduction on the cleavage fracture behaviour could be individually analysed. The following conclusions were drawn:

- 1. The RCH resulted in a 55% reduction in the PAG size. As a result, the cleavage fracture toughness was improved. However, the type of brittle inclusions initiating the fracture process influences the grain refinement effect on fracture toughness. In general, the grain size reduction decreases the ductile-brittle transition temperature, moving the material from the lower shelf to the lower transition regime at $-100\text{ }^{\circ}\text{C}$. On the one hand, Nb-rich inclusions are responsible for the lower bound fracture toughness that shows an increase by a factor of 2.5 compared to the lower bound fracture toughness of the as-received material. On the other hand, oxide inclusions and probably carbides are recognised as crack initiators in specimens in the upper bound of fracture toughness distribution where toughness is increased by a factor of 8.6 compared to the upper bound of the as-received steel.

2. Oxide inclusions are activated as crack initiators with grain refinement. Compared to the as-received steel where fracture is triggered by Nb-rich inclusions, the grain-refined material has both Nb-rich and oxide inclusions as crack initiators. This happens when there is no detrimental Nb-rich inclusion located ahead of the pre-crack tip. In this case, the crack stably propagates, and the plastic zone ahead of the crack tip increases, sampling a larger volume of the material. This increases the probability of involving microstructural features in the fracture process that were not sampled before.
3. Small enhancements in hardness and yield strength are observed despite the large decrease in grain size. This is attributed to the changes in the matrix as a consequence of grain refinement (e.g., softening effect due to larger ferritic content, lower carbide fraction that opposes the hardening effect of grain refinement).
4. The RCH replaced the elongated, parallel blocks in the martensitic/bainitic grains of the as-received steel by rounded, randomly distributed blocks. Additionally, the high dislocation density generated by grain refinement trapped carbon atoms, resulting in an inhomogeneous carbide distribution where clusters in a few matrix locations are found. and made it less available in solid solution to precipitate into carbides in the tempering step. As a consequence, the carbide fraction is observed to be reduced compared to the as-received steel. This dislocation-carbon interaction also explains the formation of carbide clusters in a few matrix locations. These locations are probably areas of high dislocation density with high carbon segregation. On the other hand, the ferritic content is increased. A smaller grain size implies a larger density of grain boundaries and, consequently, more nucleation sites. Hence, the transformation kinetics from austenite to ferrite is accelerated. Lastly, fresh martensite was formed. Due to the lower martensite start temperature and the slower cementite precipitation kinetics as a consequence of the grain refinement, martensite remained untempered in some areas.

Therefore, this study demonstrates that grain refinement can be very effective in improving the cleavage fracture toughness of multiphase high strength steels even in the presence of brittle deleterious inclusions, allowing for the improvement of steel design. Future modelling work, based on the experimental results presented in this publication, will focus on quantifying the effectiveness of grain refinement on fracture toughness of high strength steels [39]. Additionally, it is interesting to experimentally study the effect of grain refinement, following the thermal profile proposed in the present paper, in a different high strength steel with a lower inclusion fraction. This will allow us to better understand the influence of inclusions on the effectiveness of the RCH treatment for enhancing fracture toughness.

REFERENCES

- [1] Kim, H. J., Kim, Y. H., & Morris, J. W. (1998). Thermal mechanisms of grain and packet refinement in a lath martensitic steel. *ISIJ International*, 38(11), 1277–1285. <https://doi.org/10.2355/isijinternational.38.1277>
- [2] Song, R., Ponge, D., & Raabe, D. (2005). Mechanical properties of an ultra-fine grained C-Mn steel processed by warm deformation and annealing. *Acta Materialia*, 53(18), 4881–4892. <https://doi.org/10.1016/j.actamat.2005.07.009>
- [3] Morris Jr, J. W. (2001). The influence of grain size on the mechanical properties of steel. [https://doi.org/10.1016/S0965-9773\(97\)00137-2](https://doi.org/10.1016/S0965-9773(97)00137-2)
- [4] Park, M. H., Shibata, A., & Tsuji, N. (2020). Challenging Ultra Grain Refinement of Ferrite in Low-C Steel Only by Heat Treatment. *Frontiers in Materials*, 7(November), 1–10. <https://doi.org/10.3389/fmats.2020.604792>
- [5] Li, X., Zhao, J., Dong, L., Devesh Kumar Misra, R., Wang, X., Wang, X., & Shang, C. (2020). The significance of coherent transformation on grain refinement and consequent enhancement in toughness. *Materials*, 13(22), 1–15. <https://doi.org/10.3390/ma13225095>
- [6] Smoljan, B. (2004). An analysis of combined cyclic heat treatment performance. *Journal of Materials Processing Technology*, 155-156(1-3), 1704–1707. <https://doi.org/10.1016/j.jmatprotec.2004.04.121>
- [7] Hall, E. O. (1951). The deformation and ageing of mild steel: III Discussion of results. *Proceedings of the Physical Society. Section B*, 64(9), 747–753. <https://doi.org/10.1088/0370-1301/64/9/303>
- [8] Petch, N. (1953). The cleavage strength of polycrystals. *J. Iron Steel Inst.*, 174(25).
- [9] Inoue, T., Qiu, H., Ueji, R., & Kimura, Y. (2021). Ductile-to-brittle transition and brittle fracture stress of ultrafine-grained low-carbon steel. *Materials*, 14(1634), 1–14. <https://doi.org/10.3390/ma14071634>
- [10] Hanamura, T., Yin, F., & Nagai, K. (2004). Ductile-brittle transition temperature of ultrafine ferrite/cementite microstructure in a low carbon steel controlled by effective grain size. *ISIJ International*, 44(3), 610–617. <https://doi.org/10.2355/isijinternational.44.610>
- [11] Bertolo, V., Jiang, Q., Tiringer, U., Walters, C. L., Sietsma, J., & Popovich, V. (2022). Cleavage Fracture Micromechanisms in Thick-Section Quenched and Tempered S690 High-Strength Steels. *Journal of Materials Science*, 57, 20033–20055. <https://doi.org/10.2139/ssrn.4055055>
- [12] Popovich, V., & Richardson, I. M. (2015). Fracture Toughness of Welded Thick Section High Strength Steels. *TMS 2015 144th Annual Meeting & Exhibition: Supplemental Proceedings.*, 1031–1038. <https://doi.org/10.1002/9781119093466.ch125>
- [13] Srinivas, M., Malakondaiah, G., & Rao, P. R. (1987). Influence of polycrystal grain size on fracture toughness and fatigue threshold in Armco iron. *Engineering Fracture Mechanics*, 28(5-6), 561–576. [https://doi.org/10.1016/0013-7944\(87\)90053-1](https://doi.org/10.1016/0013-7944(87)90053-1)
- [14] Okitsu, Y., Takata, N., & Tsuji, N. (2009). A new route to fabricate ultrafine-grained structures in carbon steels without severe plastic deformation. *Scripta Materialia*, 60(2), 76–79. <https://doi.org/10.1016/j.scriptamat.2008.09.002>

- [15] Tsuji, N., Gholizadeh, R., Ueji, R., Kamikawa, N., Zhao, L., Tian, Y., Bai, Y., & Shibata, A. (2019). Formation mechanism of ultrafine grained microstructures: Various possibilities for fabricating bulk nanostructured metals and alloys. *Materials Transactions*, 60(8), 1518–1532. <https://doi.org/10.2320/matertrans.MF201936>
- [16] Matsumura, Y., & Yada, H. (1987). *Evolution of Ultrafine-grained Ferrite in Hot Successive Deformation* (Doctoral dissertation). <https://doi.org/https://doi.org/10.2355/isijinternational1966.27.492>
- [17] Nasiri, Z., Ghaemifar, S., Naghizadeh, M., & Mirzadeh, H. (2021). Thermal Mechanisms of Grain Refinement in Steels: A Review. *Metals and Materials International*, 27(February), 2078–2094. <https://doi.org/10.1007/s12540-020-00700-1>
- [18] Grange, R. A. (1971). The rapid heat treatment of steel. *Metallurgical Transactions*, 2, 65–78. <https://doi.org/10.1007/BF02662639>
- [19] Hidalgo, J., & Santofimia, M. J. (2016). Effect of Prior Austenite Grain Size Refinement by Thermal Cycling on the Microstructural Features of As-Quenched Lath Martensite. *Metallurgical and Materials Transactions A*, 47A, 5288–5301. <https://doi.org/10.1007/s11661-016-3525-4>
- [20] Aweda, J. O., Orhadahwe, T. A., & Ohijeagbon, I. O. (2018). Rapid Cyclic Heating of Mild Steel and its Effects on Microstructure and Mechanical properties. *IOP Conference Series: Materials Science and Engineering*, 413(012016). <https://doi.org/10.1088/1757-899X/413/1/012016>
- [21] Lv, Z., Ren, X. P., Li, Z. H., Lu, Z. M., & Gao, M. M. (2015). Effects of two different cyclic heat treatments on microstructure and mechanical properties of Ti-V microalloyed steel. *Materials Research*, 18(2), 304–312. <https://doi.org/10.1590/1516-1439.302414>
- [22] Liu, H., Zhang, H., & Li, J. (2018). Thickness Dependence of Toughness in Ultra-Heavy Low-Alloyed Steel Plate after Quenching and Tempering. *Metals*, 8(628), 1–11. <https://doi.org/10.3390/met8080628>
- [23] Bertolo, V., Jiang, Q., Scholl, S., Petrov, R., Hangen, U., Walters, C., Sietsma, J., & Popovich, V. (2022). A Comprehensive Quantitative Characterisation of the Multiphase Microstructure of a Thick-Section High Strength Steel. *Journal of Materials Science*, 57, 7101–7126. <https://doi.org/https://doi.org/10.1007/s10853-022-07121-y>
- [24] CEN. (2019). NEN-EN 10025-6: Hot rolled products of structural steels - Part 6: Technical delivery conditions for flat products of high yield strength structural steels in the quenched and tempered condition.
- [25] ASTM International. (2016). ASTM E1245-03: Standard Practice for Determining the Inclusion or Second-Phase Constituent Content of Metals by Automatic Image Analysis. <https://doi.org/10.1520/E1245-03R08.2>
- [26] Cayron, C. (2007). ARPGE : a computer program to automatically reconstruct the parent grains from electron backscatter diffraction data. *Journal of Applied Crystallography*, 40, 1183–1188. <https://doi.org/10.1107/S0021889807048777>
- [27] BSI. (2015). *BS7910:2013+A1:2015 Guide to methods for assessing the acceptability of flaws in metallic structures* (tech. rep. UK).
- [28] Bertolo, V., Jiang, Q., Terol Sanchez, M., Riemslog, T., Walters, C., Sietsma, J., & Popovich, V. (2023). Cleavage fracture micromechanisms in simulated heat

- affected zones of S690 high strength steels. *Materials Science and Engineering: A*, 868, 144762. <https://doi.org/10.1016/j.msea.2023.144762>
- [29] ISO. (2016). INTERNATIONAL STANDARD Metallic materials — Unified method of test for the determination of quasistatic fracture toughness.
- [30] Takaki, S., Fukunaga, K., Syarif, J., & Tsuchiyama, T. (2004). Effect of grain refinement on thermal stability of metastable austenitic steel. *Materials Transactions*, 45(7), 2245–2251. <https://doi.org/10.2320/matertrans.45.2245>
- [31] Song, T., & De Cooman, B. C. (2013). Effect of boron on the isothermal bainite transformation. *Metallurgical and Materials Transactions A: Physical Metallurgy and Materials Science*, 44(4), 1686–1705. <https://doi.org/10.1007/s11661-012-1522-9>
- [32] Kennett, S. C., Krauss, G., & Findley, K. O. (2015). Prior austenite grain size and tempering effects on the dislocation density of low-C Nb-Ti microalloyed lath martensite. *Scripta Materialia*, 107, 123–126. <https://doi.org/10.1016/j.scriptamat.2015.05.036>
- [33] Morsdorf, L., Jeannin, O., Barbier, D., Mitsuhashi, M., Raabe, D., & Tasan, C. C. (2016). Multiple mechanisms of lath martensite plasticity. *Acta Materialia*, 121, 202–214. <https://doi.org/10.1016/j.actamat.2016.09.006>
- [34] Morsdorf, L., Emelina, E., Gault, B., Herbig, M., & Tasan, C. C. (2021). Carbon redistribution in quenched and tempered lath martensite. *Acta Materialia*, 205, 116521. <https://doi.org/10.1016/j.actamat.2020.116521>
- [35] Park, J. H., & Lee, Y. K. (2008). Non-isothermal austenite formation behavior in an interstitial free steel with different ferrite microstructures. *Scripta Materialia*, 58(7), 602–605. <https://doi.org/10.1016/j.scriptamat.2007.11.021>
- [36] Celada-Casero, C., Sietsma, J., & Santofimia, M. J. (2019). The role of the austenite grain size in the martensitic transformation in low carbon steels. *Materials and Design*, 167. <https://doi.org/10.1016/j.matdes.2019.107625>
- [37] Gu, C., Lian, J., Bao, Y., Xiao, W., & Münstermann, S. (2019). Numerical Study of the Effect of Inclusions on the Residual Stress Distribution in High-Strength Martensitic Steels During Cooling. *Applied Sciences*, 9(455), 1–13. <https://doi.org/10.3390/app9030455>
- [38] François, D., Pineau, A., & Zaoui, A. (2012). Ductile-Brittle Transition. In *Mechanical behaviour of materials: Volume ii: Fracture mechanics and damage* (2nd ed., pp. 265–303). Springer Science & Business Media.
- [39] Jiang, Q., Bertolo, V., Popovich, V., Sietsma, J., & Walters, C. L. (2022). Microstructure-based cleavage modelling to study grain size refinement and simulated heat affected zones of S690 high strength steel. *Under Review in Materials Science and Engineering A*.

7

GENERAL DISCUSSION AND CONCLUSIONS

The focus of the present work has been to quantitatively and systematically connect the microstructural aspects and cleavage fracture behaviour of a thick-section quenched and tempered S690 high strength steel under different microstructural (commercially available, thermally simulated HAZ, and grain refined) and experimental (crack orientation and plastic constraint) conditions. This investigation allowed the identification of the cleavage micromechanisms involved in the fracture process of high strength steel structures with the potential for cleavage fracture (e.g., applied at low temperatures), assisting their failure prediction. Moreover, this work contributes to the improvement of steel design for low-temperature applications since it recognises the most critical microstructural features for fracture and validates a promising processing route for grain refinement and enhancement of cleavage fracture toughness. Eventually, the experimental qualitative and quantitative microstructural and fracture data presented herein represent the required data set for modelling the continuum-level properties of high-strength steels and prediction of their fracture behaviour.

At first, the through-thickness microstructure of the as-received S690QL steel was characterised. This allowed for an understanding of the existing microstructure and the identification of potential critical microstructural features to cleavage fracture in the as-received condition. The microstructure of S690QL has been observed to vary through the thickness of the steel plate, where, compared to the top section, the middle section has larger prior austenite grain (PAG) size, larger sizes and fraction of inclusions, and local hardness gradients due to the hard segregation bands. The middle section is also distinguished by the persistent presence of clusters of cubic Nb-rich inclusions that are sometimes observed decorating PAG boundaries and by the association of inclusions to defects such as voids and cracks. These aspects have been indicated in Chapter 3 as critical for cleavage fracture as they make the middle section more susceptible to crack initiation.

The follow-up investigation of the through-thickness cleavage fracture behaviour of the as-received steel, detailed in Chapter 4, confirmed that the fracture toughness is reduced towards the middle of the steel plate due to the larger sizes and larger area fraction of cubic Nb-rich inclusions. These particles are clearly found as the most detrimental microstructural features in the commercially available S690QL steel since the lowest fracture toughness values are found in specimens where fracture is initiated by Nb-rich inclusions. Moreover, the crack propagation micromechanisms were also studied. Cleavage fracture is transgranular and the S690QL steel predominantly cleaves on the {001} and {110} planes. The crack is seen to be deflected at high-angle grain boundaries such as PAG, packet, and block boundaries of tempered lath martensite and tempered lath bainite. In the case of packet and block boundaries, the crack is significantly diverted when the neighbouring sub-structure has a different Bain axis. In some parts of a few crack tip opening displacement (CTOD) specimens, local intergranular fracture is observed. In these areas, Nb-rich inclusions are found to decorate the PAG boundaries and elements such as C, Cr, Mn, Ni, and P are seen segregating at PAG boundaries. However, inside grains, these alloying elements were also found to be segregated where the material fails in a transgranular manner. Therefore, the elemental segregation is not considered to be sufficient to weaken the PAG boundaries, and Nb-rich inclusions along PAG boundaries are a required or sufficient condition for local intergranular fracture to

occur.

It was also of interest in this research to understand the effect of plastic constraint on the cleavage fracture behaviour of the as-received steel. This study provides a better understanding of the fracture behaviour of actual structures that are likely to contain shallow cracks. For this purpose, two constraints ($a/W=0.25$ and 0.1) other than the standard one ($a/W=0.5$) were analysed. The effect of plastic constraint on cleavage fracture is observed to change depending on the microstructure ahead of the pre-crack tip. In general, the reduction in plastic constraint results in higher fracture toughness. This is in agreement with what was observed in the top section where the crack initiates from spherical oxide inclusions. However, when the crack initiates from very brittle microstructural features such as Nb-rich inclusions, less plasticity is involved in the fracture process and the plastic constraint effect is minor, keeping a low fracture toughness. The crack initiation micromechanism is also affected by plastic constraint. With the reduction in plastic constraint, spherical oxides, which are not observed to initiate cracks in the middle section, are activated as crack initiators. Alternative initiation sites are observed to be activated when the crack initially propagates in a stable manner due to higher plasticity (e.g., low plastic constraint) and the lack of brittle particles to trigger unstable fracture ahead of the crack tip. Then, the plastic zone ahead of the crack tip increases in size, expanding the material volume that is sampled. Consequently, there is a higher probability of involving other microstructural characteristics that were not ahead of the crack tip in the previous fracture step.

Once the as-received material has been studied and the most deleterious microstructural aspects identified, welding thermal simulations were carried out on the middle section, representing the worst-case scenario. Welding processes are frequently used to join structural components and generate poor toughness heat-affected zones (HAZ). Hence, it is of great importance to study cleavage fracture in these zones. Chapter 5 individually analysed the cleavage micromechanisms in the coarse-grained HAZ (CGHAZ) and intercritically reheated CGHAZ (ICCGHAZ) and investigated if the inherited microstructure of the base material, as Nb-rich inclusions that are harder than M-A constituents, would play a role. It has been observed that despite the presence of Nb-rich inclusions, M-A constituents act as the crack initiation sites. Moreover, although M-A constituents trigger fracture in CGHAZ and ICCGHAZs, the predominant phases in the matrix are found to be the most critical aspect for fracture toughness. Due to the M-A constituent brittleness, they trigger fracture, but the critical crack length for unstable crack growth is not reached due to their small size (smaller than $1\text{ }\mu\text{m}$). Thus, the crack-growth step through the matrix and the phase properties are determining the fracture behaviour of the HAZs. This explains the worse fracture performance of the CGHAZ, predominantly composed of auto-tempered martensite, compared to the ICCGHAZ, predominantly composed of granular bainite. Besides the size of M-A constituents, their morphology is an important aspect of the crack propagation step. Secondary cracks deflect and get arrested when they interact with M-A constituents with internal high-angle sub-structures, acting as effective barriers to crack growth, and high internal plastic strains, reducing crack-tip stresses. Then, M-A constituents with these characteristics may delay the crack propagation affecting the fracture behaviour of HAZ.

Lastly, a rapid cyclic heat treatment (RCH) has been proposed in Chapter 6 aiming for

the simultaneous grain refinement and cleavage fracture toughness enhancement of the as-received steel which contains very detrimental Nb-rich inclusions. The improvement of fracture toughness with grain size reduction that results in larger fraction of high-angle grain boundaries. Consequently, more barriers to crack growth are formed and more energy is required for fracture. The rapid cyclic heat treatment is effective in refining the microstructure of the middle section of the S690QL steel by 55% and improving its cleavage fracture toughness. First, as previously mentioned, with grain refinement alternative crack initiators, oxide inclusions and probably carbides, start to play a role together with the very detrimental Nb-rich inclusions. The cleavage fracture toughness improved by a factor of up to 2.6 in the lower bound of fracture toughness when fracture is likely triggered by Nb-rich inclusions and a factor of up to 8.5 in the upper bound of fracture toughness values when cracks are likely initiated from oxides or carbides. Note that, similarly to the low plastic constraint situation, oxides were activated as initiation sites. Thus, despite the harmful effect of Nb-rich inclusions, grain refinement was favourable to cleavage fracture toughness even in their presence.

In summary, Nb-rich inclusions are the most critical initiation sites in the studied S690QL high strength steel, contributing to low fracture toughness values. In HAZs, in turn, M-A constituents initiate the fracture process but are not sufficiently large to reach the critical crack length for unstable fracture. In this case, the propagation through the matrix is an important step where the crack will grow to reach the critical crack length. Hence, the property of the matrix is a key factor for the fracture process and resulting toughness. The propagation micromechanism is consistent in all studied microstructures. The fracture is transgranular and the crack preferentially propagates through the {001} and {110} planes. Crack deflections occur at high-angle PAG boundaries and in packet and block boundaries of lath martensite and lath bainite with different neighbouring Bain axis. In HAZs, M-A constituents with internal sub-structures with high internal plastic strain are able to deflect or arrest the crack.

8

RECOMMENDATIONS

This research consists of a comprehensive experimental study of the cleavage fracture micromechanisms in an 80 mm thick quenched and tempered S690 HSS with the objective of predicting structural failure and optimising the steel's design. The obtained results give indications of the microstructural factors governing cleavage fracture and their influence on the crack initiation and propagation micromechanisms in an HSS. Thereby, this work may serve as a fundamental guide for failure assessments and steel-making processes of HSS. However, there is a broad range of aspects such as microstructures, parameters, and toughening mechanisms that could be further investigated in order to enrich the guide developed herein. Thus, the following topics are suggested for future research:

1. The middle section has a bimodal distribution of PAG size due to the smaller grain sizes of segregation bands that are distributed in layers. It may be that the plate's middle section behaves as a graded material where layers have different properties. This research can be carried out by performing fracture toughness tests where the crack grows from the top section into the middle section. Then, it will be possible to understand if the segregation bands and the bimodal grain distribution would bring beneficial effects to fracture toughness. For instance, increasing the crack deflections in the smaller grain zone and possibly arresting the crack, increasing the fracture toughness.
2. It has been acknowledged in this work that the study of thermally simulated HAZs does not account for the effects of residual stresses present in actual welded structures. Therefore, it is of great importance to analyse whether residual stresses play a role in the microstructure and fracture process, and then validate the cleavage micromechanisms observed for simulated HAZ in the cleavage fracture process of actual welded HSS. This would indicate how accurate studies based on thermal simulations are to predict cleavage fracture in actual structures.
3. Welding parameters such as heat input are known to affect the microstructure of HAZs and, consequently, the cleavage micromechanisms and the fracture toughness of the different welded zones. These micromechanisms and fracture toughness values may vary from the ones observed in this study. Hence, it would be important to evaluate the influence of different welding parameters on the microstructure, cleavage fracture toughness, and fracture micromechanisms in CG-HAZ and ICCGHAZs.
4. It would be interesting to study a different high strength steel with a lower inclusion fraction. This would allow a better understanding of the role of inclusions on the effectiveness of the proposed grain refinement heat treatment, presented in Chapter 6, in fracture toughness.
5. Study the effectiveness of other toughness mechanisms such as grain boundary engineering (e.g., grain boundary misorientation distribution) in improving cleavage fracture toughness in high strength steels. This may allow further improvements in steel's design allowing the safe use of steel in structural applications under harsh environments.

6. The HSS studied in the present research may be taken as a benchmark to qualitatively and quantitatively understand the cleavage micromechanisms in HSS. However, it would be relevant to broaden the microstructural features involved in cleavage fracture and understand their role in the fracture process by studying different types of HSSs, including other delivery conditions than quenched and tempered (e.g., thermo-mechanically controlled processed (TMCP).
7. The investigation of fracture micromechanisms can be extended to the ductile-to-brittle transition region which will allow a better understanding of the temperature effect on fracture and the scatter of toughness usually observed in this zone. Moreover, it would be possible to compare the differences, if any, in the micromechanisms between the lower shelf and the transition zone.

ACKNOWLEDGEMENTS

As much as many moments of the Ph.D. are lonely, my journey has certainly not been on my own. And it is to these people that I owe the most sincere and profound thanks.

I would like to start by thanking my promotors Dr. Vera Popovich, Prof. Jilt Sietsma, and Dr. Carey Walters. Vera, I am eternally grateful for your careful guidance on my Ph.D., always being there to think along, help me develop my critical thinking, advise, encourage, and support me. I also need to thank you for understanding me during the times I was unmotivated with some stages of the research and for pushing me so I could achieve my goal of obtaining this Ph.D. The trust you placed in me and the opportunities offered so that I could carry out research independently, supervise students, and lead meetings were crucial for me to be able to stand out as a researcher and develop my academic career. It was and remains an honor to work with you. Jilt, I need to thank you for the humble, human, and intelligent way in which you guided me and conducted our discussions. I learned a lot from you not only about Materials Science but how to deal with and motivate other people. It is admirable how naturally you do this. Moreover, thank you for sharing your knowledge and suggestions throughout the project. Having you join this project was a pleasant surprise. Carey, thank you for expanding my knowledge horizons by bringing expertise outside the materials science field, for making me think outside the box many times with your ideas in the brainstorming moments of our meetings, and for your careful text revisions, constantly raising interesting points to be considered. It was great working with you and I hope we have more opportunities in the future.

On a day-to-day basis, I also had the company of my project partner, Quanxin Jiang, who worked hard together with me to achieve our project goals and also shared many of the moments of stress, tiredness, joy for accepted papers, and relief for delivering the thesis. Thank you for your company these 4 years, Quanxin. I wish you much success on your journey!

This Ph.D. was part of an NWO project and an industrial consortium in which I had the great opportunity to work in close collaboration with our partners. Then, I would like to thank NWO, Allseas Engineering, Aktien-Gesellschaft der Dillinger Hüttenwerke, Lloyd's Register, The Dutch Ministry of Defence, and TNO. Namely, I acknowledge Sebastian Scholl, Kinshuk Srivastava, Natalia Ermolaeva, Bin Hu, Weihong He, Andre Vaders, Lili Hou, Li Xu, Okko Coppejans, Martijn Hoogeland, and Casper Versteylen. The interesting discussions we had in our progress meetings and your comments and feedback on reports, presentations, and manuscripts were enriching. Thank you all for your support!

I would like to thank the committee members, Prof. Maria Santofimia, Prof. Patricia Verleysen, Prof. Laurent Delannay, Dr. Ilchat Sabirov, and Prof. Leo Kestens, for making themselves available to be part of this committee as well as for reading, discussing, contributing, and evaluating this work.

A special thanks go to Prof. Roumen Petrov who was an active part of my Ph.D., despite not being a supervisor. Your interest in the student's difficulties and immediate

availability to help them, and your funny and light way of dealing with certain academic matters inspire me. I really want to thank you for the valuable discussions we had, including about EBSD which made me learn most of the things I know today about EBSD data post-processing. Thank you also for your dedication in always trying to get the best results when help is asked, even if it takes a considerable amount of time. I feel very happy to continue working with you, now officially having you as a supervisor.

I was really fortunate to be surrounded by such incredible colleagues and staff from the MSE department who were available countless times to give me the support I needed for my Ph.D. journey and research. Remko Seijffers, Elise Reinton, Sander van Asperen, Hans Hoffman, Nico Gerlofs, Sean Scott, Saskia Brandt Corstius, Ruud Hendrikx, Hans Brewer, and Jurriaan van Slingerland. To Ton Riemsdag and Kees Kwakernaak, I express my deepest gratitude. Ton, thank you so much for the lessons shared, for always being willing to think together and find solutions, for the many quick and last-minute works you have done in the workshop to help me perform a task, for the constant motivational words, and for the long, funny, and curious conversations about the most diverse subjects. Kees, thank you so much for sharing your knowledge and techniques, for always being available with the dedication to understand the problems involved with the use of microscopes, and for helping and supporting me in learning new and sophisticated techniques. It was and remains a pleasure working with you both!

I would like to express great gratitude to the research assistant, María Terol Sanchez, the master's student, Vishnu Cheekati, and the intern, Léa Vilasi, who were also part of this project and whom I was lucky enough to work with, supervise, and learn from. Kaustubh Deshmukh and Dionysios Dasopoulos, the same words apply to you, but I also would especially like to thank you for your support during challenging times during my Ph.D., for the conversations and funny moments we shared, and for the friendship we built.

I also thank the student assistants who saved me many times, for example, with the cutting machine that the water often did not come out, the SEM that had the filament burned out, with the SEM reservations often at the last minute, and with the conversations that were always made the days lighter. As it has been four years, many of them are already following other brilliant paths, but I must thank them for the essential help they gave me in those old days. Thank you Katja Jarc, Luis de Almeida Nieto, María Terol Sanchez, Thanasis Kefalas, Sezen Kadir, and Alice Dautezac.

I would like to thank those who encouraged and gave full support when I decided to do my Ph.D. abroad besides teaching, inspiring, guiding, and supporting me from the beginning of my academic life in Materials Engineering: Prof. Rafaella Martins Ribeiro, Prof. Fernando Luiz Bastian (*in memoriam*), and Prof. João Marcos Alcoforado Rebello (*in memoriam*) from Universidade Federal do Rio de Janeiro (UFRJ).

To the friends of the MSE department, Jia-Ning, Vitória, Nicolas, Zhaorui, Joost, Viviam, Gaojie Li, Jhon, Jaji, José, Arjun, and Aravind, thank you for the many conversations, lab times, conferences, funny moments, lunch, and coffee breaks that we have shared. In particular, I would like to thank Maxine Ankora, Urša Tiringier, and Mirsajjad Mousavi. Maxine, I consider myself very lucky to have you by my side, your fun companion, with your support and sincere opinion, ready to share with me the moments whether happy or sad, understand my delays of many days to answer a

message, and not hate me (I think). I have no words to thank you! You are an amazing friend! Urša, you were the first one I met and I need to say how fortunate I was. Your way and your generosity made everything easier. Thank you very much for the many moments shared, our walks, for the many pieces of advice, and for having introduced me to the corrosion group that was also mine for a long time. You are very special to me. Sajjad, you are that person who brings joy wherever you go and that has certainly made a difference for me over the years. Thank you for your friendship and for always being there with kindness, care, and optimism.

Despite being physically far away, I must thank my friends in Brazil, Maíra, Anderson, and Paula, who were constantly present, celebrating my achievements, vibrating together, and listening and encouraging me in difficult times.

I immensely thank my parents, Denise and Luiz, and my brother Victor, for their efforts, dedication, care, their support (or lack of support in certain decisions), motivation, understanding, and unconditional love. Also, thank you for making our family relationship a fun and friendly one, always remembering that we can count on each other for everything. All this gave me the essential basis to obtain this Ph.D. Thank you so much for always being present, despite the distance, celebrating every single achievement, and dreaming together with me! I love you!

My eternal and immense gratitude to my husband, Guilherme, who strongly encouraged me on this Ph.D. journey abroad and embraced my challenges as his own. I am extremely fortunate to share my life with you. Thank you for always trying to comfort me in difficult times, for your funny way and jokes at not-so-appropriate times (at least for me, I am extremely formal like you like to make fun of) that always bring joy, your understanding (except for my stubborn moments), patience (!!!!!), and ears always available to listen to me. These were essential for me to get here. Thank you for everything and some more! After a few years of you messing with me, I will finally be the person at home with the highest academic degree. I love you!

Virgínia Bertolo

Delft, February 2023

CURRICULUM VITÆ

VIRGÍNIA MORETE BARBOSA BERTOLO

Born on the 15th of July 1992, Rio de Janeiro, RJ, Brazil

EDUCATION

2010–2016	Bachelor of Science in Materials Engineering Universidade Federal do Rio de Janeiro (UFRJ)
2014–2015	Exchange Student in Materials Science and Engineering Swansea University
2016–2018	Master of Science in Metallurgical and Materials Engineering Awarded: CREA-RJ Award for Scientific and Technological Works 2017 Universidade Federal do Rio de Janeiro (UFRJ)
2018–2023	Ph.D. Materials Science and Engineering Delft University of Technology (TU Delft) <i>Thesis:</i> Cleavage Fracture Micromechanisms of High Strength Steel and its Heat-Affected Zones

PROFESSIONAL EXPERIENCE

2018–2023	Ph.D. Researcher Delft University of Technology (TU Delft)
Jan–Feb/2022	Guest Researcher Max-Planck-Institut für Eisenforschung GmbH (MPIE)
Oct/2022–Present	PostDoc Researcher Delft University of Technology (TU Delft) Ghent University (UGent)

LIST OF PUBLICATIONS

Peer-reviewed Journal Papers

1. **Bertolo, V.**, Jiang, Q., Terol Sanchez, M, Riemsлаг, T., Walters, C., Sietsma, J. & Popovich, V. (2023). Cleavage Fracture Micromechanisms in Simulated Heat Affected Zones of S690 High Strength Steels, *Materials Science and Engineering A*, 868, 144762. <https://doi.org/10.1016/j.msea.2023.144762>
2. **Bertolo, V.**, Vilasi., L., Jiang, Q., Riemsлаг, T., Scott, S., Walters, C., Sietsma, J. & Popovich, V. (2023). Grain Refinement by Rapid Cyclic Heating and its Effect on Cleavage Fracture Behaviour of an S690 High Strength Steel, *Journal of Materials Research and Technology*, 23, 1919-1933. <https://doi.org/10.1016/j.jmrt.2023.01.164>
3. Jiang, Q., **Bertolo, V. M.**, Pallaspuuro, S., Popovich, V. A., Sietsma, J. & Walters, C. (2023). Microstructure-based cleavage parameters in bainitic, martensitic, and ferritic steels, *Engineering Fracture Mechanics*, 281, 109146. <https://doi.org/10.1016/j.engfracmech.2023.109146>
4. Jiang, Q., **Bertolo, V. M.**, Popovich, V. A., Sietsma, J. & Walters, C. (2023). Microstructure-based cleavage modelling to study grain size refinement and simulated heat affected zones of S690 high strength steel, *Under Review in Materials Science and Engineering A*
5. **Bertolo, V.**, Jiang, Q., Tiringer, U., Walters, C., Sietsma, J. & Popovich, V. (2022). Cleavage fracture micromechanisms in thick-section quenched and tempered S690 high-strength steels, *Journal of Materials Science*, 57, 20033-20055. <https://doi.org/10.1007/s10853-022-07841-1>
6. **Bertolo, V.**, Jiang, Q., Scholl, S., Petrov, R. H., Hangen, U., Walters, C., Sietsma, J. & Popovich, V. (2022). A comprehensive quantitative characterisation of the multiphase microstructure of a thick-section high strength steel, *Journal of Materials Science*, 57, 7101-7126. <https://doi.org/10.1007/s10853-022-07121-y>
7. Jiang, Q., **Bertolo, V. M.**, Popovich, V. A., Sietsma, J. & Walters, C. (2022). Microstructure-informed statistical modelling of cleavage fracture in high strength steels considering through-thickness inhomogeneities, *Engineering Fracture Mechanics*, 267. <https://doi.org/10.1016/j.engfracmech.2022.108432>
8. Jiang, Q., **Bertolo, V. M.**, Popovich, V. A., Sietsma, J. & Walters, C. (2021). Relating matrix stress to local stress on a hard microstructural inclusion for understanding cleavage fracture in high strength steel, *International Journal of Fracture*, 232, 1-21. <https://doi.org/10.1007/s10704-021-00587-y>

Other works

1. Ghorbanpour, S., Deshmukh, K., Sahu, S., Riemsлаг, T., Reiton, E., Borisov, E., Popovich, A., **Bertolo, V.**, Jiang, Q., Terol Sanchez, M., Knezevic, M. & Popovich, V. (2022). Additive manufacturing of functionally graded inconel 718: Effect of heat treatment and building orientation on microstructure and fatigue behaviour, *Journal of Materials Processing Technology*, 306, 1-22. <https://doi.org/10.1016/j.jmatprotec.2022.117573>
2. Ghorbanpour, S., Sahu, S., Deshmukh, K., Borisov, E., Riemsлаг, T., Reiton, E., **Bertolo, V.**, Jiang, Q., Popovich, A., Shamshurin, A., Knezevic, M. & Popovich, V. (2021). Effect of microstructure induced anisotropy on fatigue behaviour of functionally graded Inconel 718 fabricated by additive manufacturing, *Materials Characterization*, 179, 1-18. <https://doi.org/10.1016/j.matchar.2021.111350>

International Conference Proceedings

1. Jiang, Q., **Bertolo, V. M.**, Popovich, V. A., Sietsma, J. & Walters, C. L. (2022). Numerical modelling of cleavage in high strength steels with parametric study on microstructures, *Procedia Structural Integrity, Proceeding of European Conference on Fracture 2022*, 42, 465-470. <https://doi.org/10.1016/j.prostr.2022.12.059>
2. **Bertolo, V.**, Jiang, Q., Walters, C. L. & Popovich, V. A. (2020). Effect of Microstructure on Cleavage Fracture of Thick-Section Quenched and Tempered S690 High-Strength Steel, *Characterization of Minerals, Metals, and Materials 2020*. The Minerals, Metals & Materials Series. Springer, Cham. https://doi.org/10.1007/978-3-030-36628-5_15
(Awarded the EPD Materials Characterization Best Paper)
3. Jiang, Q., **Bertolo, V.**, Popovich, V. A. & Walters, C. L. (2019). Recent Developments and Challenges of Cleavage Fracture Modelling in Steels: Aspects on Microstructural Mechanics and Local Approach Methods, *Proceedings of the ASME 2019 38th International Conference on Ocean, Offshore and Arctic Engineering OMAE 2019* <https://doi.org/10.1115/OMAE2019-95464>

